Max-Planck-Institut
für Meteorologie

EXAMENSARBEIT Nr. 59

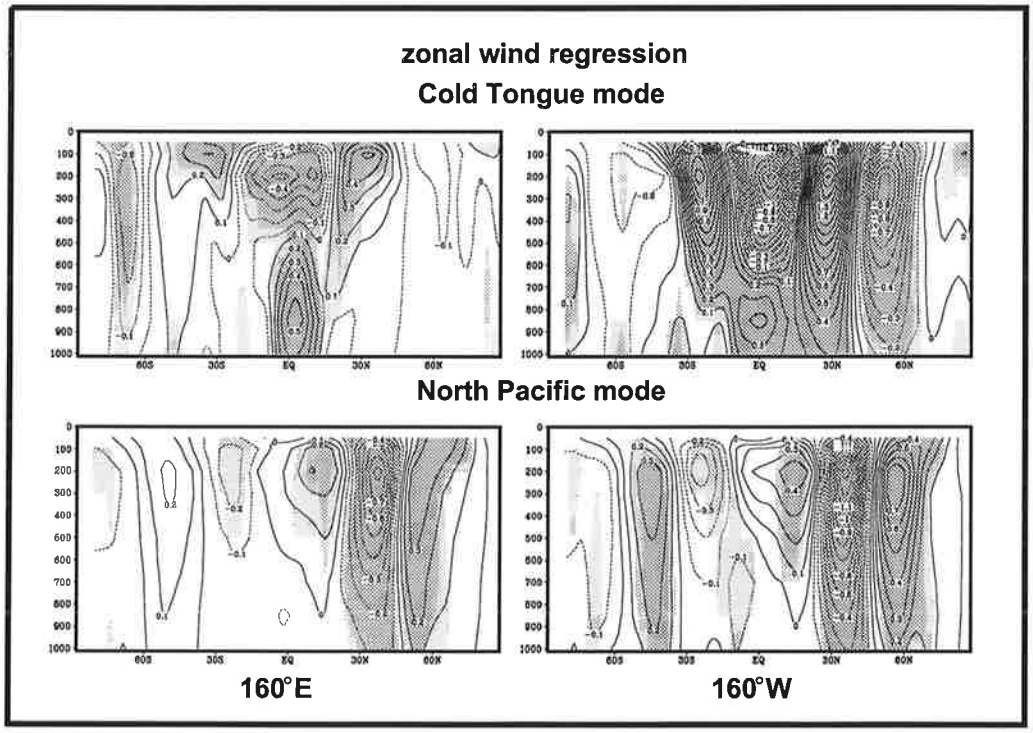

VARIABILITY ON DECADAL SCALES IN PACIFIC SEA SURFACE TEMPERATURES AND ATMOSPHERE OCEAN INTERACTION IN THE COUPLED GENERAL CIRCULATION MODEL ECHAM4/OPYC3

von
Andreas Bacher

HAMBURG, August 1998

Dissertation zur Erlangung des Doktorgrades

Autor:

Andreas Bacher

Max-Planck-Institut
für Meteorologie

MAX-PLANCK-INSTITUT
FÜR METEOROLOGIE
BUNDESSTRASSE 55
D - 20146 HAMBURG
GERMANY

Tel.: +49-(0)40-4 11 73-0
Telefax: +49-(0)40-4 11 73-298
E-Mail: <name> @ dkrz.de

Variability on decadal scales in Pacific sea surface temperatures and atmosphere ocean interaction in the coupled general circulation model ECHAM4/OPYC3

Dissertation
zur Erlangung des Doktorgrades
der Naturwissenschaften im Fachbereich
Geowissenschaften
der
Universität Hamburg

vorgelegt
von
Andreas Bacher
aus Unkel

Hamburg
1998

ISSN 0938-5177

Als Dissertation angenommen vom Fachbereich Geowissenschaften
der Universität Hamburg

auf Grund der Gutachten

von	Dr. habil. E. Roeckner
und	Dr. U. Mikolajewicz

Hamburg, den 9. Juli 1998

Prof. Dr. G. Miehlich
Dekan
des Fachbereichs Geowissenschaften

Contents

To I. H.

Abstract

The work presented in this thesis consists of both practical development and analytical investigation of a run with the coupled climate model ECHAM4/OPYC3. The practical aspect involved the development of a coupling interface for synchronizing ECHAM and OPYC and performing the regridding of the surface fluxes and SST. The numerical treatment of the regridding problem is innovative in coupled climate modelling. A meshwidth refinement strategy in analogy to interpolatory subdivision, widespread in Computer Aided Geometric Design (CAGD), was developed which preserves positivity for fields such as river discharge. It includes special treatment of the irregular domain given by ocean grid points only and employs open boundaries at the latitudinal extremities. The annual mean flux adjustment used was based on ideas by Oberhuber (pers. comm.), in collaboration with whom a scheme for heat flux adjustment for sea ice covered grid points was implemented.

The coupled model simulation for the Pacific reproduces the mean climate simulated by the uncoupled model as discussed in Roeckner et al. (1996b). Temperature, zonal wind, 500 hPa height and preciptation annual mean and seasonal results deviate little from the uncoupled reference. For sea surface temperature (SST) the seasonal cycle of warm pool and cold tongue extent is similar to observations, apart from cooling in the north-eastern warm pool area about one month prematurely and a premature termination of the cold tongue cold phase. Surface heat fluxes and wind stress agree with the Oberhuber (1988) and ECMWF reanalysis climatologies, respectively, if the uncertainties in the heat flux climatology, e.g. over the warm pool domain, are taken into account. Exceptions are excessive heat flux in areas with stratus over the eastern subtropical oceans and the substantial overestimation of boreal summer south-eastern trades on the equator. Mixed layers are predicted successfully. The tropical thermocline and currents due to the use of isopycnic coordinates are located correctly, but currents are artificially broadened and attain only about half the observed maximum speeds. Sea ice seasonal evolution agrees with observations except for underestimated Antarctic winter sea ice cover.

Decadal scale Pacific SST variability was mostly captured by the projection onto two modes. One mode was linearly related to decadal eastern equatorial Pacific cold tongue ('CT') variability. The other, termed the 'NP' (North Pacific) mode, was obtained as the dominant mode of an SVD analysis of Pacific domain SST and 500 hPa geopotential height both of which had first been transformed to residual fields by removing the variability linearly related to the CT index. These modes were found both in the coupled control integration and in an integration of the ECHAM4 model with the boundary condition prescribed from the GISST 2.2 dataset. Explained fractions of variance for these modes of covariability of SST and the general circulation are substantially greater than expected for a null continuum. The associated regression patterns closely resembled the patterns of Pacific SST variability found by Deser and Blackmon (1995) or those found in Zhang et al. (1996). A regression analysis for zonal wind and temperature on latitude-pressure sections both at 160° E and 160° W was performed to address the problem of a robust atmospheric response to the two types of SST anomalies. A significant signal consistent with equivalent barotropic structure and thermal wind balance was associated with each mode. Due to the substantial midlatitude contribution found in the NP mode SST pattern, the regression result is of interest regarding the persistent controversy as to whether midlatitude SST has a detectable influence on the extratropical circulation (Namias, 1959, Pitcher et al., 1988, Latif and Barnett, 1994, Peng et al., 1997). The CT related anomalies were consistent with a weakened Walker circulation familiar from ENSO, consistent with which there was

also a North East Pacific response (Roeckner et al., 1996a).

The analysis of SST tendency terms examined heat flux components, but also lateral and vertical heat fluxes through the depth of the mixed layer. Heat fluxes for the CT mode exhibit negative correlation dominated by latent heat flux and shortwave radiation, mostly confined to the tropics as in the study by Lau and Nath (1994). For the decadal scale, a sizable negative correlation with the CT pattern was found for shortwave radiation between 10° N and 25° N along the northern flank of the triangular tropical SST anomaly, explained by anomalous moisture convergence in the PBL and associated midlevel convection. For the NP mode, positive shortwave radiative flux anomalies associated with negative SST anomalies were found near the date line south of the equator. The other prominent signal for this mode consisted in turbulent heat flux in the western North Pacific associated with warm SST anomalies, heating the surface south-east of Japan but cooling it further north. In the eastern subtropical North Pacific the anomalous heat budget was dominated by upwelling (downwelling) associated with cold (warm) SST anomalies. For both modes this could be attributed to oceanic Rossby waves in consequence of more than one ENSO (cf. Meyers et al., 1996). The North Pacific SST anomalies were predominantly maintained by the advective Ekman contribution. Applying Sverdrup balance, the wind stress anomalies associated with a warm (cold) midlatitude SST anomaly implied anomalous meridional convergence (divergence) in the thermocline. A complex regression analysis of sea level confirmed this ocean response. It also corroborated the Rossby wave mechanism for the CT mode, yielding patterns similar to the coupled model study by Yukimoto et al. (1996). The results for the NP mode were similar to those obtained in the coupled models of Latif and Barnett (1994) and Storch (1994).

Difference patterns for periods after and before the 1976 'climate shift' shown for SST by Namias (1979), for SLP by Trenberth (1990) and for net surface heat flux and wind stress by Yasuda and Hanawa (1996) were found to be reproduced by the coupled model in terms of the regression patterns for the NP mode.

Zusammenfassung

Die vorliegende Arbeit beschreibt technische Entwicklungsarbeiten und statistische Analysen des Autors hinsichtlich des gekoppelten Atmosphäre-Ozean-Klimamodells ECHAM4/OPYC3. Der technische Beitrag des Autors besteht in der Entwicklung eines eigenständigen Programmpaketes und der Modifikation des Datenflusses beider Einzelmodelle derart, daß eine synchron gekoppelte Simulation beider Komponenten abläuft. Für die tägliche Übergabe der Flüsse von Wärme, Impuls und turbulenter kinetischer Energie an der Meeresoberfläche sowie von Netto-Niederschlag und Flußeintrag wurde ein in der gekoppelten Klimamodellierung neuartiges numerisches Verfahren entwickelt. Integralerhaltende Gittertransformation von ECHAM zu OPYC wird erzielt, indem ein von ECHAM berechneter Fluß an der Meeresoberfläche zunächst als Histogramm auf dem rekursiv verfeinerten Gitter dargestellt und anschließend durch einfache Flächenmittelung auf das Gitter in OPYC übertragen wird. Der Fall der Positivität, z. B. beim Flußeintrag, wird berücksichtigt. Die durch Küsten gegebenen irregulären Randstücke und die meridionale Einschränkung auf Tropen und Subtropen werden geeignet behandelt. Die Simulation verwendet nach Oberhuber (pers. Mitteilg.) eine Flußkorrektur, die keinen Jahresgang aufweist und nur auf die Flüsse von Wärme und Frischwasser (Kombination von Niederschlag, Verdunstung und Flußeintrag) wirkt.

Das mittlere Klima der gekoppelten Kontrollsimulation stimmt gut mit dem des ungekoppelten Atmosphärenmodells überein (Roeckner et al. 1996b). Temperatur, Zonalwind, geopotentielle Höhe der 500-hPa-Fläche und Niederschlag weichen im Jahres-, Winter- und Sommermittel wenig vom ungekoppelten Modus ab. Der Jahresgang der in OPYC berechnete Meeresoberflächen-Temperatur (engl. 'sea surface temperature', SST) reproduziert die Beobachtungen, abgesehen von einer etwa einen Monat verfrüht einsetzenden Abkühlung des nordöstlichen Randbereichs im westpazifischen Warmwassergebiet und einem vorzeitigen Übergang von der Kalt- zur Warmphase in Bereich der kalten Zunge im östlichen Äquatorialpazifik. Oberflächenflüsse von Wärme und Impuls liefert die Simulation in guter Übereinstimmung mit der Klimatologie von Oberhuber (1988) bzw. der Reanalyse des Europäischen Zentrums für Mittelfrist-Wettervorhersage (EZMW). Ausnahmen hiervon bilden überhöhte Wärmefluß-Werte in Bereichen maritimer Stratusbewölkung und deutlich überhöhte Werte der Windschubspannung (=Impulsfluß) im Äquatorialpazifik im nordhemispärischen Sommer. Der Jahresgang der Tiefe der ozeanischen Deckschicht wird von OPYC mit gutem Erfolg simuliert. Dank der in Länge, Breite und Zeit variierenden vertikalen Diskretisierung nach Isopyknen haben äquatoriale Strömungen und Sprungschicht (Thermokline) einen realistischen Verlauf, doch zeigen die Strömungen eine erheblich überschätzte laterale Ausdehnung und nur etwa die Hälfte der beobachteten Maximalgeschwindigkeiten. Die simulierte Meereisbedeckung reproduziert die Beobachtungen, abgesehen von einer Unterschätzung der antarktischen Eisausdehnung im Wintermaximum.

Im wesentlichen läßt sich die simulierte dekadische Variabilität der SST im Pazifik durch ein Paar Indexzeitreihen und die zugehörigen Regressionsmuster der SST darstellen. Der erste Index beschreibt den durch Tiefpaßfilterung mit Transmission für dekadische und längere Skalen gewonnenen Anteil der Variabilität in der äquatorialen kalten Zunge (engl. 'cold tongue', CT). Der zweite Index wird als 'NP'-Index (für 'Nordpazifik') bezeichnet und ergibt sich als Entwicklungskoeffizient für das führende Paar singulärer Vektoren in der Singulärwertzerlegung ('SVD') der Kreuzkovarianzmatrix der nach Elimination des CT-Anteils verbleibenden Residualgrößen pazifischer SST und der geopotentiellen Höhe der 500-hPa-Fläche. Beide Indizes können aufgrund des jeweiligen Anteils erklärter Varianz, der deutlich über dem für ein Nullkontinuum erwarteten Wert liegt, als Moden der

Kovariabilität pazifischer SST und der allgemeinen Zirkulation auf dekadischen und längeren Zeitskalen angesehen werden. Beide Moden wurden sowohl für die gekoppelte Kontrollsimulation als auch für eine multidekadische Simulation mit ECHAM4 unter Vorgabe von SST des GISST 2.2 Datensatzes erhalten. Meridionalschnitte bei 160° E und 160° W für Temperatur und Zonalwind zeigen signifikante Regressionsmuster, die der thermischen Windgleichung genügen. Da das SST-Muster des NP-Index wesentliche Beiträge im Nordpazifik zeigt, weist dies auf mögliche Verursachung von Zirkulationsanomalien durch extratropische SST hin, worüber bis heute eine Kontroverse besteht (Namias 1959, Pitcher et al. 1988, Latif und Barnett 1994, Peng et al. 1997). Bzgl. des CT-Index beschreiben die Regressionsmuster eine Abschwächung der äquatorialen zonalen 'Walker'-Zirkulation, wie sie auch bei einem El-Niño/Südliche-Oszillations-Ereignis (ENSO) auftritt, sowie eine entsprechende Reaktion in mittleren Breiten im Nordpazifik (vgl. Roeckner et al., 1996a).

Mittels linearer Regression für beide Indizes wurde die Bedeutung der einzelnen Tendenzterme in der SST-Gleichung unter besonderer Berücksichtigung der turbulenten und strahlungsbedingten Anteile am Wärmefluß an der Meeresoberfläche untersucht. Letzterer zeigt bzgl. des CT-Index ein auf die Tropen konzentriertes Muster mit vorwiegend negativer Korrelation und wird im wesentlichen durch den Fluß latenter Wärme und die absorbierte kurzwellige Strahlung bestimmt. Dies wurde für interannuale Skalen von Lau und Nath (1994) in ähnlicher Form festgestellt. Im Unterschied zu deren Ergebnissen führt die Konzentration auf dekadische Skalen zu erheblichen Werten der Regression des Wärmeflusses in einem Bereich von 15° N bis 25° N, was der Nordflanke der meridional auf Dreiecksgestalt verbreiteten ENSO-ähnlichen SST-Anomalie entspricht. Hier dominiert die Abschwächung der kurzwelligen Strahlung aufgrund anomaler bodennaher Konvergenz und dadurch bedingte vermehrte mittelhohe Konvektion. Beim NP-Index ergibt sich im Zentral-/Westpazifik leicht südlich des Äquators vermehrte Einstrahlung bei negativen SST-Anomalien, während im westlichen Nordpazifik bei positiven SST-Anomalien der Netto-Wärmefluß eine Erwärmung der Meeresoberfläche südöstlich von Japan sowie eine Abkühlung weiter nördlich bewirkt. Im nordöstlichen subtropischen Pazifik dominiert für positive (negative) SST-Anomalien die Abschwächung (Verstärkung) des Abkühlungseffekts infolge aus der Thermokline in den turbulenten Deckschichtbereich aufsteigenden Wassers. Dies läßt sich für beide Indizes im wesentlichen als Auswirkung von Störungen der Thermokline infolge subtropischer Rossbywellen-Aktivität im Zusammenhang mit aufeinanderfolgenden ENSO-Ereignissen interpretieren (vgl. Meyers et al. 1996). Für die nordpazifischen SST-Anomalien in mittleren Breiten sind anomale advektive Wärmeflüsse infolge Ekman-Drift maßgeblich. Hier ergibt eine qualitative Argumentation unter Annahme Sverdrupscher Strömung für die zu positiven (negativen) SST-Anomalien assoziierten Windschubanomalien anomale Konvergenz (Divergenz) in der Thermoklinen. Diese Thermoklinenreaktion wurde durch eine komplexwertige Regression des Wasserstandes bzgl. der beiden Indizes bestätigt, ebenso die Rolle von Rossbywellenaktivität in den Subtropen. Die komplexe Regression ergab für den CT-Index qualitative Übereinstimmung mit dem bei Yukimoto et al. (1996) beschriebenen gekoppelten Modell, während für den NP-Index Modellergebnisse von Storch (1994) und Latif und Barnett (1994) reproduziert wurden.

Übereinstimmung zeigen die Ergebnisse der vorliegenden gekoppelten Simulation mit Analysen von Beobachtungen im Hinblick auf die 1976 verzeichnete 'Klimaverschiebung' im nordpazifischen Raum. Differenzmuster für Zeiträume nach und vor diesem Ereignis finden sich bzgl. SST bei Namias (1979), bzgl. Bodendruck bei Trenberth (1990) sowie bzgl. der Flüsse von Wärme und Impuls an der Meeresoberfläche bei Yasuda und Hanawa (1996). Diesen entsprechen in der gekoppelten Simulation die Regressionsmuster des NP-Index.

Chapter 1

Introduction

Pacific Ocean sea surface temperature (SST) anomalies with interannual and decadal timescales and their role in sustained anomalous climate states have been the focus of a vast body of modelling and observational research. The largest climate variation on the interannual scale, the El Niño/Southern Oscillation phenomenon, has profound climatic impacts on the economies primarily of the South American continent and the Australian-Indonesian region. The characterization of this climate variation as a trans-Pacific seesaw in sea level pressure by the work of Walker (1924, 1925, 1928) and Walker and Bliss (1930, 1932, 1937) captured the anomalous atmospheric circulation state which induces the changes in precipitation over land adjacent to the Pacific Ocean both to the east and the west. These anomalies in the zonal equatorial 'Walker' circulation are characterized by the difference in the sea level pressures of Darwin and Tahiti, termed the 'Southern Oscillation Index' (SOI). The realization that these anomalies are related to large scale anomalies of sea surface temperature in the equatorial central and eastern Pacific came with the work by Ichie and Petersen (1963) and Berlage (1966). The robustness of the atmospheric response to the tropical SST anomalies was demonstrated in simulations using models of the atmospheric general circulation by, e.g., Rowntree (1972), Shukla and Wallace (1983) and Palmer and Mansfield (1986a,b), to name a few. This response is strongest in the equatorial Walker cell, but various parts of the globe, particularly North America, central and southern Africa and India experience significant climate variation during extremes of the Southern Oscillation (Ropelewski and Halpert, 1987).

The SST anomalies generally associated with a low value of the SOI form a global pattern but the dominant contribution is found in the equatorial east Pacific, evident, e.g., in the empirical orthogonal function analysis of Weare et al. (1976). The oceanic equatorial cold tongue in 'low' phases of the SOI exhibits large deviation from the normal seasonal cycle. Normal conditions are characterized by minimum extent in April but subsequent westward shifting of isotherms linked to the cold phase which lasts through the second half of a normal year. Anomalously low SOI is accompanied by warm conditions in the cold tongue region and maximum warm anomalies in the upwelling region along the Peruvian coast. The high sensitivity in the upwelling regions along the coast and on the equator was taken as an indication that a dynamic ocean response to wind changes rather than changes in surface heat flux was crucial in favouring the growth of the SST anomalies over several months.

In fact, the principal ideas were expressed by Bjerknes (1966). The trade winds drive westward transport through two major upper ocean current systems, the North Equatorial Current and the South Equatorial Current. A west-east sloping of the sea surface results with sea surface elevation in the west exceeding that in the east by roughly 40 cm. Reverse flow takes place in the North Equatorial Countercurrent and the Equatorial Undercurrent such that upwelling of the substantially colder water of the undercurrent becomes important particularly in the east where the current comes closest to the surface. Wavelike propagation of thermocline disturbances along the equator in the form of eastward travelling Kelvin waves then provides the central mechanism that can induce SST anomalies in these sensitive regions as emphasized by Wyrtki (1975) with supporting evidence from tide gauge measurements. Via the modified SST the lower branches of the Hadley and Walker circulations are affected and the trades deviate from their normal annual cycle. The relationship between

surface winds and horizontal SST gradients was discussed, e.g., by Lindzen and Nigam (1987). The response of the upper ocean to changes in the wind provides a feedback on the currents and associated heat transports and hence, on SST. Positive SST anomalies in the cold tongue act to delay and weaken the normal maximum north-westward expansion of the south-eastern trades in the second half of the year. This is linked to anomalous low level convergence and anomalous equatorial westerly winds near the date line. The effect on the upper ocean currents is accompanied by changes in the equatorial thermocline which normally slopes upward to the east, shoaling in the cold tongue region. Thus the anomalous westerlies lead to a deepening of the thermocline in the east over several months such that the surface temperature anomalies in the east continue to grow. The reversal of this tendency also comes about by equatorial wave propagation but with the sign of the thermocline depth displacements reversed. In the narrow coastal upwelling region the effect is the largest, and the effects on the currents are superimposed on an annual signal consisting of a warm poleward current long known to Peruvian fishermen due to its effect on catches in the coastal region. The annual current which occurs around the turn of the year was named 'El Niño' for Christ Child, but this term now applies to the anomalous signal on the interannual scale. The coupled anomaly consisting of anomalously warm tropical central and eastern Pacific sea surface temperatures and the eastward/equatorward shift of the ascending branch of the Walker circulation then is known as El Niño/Southern Oscillation, or ENSO.

The common paradigm to explain this interaction of downwelling and upwelling thermocline signals, the 'delayed oscillator' mechanism (Suarez and Schopf, 1988), was derived from a simple coupled atmosphere-ocean model that exhibited interannual oscillations. The oscillations were neither simply periodic nor could they be viewed as chaotic variability (Schopf and Suarez, 1988). The observed ENSO is strongly irregular although standard index timeseries exhibit a strong peak in a frequency spectrum near periods of four years (e.g., Cleaveland et al., 1992). The identification of an oscillator mechanism proved useful in that it supports the idea of predictability of ENSO evolution on longer than seasonal timescales. In fact, operational ENSO prediction is realized, in particular, in a number of coupled ocean-atmosphere models, some with only a simple statistical atmospheric component (Barnett et al., 1993), others of the type of an AOGCM, i.e. consisting of an atmospheric general circulation model (AGCM) and an ocean general circulation model (OGCM) (Ji et al., 1996, Stockdale et al., 1998, Oberhuber et al., 1998). The fully coupled models commonly use some form of data assimilation for the ocean model, in particular, and thus do not pursue the goal of a multi-year coupled simulation of the ENSO phenomenon. AOGCMs are also used in the context of simulations of climate change forced by increasing concentrations of greenhouse gases in the atmosphere. In this context it is a major concern whether the model is able to simulate a realistic level of ENSO variability, an issue which can be addressed in the context of integrations conducted under present day conditions.

Climatic anomalies on the interannual to decadal scale linked to the Pacific Ocean have been observed for which the characteristic evolution expected for ENSO events could not be verified. In particular, the fact that ENSO warm phases (or the cold 'La Niña' phases) commonly do not last much longer than a year, sets this phenomenon apart from at least one other major climate anomaly that was observed in the North Pacific climate system around the year 1976. Sea surface temperatures in a pattern spanning the North Pacific zonally at about 40° N exhibit a difference pattern with negative amplitude of up to about 1 K, except for anomalies along the west coast of North America of opposite sign, if the difference is taken for the years 1977-1982 minus 1971-1976 (Graham,

1994). Many climatic variables over the same period exhibited substantial decadal changes both in oceanic and atmospheric aspects. A strengthened Aleutian Low implied strengthened westerlies and a concomitant increase in stormtrack activity over the North Pacific (Rogers and Raphael, 1992). Downstream effects of the circulation, particularly over the eastern and southern United States, induced higher incidence of cold air outbreaks across the plains of North America, in consequence leading to major freezes affecting Florida citrus crops (Rogers and Rohli, 1991). Associated changes in the heat and moisture advection by the quasistationary flow significantly contributed to the reinforcement of the anomalous SSTs (Rogers and Raphael, 1992). These temperature changes and related changes in ocean currents provided a plausible explanation for the changes in migration patterns of fish, e.g., salmon (Mysak, 1986).

The change in North Pacific climate was described as a discrete shift, e.g., by Nitta and Yamada (1989) and also Graham (1994). This term suggests unpredictably changing conditions within a few years, and index timeseries for some climatic variables, including an index for SST in the equatorial cold tongue, seem to support this understanding. However, the examination of multi-decadal timeseries for several SST indices (Zhang et al., 1997) and, moreover, an index for sea level pressure (SLP) used by Trenberth and Hurrel (1994) reveal pronounced variability on decadal scales for the entire period 1925 - 1992 in which the changes around 1976 are embedded. Identification of periodicities is difficult. An examination of the power spectral density of Trenberth and Hurrel's NP index (for 'North Pacific') - which represents an average over 30° N to 65° N, 160° E to 140° W and thus captures the variability of the North Pacific centre of the Pacific North American teleconnection pattern (Wallace and Gutzler, 1981) - reveals a pronounced redness but no peak outside standard significance limits. Attempts to identify a timescale can be found in recent observational studies, such as Mantua et al. (1997) who describe changes in the fish population or Minobe (1997) who analyses tree ring data. Both of these studies arrive at a timescale of about 50 to 70 years. The coupled model studies of Storch (1994) and Latif and Barnett (1994) yield estimates of slightly less than 20 years. Robertson (1996) using a 122 year version of the GISST dataset for SST arrives at two timescales, both in the interannual range, close to 6 years, and in the interdecadal range, close to 30 years.

Regardless of whether or not a robust oscillatory signal exists, the existence of a robust mode of climate anomalies independent from cold tongue variability characteristic of ENSO can be supported from statistical analyses. Zhang et al. (1996) define residual quantities by removing the linear contribution by cold tongue variability in observed SST and 500 hPa height and isolate a mode with similar spatial structure as found during the 'climate shift'. Similar results are obtained by Deser and Blackmon (1995) and Kawamura (1994). Independence from variability in the cold tongue in these cases is defined as linear independence in the statistical sense. In other words, there is zero correlation between the timeseries of a standard ENSO index and the index of the independent mode.

As noted, decadal changes in the ocean and atmosphere in the North Pacific proceeded in parallel. As in the case of ENSO, coupled processes possibly masked by the otherwise irregular variability characteristic of the midlatitude westerly flow have been put forward as one possible explanation for the presence of decadal variability. However, the single season SST anomalies in the North Pacific in the analysis by Luksch and von Storch (1992) originated from one-way forcing of the oceanic mixed layer by advected air mass of anomalous temperature which produced anomalous turbulent heat fluxes at the ocean surface. Atmospheric anomalies driving the ocean to produce SST anomalies are also put forward by Cayan (1992). Even if the oceanic mixed layer responds only passively to atmos-

pheric forcing low frequency variability of SST may result simply due to the large heat capacity of the mixed layer. Mixed layer temperatures resulting from the integration of surface heat flux, assuming that it dominates the SST tendency and is proportional to the air-sea temperature difference, exhibit a red spectrum of variability (Hasselmann, 1976). In the atmosphere, uncoupled variability in the decadal range for the midlatitude Northern Hemisphere circulation can be obtained even without forcing from the ocean, as confirmed by long term integrations with a fixed seasonal cycle, e.g., Perlwitz (1997).

The crucial point is the effect of SST anomalies on decadal scales on the midlatitude circulation. One straightforward line of argument was pursued by, e.g., Nitta and Yamada (1989) and Graham (1994). Supported by the outcome of the response experiments with SST anomalies prescribed in the equatorial Pacific, they focused on the difference in observed tropical central Pacific SSTs after and before the 'climate shift' of typically about half a degree, evident also from index timeseries representative of ENSO variability. Atmospheric teleconnection would induce a circulation response (evident, e.g., in the extratropical 500 hPa height field) which in turn would be capable of inducing the ocean response to anomalous wind and heat flux forcing. It then remains to be investigated how the drift in the slowly varying ENSO background comes about.

Atmospheric (Barnett et al., 1998) as well as oceanic (Deser et al., 1996, Gu and Philander, 1997) transfer of information from the extratropics to the tropics have been proposed. Ultimately, these processes would affect the tropical thermocline and thus, the mechanism known to operate in ENSO variability. Barnett et al. (1998) see evidence that an extratropical-tropical atmospheric teleconnection induces an equatorial wind stress response, with the decadal timescale set by decadal variability originating in the North Pacific, similarly as discussed below. A further relevant mechanism could be a closed loop with SST in the extratropics influenced by atmospheric teleconnection from the tropics and the decadal timescale set by the oceanic process of isopycnal downward and equatorward advection of anomalies generated in the North Pacific subduction zone (Gu and Philander, 1997, Zhang et al., 1998). That subducted anomalous watermass actually causes substantial modification in the equatorial thermocline may be a rare case. A further possibility for generating decadal ENSO background variability could result from oceanic Rossby wave propagation in the off-equatorial tropics and subtropics and their effect on the thermocline and consequently, on SST (Meyers et al., 1996). These wavefronts could ultimately be a consequence of Kelvin wave signals propagating eastward along the equatorial thermocline in the course of El Niño (or La Niña). On reaching the eastern boundary of the equatorial waveguide these disturbances in the thermocline propagate poleward as coastal Kelvin waves which during their journey cause Rossby waves to radiate away from the coast and propagate westward into the basin (e.g., White and Saur, 1983). The latitudinal dependence of the Rossby wave speed could be a factor in causing complicated low frequency variations in the thermocline, hence in SST, and consequently affect the lower branch of the atmospheric Hadley and Walker circulations, the response of which to SST during ENSO is well established.

Apart from tropical forcing, the possibility that midlatitude SST anomalies could induce a detectable response in the extratropical circulation has been debated for over three decades (e.g., Namias, 1959, Barnett, 1981, Frankignoul, 1985, Pitcher et al., 1988, Latif and Barnett, 1994, Peng et al., 1997, Bladé, 1997). If this midlatitude SST effect is significant, then atmosphere-ocean interaction could contribute substantially to decadal variability in the North Pacific. In particular, positive feedback could be induced if the Aleutian low reacts to anomalously cold midlatitude SST in such a way that

enhanced westerlies result. Moreover, enhanced cyclogenesis in the North West Pacific could act to enhance the westerlies. The wind changes would induce changes in the large-scale wind-driven flow in the Kuroshio western boundary current extension, apart from effects of modified wind stirring on the entrainment of cold subsurface water at the base of the oceanic mixed layer. The changes in large scale wind-driven flow cannot reach equilibrium with the forcing instantaneously but instead baroclinic adjustment takes place via midlatitude Rossby wave propagation. The timescales to be considered thus are given by the time taken by the gravest baroclinic Rossby wave for crossing the basin which in midlatitudes is on the order of a decade. This delayed spinup of the subtropical gyre, and the concomitant displacements of the thermocline which could affect SST, in the coupled AOGCM of Latif and Barnett (1994) lead to an oscillatory coupled mode with a timescale of about 20 years. The above positive feedback between wind and SST leads to SST anomaly growth which would be reversed ultimately by thermocline anomalies with the sign reversed as compared to the initial anomaly. Spatial separation between the thermocline displacements of opposite sign would induce the lag of the reverse signal reaching the location of the original anomaly, after travelling within the North Pacific subtropical gyre with a speed governed by both advective and wave timescales. The basin boundaries would act to deflect wavelike disturbances. Elements of such a mechanism are found in the work of Namias (1959) and White and Barnett (1972). In simple models, coupled dynamics has been demonstrated, e.g., by assuming a direct dependence of wind stress anomaly on thermocline depth anomaly at a single point (Münnich et al., 1998). Jin (1997) approximates the interaction between the westerlies and SST (which is modified by wind-driven flow) as dominated by atmospheric thermal wind balance and the balance between atmospheric eddy heat transport and air-sea heat exchange. Both approaches lead to variability with a spectrum characterized by a peak at decadal timescales.

Studying Pacific decadal SST variability in a coupled AOGCM is a plausible approach from several aspects. Observational datasets are short in relation to the timescales under consideration, particularly for oceanic quantities. Thus, reliable subsurface temperature data exist mainly for the period after 1970 when standard expendable bathythermograph data could be included in the record (White, 1995). Model output is supplied with homogeneous coverage in both space and time. The variability simulated by the coupled model can be studied imposing controlled boundary conditions, usually consistent with present day climate. The simulated variability can be analyzed statistically on the basis of the long integration periods achievable on current supercomputers. It can then be compared against the results obtained from simple models, thus providing an aid to decide among several possible candidate mechanisms which might be consistent with the available observations. It should be noted that among the coupled model studies addressing Pacific decadal variability there is a diversity of mechanisms found particularly for the contribution of wind-driven ocean dynamics. The thermocline signals analyzed in the model study by Yukimoto et al. (1996) differ from those shown by Storch (1994) and, similarly, by Latif and Barnett (1994). It is thus of interest to consider variability simulated in a variety of model setups and runs.

A coupled model was developed at the Max Planck Institute for Meteorology (Roeckner et al., 1996a) at the time when work summarized in the present thesis progressed. The component models which are described in chapter 2 of this thesis are the AGCM ECHAM4 and the isopycnic OGCM OPYC3. The ECHAM4 model is the climate model in use at the Max Planck Institute and the most recent generation in the line of ECHAM models (Roeckner et al., 1992). The OPYC model was developed by Oberhuber (1993a,b). The coupled model uses a flux adjustment technique which fol-

lowing Oberhuber (pers. comm.) applies additive annual mean adjustments to the fluxes of heat and freshwater passed from ECHAM to OPYC, with a method for flux adjustment in sea ice covered areas developed jointly by Oberhuber and this author. To couple the two components a numerical method for regridding the fluxes (including momentum flux, turbulent kinetic energy flux and river discharge) conservingly was developed by this author, treatment of SST was also provided. Chapter 2 apart from the component models describes the coupling strategy, from the outset of the spun-up model ocean state. The simulated climate is validated in chapter 3. Chapter 4 characterizes two modes of decadal Pacific SST variability extracted from 170 years of coupled simulation and associated variability of the extratropical Northern Hemisphere circulation. Chapter 5 analyzes the tendency terms for SST variability, considering turbulent as well as radiative surface heat flux components. In addition, that chapter discusses heat exchange between the oceanic mixed layer and the thermocline, taking into account wind-driven large-scale ocean dynamics. Results are summarized and conclusions stated in chapter 6.

Chapter 2

The simulation

The AGCM and OGCM component, as well as the technique of coupling, represent recent developments. The coupling of earlier versions of the component models by a different technique, involving seasonal flux adjustment essentially for all quantities exchanged between them, is described by Lunkeit et al. (1996). The present coupled simulation has first been described in Roeckner et al. (1996a) who analyze the atmospheric response to SST anomalies associated with the El Niño/ Southern Oscillation variability simulated by the model. Bengtsson (1996) describes the climate response to changing greenhouse gas concentrations simulated by the coupled model. The general tendency for more modest greenhouse warming predicted by the present generation of coupled models is noted by Hasselmann (1997) drawing on a set of simulations with the same coupled model which included an integration with a prescribed change in sulfate aerosol concentration. The model has also been adapted in an ENSO forecast scheme which enabled the successful prediction of the 1997/98 El Niño event by Oberhuber et al. (1998).

2. 1. Overview of atmospheric and oceanic general circulation models

The AGCM component is the ECHAM4 general circulation model developed at the Max Planck Institute for Meteorology. It is the current generation in the line of ECHAM models (Roeckner et al., 1992) which evolved from the European Centre for Medium Range Weather Forecast (ECMWF) model. ECHAM is distinct from the ECMWF model due to extensive modification and augmentation in parameterizations for soil processes, local runoff, simple prognostic sea ice skin temperature, boundary layer physics, prognostic cloud liquid water and ice. A summary of recent developments regarding model physics in ECHAM4 and a description of the simulated climate obtained with the uncoupled ECHAM4 model is given in Roeckner et al. (1996b).

The prognostic variables, vorticity, divergence, temperature and logarithm of surface pressure are represented as expansions in spherical harmonics with triangular truncation at wavenumber 42 (T42). Different from previous versions of the ECHAM model, advection of the prognostic water vapour and cloud liquid water/ice are treated by a semi-Lagrangian scheme (Williamson and Rasch, 1994). The physical parameterizations run on a 128×64 (lon × lat) Gaussian grid yielding a mesh-width of approximately 2.8°. In the vertical, 19 hybrid σ-p levels are used extending from the topography to 10 hPa. Highest resolution is used for the planetary boundary layer. The lowest model level is placed at 30 m above the topography which roughly corresponds to the height of the surface layer. The remainder of the boundary layer is resolved by four additional levels reaching up to about 1.5 km height. The time integration uses a leap-frog scheme with a weak time filter. The timestep is 24 minutes except for radiation which uses 2 hours. The diurnal cycle of solar radiation is thus resolved.

Most land surface data are input as a time-independent dataset from the compilation by Claussen et al. (1994), comprising parameters such as orography, background albedo, roughness length, vegetation type, leaf area index. Soil water holding capacity, heat capacity and thermal conductivity are also prescribed.

Horizontal diffusion is scale-selective due to the use of a ∇^{10} scheme with a sponge zone in the lower stratosphere. Vertical turbulent exchange is parameterized by a higher order turbulence closure with coefficients dependent on turbulent kinetic energy (Brinkop and Roeckner, 1995) for which turbulent transport, dissipation, wind shear and buoyancy flux are considered as sources and sinks but advection is neglected. Cloud-turbulence interactions comprise vertical exchange of turbulent kinetic energy generated through radiative cooling at cloud top, turbulent flux of cloud water at cloud top, and the impact of cloud water on buoyancy flux. Monin-Obukhov similarity theory yields the turbulent surface fluxes. Gravity wave drag is parameterized after McFarlane (1987), Palmer et al. (1986), with modifications by Miller et al. (1989).

The Tiedtke (1989) mass flux scheme is the basis for cumulus convection but subject to modifications following Nordeng (1996). Buoyancy determines organized entrainment whereas detrainment occurs at the tops of clouds which are treated as an ensemble. Convective available potential energy (CAPE) is used for the closure assumptions in deep cumulus. Midlevel convection depends on low level moisture convergence while shallow cloud depends on surface evaporation. Stratiform cloud depends on microphysical processes involved in precipitation formation as well as phase changes and settling of ice crystals. Also, the water detrained from cumulus tops is used as a source term. Sub-gridscale vertical extent in thin maritime stratus is parameterized by a lowered condensation threshold.

Radiation is treated as in the European Center for Medium Range Weather Forecasts (ECMWF) numerical weather prediction model. Two stream approximations are used for six spectral bands in the infrared (Morcrette, 1991) and two in the solar part (Fouquart and Bonnel, 1980) of the spectrum. The physical package is capable of an optional treatment of ozone as well as methane, nitrous oxide and 16 CFCs. The water vapour continuum includes temperature weighted band averages of e-type absorption, with a band dependent ratio of (p-e) type to e-type absorption (Giorgetta and Wild, 1995). Mie theory is suitably adapted to the broadband ansatz for the treatment of single scattering at cloud droplets and ice crystals (Rockel et al., 1991) the effective radius of which is parameterized in terms of the liquid and ice water content (Roeckner, 1995).

The OGCM component is an updated version of the OPYC general circulation model by Oberhuber (1993a,b). It solves the primitive equations in the form of conservation laws for momentum, mass, heat and salt on isopycnal layers, with a realistic equation of state, and the sea level, given by vertical summation of layer thickness at any time, evolving freely. Diapycnal and isopycnal mixing are parameterized, respectively, using a Richardson-number dependent criterion and Laplacian diffusion with temporally and spatially varying coefficients. The latter for momentum depend on local Rossby-radius, for scalars on the local deformation of the flow field. The convective adjustment completely removes unstable stratification in one timestep.

A mixed layer is included as the top layer with an arbitrary potential density and a minimum thickness of 10 m . The same governing equations as for the interior ocean are applied, but with a detailed calculation of turbulent entrainment/detrainment based on turbulent kinetic energy input by wind stirring, buoyancy flux due to heat and freshwater, and local shear. A fraction of solar radiation is allowed to penetrate below the mixed layer.

Sea-ice and snow-cover is predicted in the form of grid-cell averaged thicknesses and a common area concentration, together with an equation of motion neglecting momentum advection and using vis-

cous-plastic rheology in the stress term (Hibler, 1979). A simple computation of ice and snow top temperatures and thermodynamic mass tendencies provides input to the prognostic equations.

In uncoupled simulations, surface fluxes everywhere are entirely given by bulk laws involving observed climatological atmospheric quantities and simulated surface temperature (Oberhuber, 1988, 1993a,b). However, surface salinity forcing includes Haney (1971) type restoring in addition to precipitation and evaporation with a restoring time constant of about 12 days.

The diurnal cycle is omitted, and half a day is used in the semi-implicit timestepping. The scalar gridpoints of an Arakawa B-grid coincide with those of the AGCM grid except equatorward of 36° latitude where the meridional spacing is gradually decreased to approximately 0.5° (1.0°) equatorward of 5° (10°) latitude to resolve the equatorial waveguide. Including the mixed layer, 11 layers are used.

2. 2. Coupling strategy and flux adjustments

As compared to the uncoupled model components, their combination in the form of a coupled climate model necessitates extra tasks. Climate drift can occur in response to coupling the two separately tuned components. One possible source of drift lies in the slow advective timescales associated with the thermohaline ocean circulation which are involved in the response to changes in the imposed boundary conditions after coupling. Generally an ocean-only spinup integration is performed to achieve an initial state prior to coupling which is reasonably close to cyclostationary behaviour (Manabe et al., 1991, Cubasch et al., 1992, Murphy, 1995, Lunkeit et al., 1996). Nonetheless, coupling a spun-up ocean model to an atmospheric circulation model in general induces additional drift away from the uncoupled equilibrium solutions of both component models. Theoretical studies (Sausen and Lunkeit, 1990, Power, 1995) indicate that non-linearity, for instance associated with the influence of extremes in the coupled interactions on the mean state, is capable of inducing new stable solutions. Starting from a linearization of the model variability about the reference climatologies in both models Sausen et al. (1988) proposed that additive correction terms dependent only on the month of the year could reduce possible drift if, in each component model, the annual periodic part of the boundary condition could stabilize the model climatology near the uncoupled reference. With the seasonal cycles of both components thus decoupled, only coupling of anomalies would be permitted. Such flux corrections (or 'adjustments') generally apply to heat and freshwater fluxes (e.g., Manabe et al., 1991, Johns et al., 1997) but sometimes also to SST and sea ice mass (Cubasch et al., 1992, Murphy, 1995, Lunkeit et al., 1996). In the present coupled model a flux adjustment technique is also used. The adjustment, following ideas by Oberhuber (pers. comm.) is applied in the form of constant annual mean fields and restricted to net surface heat flux and freshwater flux (precipitation minus evaporation). Modes of climate variability such as El Niño/Southern Oscillation (ENSO), which in nature are known to interact with or exhibit phase-locking to, the seasonal cycle, could be more easily distorted or modulated artificially if seasonal flux adjustments were used. Implementation of annual mean flux adjustment requires special treatment of areas of seasonal sea ice cover, for which a basic framework was designed jointly with J. M. Oberhuber. In the present coupled model specific modifications to both model components used here regarding sea ice treatment were therefore introduced by this author.

For the derivation of the flux adjustment fields an approach due to Oberhuber (pers. comm.) was taken. The traditional approach (Manabe et al., 1991, Cubasch et al., 1992, Murphy, 1995, Lunkeit et

al., 1996) is to derive AGCM fluxes from an integration forced by observed SST and subsequently run the OGCM with Haney (1971) type restoring terms but with the boundary condition also including the derived AGCM fluxes. Flux adjustments are then obtained as averages of the restoring terms. Murphy (1995) and Johns et al. (1997) use additional portions of fully coupled integration with restoring terms active to base the flux adjustments on a type of interaction between model components resembling as closely as possible the fully coupled mode of integration. In the present thesis, for determining flux adjustments prior to the present control integration, following Oberhuber (pers. comm.) a coupled integration period is used that conceptually extends the restored coupled approach. The latter due to the restoring cannot permit coupled variability on interannual scales which is effectively damped out. The approach discussed below attempts to admit a smooth transition from a coupled restored to a merely annual mean flux adjusted integration and therefore to gradually include effects of interannual variability even while flux adjustments are still being determined. Details are found below.

Since meridional resolution in the ocean model is variable and equatorward of 36° latitude is higher than that of the atmosphere model regridding of flux fields and SST is necessary. A special numerical package has been developed by the author of the present thesis to guarantee local flux conservation. The description is given in appendix B. This section details the full set of variables used for coupling and discusses the strategy for calculating the flux adjustments.

Fig. 2.1 summarizes the quantities passed between models for coupling. This setup was proposed by Oberhuber (pers.comm.), and the OPYC model code includes special routines for handling each of the quantities passed from the ECHAM model. For grid boxes with sea ice cover this setup is particularly suited for the task of computing the heat flux adjustment. The idea is to switch off the melting/freezing parameterizations and change in temperature profiles in the OPYC model and compute these terms in the ECHAM model instead. Thus ECHAM is required to deliver the terms $Q_{s,\,melt}$ and $Q_{s+i,\,\text{heat./cool.}}$ to the OPYC timestepping for sea ice and snow cover. These in addition to the standard net heat flux, denoted. Q_{tot} below, provide sufficient information to determine the melting/freezing rates for sea ice and snow cover needed in the OPYC model. Details are found below. This is a distinct approach from the common one where quantities from the atmospheric boundary layer are passed to the ocean model where they enter bulk formulae for surface heat fluxes, which in turn enter a scheme like that of Semtner (1976) for sea ice thermodynamics. The setup in fig. 2.1 therefore implies the need to add a routine in ECHAM to compute thermodynamic quantities for grid boxes with sea ice cover. This routine was developed by this author (see appendix A) and also used in OPYC to replace a former scheme. The interface code to synchronize models and perform the regridding was developed by this author.

The models are coupled quasi-synchronously, exchanging daily averaged quantities once a day. The AGCM receives the mixed layer temperature, T_w , and sea ice concentration, A_i , thickness, d_i , and snow depth, d_s without any adjustment (in the OPYC sea ice time stepping, d_i and d_s are replaced by grid box averages, i.e. volume divided by total grid box area). For the OGCM, downward solar radiation, $Q^{\downarrow}_{SW}$, river discharge, r , windstress, $\vec{\tau}$, and the cube of the friction velocity, u_*^3 , are passed, again, without adjustments. u_*^3 is passed separately since deriving it from daily mean windstress would lead to underestimation of the turbulent kinetic energy input into the mixed layer. $Q^{\downarrow}_{SW}$ is used to estimate the amount of shortwave radiation penetrating the mixed layer. The total heat flux at the bottom of the lowest atmosphere layer, Q_{tot} , not shown explicitly in fig. 2.1, is used

to transfer the thermal boundary condition to OPYC. Q_{tot} is given by the sum of the surface absorbed shortwave flux (with grid box albedo in the presence of sea ice taken as a suitable weighted average of albedo for ice-free and ice-covered portions), longwave radiative flux, Q_{LW}, and turbulent fluxes of sensible heat, Q_{SH}, and latent heat, Q_{LH}. The latter three are assumed to depend on an effective surface temperature, T_{eff}, representing the entire grid box. For nonzero sea ice concentration the insulating effect and melting at the interface between atmosphere and snow or bare ice need to be accounted for additionally, and energy transfer at the ice-water interface is obtained by subtracting these terms from Q_{tot}. The details of this procedure and the treatment of flux adjustment in the general case are described below. The second flux corrected field is $P-E$, with P total precipitation, E evaporation. In grid boxes with sea ice cover this term contributes to snow changes except when the parameterization for sea ice thermodynamics described below produces surface melting, in which case all of $P-E$ enters the ice-free grid box fraction. Without melting, $(1-A_i)(P-E)$ enters the lead fraction of the grid box. The use of $P-E$ and the criterion for snow accumulation are analogous to what is used in the OPYC code. River discharge is computed by the river routing scheme of Sausen et al. (1994) using runoff from each grid box as computed in ECHAM. The other parameterizations are detailed in Roeckner et al. (1996b).

If the fraction A_i of the grid box is covered by sea ice the immediate exchange of heat between the mixed layer and the atmosphere only takes place in the lead fraction $1-A_i$ and otherwise is drastically reduced due to mass exchange at the ice bottom (melting or freezing), possible melting at the surface of snow or bare ice, and a small amount of heat used in changing the vertical temperature profile, with largest variations occurring in skin temperature, T_s. Thus similarly to OPYC, thermal inertia of sea ice and snow cover is included (Oberhuber, 1993b, Holland et al., 1993), and for these effects the present author chose a similarly simple ansatz. Thermal diffusive flux through ice and snow is assumed to vary piecewise linearly in the vertical and match continuously to the absorbed shortwave flux plus the sum of longwave radiative flux and turbulent fluxes of sensible and latent heat. Absorbed shortwave flux is calculated using an ice albedo value dependent crudely on T_s, assuming $0.6\ldots0.7$ below -4 °C and following an exponential curve to reach 0.3 at the melting point. The remaining heat flux components are extrapolated from the grid box average using a Taylor expansion about the effective surface temperature

$$T_{eff} = (1-A_i)T_w + A_i T_s \qquad (2.1)$$

T_w is prescribed at the freezing point, and T_s is predicted from coupled thermal diffusion equations for snow and ice with these boundary conditions for surface flux and T_w. The upper boundary condition for the thermal diffusion equation is redefined by setting T_s to the melting point if otherwise the predicted T_s would be higher. In this case the diffusive flux at the surface differs from the surface flux at the top of snow or bare ice given by the above treatment of shortwave flux and the remaining heat flux contributions, recomputed using the melting point. The difference yields the amount $Q_{s,melt}$ which is multiplied by A_i to obtain the relevant quantity for melting snow or the top of bare ice. Further details such as the diffusion equations for snow and ice with the approximation for the vertical dependence are given in appendix A.

The computed diffusive flux at the ice-water interface - which is obtained by subtracting the snow melt $Q_{s,melt}$ and thermal heating rates, $Q_{s+i,\,\mathrm{heat./cool.}}$ from the surface flux for the ice-covered portion of the grid box - is multiplied by A_i and added to the heat exchange between the mixed layer

and the atmosphere through leads. Adding the result to the remaining tendency terms for T_w, such as entrainment, defines a melting or freezing rate at the bottom of the ice floe, consistent with the prescription of holding T_w constant in the presence of ice.

Thus a quantity can be defined for both ice-free and ice-covered grid boxes, to which a heat flux adjustment can be applied, by setting

$$Q_{net} = Q_{SW,\,abs,\,sfc} + Q_{LW,\,sfc} + Q_{LH} + Q_{SH} - A_i(Q_{s,\,melt} + Q_{s+i,\,\text{heat./cool.}}) \qquad (2.2)$$

On the right hand side, the last expression is a product of two factors that vanish independently in ice-free grid boxes, while the remaining terms are dependent on grid box averages of the surface parameters, albedo and T_{eff}. The calculation of heat flux adjustment thus requires the implementation of the above thermodynamic treatment in both component models, each of which contains heat flux parameterizations as needed. This was done for the present thesis, and the modified OPYC code was also used for the uncoupled spinup.

For the computation of freshwater flux adjustment, the $P-E$ value in OPYC is determined by climatological precipitation and the bulk formula for latent heat flux using T_{eff} as from the modified thermodynamic calculations. As discussed above, apart from the case of melting at the top of snow or bare ice, the freshwater flux entering the mixed layer is $(1-A_i)(P-E)$. River discharge from ECHAM4 is added to the mixed layer irrespective of sea ice cover. The restoring term for salinity is used as described below during the coupled integration to determine flux adjustments. Thus the adjustment again applies to the mixed layer, leaving snow unaffected.

Fig. 2.2 and 2.3 summarize the strategy for the spinup and production runs. An initial state of the ocean from the end of a pre-existing spinup integration supplied by J. M. Oberhuber (pers. comm.) was used, for which approximately 1000 years of integration were conducted with the uncoupled setup described above, but including the ice modifications and further ones, as follows. Over the first 500 years observed climatological quantities, such as air temperature, entered the bulk laws in OPYC, except that the full daily windstress was taken from an uncoupled integration of ECHAM3 with observed SST from 1979 - 1988 (ECHAM4 was still under construction). Subsequently, day-to-day variability in the form of anomalies of net heat flux and precipitation minus evaporation anomalies from ECHAM3 was added, since full values would lead to problems at the ice edge which varies during spinup but was fixed during the ECHAM3 run. Since ECHAM4 was used for the coupled model, a separate ocean-only integration was performed by this author for 50 yr as a continuation of the main spinup run. In this separate run, the only modification consisted in a new set of forcing data, extracted from an extended AMIP (Gates, 1992) integration of ECHAM4 rather than ECHAM3. Fig. 2.2 shows globally averaged temperature and salinity at various depths for this period. Evidently, the effect of a change in forcing is of little importance.

Next follows a transition phase of coupling with continuously updated flux adjustments in an approach due to Oberhuber (pers. comm.). We denote F_A the flux - Q_{net} or the freshwater flux including river discharge, - passed by the AGCM, F_O the flux resulting from the OGCM bulk parameterization under the same surface conditions. OPYC does not use a parameterization for river discharge which is compensated for by the salinity restoring. The Haney (1971) type restoring term F_{rest} for the present setup was introduced also for heat, except where ice exists, in the form

$$\alpha(SST_{obs} - SST_{mod})$$

with α dependent on SST as in Oberhuber (1988) yielding a restoring timescale on the order of two months. Then the flux F seen by the OGCM in the final phase (fixed flux adjustment) is

$$F = F_A + \langle\langle F_O + F_{rest} - F_A \rangle\rangle \qquad (2.3)$$

where the second term on the right represents a long-term annual mean. The transition phase is used to initially estimate this term on a daily update basis and then smoothly relax to only annually updated estimates in the form of averages over all completed years. More specifically, during this phase

$$F = F_A + (F_O + F_{rest} - F_A - \langle F_O + F_{rest} - F_A \rangle)\beta(t) + \langle F_O + F_{rest} - F_A \rangle \qquad (2.4)$$

with $\beta(t)$ initially set to 1 but decreasing quite rapidly such that after 30 years, $\beta(t) \cong 10^{-2}$. The term in single angle brackets is an estimate of the term in double angle brackets. Tendencies for local cyclostationarity in the freshwater flux adjustment estimates are found during the entire transition phase which was extended over 100 years. Thus, for the average of the estimates for the Pacific, decadal scale oscillations with a range of ± 0.2 mmd^{-1} are found. For both flux adjustment fields, after an initial drift over the first 50 years, the remainder of the transition period yielded sufficiently well defined expectation values of the sequences of yearly updates to define the term in double angle brackets.[1] The fully coupled run with adjustments fixed was then initialized with the state at the beginning of year 91.

Fig. 2.4 shows the flux adjustments obtained in this way for heat flux and freshwater flux for the Pacific basin. The heat flux adjustment, fig. 2.4.a, generally exhibits large-scale structure. Although in the next chapter the net surface heat flux is discussed in more detail in comparison to the climatology published by Oberhuber (1988), a general overview reveals that the flux adjustment is not simply the difference between the atmospheric heat flux and the observed climatology, thus pointing to ocean model inaccuracies. An area where this is particularly evident is situated north-east of Japan where, similarly to most coupled models, the strong cooling exerted by the flux adjustment is explained by inaccuracy of the advective transport. Generally OGCMs encounter problems in simulating the correct separation of the western boundary current and therefore produce excessive heating by the Kuroshio in this region. The main area of the North Pacific exhibits positive flux adjustment values which cannot be explained fully by the difference of the AGCM simulated heat flux and the climatology, both of which are shown in the next chapter. It may be of interest that in the non-flux-adjusted coupled integration of Frey et al. (1997) with the same AGCM an area across the North Pacific exhibits a cold bias which has a quite similar outline as the 20 Wm^{-2} contour of the flux adjustment. With the signs reversed a similar correspondence applies between 40° N and 50° N where in the present simulation, due to inaccurate heat advection associated with the Kuroshio extension the required flux adjustment is a cooling. A combination of cloud-radiative effects and ocean mixed layer physics is likely responsible for the positive heat flux adjustment required in the warm

1. The regional variation of the timescales of decadal variation made it necessary to compute expectations at each grid point separately, such that appropriate individual averaging periods were selected. The averaging period was a multiple of the decadal oscillation period, which in turn was estimated from the first sidelobe of the autocorrelation function.

pool area. Finally, along the eastern boundary, stratus cloud may form insufficiently, thus admitting a stronger insolation of the sea surface which is compensated for by negative flux adjustments.

Freshwater flux adjustment is shown in fig. 2.4.b. One of the most conspicuous features is a dipole in the western North Pacific consisting of strong positive flux adjustment near Japan and nearly equally strong negative values further east. This is consistent with the inaccurate advective transport mentioned in the context of the heat flux adjustment, since the waters of the Kuroshio are at the same time warmer and saltier than in the subtropics in general. The flux adjustment then is dominated by the contribution from F_{rest} and thus cancels the errors that would otherwise result. A further pronounced feature is a pair of almost zonal structures of positive flux-adjustment, more or less straddling the equator. Poleward of both lobes of this structure there are patterns of negative flux-adjustment input of similar zonal extent. This entire pattern can again be assumed to be dominated by the contribution from F_{rest} and indicates that deep convection in the model associated with the ITCZ and SPCZ occurs in more narrowly confined structures. In the next chapter this may be seen to be consistent with an overestimation of the equatorial portion of the south-eastern trades, and a similar tendency also occurs in the uncoupled model as noted by Roeckner et al. (1996b).

List of figures

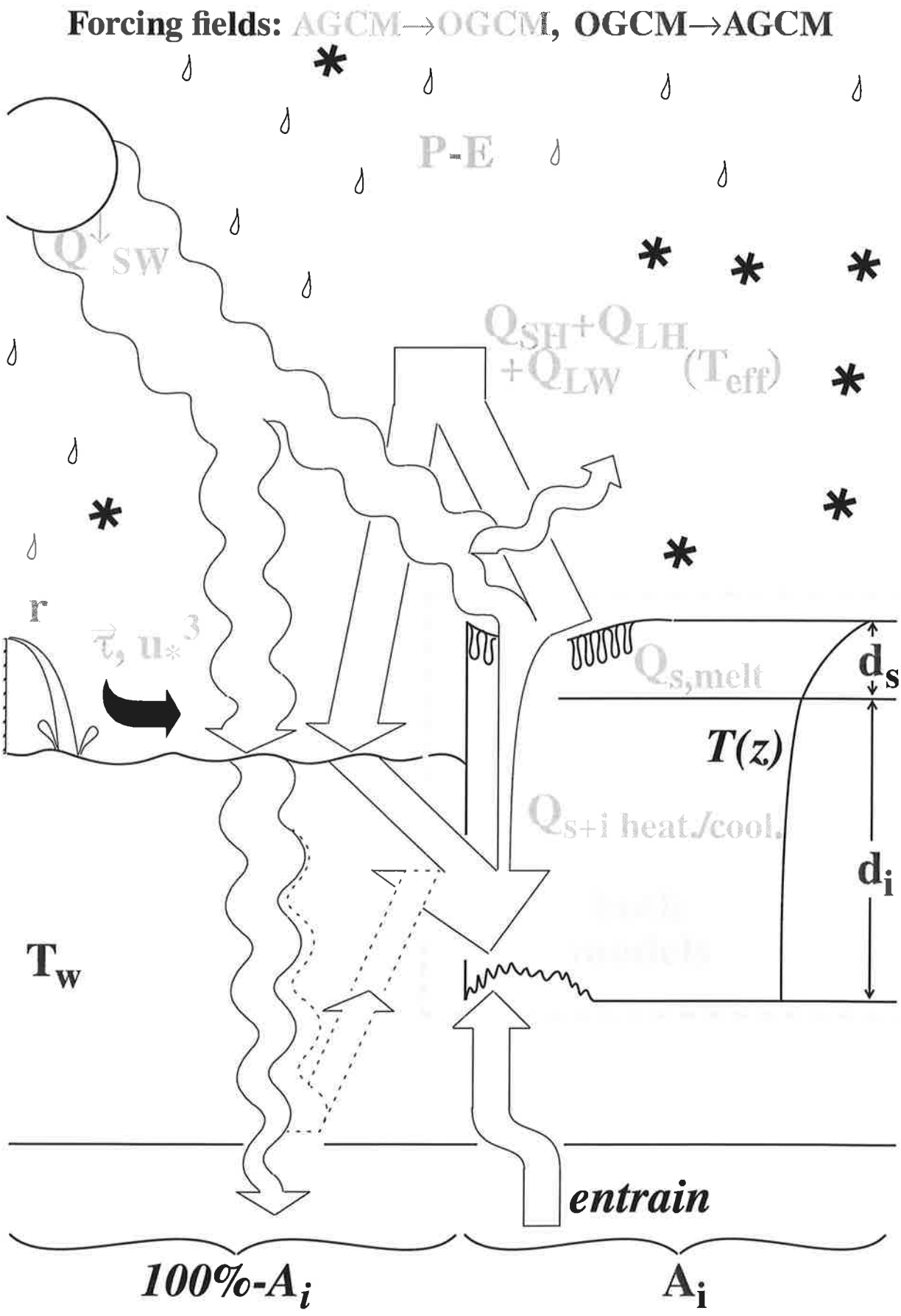

Fig. 2.1 Coupled model interface (details see text)

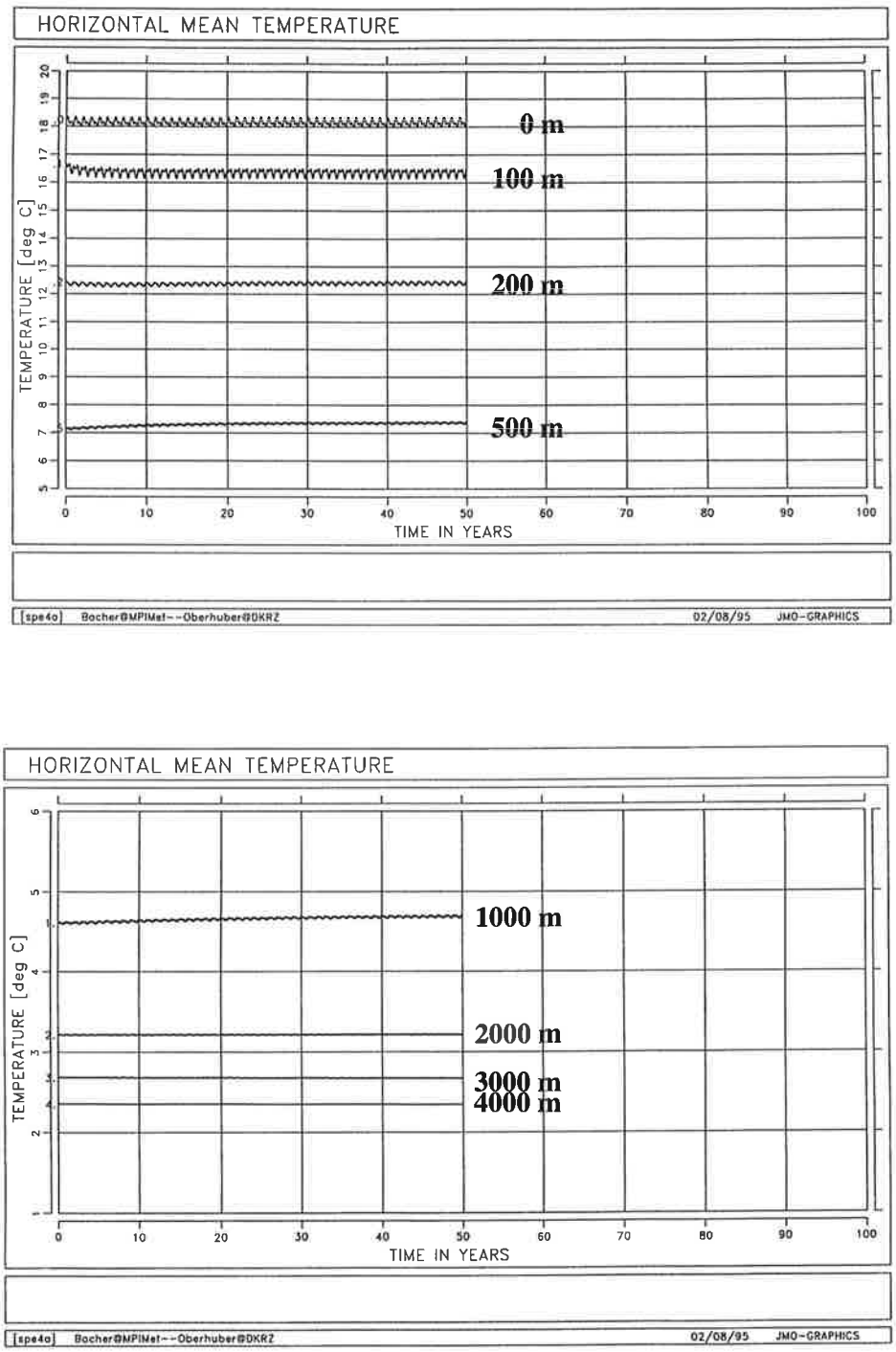

Fig. 2.2 Globally averaged temperature for various depths from an ocean-only integration with the identical code, appended to the main spinup integration but using ECHAM4 data for forcing. Unit: °C

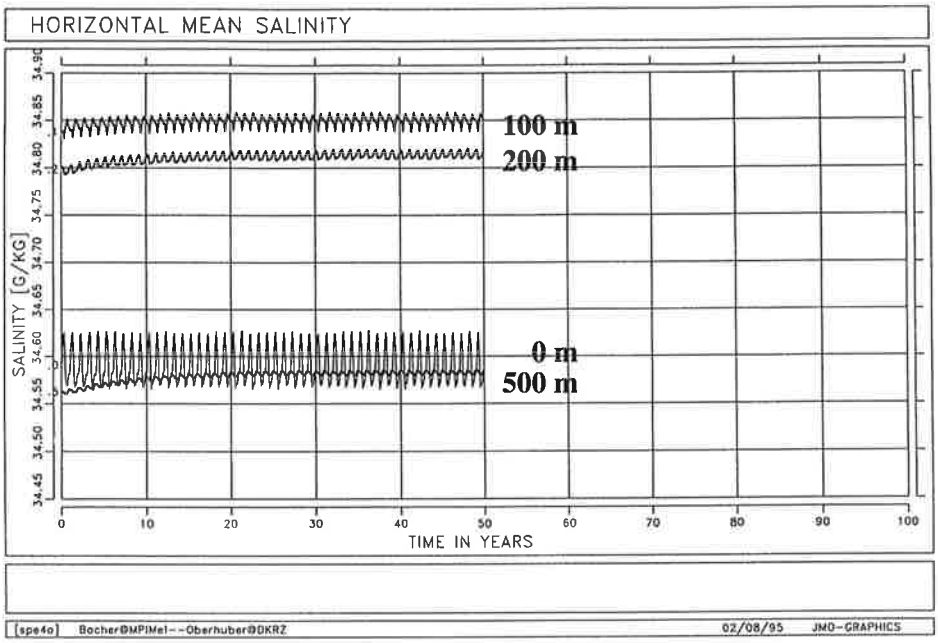

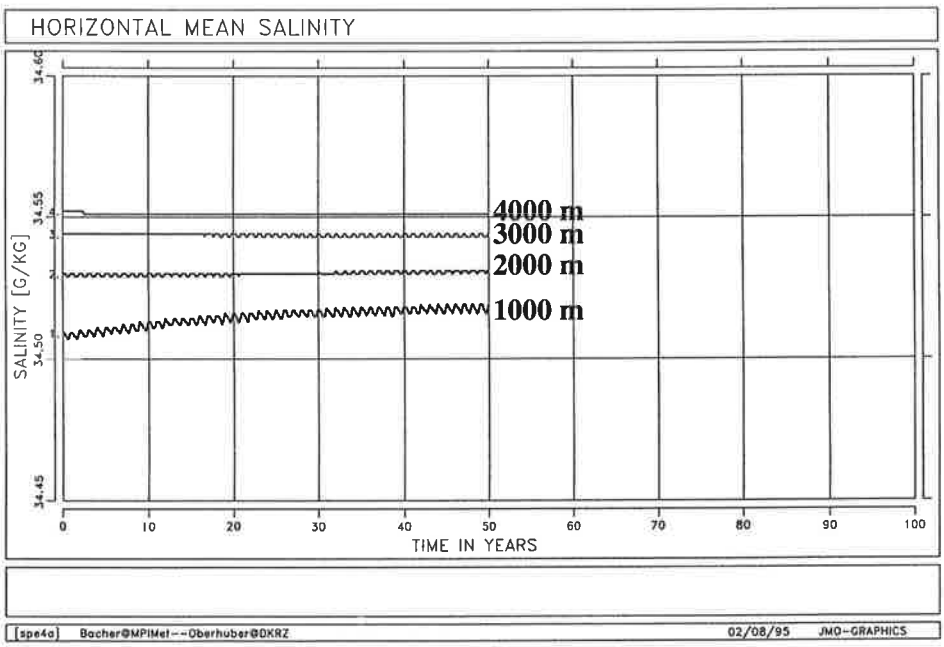

Fig. 2.2 (contd.) Globally averaged salinity for various depths from an ocean-only integration with the identical code, appended to the main spinup integration but using ECHAM4 data for forcing. Unit: g kg^{-1}

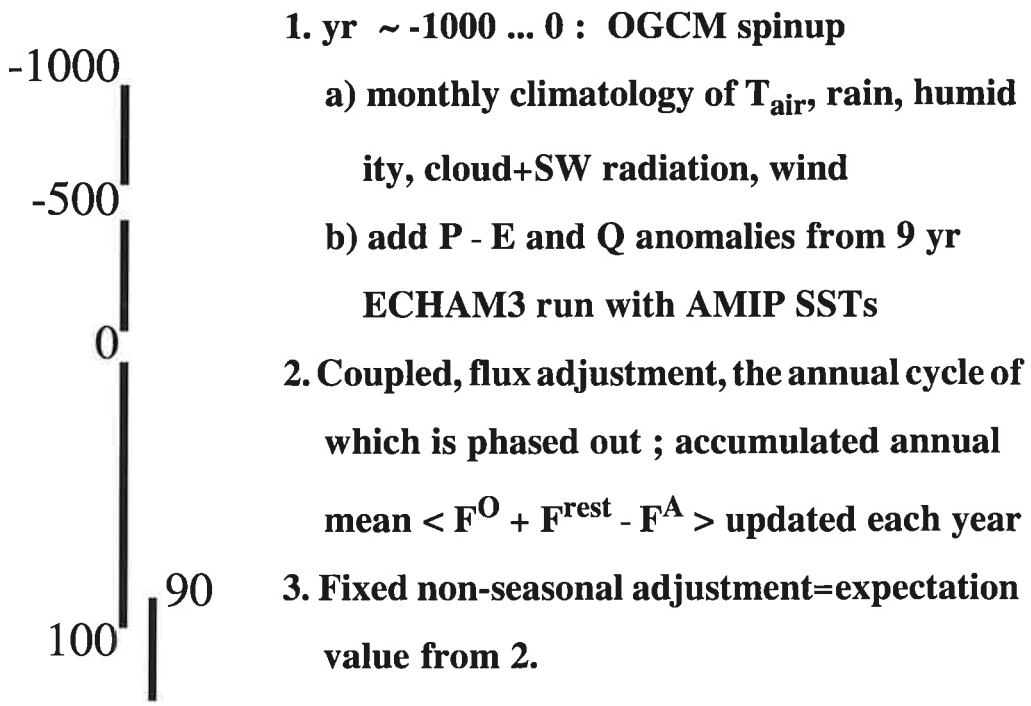

Fig. 2.3 Strategy used in ocean-only spinup run (Oberhuber, pers. comm.) and coupled integration leg for determining heat and freshwater flux adjustments

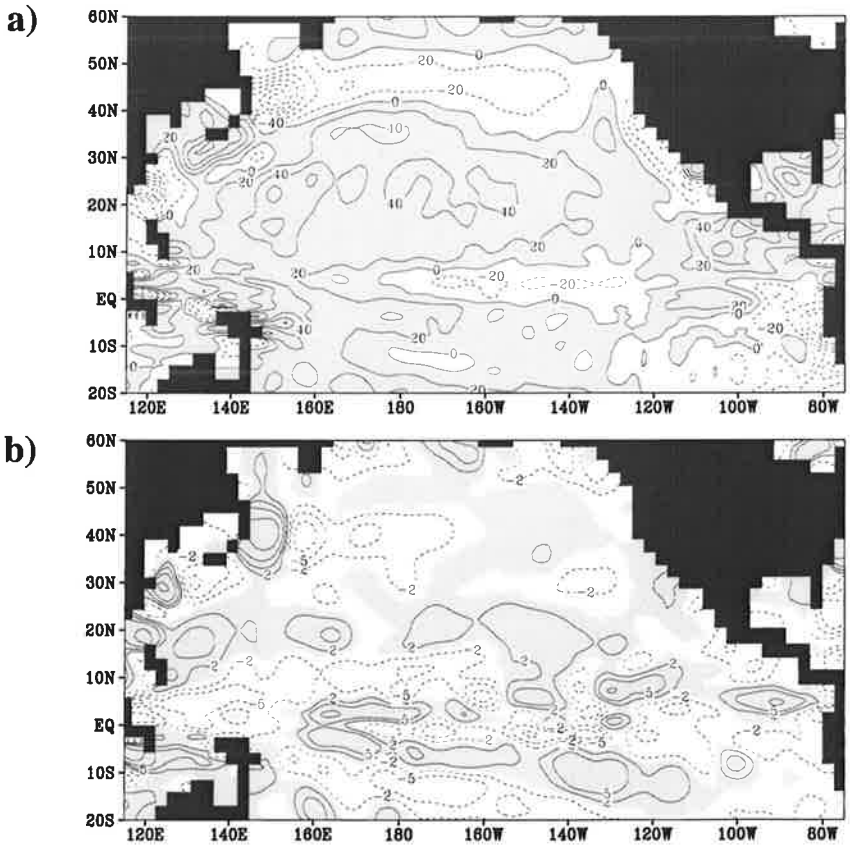

Fig. 2.4 Flux adjustments used for coupled model integrations for the Pacific basin. a) heat flux adjustment, unit: Wm^{-2}, b) freshwater flux adjustment, unit: mmd^{-1}. In shaded areas the adjustment yields a flux from the atmosphere to the ocean

Chapter 3

Model climatology and validation

The seasonal cycle of the present simulation due to the fact that annual mean flux adjustment was employed evolves without the constraint commonly used in seasonally flux-adjusted coupled models. The validation of the seasonal cycle is the subject of the present chapter with the focus on the Pacific Ocean domain. The period used is from year 91, the first year with non-varying flux adjustments prescribed for performing the control integration, until year 260. The actual start of the control integration was defined to be year 100.

3. 1. Temperature, wind, geopotential height and precipitation

In this section the approach for validation is to refer to the discussion of the uncoupled model forced with observed SST by Roeckner et al. (1996b) who used results from the ECMWF analysis for temperature, wind, and geopotential height and compared precipitation to the Legates and Wilmott (1990) climatology. Also discussed were sea level pressure and measures of the contributions of stationary and transient eddy activity to the variability in the standard band pass and low pass regimes; this part is not included in the present discussion.

Fig. 3.1 shows zonal means of annually and seasonally averaged latitude-pressure distributions of the temperature difference between the coupled simulation and the mean climatology of two realizations of the uncoupled model for an extended AMIP period (Gates 1992). These integrations are the same as used by Roeckner et al. (1996b) for validating the uncoupled model. Compared to the error distribution given by Roeckner (1996b), the deviation of the coupled simulation from the AMIP results is negligible and hardly reaches 1 K. The exception is the Antarctic periphery where the coupled model simulates temperatures which exceed those found in the AMIP runs by up to 2 K but the latitudinal and vertical extent is not large. In northern winter the difference between the coupled and uncoupled simulations is 1 to 1.5 K in the polar lower and middle troposphere, whereas in the northern summer the largest difference occurs near the Antarctic periphery where values are about twice those found in the annual mean.

Zonal wind latitude-pressure distributions are shown in fig. 3.2. As with temperature, fig. 3.3 shows the difference between the coupled model and the AMIP results. Fig. 3.2.a shows annual mean conditions. Compared to the uncoupled model, the location and strength of the subtropical jets in both hemispheres is similar since the zonal speed in the coupled model is only about 1 ms^{-1} less. Compared to the ECMWF analysis quoted by Roeckner et al. (1996b) the NH jet is equally overestimated. The easterlies near the tropopause are further enhanced by about 2 ms^{-1}. In DJF (fig. 3.2.b), the enhancement near the tropical tropopause in the coupled simulation is stronger. In JJA (fig. 3.2.c), the SH subtropical jet is about 3 ms^{-1} weaker than in the uncoupled model, leading to a reduction in the deviation from the analysis.

The geopotential height of the 500 hPa surface is shown in fig. 3.4. Fig. 3.5 shows the difference between the coupled model and the AMIP integrations. In DJF over the NH (fig. 3.4.a), the polar low is underestimated in a similar manner to the uncoupled simulation but the deviation remains within

about 10 gpdam. Over the North Pacific, particularly the far north-west, the coupled model still overestimates geopotential height but the bias is reduced by about 2 gpdam compared to the AMIP simulations. In the SH the distribution in DJF agrees to within 1 gpdam between the coupled and the uncoupled simulation. Hence, as mentioned in Roeckner et al. (1996b) the wavenumber 3 structure in the height field on the Southern Hemisphere is less pronounced than in the analysis data. In JJA in the case of the SH (fig. 3.4.d) the negative bias south of Australia and the southern part of South America is compensated about halfway. The NH (fig. 3.4.c) exhibits a polar low with heights overestimated by a similar amount (typically about 8 gpdam) as in the uncoupled simulation.

Fig. 3.6 shows the geographical distribution of precipitation (sum of convective and large scale precipitation). Fig. 3.7 shows the difference between the coupled model simulation and mean of the two AMIP integrations. The domain is the Pacific Ocean basin only as distinct from Roeckner et al. (1996b) who compare the global distribution of precipitation to the Legates and Wilmott (1990) climatology. In that study it was noted that the precipitation estimate given in this climatology over the oceans differed considerably from the GPCP estimate (Arkin and Xie, 1994), and it was concluded that the variation among the available observational estimates could be an indication of a general uncertainty in estimating precipitation over ocean areas (see also Janowiak et al., 1995). The annual mean, shown in fig. 3.6.a, exhibits a very similar structure to the result from the uncoupled simulation. This is true for the dry tongue with precipitation below 1 mmd^{-1} in the eastern Pacific and the location of areas of deep convection, in particular, the annual mean Intertropical Convergence Zone (ITCZ) and the South Pacific Convergence Zone (SPCZ). As in the uncoupled simulation, the orientation of the latter is more realistic than in the previous version of the model. The areal extent of heavy preciptation (greater than 10 mmd^{-1}) is somewhat greater than found for the uncoupled model in Roeckner et al. (1996b). The equatorial portion of the warm pool exhibits a difference between the coupled and the uncoupled simulation which is similar to the difference between the uncoupled model and the Legates climatology which was shown in Roeckner et al. (1996b) but of opposite sign. The coupled model thus reproduces this particular climatology more closely. In DJF (fig. 3.6.b) the precipitation in the North Pacific storm track region is set apart less clearly from Japan in the coupled model than in the uncoupled simulation. Also, the extent of the dry zone in the trade wind belt is somewhat greater in the coupled model. In JJA (fig. 3.6.c), the coupled model exhibits a greater intensity and larger extent of precipitation within the South Pacific convergence zone. This is related to a deviation of the simulated seasonal cycle of SST from observations as discussed below. In the observations the area with SST above 27° C known as the warm pool in the western Pacific extends northward to about 25° N until September in observations, whereas in the coupled model the southward retreat sets in at least a month earlier. Roughly at the same time a south-eastward extent of the warm pool area is found which is larger than observed, and this at least partly explains the enhanced precipitation in that area. The close correspondence of the area of ocurrence of deep convection with the location of surface waters with a temperature in excess of 27.5° C was highlighted by Graham and Barnett (1987).

To summarize the validation performed for the above characteristics of the general circulation, good agreement is generally found between the coupled simulation and the reference using prescribed SST as described by Roeckner et al. (1996b). This is an expected result given that the SST annual cycle in the coupled run is in fairly good agreement with observations as shown in the subsequent discussion. Apart from the SST, the validation is performed for the fluxes of heat and momentum and, finally, for the large scale upper ocean dynamics given that strong currents exert a significant

influence on SSTs particularly in the equatorial region.

3. 2. Sea surface temperature and surface fluxes of heat and momentum

Fig. 3.8. shows the geographical distribution of SST over the Indo-Pacific domain for January, April, July, and October for the coupled model. In fig. 3.9 results from the global ice and sea surface temperature dataset (GISST), version 2.2 (Parker et al. 1995) are displayed for comparison, where the time period was taken from 1951 through 1975. Near the western boundary, in all four months, the isotherm for, say, 23° C, in the simulation is found further north than in the GISST data. However, north of Japan SSTs become comparable between both. In the coarse resolution models typically used for climate studies (e.g., Latif 1997), it is generally not possible to resolve details of the flow in the Kuroshio and Oyashio currents near the western boundary, and the correct separation of the currents is difficult to achieve even in relatively higher resolution (1 degree, say). Thus inaccuracies in the advective heat transport call for heat flux adjustment. Since only annual means are adjusted, errors are still to be expected for the seasonal cycle of SST. Across the North Pacific, during the second half of the year the model overestimates the tendency for isotherms in the Kuroshio/Oyashio current extension to become more zonal and more tightly spaced. Although this may indicate an inaccuracy in the sensitivity, particularly with respect to large scale upper ocean dynamics in response to surface winds in accordance with the Sverdrup relation (see also chapter 5) it should be noted that data coverage over the period used is not homogeneous (Parker et al. 1994).

Over the tropical oceans there is a satisfactory representation of the seasonal cycle by the coupled model. In the tropical Pacific in particular, the warm-pool/cold-tongue configuration is similar to the observations. Since a detailed discussion was given in Bacher et al. (1998) it is sufficient to repeat the key points here. The warm pool is represented graphically by shading the area with SST exceeding 27° C. This area therefore encompasses the region where SSTs satisfy a criterion for deep convection first established by Graham and Barnett (1987). They arrived at a threshold of 27.5° C. In the shaded area the contouring is at intervals of 0.5° C, otherwise 1° C is used. The greatest extent of the shaded area south of the equator is found in April both for the simulation and for the observations. The model correctly positions the eastern boundary of this area near 120° W. Further west the seasonal cycle is weak in both the simulation and the observations and on the equator and south of it the very high SST, in excess of 29° C, are reproduced to within less than 0.5° C in January and April, whereas a warm bias of about 0.5° C is seen in July and October. North of the equator both the simulation and the observations attain maximum northeastward extent in July, and the 27.5° C contour in the model is positioned similarly to the 28° C contour in the observations. This accounts for the similarity of the distribution of precipitation in the coupled and uncoupled model simulations (cf. Roeckner et al. 1996b). In October, the retreat of the 27° C contour from its north-eastern extreme position is less pronounced in the observations, thus indicating that in the coupled model this process sets in at least a month earlier. The seasonal variation of the cold tongue in the coupled model involves a broadly realistic westward expansion in early boreal summer, such that near the date line SST is never below 28° C. Particularly in July and October, the zonal SST gradient about midbasin is stronger in the simulation which enhances the tendency for stronger than observed surface wind at this time of the year. Surface wind stress provides a positive feedback on SST at the equator which is discussed in more detail below. A shortcoming in the coupled simulation of the seasonal cycle is evident in the cold tongue which exhibits a cold bias in January and, particularly, in April. As noted in Bacher et al. (1998), the highest sensitivity is found in this region where in both the simulation and

the observations the equatorial thermocline shoals and a strong vertical temperature gradient (yielding an observed temperature difference of about 6 K between the surface and 100 m depth; e.g., Colin et al., 1971) develops. The model thermocline is too shallow and an excessive vertical temperature gradient develops, a problem found similarly in some other models (e.g., Frey et al. 1997). The effect on the low level winds (Lindzen and Nigam 1987), and thus on the Hadley and Walker circulation, can be expected to be minor due to the spatial confinement.

For the validation of the net surface heat flux and the surface shortwave and longwave radiative fluxes as well as the latent and sensible heat flux components the Oberhuber (1988) climatology is used. For all flux components the distribution for the annual mean as well as for January and July monthly means is shown. It should be noted that Gleckler and Weare (1997) estimated the uncertainties in this climatology over the North Pacific to be greater than 10 Wm^{-2} for the shortwave flux (which is the larger of the radiative fluxes) and greater than 20 Wm^{-2} for the latent heat flux, with respect to annual mean values.

Fig. 3.10.a shows the annual mean net surface heat flux over the tropical and North Pacific Ocean domain. Fig. 3.10.b and 3.10.c show monthly means for January and July, respectively. Fig. 3.11.a through 3.11.c show the corresponding fields from the Oberhuber (1988) atlas. For the annual mean, the most important differences are a bias within the cold tongue where the simulated fluxes exceed the observed ones by about 40 Wm^{-2}, and a negative deviation of about 30-40 Wm^{-2} magnitude in the western Pacific warm pool region. In the cold tongue in January the excess of the simulated heat flux over the observed is close to 30 Wm^{-2} whereas for July it is about 40 Wm^{-2}. For the warm pool, results from an analysis of uncoupled simulations with ECHAM4 and ECHAM3 by Chen and Roeckner (1996) place caveats on the present comparison. These authors used different observed heat flux datasets which indicate a net heat flux closer to zero in the western equatorial Pacific than estimated by Oberhuber (1988).

Surface sensible and latent heat flux annual means along with January and July monthly mean values are shown for the coupled model in fig. 3.12.a through 3.12.c and 3.14.a through 3.14.c. The corresponding plots for the Oberhuber (1988) climatology are shown in fig. 3.13.a through 3.13.c and 3.15.a through 3.15.c.

For the annual means, the main difference is an excess evaporative cooling of 20-30 Wm^{-2} in the coupled model in the off-equatorial tropics. In January, there is general agreement in sensible heat flux to within about 10 Wm^{-2} while latent heat loss by the ocean in the subtropical North Pacific is simulated about 20 Wm^{-2} stronger than observed. In July, simulated and observed sensible heat loss agree to within 10 Wm^{-2} while evaporative cooling in the equatorial Pacific is stronger in the simulation by about 30 Wm^{-2}. Stronger than observed trade winds are the most natural explanation. Near Japan, the January evaporative cooling is stronger by more than 60 Wm^{-2} compared to the climatology.

Radiative fluxes at the ocean surface are examined in fig. 3.16 for the shortwave contribution and in fig. 3.18 for the longwave contribution in the coupled model simulation and in fig. 3.17 and fig. 3.19 for the climatology.

In the shortwave component the greater magnitude of the typical fluxes compared to the other heat flux components points to the effort required for reducing possible inaccuracies. In comparison to the previous model cycle, ECHAM3, significant improvements in ECHAM4 benefit the coupled model

discussed here. The present model simulates a shortwave flux at the surface which in the annual mean exceeds the climatological values by close to 30 Wm^{-2} in the tropical region near the eastern boundary. In coupled integrations with ECHAM3, which employed no flux adjustment (Latif et al., 1994), the central and eastern Pacific were heated unrealistically mainly by radiative fluxes which caused an excess in total heat flux close to 100 Wm^{-2} compared to the Oberhuber (1988) estimate. A detailed comparison of ECHAM3 and ECHAM4 can be found in the study by Chen and Roeckner (1996) which focusses on the heat budget in the warm pool region. The climatology used in the present comparison has an annual mean surface shortwave flux which exceeds the model simulated flux by about 10-30 Wm^{-2} in areas of deep convection whereas the simulated shortwave flux is greater in the subtropical dry zones by about 20-40 Wm^{-2}. The comparison for January yields similar results, i.e. over the southern subtropical Pacific the model simulates 270 Wm^{-2} instead of about 230, whereas near 10° N a small area with 180 Wm^{-2} instead of about 150 Wm^{-2} is found. In July most notably there is a deficit of about 30-40 Wm^{-2} in parts of areas with deep convection but it should be stressed again that the climatology is subject to considerable uncertainty.

Surface longwave radiative flux annual means, displayed in fig. 3.18 for the model and in fig. 3.19 for the climatology shows that less heat is lost by the ocean in areas of deep convection in the simulation which indicates enhanced downward backradiation. The difference is typically about 10 Wm^{-2}. A similar magnitude is found near the position of the subtropical anticyclone. Similar differences occur in the case of the January and July means.

Surface wind stress as simulated by the coupled model is shown in fig. 3.20 and compared to the output from operational ECMWF reanalysis for the period 1979 through 1994 (Gibson et al., 1997), shown in fig. 3.21. January and July are used for comparison in a manner similar to Bacher et al. (1998) who compared the coupled model wind stress to the FSU dataset (Stricherz et al. 1992,1993) but in that study the comparison was restricted to the tropical strip 30° S to 30° N. The results from the reanalysis exhibit little difference from the FSU results used by Bacher et al. (1998). The midlatitude westerlies in January are simulated rather accurately by the coupled model regarding both spatial distribution and strength. Near Japan, at latitudes where the separation of the Kuroshio occurs, the excessive meridional temperature gradient via an increase in the baroclinicity leads to substantial overestimation of surface wind stress compared to the reanalysis. Further east, however, the maximum of 0.220 Nm^{-2} is only about 10 % stronger than found in the reanalysis. The trade winds simulated by the coupled model are generally more than 30 % stronger than given by the reanalysis. The spatial structure is similar, with slightly shifted emphasis of the south-eastern trade winds towards the equator. In July the East Pacific portion of the south-eastern trades exhibits similar strength to the reanalysis but around 150° W near the equator they reach 0.100 Nm^{-2} rather than diminishing to about half the East Pacific value as in the reanalysis. The results for the uncoupled model given by Roeckner et al. (1996b) are indicative of a pronounced sensitivity of the surface wind over tropical oceans to horizontal SST gradients. In the coupled simulation an overestimated zonal wind stress on the equator will lead to a strengthened equatorial upwelling of cold water and thus to a strengthened zonal SST gradient. The effect will be to further enhance the surface wind; thus a positive feedback loop operates which influences the simulation of the seasonal cycle as well as the interannual variability in a coupled simulation. The strength of the simulated mean July winds thus indicates a sensitivity that needs to be accounted for, especially since the flux adjustment applies only to the annual mean heat flux while wind stress is left altogether unadjusted. An overestimation of surface wind stress of about 0.020 Nm^{-2} is generally found in the Northern Hemisphere trades in

July. Winds near 50° N along the Northern flank of the subtropical anticyclone in the reanalysis are stronger by about 0.010 to 0.020 Nm^{-2}.

3. 3. Sea surface height, oceanic mixed layer, sea ice, tropical thermocline and currents

Simulated annual mean sea surface heights are shown in fig. 3.22 and compared to results from TOPEX/Poseidon satellite altimetry (Fu et al. 1994) shown in fig. 3.23. In the latter figure, additional arrows indicate the direction of the large scale ocean currents and roughly follow the contours of sea surface height. The western boundary currents are visible which form the continuation of the equatorial westward currents. In the North Pacific in particular, the Kuroshio/Oyashio extension is evident in the TOPEX data, and the continuation of this system leads into the return flows both further north in the subpolar gyre and towards lower latitudes in the subtropical gyre. This well-known double gyre circulation, as can be inferred from the simulated sea surface height, is reproduced by the model. There is also a reasonable quantitative agreement in the sea level gradient. Thus, the maximum surface heights in the model reach 90 cm near the western boundary current south of Japan compared to about 40 cm near 10° N in the western North Pacific, such that the difference relevant for the large scale currents is 50 cm. In the observations values are about 120 cm south of Japan and about 80 cm in the western Pacific area, yielding a difference of 40 cm. The near zero values occur at the boundary between the subtropical and subpolar gyres in the model where the observations exhibit values near 40 cm. Relative to the value near Japan there is thus a similar difference in the model and the altimeter observations.

The model predicted mixed layer depth is shown in fig. 3.24 for March and in fig. 3.25 for September. March is used because it is well-known, as discussed, e.g., in the Levitus (1982) atlas, that in the Northern Hemisphere subtropical gyres the maximum mixed layer depth is reached in March. In September mixed layer depths are still quite close to their minimum summer values.

The Levitus (1982) atlas gives mixed layer depths estimated from two different criteria for temperature and salinity to lie within a specified range from the surface values. Here the estimate based on temperature lying within 0.5 K from the surface temperature is reproduced. The results for March are shown in fig. 3.25.

The model captures the shallow tongue in the tropical eastern Pacific. South of the equator the mixed layer deepens toward the east. In the western half of the basin deep mixed layers are situated 5° N to 15° N. Thicknesses simulated by the model here are around 100 m similar to Levitus (1982). The subtropical North Pacific minimum is also captured. Around the latitude of the Kuroshio/Oyashio separation the cross-basin extent of deeper mixed layers in the model is represented by the 80 m contour which corresponds to the 100 m contour in Levitus (1982). East of Japan, mixed layer depth in the model which reaches values near 220 m is substantially greater than the observed values which hardly exceed 150 m. In this region we noted that winter wind stress found in the model was substantially stronger than that derived from the observations, although the comparison for this quantity refers to January values. Stronger wind stirring would be a consistent explanation for the overestimated mixed layer depth. In the western equatorial Pacific the substantially shallower model mixed layer, compared to the Levitus estimate, reflects the presence of a shallow halocline. In the observational study of Lukas and Lindstrom (1991) this was taken as indicative of a shallower mean depth for the turbulent region than the local thermocline depth would suggest.

The September model mixed layer depths are shown in fig. 3.26 and compared to the Levitus (1982) values, fig. 3.27. South of Hawaii, thicknesses are greatest in the North Pacific and close to 50 m in the observed estimate and just over 60 m in the model. A tongue of shallow mixed layers is found on the equator in the east. Much deeper mixed layers are found in the area extending southeastward from the central equatorial Pacific almost to the eastern boundary in both the model and the Levitus (1982) results.

Two peripheral seas of the Pacific, the Bering Sea and the Sea of Okhotsk, exhibit seasonal sea ice coverage which in a climate model should be validated similar to SST. In the present thesis this is done for the months of March and September which are close to the extremes of the seasonal cycle of sea ice coverage in both hemispheres. The dataset used for validation is the GISST dataset, version 2.2 (Parker et al. 1995), and the climatology is taken over the period 1979 through 1994.

Fig. 3.28.a and fig. 3.28.b show the sea ice cover in March simulated by the coupled model in the Arctic and the Antarctic, respectively. For the GISST dataset, the corresponding results are shown in fig. 3.28.c and fig. 3.28.d. The model captures the positioning of the ice edge in the Greenland-Iceland-Norwegian Sea and between Spitsbergen and Novaya Semlya. The sea ice coverage in the Baffin and Hudson Bays is also reproduced, but in the model there is no ice coverage surrounding Labrador. Sea ice cover in the Sea of Okhotsk is reproduced while in the Bering Sea the simulated sea ice cover is substantially less extensive. While insufficient sea ice coverage in the Wedell and Ross Seas is obtained in the simulation, the model produces a spurious extent of sea ice in the Indian Ocean sector.

For the month of September, the coupled model results are shown in fig. 3.29.a and fig. 3.29.b for the Arctic and the Antarctic, respectively. Fig. 3.29.c and fig. 3.29.d show the results for the GISST dataset. The model simulates the observed melting in the Barents Sea and the position of the ice edge between Spitsbergen and Greenland. It does not capture the remains of ice coverage in the Baffin Bay. In the Antarctic, sea ice coverage is insufficient mainly in the Atlantic and south-western Pacific sectors.

Since the focus of the present dissertation is not the Southern Hemisphere circulation, the shortcomings in the simulation of the maximum of Antarctic sea ice extent can be neglected, although they indicate scope for future improvement of the present coupled model. Simulated Northern Hemisphere sea ice coverage in both the winter and the summer extremes exhibits a geographical distribution with sufficient accuracy for studying the seasonal cycle and variability up to decadal scales in the Northern Hemisphere general circulation.

The discussion of the annual cycle simulated by the coupled model is concluded with a discussion of the tropical thermocline and currents. Since in Bacher et al. (1998) a complete description is given, only the main points are repeated here.

Fig. 3.30 shows a meridional section of simulated temperature and zonal currents for 150° W for the month of April and an annual mean section for these quantities along the equator. The results from the Hawaii to Tahiti shuttle experiment (Wyrtki and Kilonsky, 1984) use a section along 155° W. The surface currents, in particular the North Equatorial Countercurrent (NECC) and the North Equatorial Current (NEC), are weak in April as observed. In October they straddle the ridge in the thermocline structure near 11° N as observed, consistent with thermal wind balance (e.g., Picaut and Tournier 1991). The Equatorial Undercurrent (EUC) is a problematic feature in most models; in the present

model it is fully collinear with the equatorial thermocline, in line with recent theoretical results (Pedlosky 1987). The thermocline depth is consistent with observations (Colin et al. 1971). These features are benefits of the isopycnic coordinates used. The speed of the undercurrent, however, is underestimated by a factor of 2. Although the current is substantially broadened in the simulation due to a high value of numerical viscosity ($10^5 m^2 s^{-1}$) which explains that the observed maximum speeds are not attainable, all equatorial currents are generally also too weak. However, equatorial wave dynamics is successfully modeled (Bacher et al. 1998, Oberhuber et al. 1998). The observed strong April maximum is absent in the simulation of the seasonal cycle of the undercurrent.

The simulated vertical structure of the temperature and salinity field is shown in fig. 3.31 and fig. 3.32, respectively. Shown are zonal average quantities which implies the same format as used in the Levitus (1982) atlas. The isotherms above 6° C belong to the main thermocline which in the North Pacific reach down somewhat deeper than in the Levitus dataset. Thus the 6° C isotherm is deeper by about 100 m than given by Levitus. In this zonally averaged picture, the thermocline structure is similar to the observed with the trough-ridge structure of the equatorial Pacific temperature evident from the section in fig. 3.30. Salinity exhibits a tongue of intermediate water in the Southern Ocean which is given by the 34.4 psu isotherm which in the model extends to about 20°S such that simulation and observations agree well. A problem in the simulation is evident in the deep ocean which is too warm as evident from the position of the 2 K isotherm which is simulated at a depth of 3000 m rather than 2000 m as in the observations. Similarly, the highest salinity values of about 34.71 psu are not attained in the model.

3. 4. Validation Summary

The reference simulation for validating the time mean climate in the coupled model simulation consisted of two runs with the uncoupled ECHAM4 model identical to those described by Roeckner et al. (1996b). The general circulation was captured by using zonal mean temperature and zonal wind, 500 hPa height and preciptation over the Pacific area. While there was no essential deviation of the coupled simulation from the uncoupled climate for the zonal mean fields, the underestimation of the polar low was reduced slightly (by about 2 gpdam). For precipitation the deviation from the Legates and Wilmott (1990) climatology was less in the coupled simulation than in the reference climatology. The importance for the seasonal cycle of precipitation attributable to SST in the western Pacific, particularly the warm pool region, is known, e.g., by the work of Graham and Barnett (1987) who established a threshold for deep convection of 27.5° C. The general result was that the 1951-1975 climatology of the GISST 2.2 dataset was reasonably reproduced by the coupled model but with the retreat of the northern portion of the western Pacific warm pool occurring one to two months too early. In the cold tongue region, the main shortcoming is an unrealistically cold state in April while in the observations April cold tongue temperatures are close to the highest ones throughout the year.

The surface heat flux climatology used for validation is the Oberhuber (1988) atlas which is subject to uncertainties in the 10-20 Wm^{-2} range for shortwave and latent heat flux components. Apart from annual means, January and July means were intercompared. Differences were mostly within this observable uncertainty. Considerable deviation was found in the warm pool, where the dataset used by Chen and Roeckner (1996) yields less deviation of the coupled model from climatology. In the regions of seasonal stratus cover the deviation definitely exceed the observational uncertainty. For wind stress the data from ECMWF reanalysis 1979-1994, were well reproduced in the North Pacific for both January and July means. Trade winds are overestimated to a greater extent than in the

uncoupled model. In particular, the overestimation of the equatorial portion of the south-eastern trades in the coupled model on the equator in July is substantially greater than in the uncoupled simulation by Roeckner et al. (1996b). This is an indication of an oversensitivity to horizontal SST gradients in the model, with some bearing on the seasonal cycle and interannual variability.

Validation of the wind-driven large scale circulation was performed by comparing sea surface elevation simulated by the coupled model to data produced by TOPEX/Poseidon satellite altimetry. The inferred large-scale dynamics was found to be acceptable in the simulation, with the double gyre circulation reasonably reproduced. The ocean model predicts mixed layer depth which was compared to the Levitus estimate for March and September. Apart from regional deficits, such as a considerable overestimation off Japan in January caused probably by coupled interaction involving wind stress and upper ocean currents, there was a reasonable simulation of the seasonal extremes. For the same months, simulated sea ice cover was in good agreement in the Northern Hemisphere while in the Southern Hemisphere the maximum extent was underestimated in the coupled model. Equatorial surface currents exhibited little error in the seasonal phasing. High numerical viscosity was responsible for excessive broadening of the undercurrent, in particular, and the undercurrent core speed was only about half the observed. Pacific zonal mean temperature and salinity distributions indicated a reasonable main thermocline simulation.

List of figures

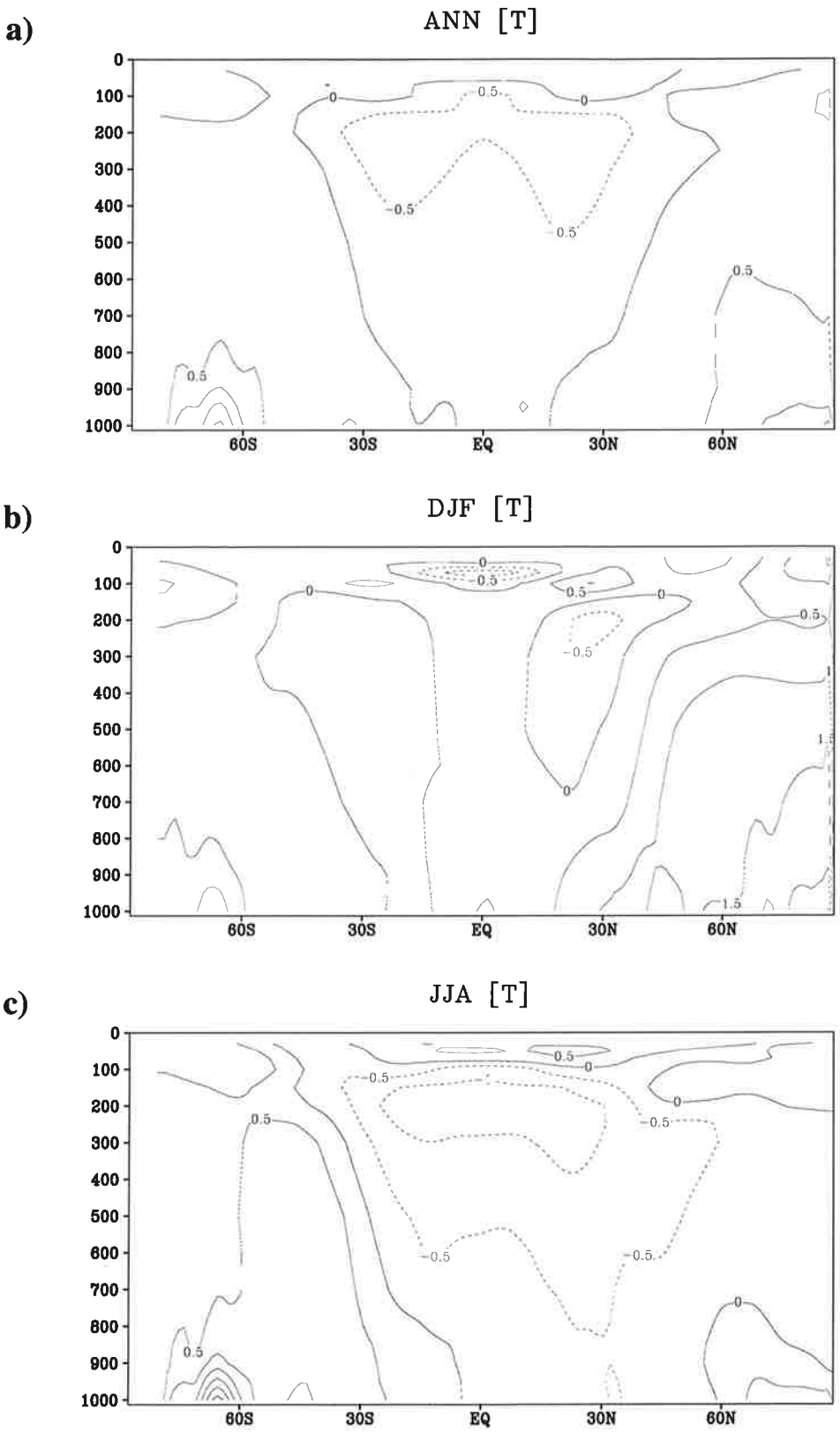

Fig. 3.1 Zonal mean temperature: coupled model minus average of two extended AMIP simulations with ECHAM4; a) annual mean, b) December - February, c) June - August. Contour spacing is 0.5 K

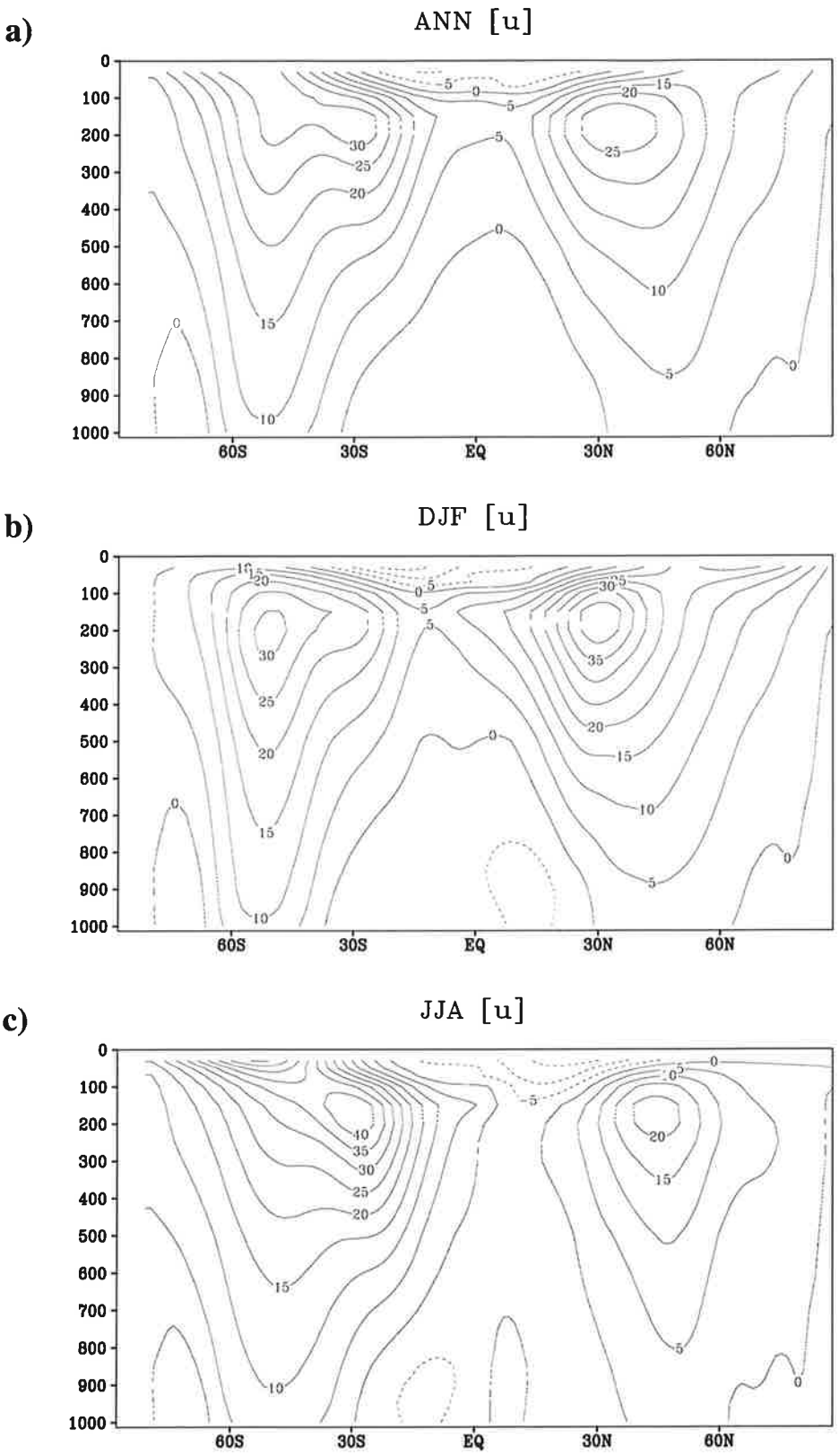

Fig. 3.2 Zonal mean zonal wind: coupled model. a) annual mean, b) December - February, c) June - August. Contour spacing is 5 ms^{-1}

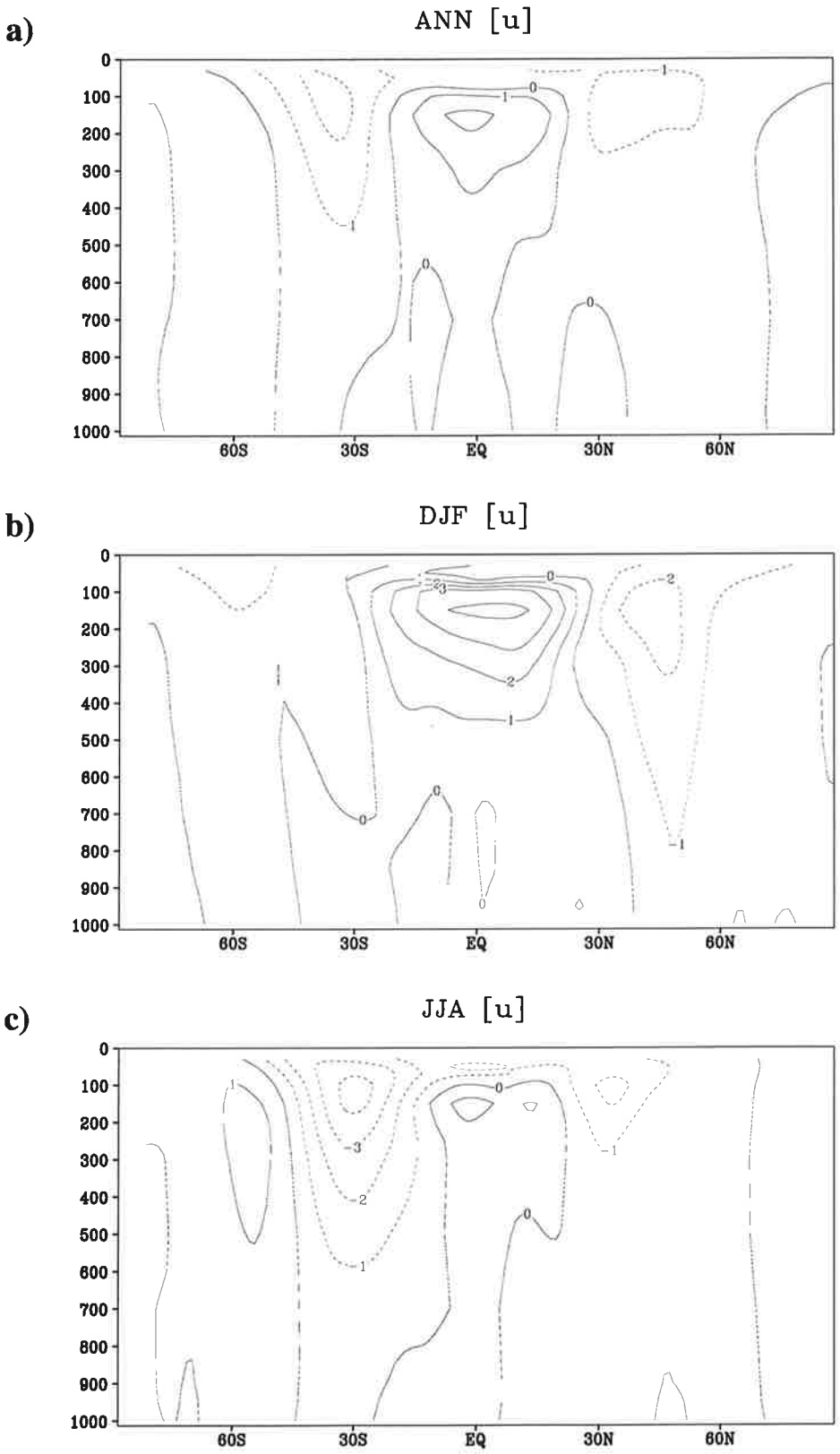

Fig. 3.3 Zonal mean zonal wind: coupled model minus AMIP results a) annual mean, b) December - February, c) June - August. Contour spacing is 1 ms^{-1}

a)

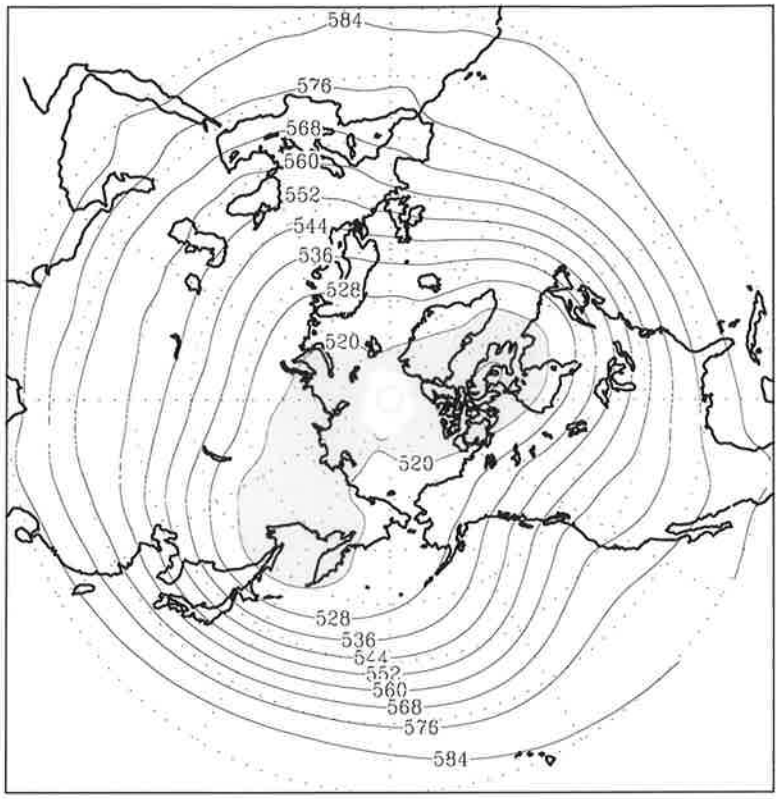

b)

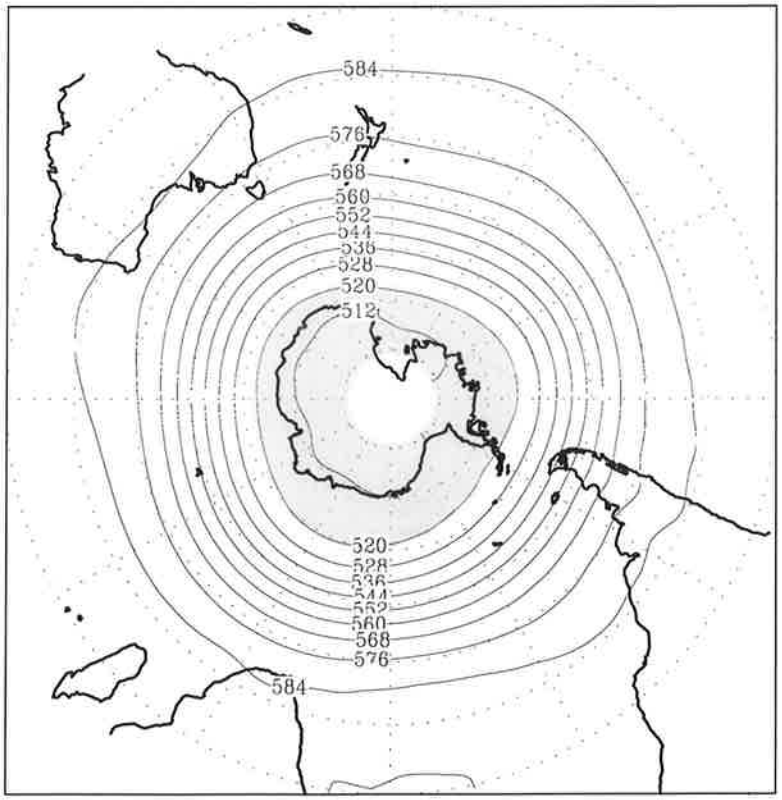

Fig. 3.4 500 hPa height in DJF: coupled run. a) Northern Hemisphere, b) Southern Hemisphere. Contour spacing is 8 gpdam. Shading indicates heights less than 520 gpdam

c)

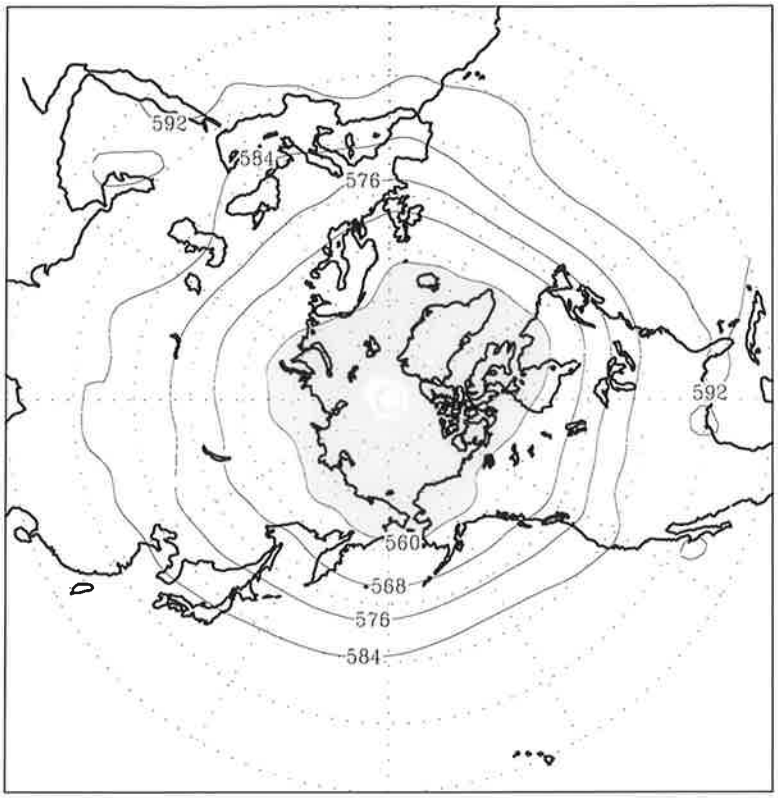

d)

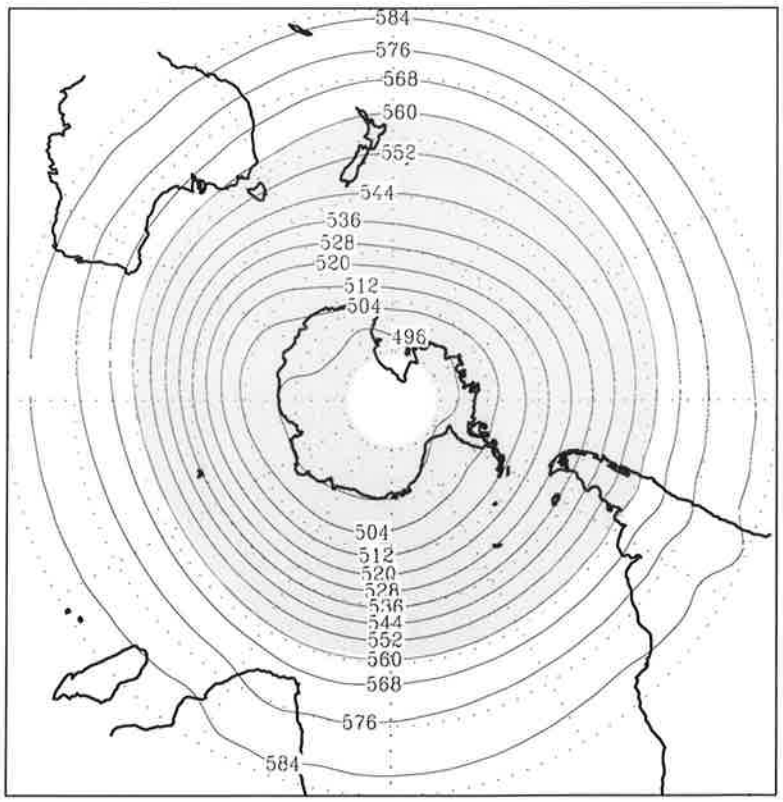

Fig. 3.4 (contd.) 500 hPa height in JJA: coupled run. c) Northern Hemisphere, d) Southern Hemisphere. Shading indicates heights less than 560 gpdam

a)

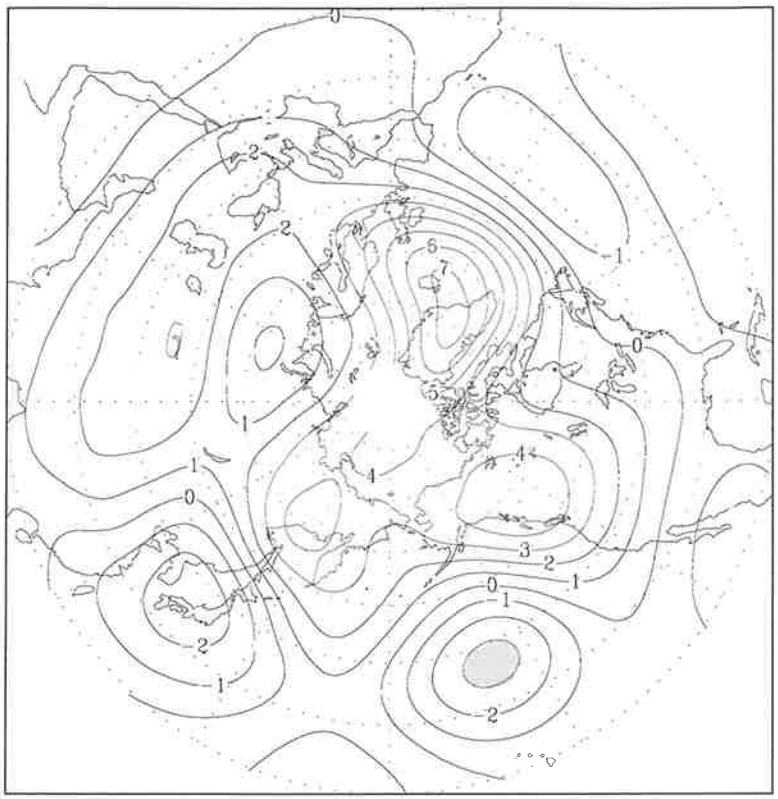

b)

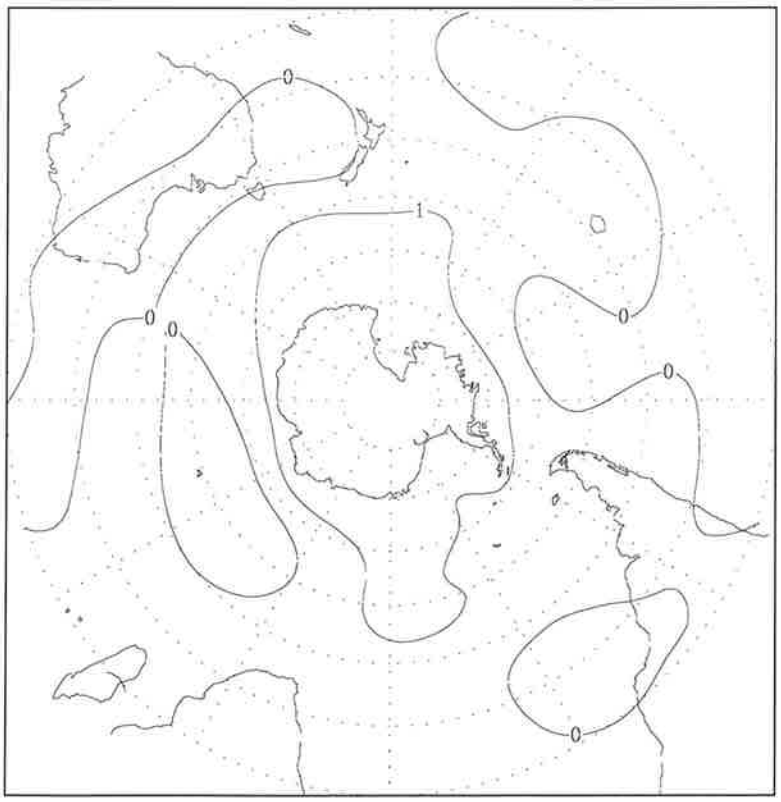

Fig. 3.5 500 hPa height in DJF: coupled model minus AMIP results a) Northern Hemisphere, b) Southern Hemisphere. Contour spacing is 1 gpdam. Shading indicates errors in excess of ±3 gpdam

c)

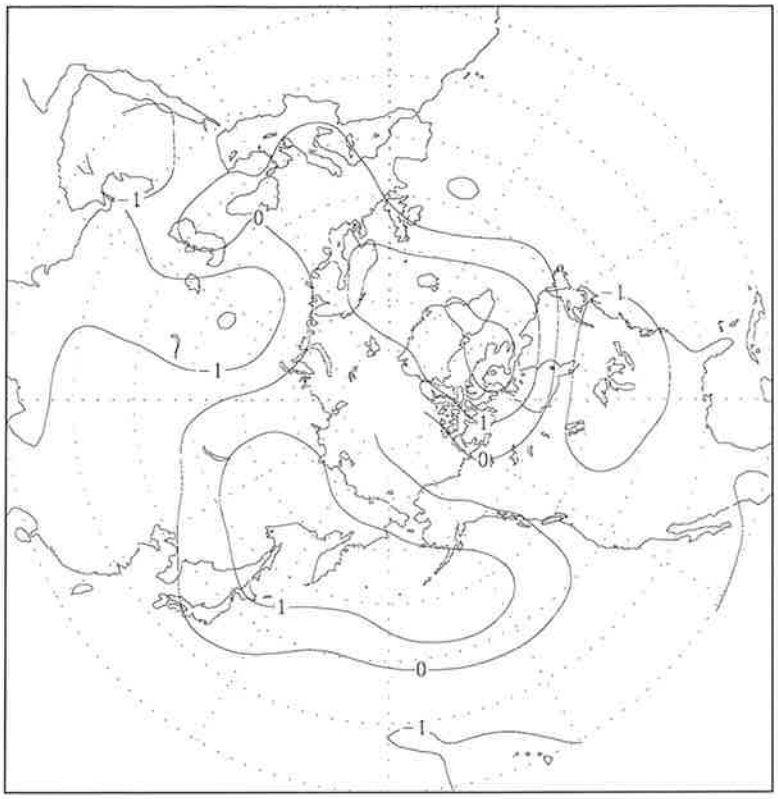

d)

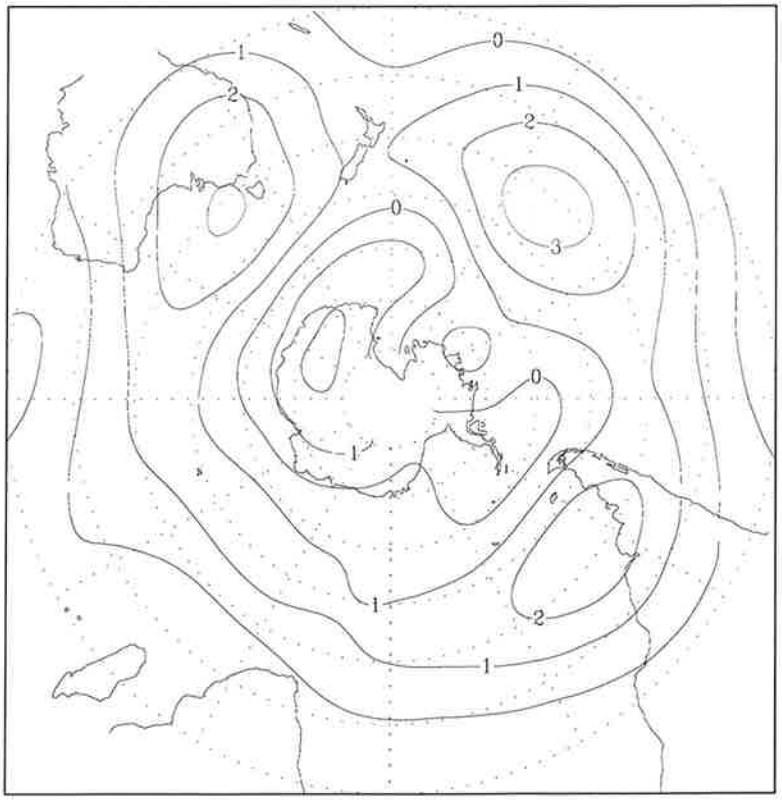

Fig. 3.5 (contd.) 500 hPa height in JJA: coupled model minus AMIP results c) Northern Hemisphere, d) Southern Hemisphere

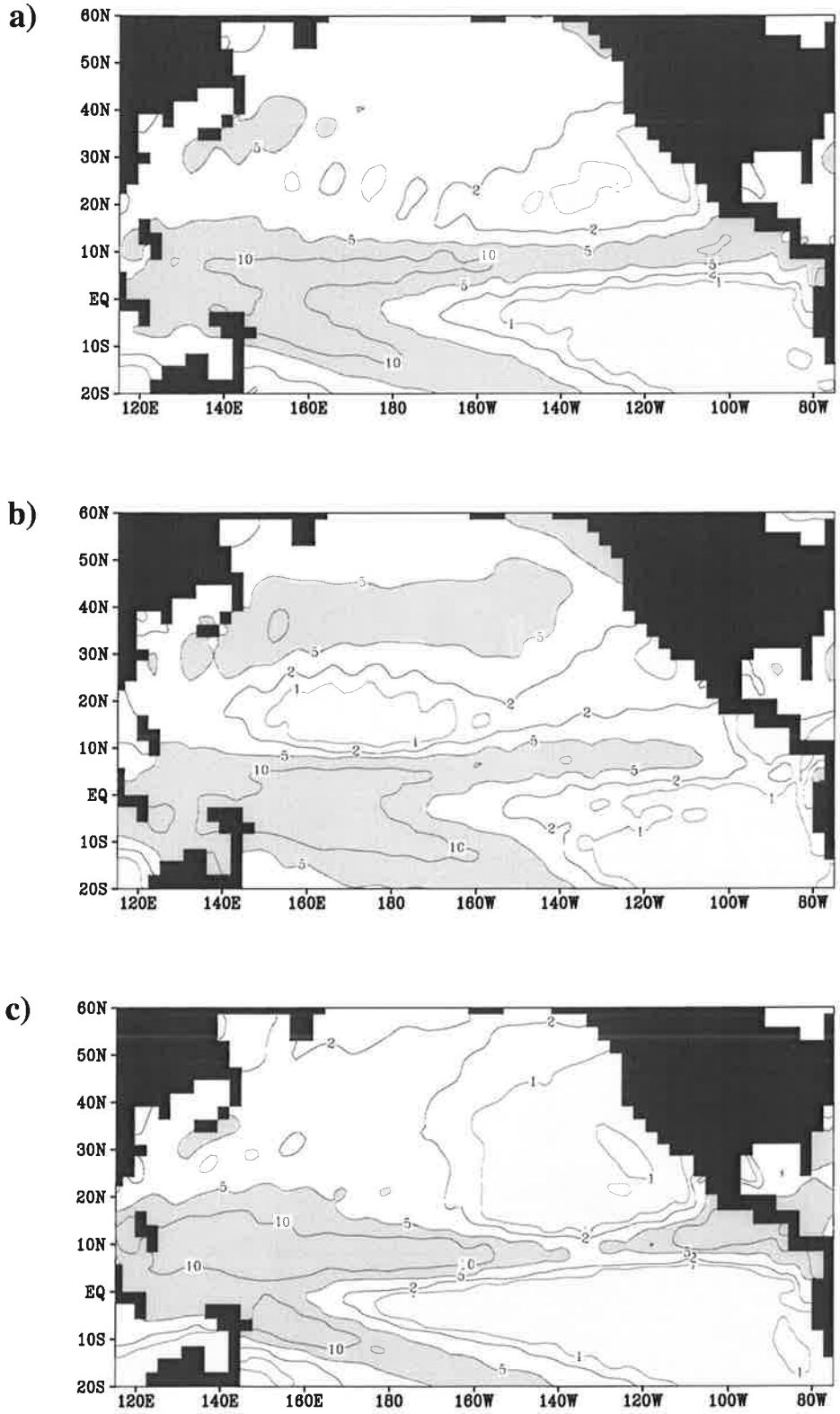

Fig. 3.6 Precipitation over the Pacific ocean, a) annual mean, b) December - February, c) June - August. Contours indicate 1, 2, 5, 10 mmd^{-1}. Areas with precipitation less than 1 mmd^{-1} (greater than 5 mmd^{-1}) are lightly (heavily) shaded

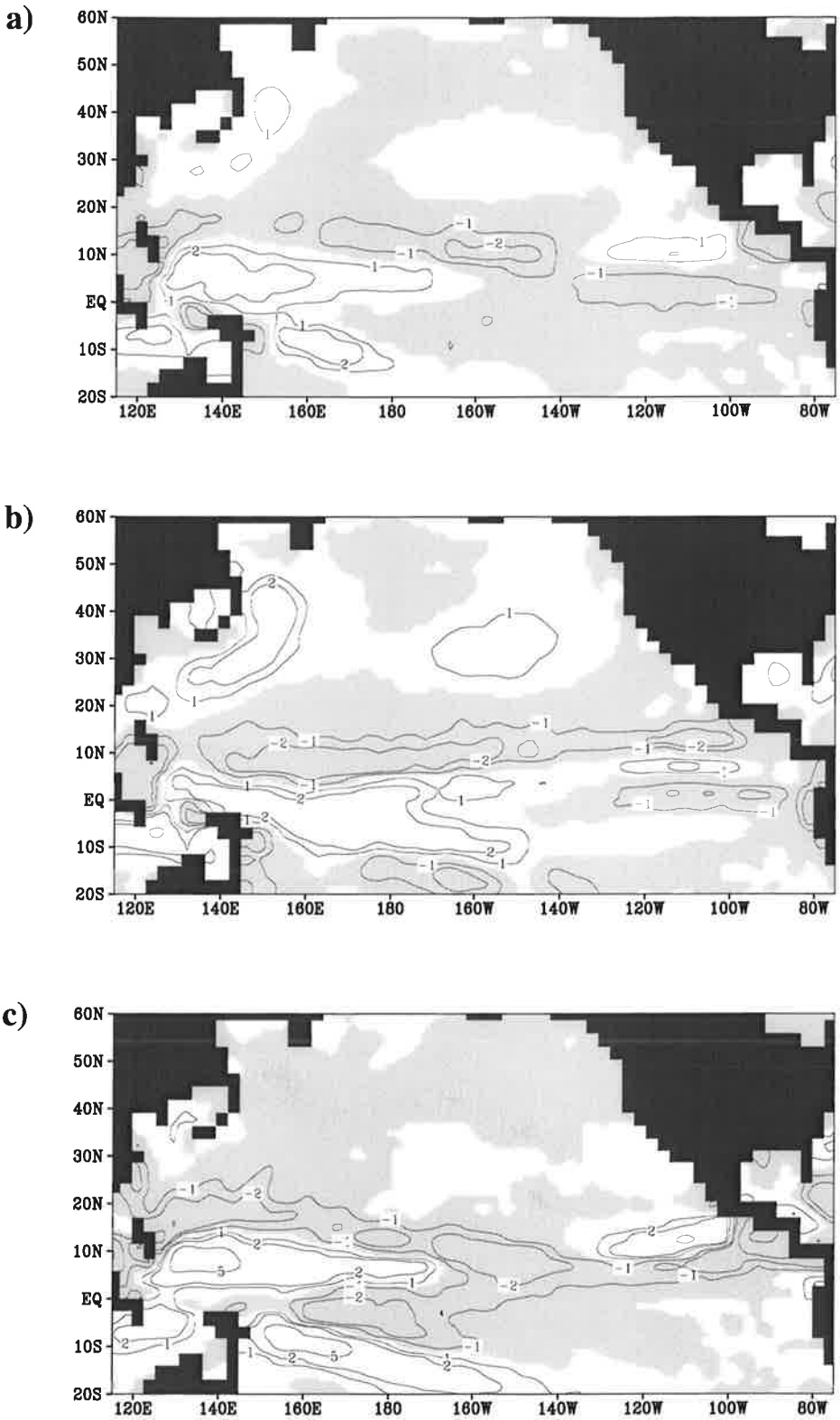

Fig. 3.7 Precipitation over the Pacific ocean: coupled model minus AMIP results, a) annual mean, b) December - February, c) June - August. Contour spacing is 1 mmd^{-1}. Shading indicates negative values

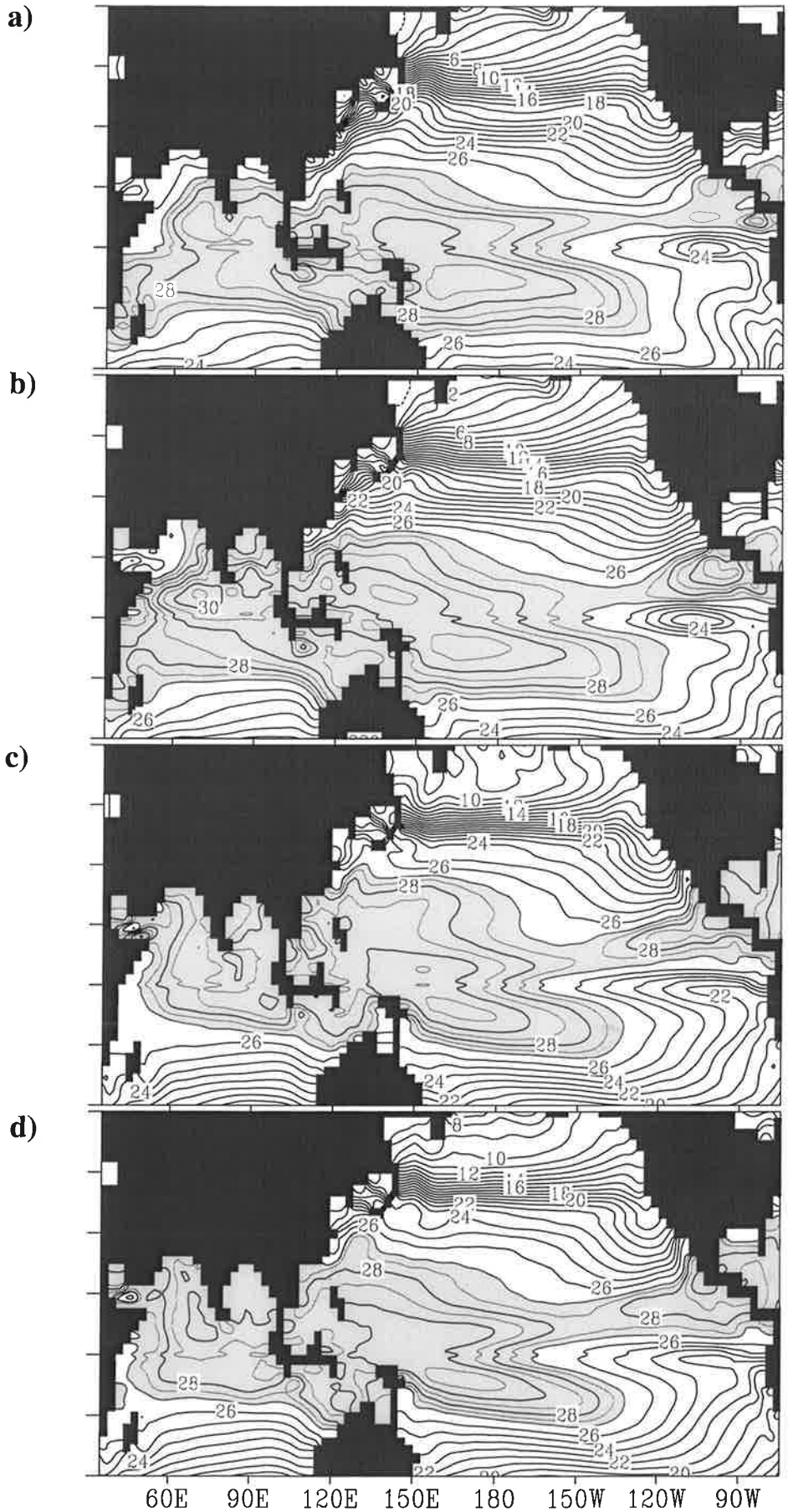

Fig. 3.8 Coupled model SST for a) January, b) April, c) July, d) October. Unit:°C. Ticks indicate 60°, ±30°, ±15°, 0° latitude.

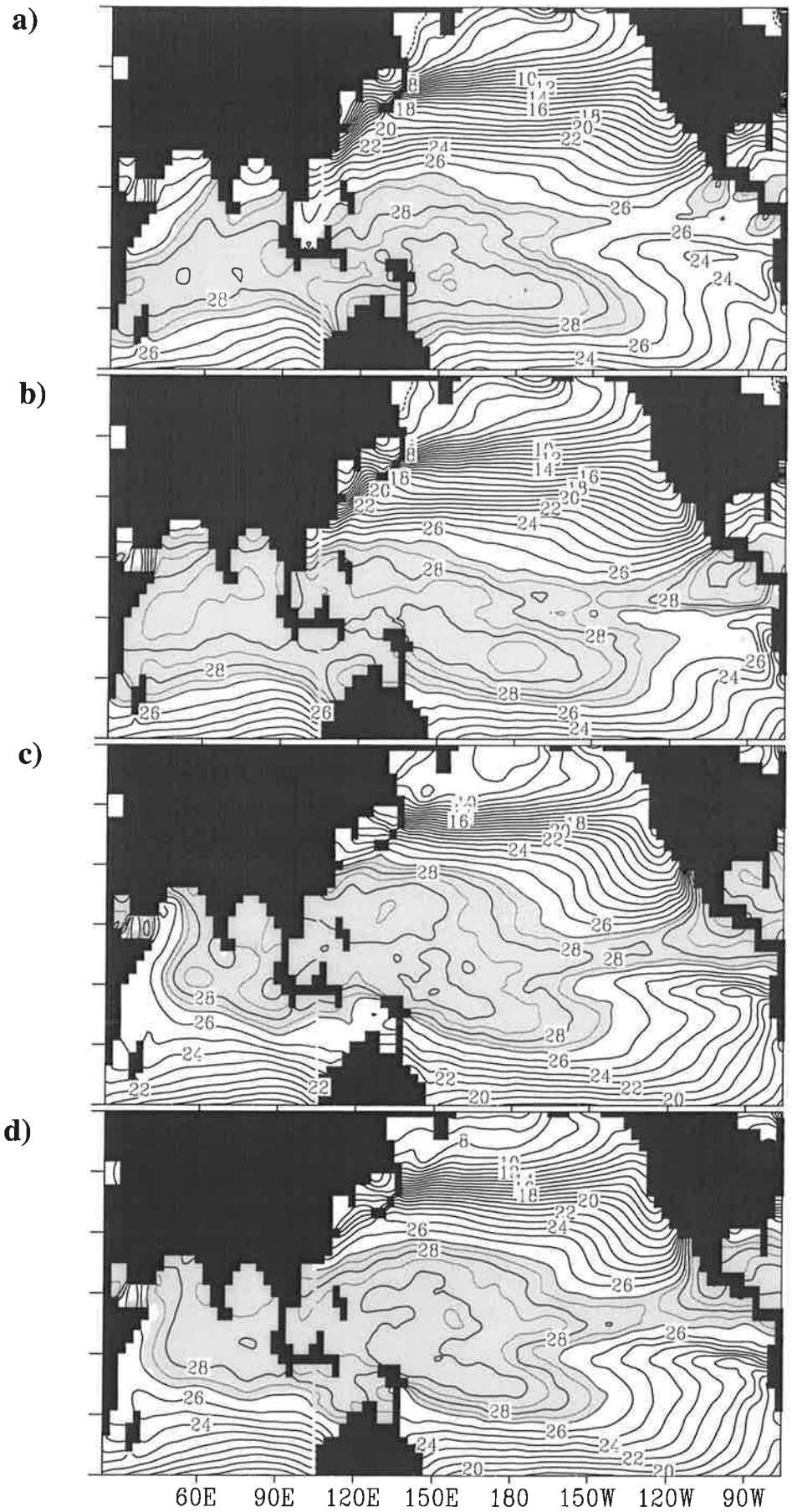

Fig. 3.9 GISST SST for a) January, b) April, c) July, d) October for 1951 - 1975

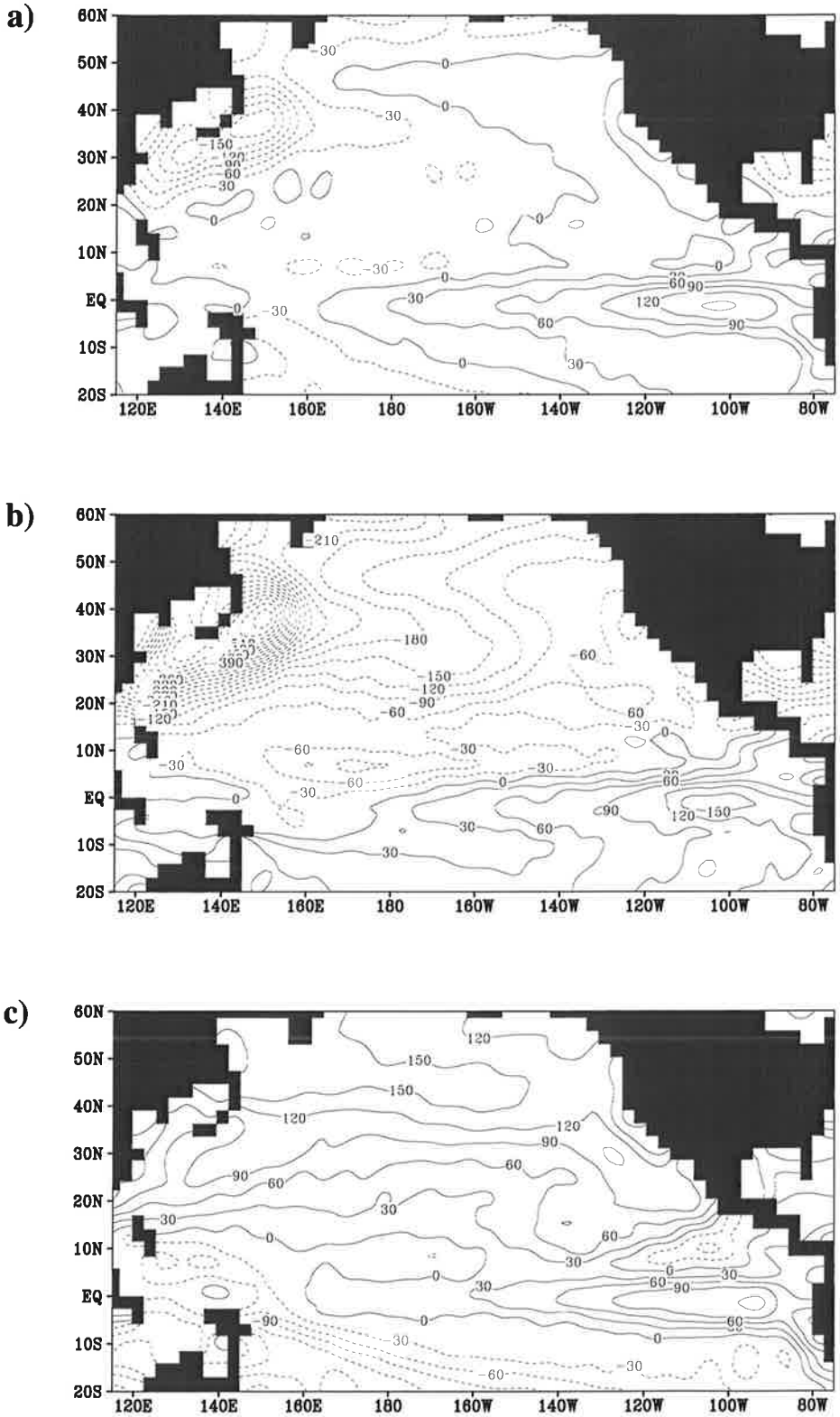

Fig. 3.10 Net surface heat flux over the Pacific ocean area for coupled model. a) annual mean, b) January, c) July. Contour spacing is 30 Wm^{-2}

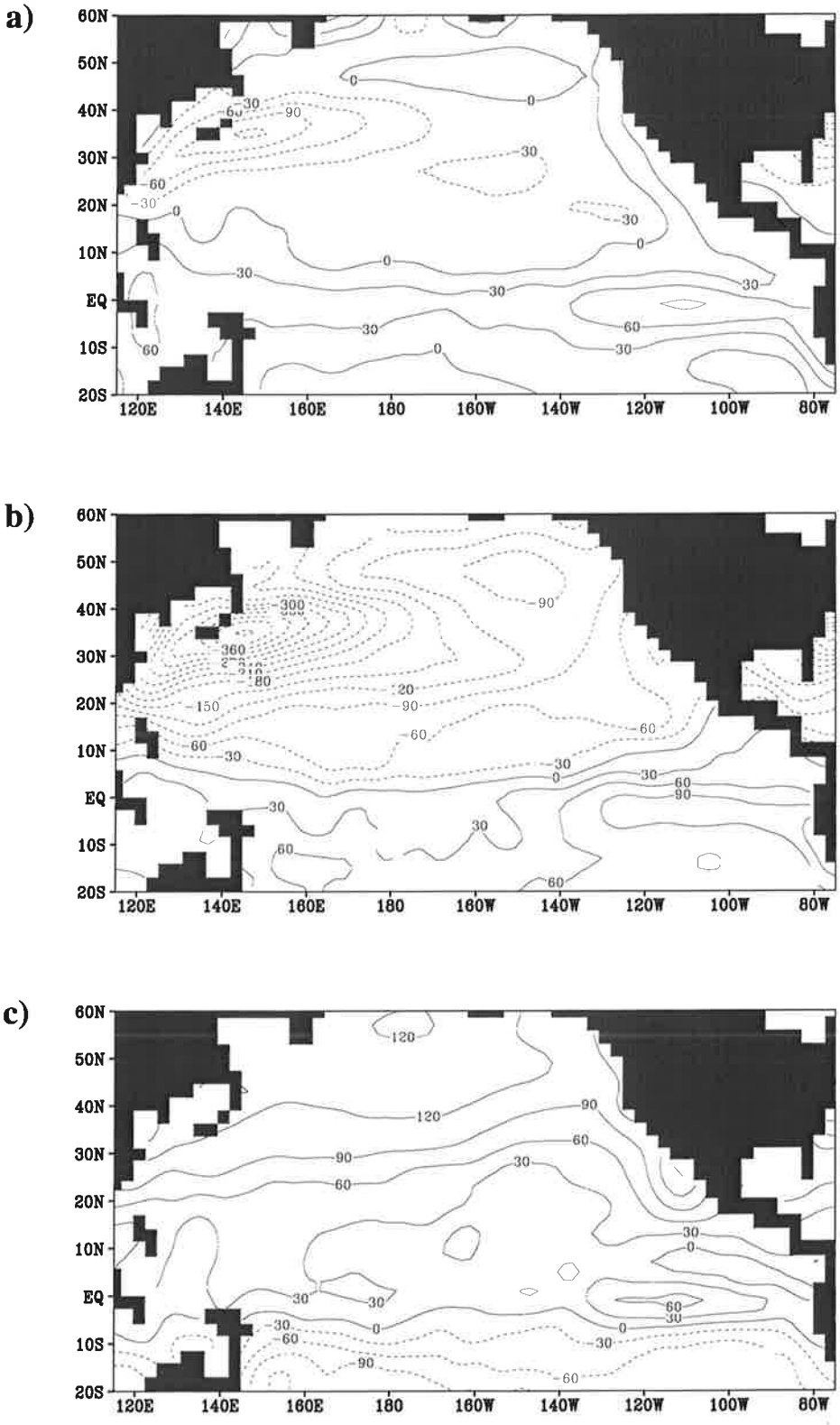

Fig. 3.11 Net surface heat flux over the Pacific ocean area from the Oberhuber (1988) climatology. a) annual mean, b) January, c) July. Contours as in fig. 3.10

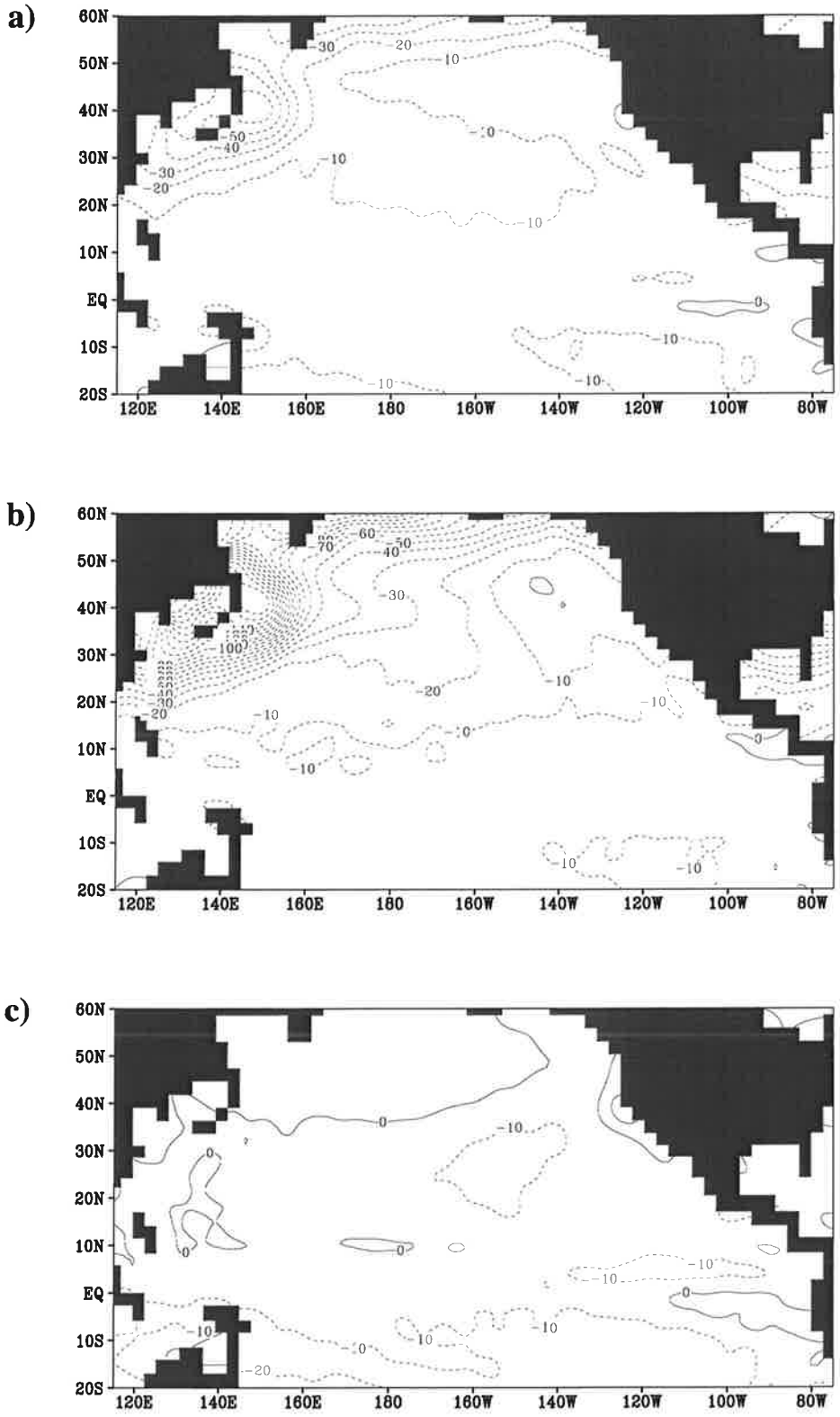

Fig. 3.12 Sensible heat flux over the Pacific ocean area for coupled model. a) annual mean, b) January, c) July. Contour spacing is 10 Wm^{-2} .

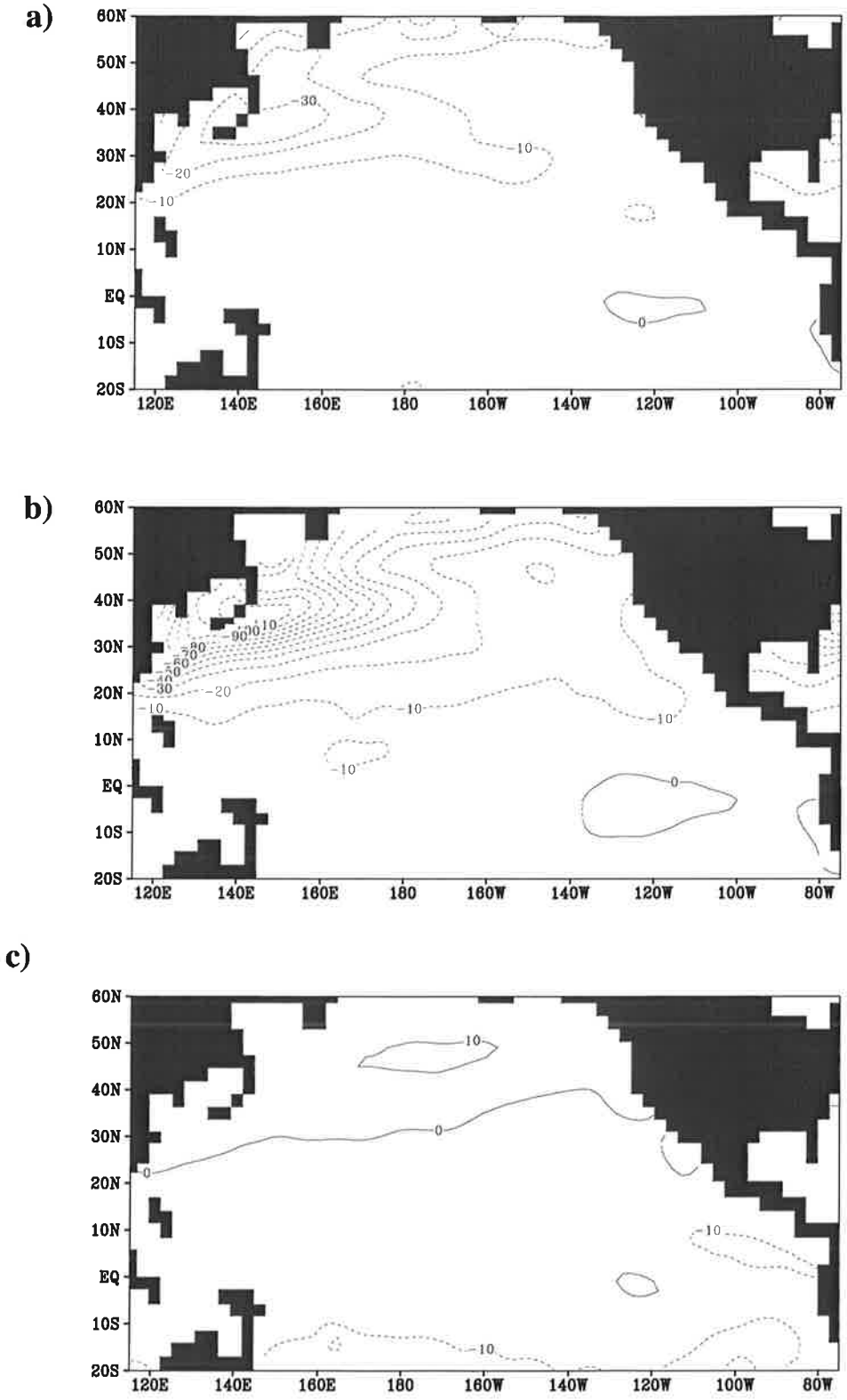

Fig. 3.13 Sensible heat flux over the Pacific ocean area from the Oberhuber (1988) climatology. a) annual mean, b) January, c) July. Contours as in fig. 3.12

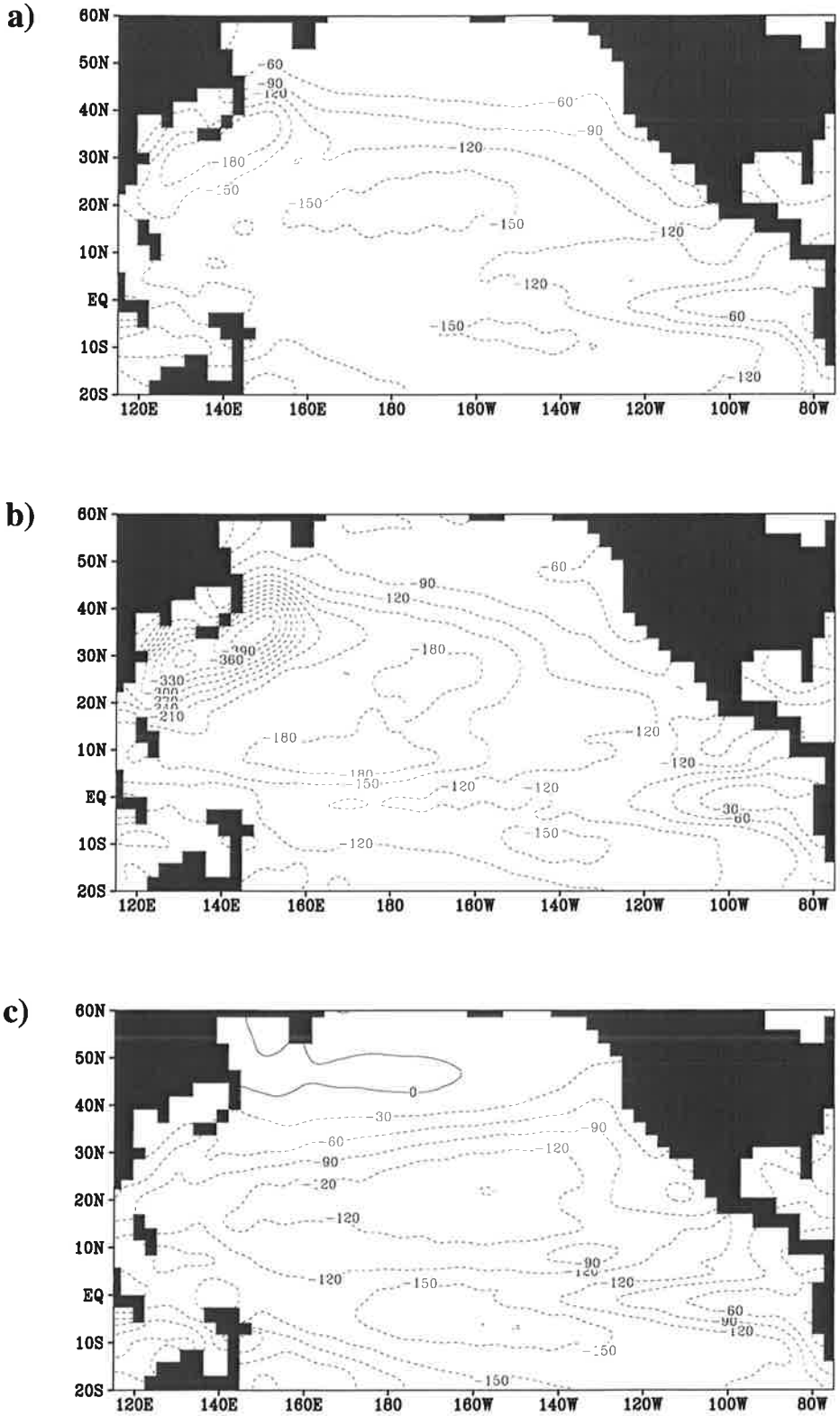

Fig. 3.14 Latent heat flux over the Pacific ocean area for coupled model. a) annual mean, b) January, c) July. Contour spacing is 30 Wm^{-2} .

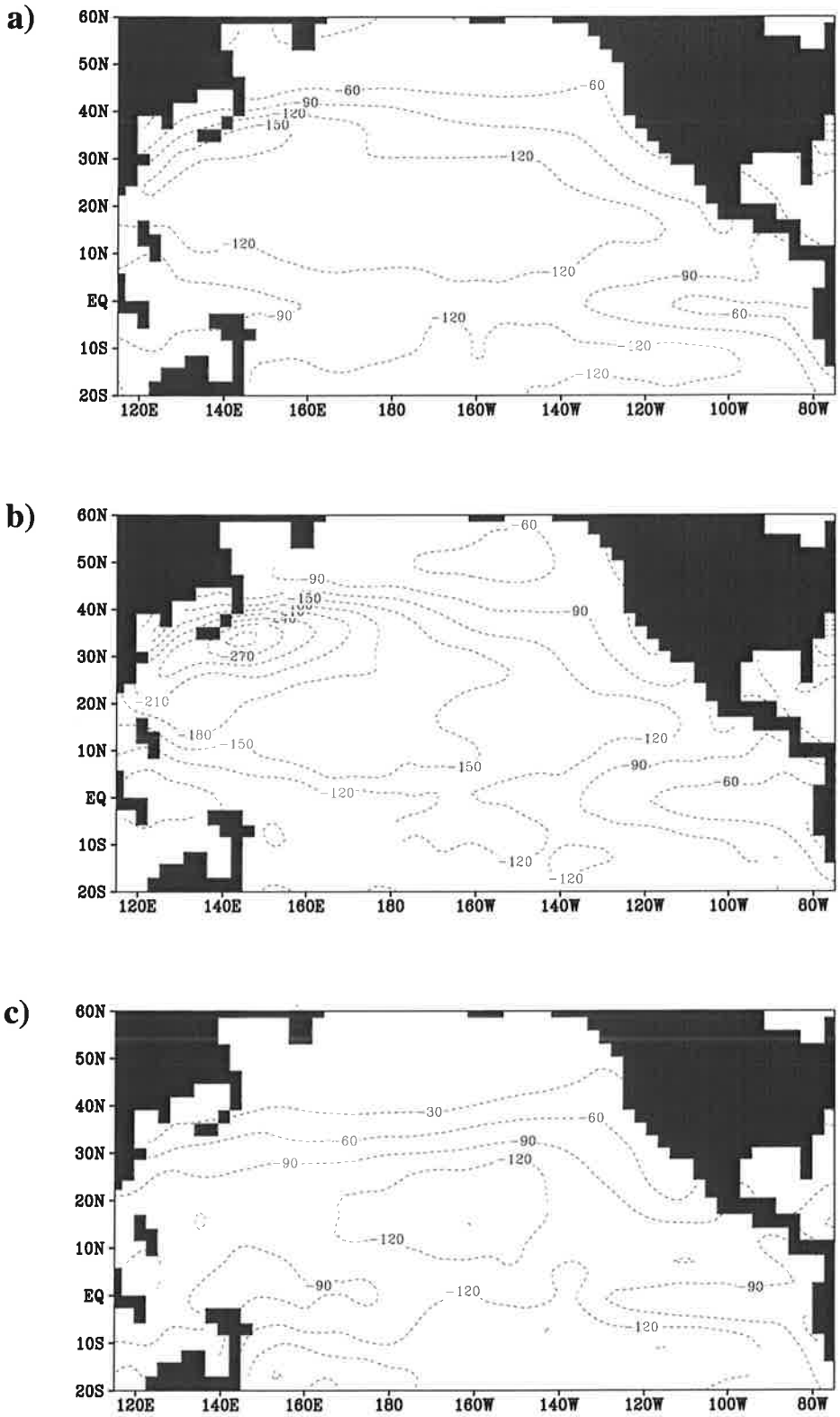

Fig. 3.15 Latent heat flux over the Pacific ocean area from the Oberhuber (1988) climatology. a) annual mean, b) January, c) July. Contours as in fig. 3.14

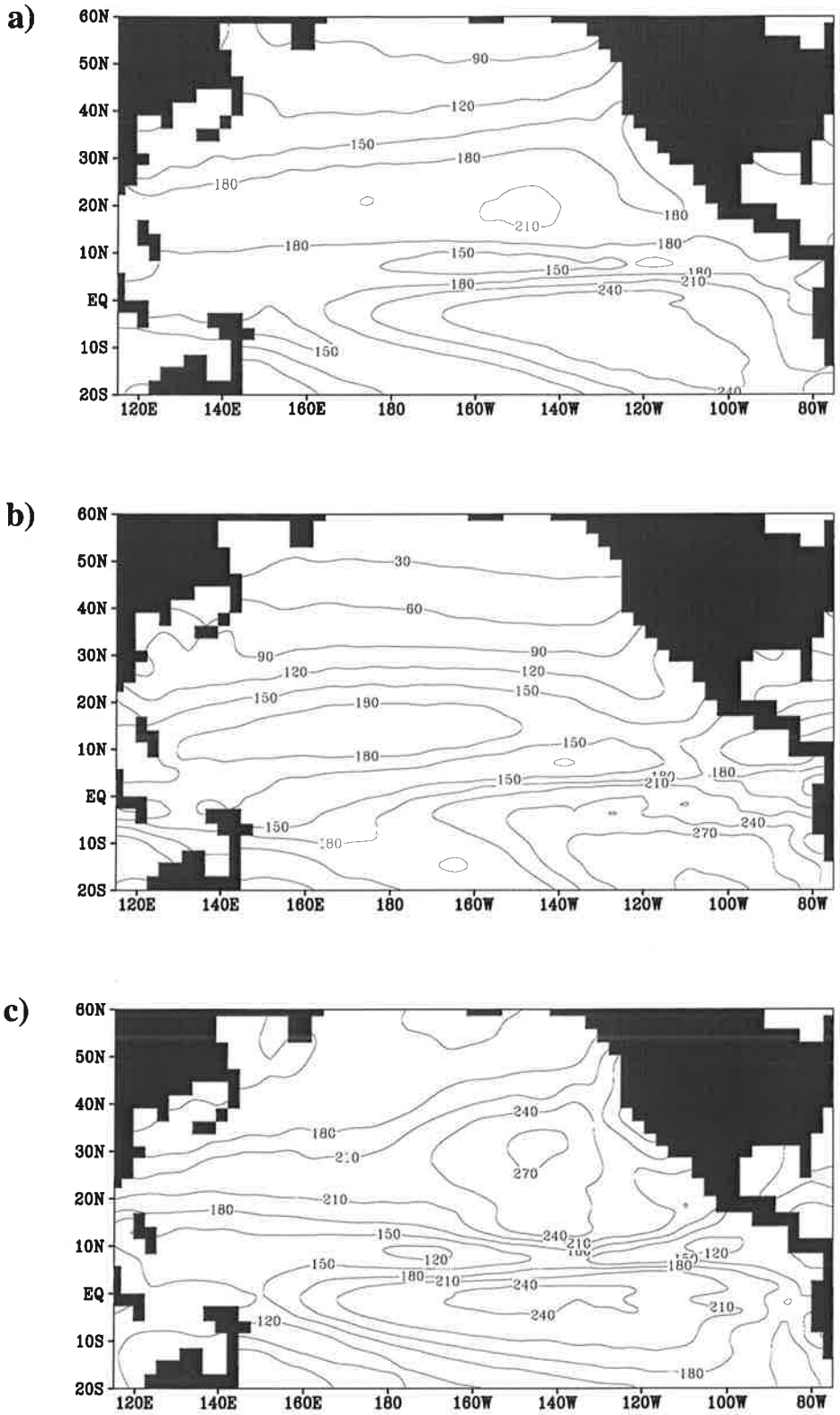

Fig. 3.16 Surface shortwave radiative flux over the Pacific ocean area for coupled model. a) annual mean, b) January, c) July. Contour spacing is 30 Wm^{-2} .

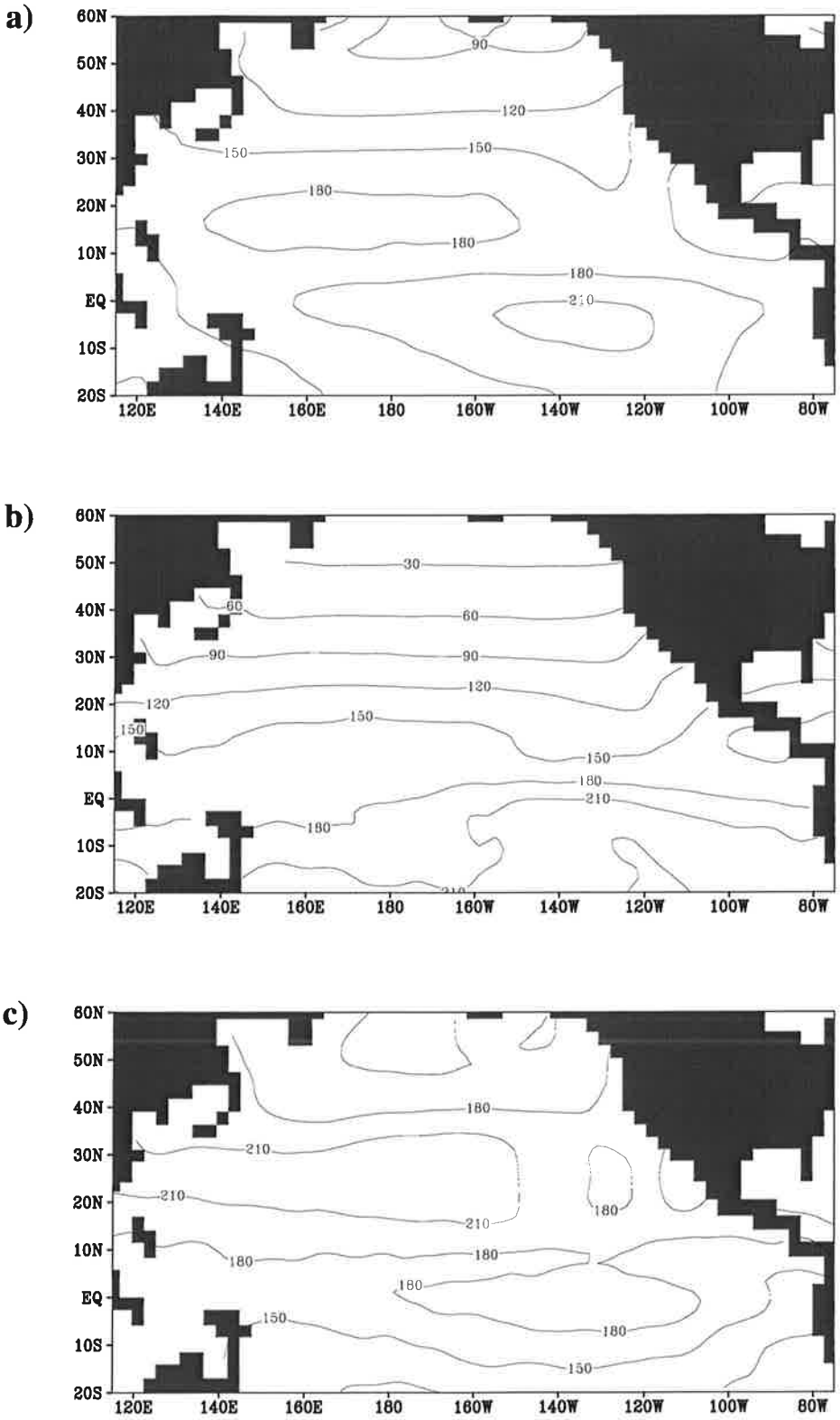

Fig. 3.17 Surface shortwave radiative flux over the Pacific ocean area from the Oberhuber (1988) climatology. a) annual mean, b) January, c) July. Contours as in fig. 3.16

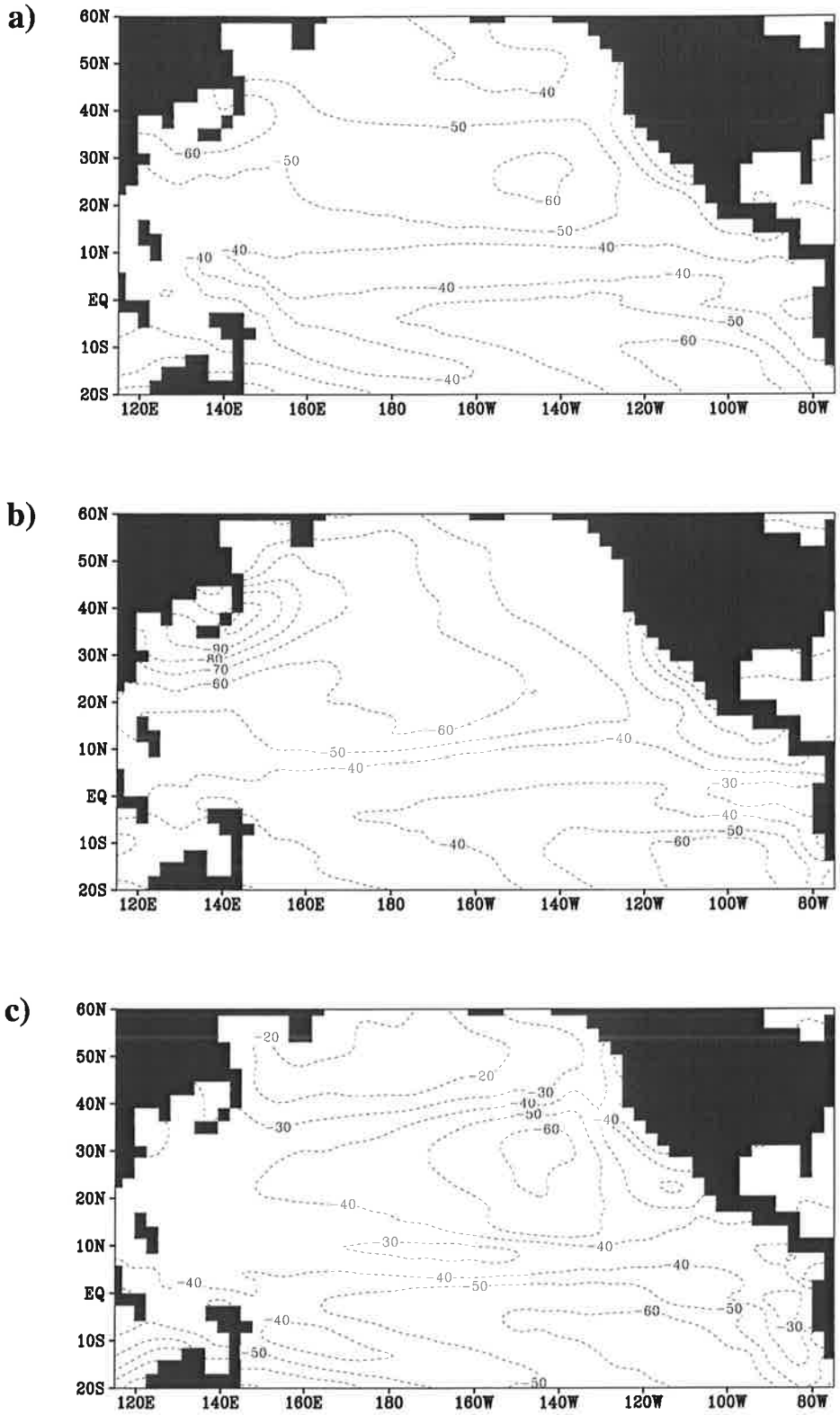

Fig. 3.18 Surface longwave radiative flux over the Pacific ocean area for coupled model. a) annual mean, b) January, c) July. Contour spacing is 10 Wm^{-2} .

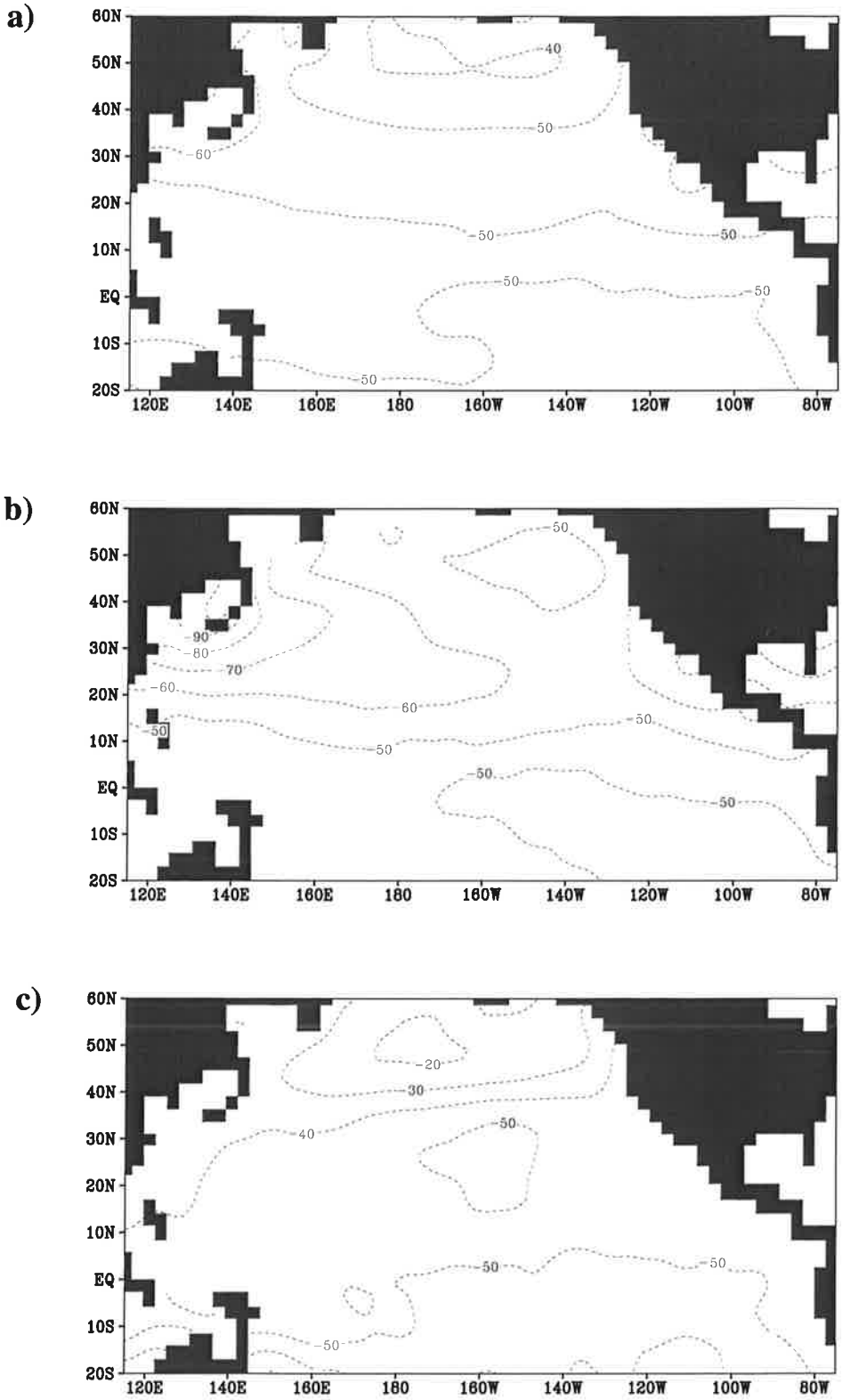

Fig. 3.19 Surface longwave radiative flux over the Pacific ocean area from the Oberhuber (1988) climatology. a) annual mean, b) January, c) July. Contours as in fig. 3.18

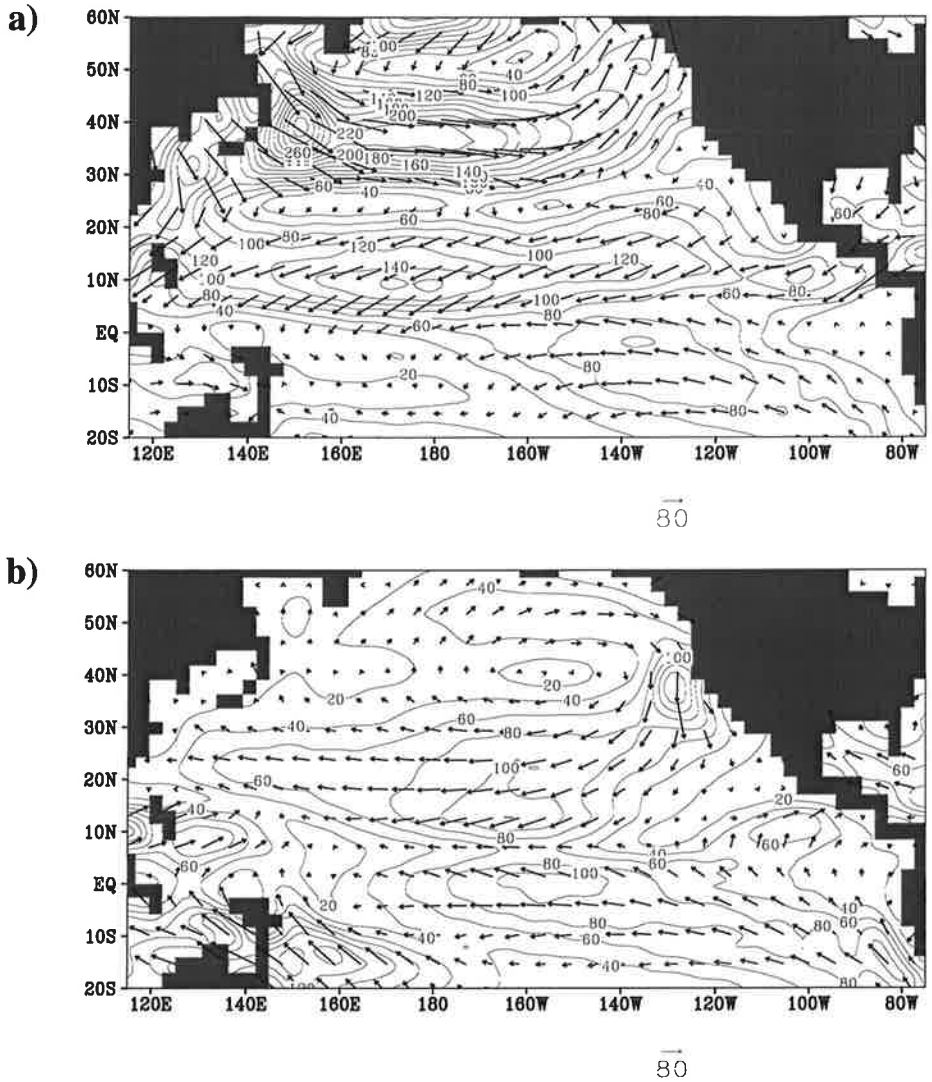

Fig. 3.20 Surface wind stress over the Pacific ocean area for coupled model. a) January, b) July. Unit is 10^{-3} Nm^{-2}. Arrow scale indicated below plot. Modulus contoured at intervals of 20×10^{-3} Nm^{-2}

a)

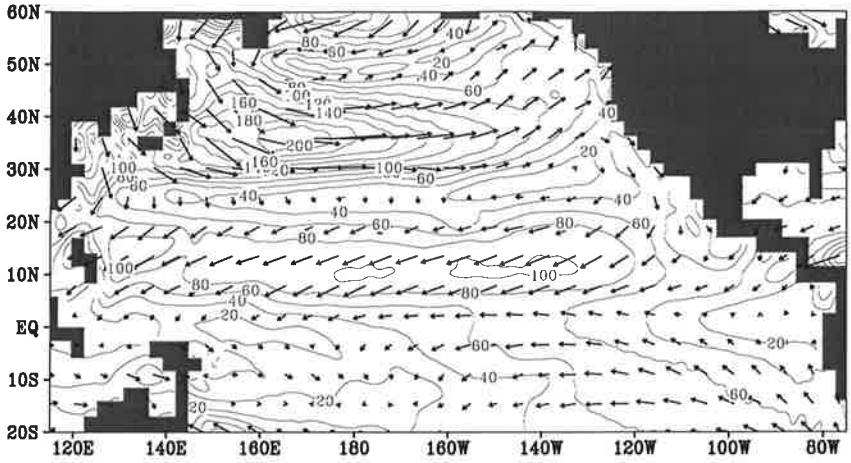

b)

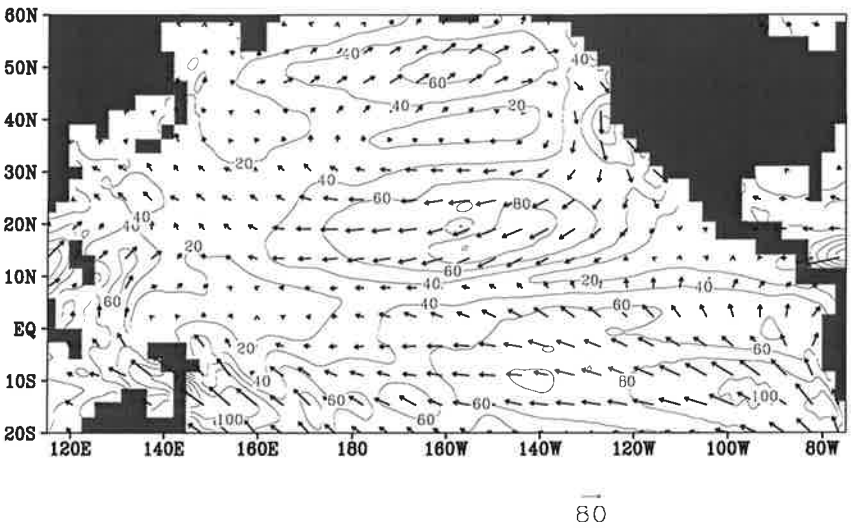

Fig. 3.21 Surface wind stress over the Pacific ocean area from ECMWF reanalysis. a) January, b) July. Arrows and contours as in fig. 3.20

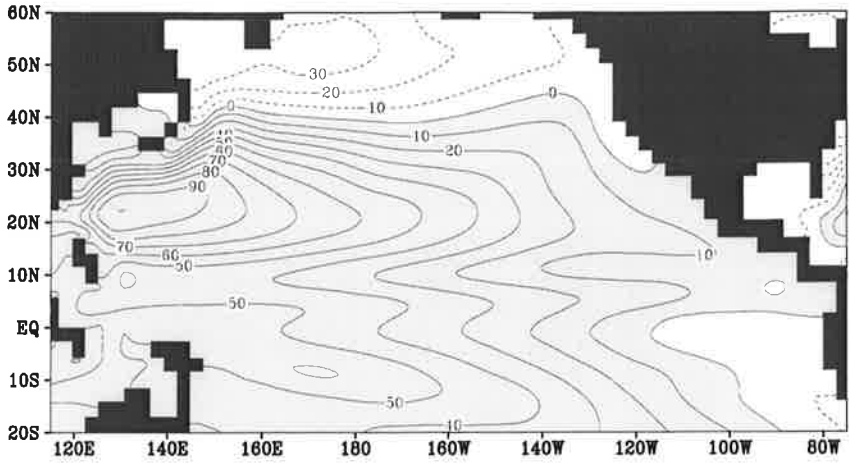

Fig. 3.22 Annual mean sea surface height for coupled model. Contour spacing is 10 cm. Shading indicates positive values

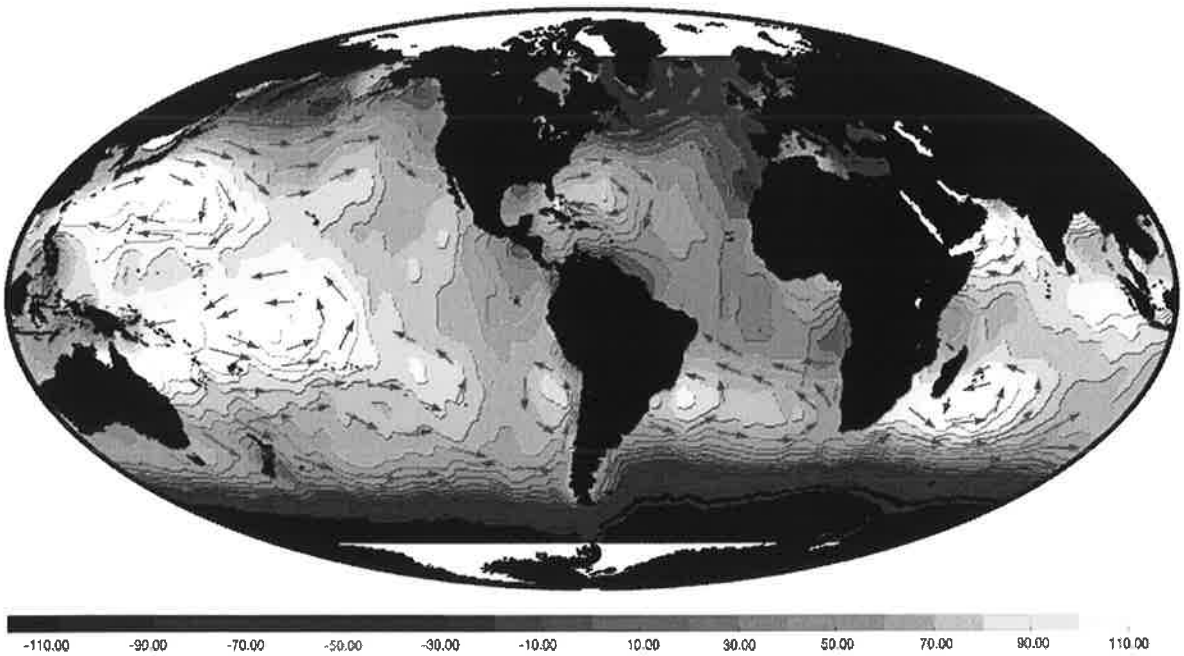

Fig. 3.23 Annual mean sea surface height as measured by TOPEX/Poseidon satellite altimetry. Unit used in shading is cm.

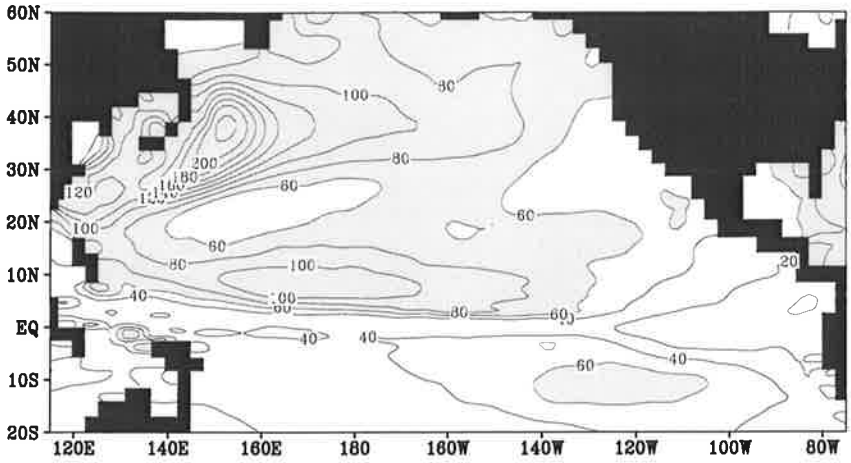

Fig. 3.24 Monthly mean depth of the surface mixed layer for March as simulated by the coupled model. Contour spacing is 20 m. Values in excess of 60 m are shaded.

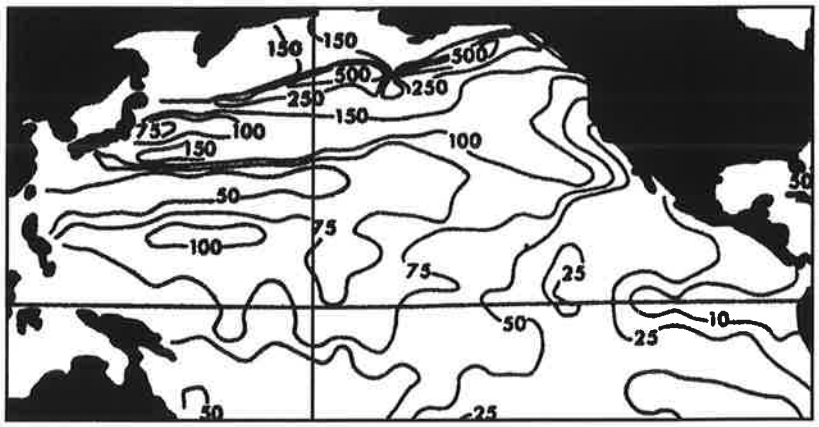

Fig. 3.25 Monthly mean depth of the surface mixed layer for March as estimated by Levitus (1982). Contour spacing is 25 m

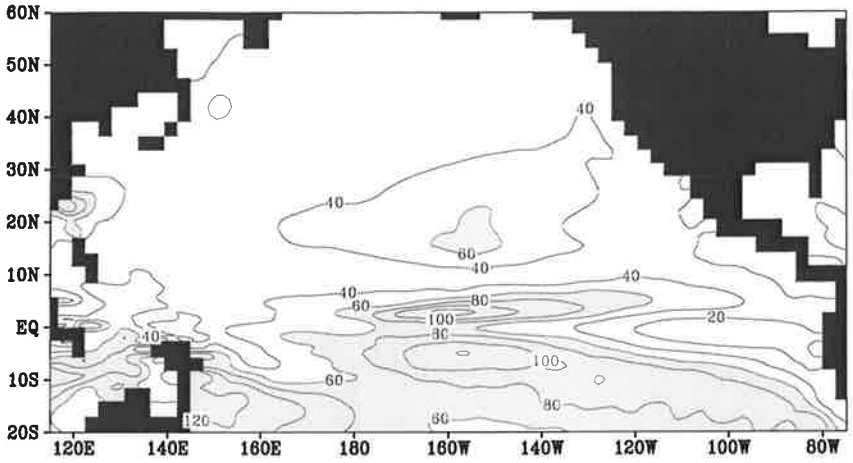

Fig. 3.26 Monthly mean depth of the surface mixed layer for September as simulated by the coupled model. Contour spacing is 20 m. Values in excess of 60 m are shaded.

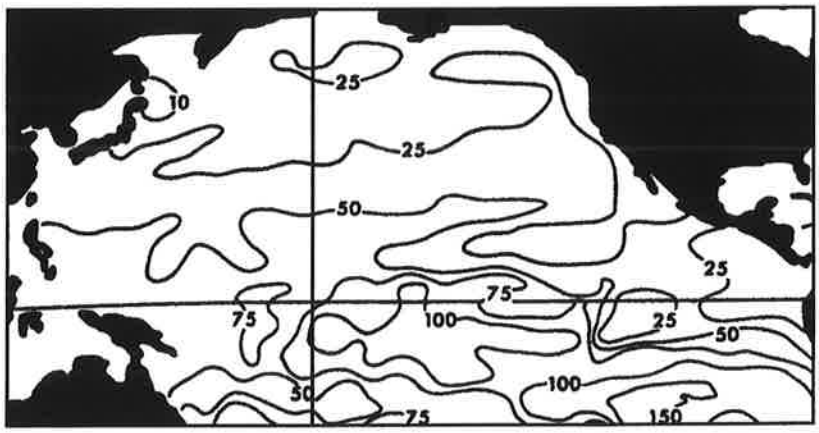

Fig. 3.27 Monthly mean depth of the surface mixed layer for September as estimated by Levitus (1982). Contour spacing is 25 m

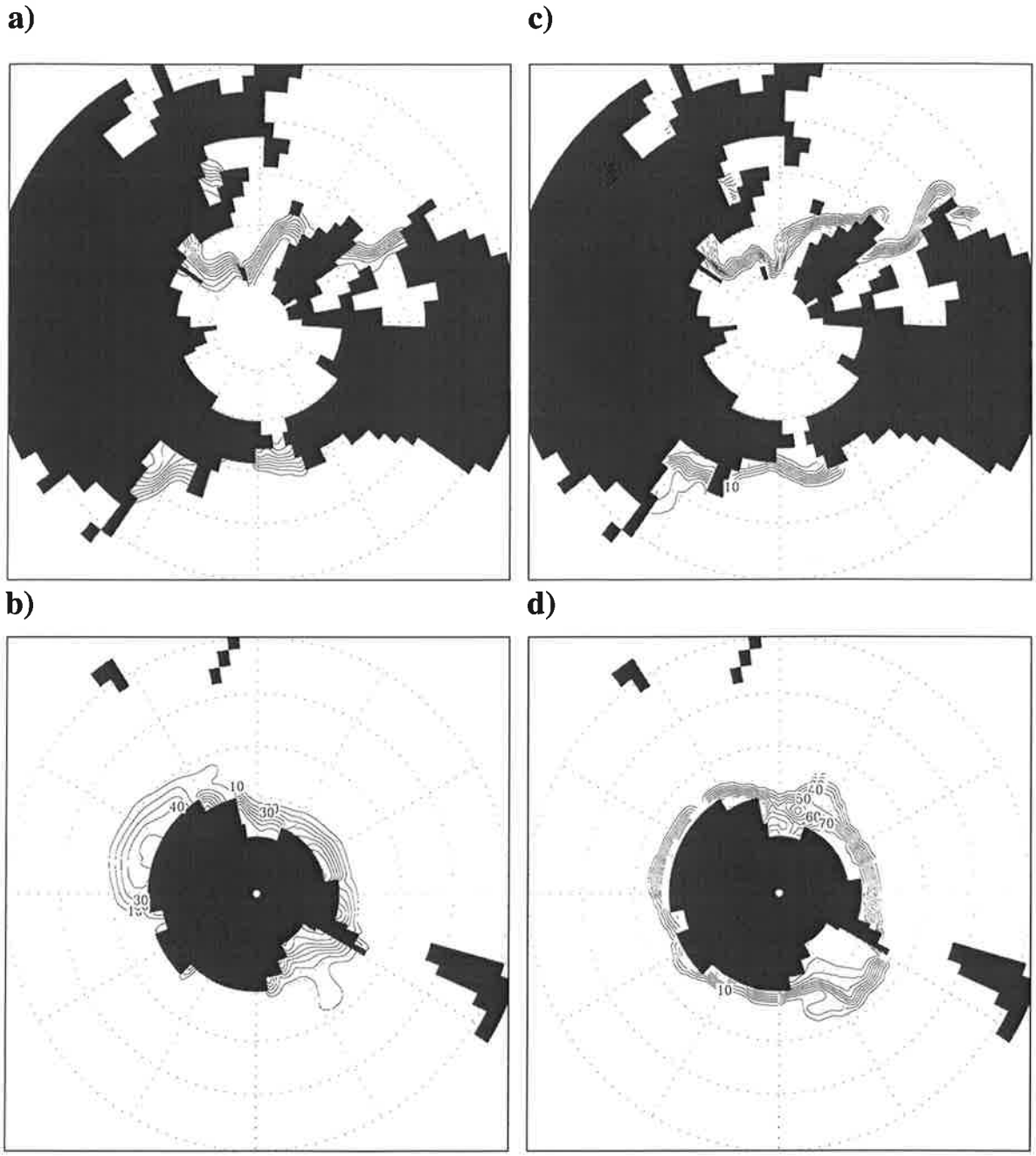

Fig. 3.28 Monthly mean sea ice cover for March a) coupled model, Northern Hemisphere, b) coupled model, Southern Hemisphere, c) GISST 2.2 dataset, Northern Hemisphere, d) GISST 2.2 dataset, Southern Hemisphere. Contour spacing is 10 percent.

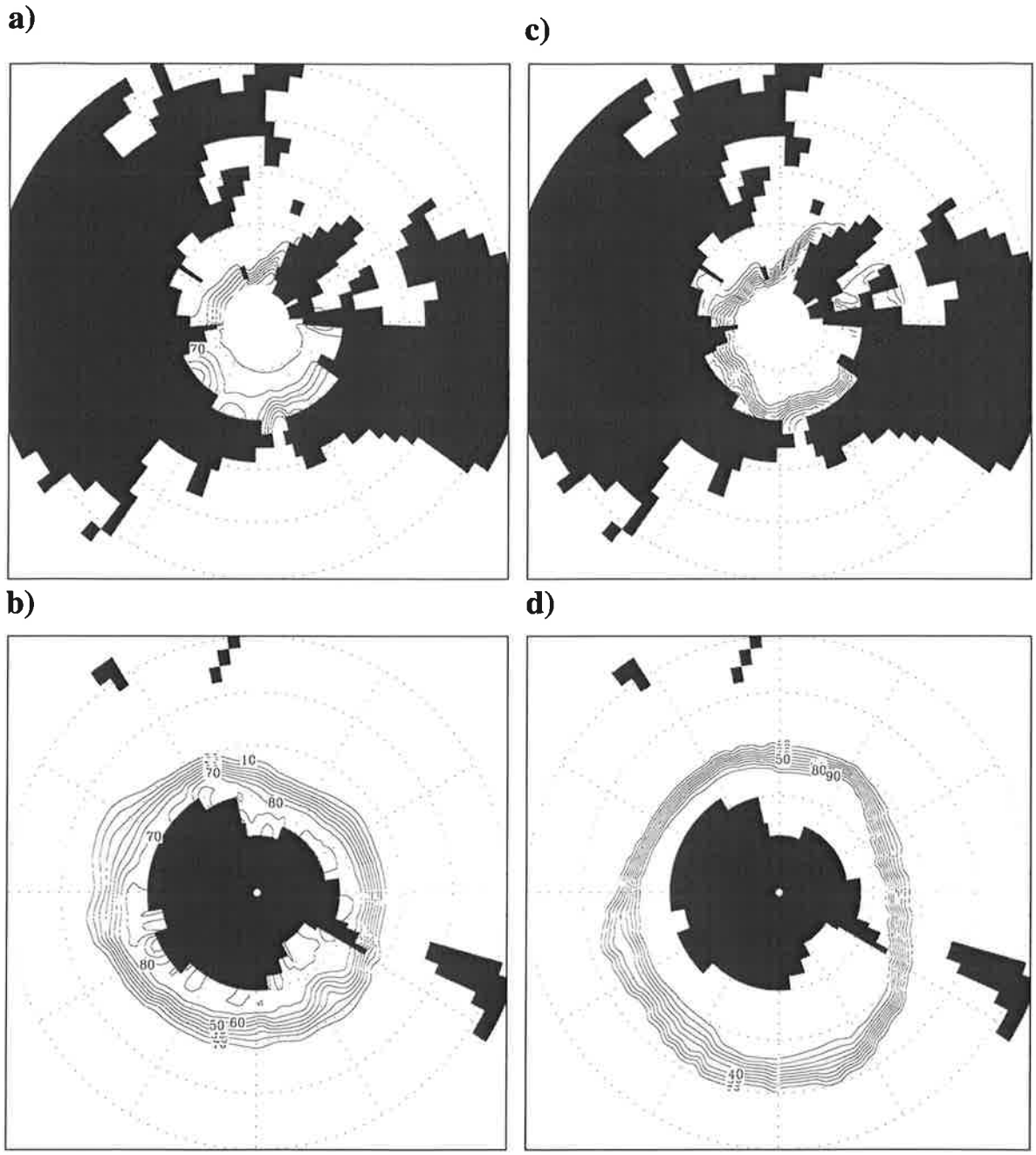

Fig. 3.29 Monthly mean sea ice cover for September a) coupled model, Northern Hemisphere, b) coupled model, Southern Hemisphere, c) GISST 2.2 dataset, Northern Hemisphere, d) GISST 2.2 dataset, Southern Hemisphere. Contour spacing as in fig. 3.28

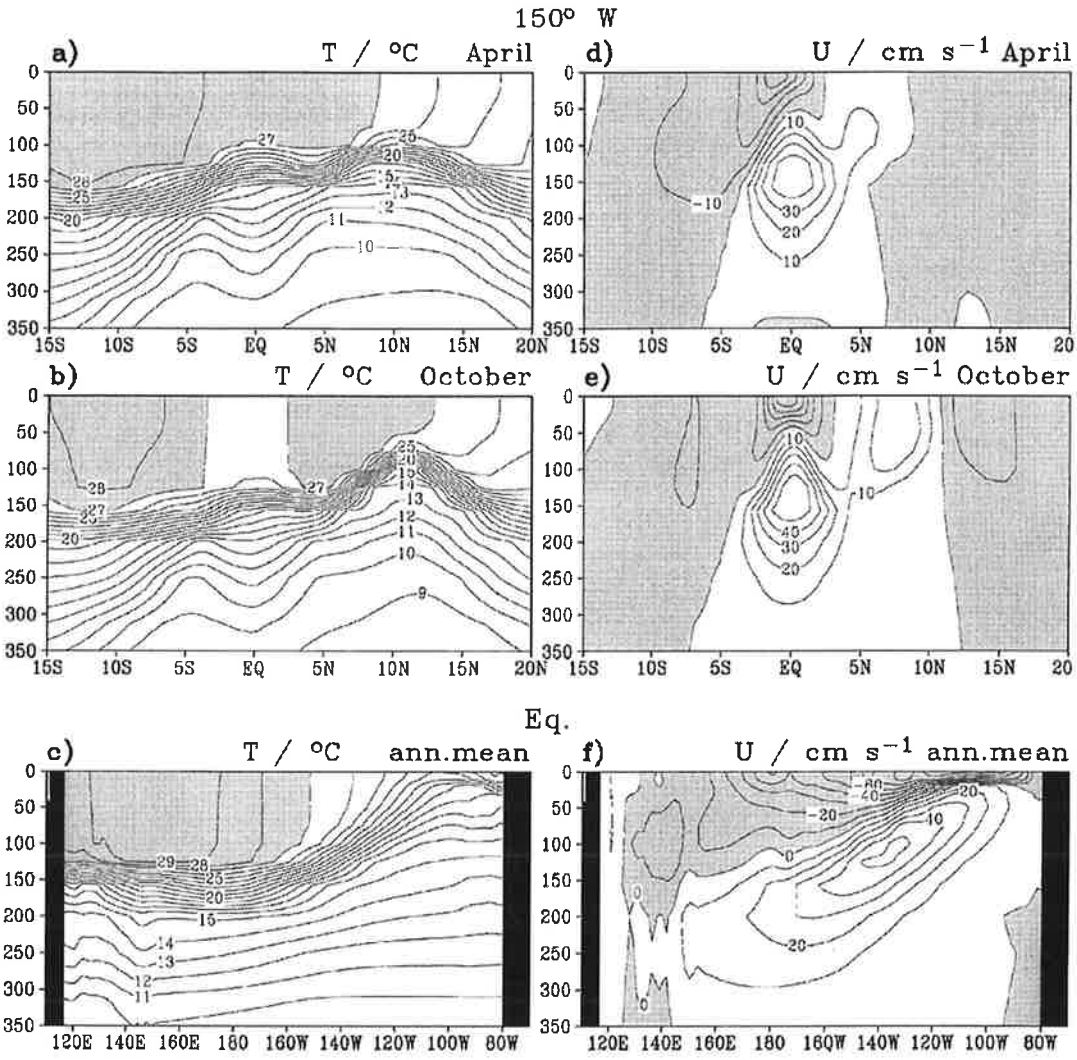

Fig. 3.30 a) Meridional temperature section at 150° W for April; b) as a) but for October; c) annual mean temperature section along the equator. d), e), f), as a), b), c) but for zonal velocity. Contours at intervals of 1 °C for temperature and at 10 cms^{-1} for zonal velocity. Shading indicates regions warmer than 27° C, or where motion is westward.

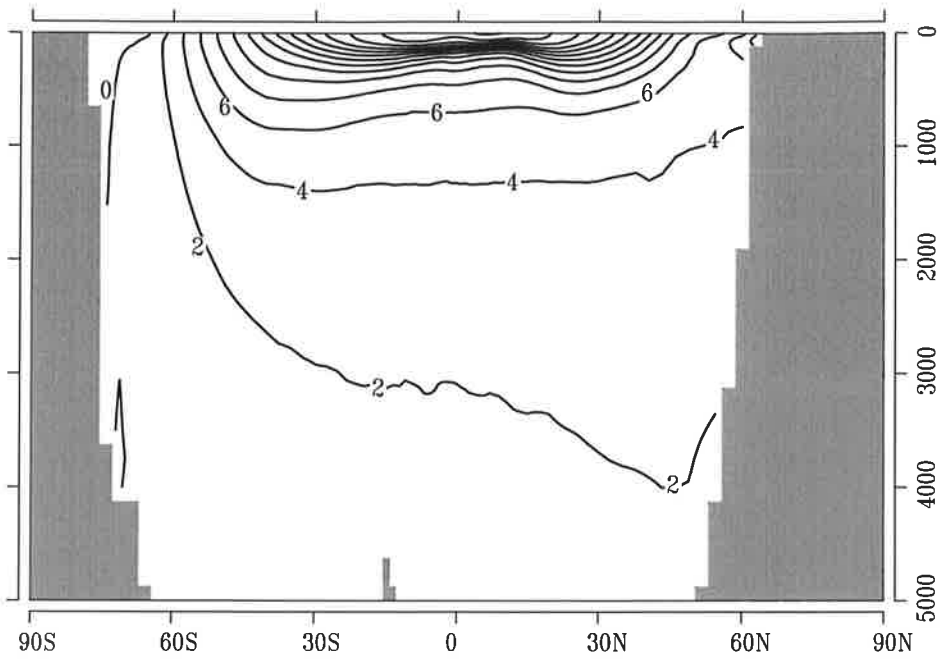

Fig. 3.31 Zonally averaged temperature for Pacific, annual mean. Unit: °C

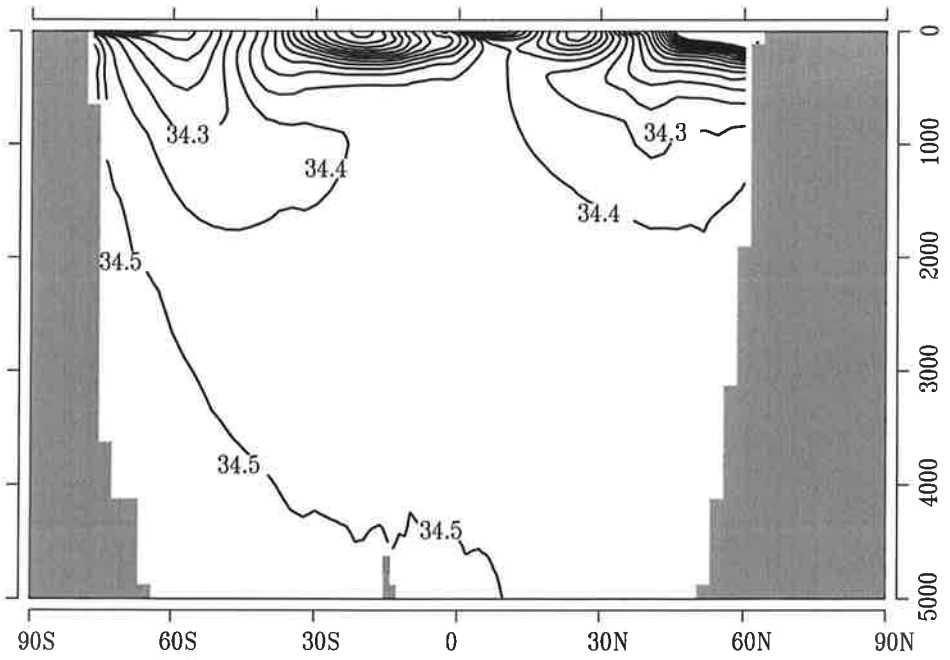

Fig. 3.32 Zonally averaged salinity for Pacific, annual mean. Unit: gkg^{-1}

Chapter 4

Decadal variations of sea surface temperatures and circulation changes

The role of SST in the observed decadal climate variability around the Pacific, in particular, changes associated with the 1976 'climate shift', has been adressed in the introduction to this thesis, and two complementary lines of argument summarized. The present analysis addresses both views. How important are tropical decadal El Niño background SST variations and atmospheric teleconnection in response to tropical SST (cf. Nitta and Yamada, 1989, Graham, 1994). Alternatively, what indications exist that midlatitude multi-year SST anomalies excite a robust response (cf. Namias, 1979, Pitcher et al., 1988, Latif and Barnett, 1994, Peng et al., 1997).

Large-scale patterns of SST variability are commonly published which depict the value of the regression coefficient with respect to an index of decadal SST variability, such as the set of indices discussed by Zhang et al. (1997). As a common approach to obtain an index, principal component analysis results in a collection of timeseries that yields the empirical orthogonal functions (EOFs) as spatial patterns. Their usefulness in the case of ENSO has been known since the analysis of Weare et al. (1976). While propagation is a characteristic feature for SST anomalies on the seasonal scale, especially on the equator in the course of an ENSO event (Rasmussen and Carpenter, 1982, Mitchell and Wallace, 1996), for long-term SST behaviour basin scale SST patterns typically exhibit a standing character which is captured by a regression pattern and the index timeseries with which it is associated. Variability in the general circulation examined by regression on the same index can reveal statistically significant association, as frequently performed in observational studies (Wallace et al., 1990, Zhang et al., 1997). Beyond this association, establishing a sensitivity of the circulation to SST variations requires general circulation model (GCM) experiments, and the excitation of the Southern Oscillation and the Pacific North American pattern by tropical SST forcing have been confirmed in many such studies (Rowntree, 1972, Shukla and Wallace, 1983, Palmer and Mansfield, 1986a,b, Bengtsson et al., 1996). The controversy as to whether midlatitude SST anomalies induce a detectable atmospheric response was summarized in the introduction.

Analysis of the decadal variability simulated by the coupled model in the present chapter is based on two index timeseries for SST; associated variability in 500 hPa geopotential height is examined by regression. The approach is similar to Zhang et al. (1996) who use COADS SST and NMC data for 500 hPa geopotential height for the years 1951-1994. The analysis is done in parallel both for the coupled simulation using the 170 years period yr 91 through yr 260, and for a multidecadal AGCM simulation with ECHAM4 using observed SST from the GISST 2.2 dataset (Parker et al., 1995) for the period 1903-1994[1]. In the latter run no modification of SST by surface fluxes is possible. SST anomalies evolve independently in the dataset and may induce effects in the simulated circulation. Analysis of the statistical association between SST and, e.g., 500 hPa height in an uncoupled simulation with variable SST cannot replace controlled response experiments. The key point, however, is to verify a similar pair of modes of SST/500 hPa height variability in both runs. As verified by the

1. GISST SST was used north of 35°S, but a linear transition to climatology occurs between 35°S and 45°S

forced simulation, we thus obtain two decadal SST timeseries for the coupled simulation one of which captures variability linearly independent of ENSO. The 500 hPa patterns are discussed with reference to the well-known ENSO response but also to the response obtained for a North Pacific SST anomaly by Latif and Barnett (1994). The North Pacific (NP) index defined by Trenberth and Hurrel (1994) can be identified with one of the two indices for the forced run and consequently, for the coupled run. Both indices are then used for regressions to discuss associated three-dimensional variations of the circulation in the coupled run. Chapter 5 discusses a regression analysis for all tendency terms for the mixed layer temperature, accounting in detail for all components of surface heat flux in a manner comparable to Lau and Nath (1994). On the condition that the SST changes are effective in forcing circulation changes, surface heat flux, as well as surface wind stress via its effect on ocean dynamics, establishes a feedback which may be captured by the regression patterns.

4. 1. Temporal characteristics and spatial structure of long-term variability in Pacific SST and 500 hPa geopotential height

In fig. 4.1, the average SST anomaly over the NINO3 region, 90° W - 150° W, 5° N - 5° S is shown. The NINO3 region is a standard index region for representing the eastern tropical Pacific SST variability associated with the El Niño phenomenon. El Niño warm events according to a widely accepted phenomenological description (Rasmussen and Carpenter, 1982) attain a mature phase around the turn of the year which coincides with the peak of the anomalous temperature in the NINO3 region. Fig. 4.1.a shows the monthly mean anomalies for the GISST data which were obtained by subtracting the monthly mean climatology based on the years 1951 to 1975. For the coupled simulation, fig. 4.1.b shows the 170 years period from year 91 to 260, inclusive, with the model climatology estimated from this full period. Included in each panel of these two figures are two smooth curves obtained by various degrees of low pass spline filtering (Reinsch, 1967). For the full line, half power was tuned to 7 years. Additionally the dashed curve represents only the multidecadal variability, obtained by setting half power to 60 years, so that variability at all shorter scales is strongly suppressed. Considering that the GISST dataset covers only 92 years, from 1903 to 1994, this curve represents variability which from the present length of the record cannot be properly assigned to any timescale and which further may overlay any deterministic trend. By itself the dataset does not provide a means for distinguishing trend and multidecadal variability. We therefore analyse only the portion represented by the difference between the full line and the dashed line. This is equivalent to a bandpass filter with half-power points at seven and sixty years. All quantities subsequently analyzed will be subject to the same band pass filtering. Also we restrict our attention to the case of filtered monthly mean anomalies. Winter season data are not considered specifically in this work.

Despite including some residual interannual variability, we have already suppressed the El Niño signal almost completely and thus retained only variability with a decidedly lower frequency character. For the observations, NINO3 SST anomalies were below the general trend in the forties and through the first half of the fifties as well as in the period of about 1968 through 1976, whereas the reverse is true for the second half of the fifties. In the simulation, the most notable period is from the year 190 to 220 which is characterized by about three cycles of oscillatory evolution. The observed data indicate the shift in ENSO background state in 1976 identified by Nitta and Yamada (1979) and Graham (1994) as a probable cause for the dramatic climate change particularly in the North Pacific.

It is worth noting that the variability of NINO3 SST in the coupled model (fig. 4.1.b) is both quite irregular, in contrast to some other coupled ocean-atmosphere model simulations, as well as possess-

ing an amplitude of the stronger events comparable with the observed. This is what makes the model suitable for the present analysis.

Similar to Zhang et al. (1996) who addressed the linear dependence of extratropical variability on decadal scales on ENSO the filtered NINO3 SST anomaly is normalized to unit variance. Using this normalized index at each gridpoint a linear regression is performed. The spatial distribution of the regressed SST pattern, fig 4.2.a for the observations and fig. 4.2.b for the coupled model, as a result of the normalization is obtained in units of K. Throughout this thesis physical units are given for regression patterns which are obtained as a result of this normalization. To the second index, defined later, the same normalization is applied.

The patterns of fig. 4.2.a and 4.2.b are largely similar with maximum variance in eastern equatorial cold tongue SSTs and an amplitude in excess of 0.2 K. The observations show more variability near the eastern boundary where the model ocean is too coarsely resolved zonally to produce realistic mean upwelling near the coast. As discussed in Bacher et al. (1998), the impact of oceanic coastal Kelvin waves, generated by equatorial Kelvin waves during El Niño episodes, on the cool upwelled waters is therefore underestimated by the model. Furthermore this plays a role in a positive feedback loop since stratus overlies cold waters advected by offshore Ekman transport due to the longshore surface wind component. Thus, if water temperature changes due to modified upwelling, the reduction in stratus cloud caused by this anomalos warming leads to increased insolation of the sea surface which hence warms further and is conducive to further stratus removal. Apart from the cold tongue region the second most conspicuous feature in the SST pattern is a region from 150° W to the date line near 30° N where SST varies out of phase with the cold tongue. Here the coupled model produces a stronger response than the observations. This is consistent with SSTA composites of El Niño type anomalies in the coupled model and the AMIP dataset in Roeckner et al. (1996a).

The decadal scale SST variability explained by the NINO3 variability exhibits a similar structure compared to that familiar from typical El Niño type anomalies. An exception is the strength of covariance between the anomalies within the cold tongue region and the eastern subtropical North Pacific which on interannual timescales is known to be relatively weak (e.g., Weare et al., 1976). In the canonical ENSO pattern (Rasmussen and Carpenter, 1982) the cold tongue region is more dominant. By contrast for the decadal scale both model and observations over a large area show NINO3 related variability of nearly half the amplitude as in the cold tongue. This leads to a triangular spatial structure. The term 'horseshoe' has been used in connection with decadal Pacific SST variability (Latif et al., 1997), but it should be noted that the characteristics of the pattern obtained by Latif et al. as one of the modes in a Principal Oscillation Pattern (POP) analysis differ somewhat from the pattern presented here. The most notable difference is the phase relationship between central and eastern equatorial Pacific SST variations which in the 'horseshoe mode' are out of phase whereas an in-phase relationship results for both the coupled model and the GISST dataset for the NINO3-related SST variability. The 'horseshoe' can be regarded as independent from variations in the cold tongue according to Latif et al. (1997). In the present coupled simulation, a pattern which largely reproduces characteristics of the 'horseshoe' in Latif et al. is found in the residual variability (where the linear contribution by the cold tongue index has been removed), and is discussed below.

Fig. 4.3 shows the regression pattern of 500 hPa geopotential height with respect to the filtered NINO3 index for the coupled model. Prominent features are evident primarily over the high latitudes of the Western Hemisphere and the subtropical North Pacific and Atlantic. In the tropics, departures

from zonality are small but resemble a Southern Oscillation pattern, i.e. consistent with a weakening and eastward contraction of the Pacific Walker circulation, along with an intensification of the Hadley circulation. This response to decadal cold tongue SST anomalies resembles the ENSO response in the coupled model discussed by Roeckner et al. (1996a).

A significant fraction of the variability on decadal scales is retained if one eliminates NINO3-related variability to obtain residual fields, a procedure used also by Zhang et al. (1996, 1997). The filtered SST and 500 hPa geopotential height fields are transformed into residual fields by subtraction of the contribution linearly related to the filtered NINO3 index. Following further standard practice we perform an SVD analysis of the covariance matrix the SST and 500 hPa geopotential height residual fields. The SVD yields a sequence of SSTA/500 hPa height pairs of timeseries. The leading pair is defined by the requirement that the covariance between its members attain the maximum possible value. We have selected only the ocean area of the Pacific from 20° S to 60° N for analysis, both for the SST and the 500 hPa height fields.[1] The SVD was computed based on an empirical orthogonal function (EOF) expansion which was truncated to include only as many EOFs as needed to explain at least 95 % of the variance. The mathematics of this technique is described in Wallace et al. (1992).

The leading SVD pair of timeseries is shown in fig. 4.4.a for the integration with observed SSTs and in fig. 4.4.b for the coupled model. Linear regression onto the timeseries yields the so-called homogeneous covariance map, and these maps are shown in fig. 4.5.a and fig. 4.5.b, respectively. Table 4.1 summarizes how much in-field variance is explained by the leading modes, as well as the squared covariance fraction (SCF). In both integrations the leading mode explains a similar fraction of covariance, close to two thirds, and the explained in-field variances are also similar. These fractions all relate to the residuals of the filtered quantities.

Table 4.1: Singular Value Decomposition of residuals of Pacific SST and 500 hPa height

	GISST			**Coupled Model**		
SVD pair	SCF (%)	variance SST(%)	variance z_{500} (%)	SCF (%)	variance SST (%)	variance z_{500} (%)
1	65.5	23.3	36.1	60.8	16.6	30.1
2	15.3	11.4	19.2	19.3	10.9	15.2
3	9.8	9.7	13.0	10.0	3.6	34.8
4	4.8	8.4	9.0	5.1	8.6	6.8

For both the GISST forced AGCM integration and the coupled model the pair of timeseries is almost perfectly aligned, as expected. The timeseries do not exhibit any regularity, and the coupled run in particular shows an alternation of larger and smaller variations, such that the periods from simulation year 145 to 180 and from 205 to 240 show smaller variance than the remaining part. A feature worth noting in both integrations is a single realization of a quasi-decadal oscillation with growing amplitude and a timescale of roughly eight to nine years which performs two cycles from year 1954 to year 1968 for the observed dataset and almost four cycles from year 90 to year 118 in the coupled

1. Restricting the domain for the 500 hPa height implies that the full spatial extent of the field must be reconstructed which necessitates a regression of the residual height field onto the leading SVD timeseries and subsequent normalization of the pattern.

run. However, this signal is not robust through the entire record length. Fig 4.6 shows the power spectral density for the unfiltered timeseries in fig. 4.4.b, together with the power spectral density for the appropriate first order autoregressive (AR(1)) equal variance process. In a seminal paper on low frequency climate variability Hasselmann (1976) proposed that low frequency variability could be explained by approximating the travelling disturbances of the real atmosphere at midlatitudes by white noise exerting a stochastic heat flux forcing of mixed layer temperature changes. The integral temperature response in the mixed layer with its huge heat capacity would be autocorrelated noise which exhibits a spectrum with slope -2 since the finite difference form of the governing Langevin equation is an AR(1) process. It is evident in fig. 4.6 that deviations from this theoretical shape are hardly significant. The effects of stochastic fluctuations in wind stress on heat transports by currents follow from the work of Frankignoul et al. (1997) who in a two-layer model incorporate baroclinic midlatitude Rossby wave propagation. This suggests a particular emphasis on the decadal scale set by ocean basin width. The resulting spectrum of SST fluctuations does not exhibit significant peaks. Chapter 5 considers changes in the wind-driven Ekman and Sverdrup transports, which are shown to substantially influence the mixed layer heat budget.

The leading pattern pair for SST and 500 hPa geopotential height (fig. 4.5) shows a structure in the Northern Hemisphere which corresponds well between both runs. Note that the SVD modes are only unique up to sign. Therefore, to provide matching displays the negative of both the SST and 500 hPa height patterns for the run with GISST SSTs is shown. The phasing is such that for the coupled run there is a warm anomaly stretching across the midlatitude North Pacific with two enhanced centres situated near Japan and in the central eastern North Pacific. Up to the above-mentioned sign convention, there is a closely similar but weaker SST anomaly seen in the analysis of the GISST data. Stronger confinement to the Northern Hemisphere occurs for the coupled model, and in the equatorial region and South Pacific the anomalies are in fact weaker than in the case of the GISST data. South of the North Pacific anomaly there is a cross-basin structure of oppositely signed anomalies in both the coupled run and the GISST data. It extends from south-west of the Californian coast into the West Pacific warm pool region. In the equatorial region there is an area towards the eastern boundary where anomalies are in phase with the North Pacific region.

Other studies have identified similar SST patterns associated with observed decadal Pacific SST variability. The two activity centres in the North Pacific near Japan and east of the date line are evident in the pattern shown by Namias (1979). For the run with GISST SSTs, the overall pattern closely matches that found in the principal oscillation pattern (POP) analysis by Latif et al. (1997). The close resemblance of this SST pattern in fig. 4.5.a with the result from the POP analysis in Latif et al. (1997) is interesting because those authors explicitly state that the notion of a normal mode with a specific timescale, as the POP analysis would suggest, in view of the short period they used (1951 - 1994), is poorly supported (record length corresponds to about two cycles), and it is more appropriate to stress the spatial aspects. The timeseries in fig. 4.4.a shows little evidence for a constant timescale, which could aid long term prediction, but instead exhibits irregular decadal variability.

For 500 hPa geopotential height a PNA pattern with a strongly enhanced North Pacific centre is dominant in both runs. There is also a NAO contribution but its phase relation to the PNA is opposite in the run with GISST SSTs and the coupled run. This NAO related portion, however, is weak and insignificant. A weak signal in phase with the North Pacific centre is seen over central and eastern Europe. Although neither of the two integrations forms a controlled response experiment, it is impor-

tant that the SVD yields a closely matching result for both. This correspondence between the forced run and the coupled model may be taken as an indication that a multi-year SST pattern as found here is potentially capable of exciting a robust atmospheric response as the one described. Furthermore, a rather similar response was obtained by Latif and Barnett (1994) who prescribed a midlatitude SST anomaly quite similar to the above SVD pattern. The perpetual January and perpetual February experiments by Peng et al. (1997), both performed with the same midlatitude North Pacific SST anomaly, which closely resembled the midlatitude portion in fig. 4.5.b, yielded significant responses in temperature and 500 hPa height. These responses, however, exhibited little similarity between January and February, a result attributable to significant influence by the monthly background flow.

The dominant mode in the residuals corresponds to a pressure pattern that in nature was the characteristic background in the 1976 'climate shift' in the Pacific. The enhanced North Pacific centre is the basis for the North Pacific (NP) sea level pressure index defined by Trenberth and Hurrel (1994). They explain the 'climate shift' as part of the natural multi-year variability evident in the low-pass filtered NP index. Subsequent sections show that various fields in linear regressions on the residual index exhibit patterns consistent with observational findings associated with the 'climate shift'.

Two modes of decadal variability have been defined in a purely statistical manner, which will be termed the decadal cold tongue (CT) mode and the decadal North Pacific (NP) mode. These modes are uncorrelated in time since the elimination of the CT related variability at each gridpoint yields a timeseries uncorrelated to the CT timeseries. To contrast their time evolution, fig. 4.7 shows the 7-60 year band pass filtered CT and NP mode timeseries for both runs. Apart from the SVD analysis of observations by Zhang et al. (1996), similar modes were obtained by rotated empirical orthogonal function analysis (Kawamura, 1994), POP analysis (Latif et al., 1997), and empirical orthogonal function analysis (Deser and Blackmon, 1995). Their physical significance is suggested by the similarity in the spatial structure of the modes in both the forced run and the coupled run and by the fact that physically meaningful relationships of most quantities with these modes are obtained by linear regression on each index.

4. 2. Atmospheric circulation changes associated with the CT and NP modes

The 500 hPa geopotential which was used together with SST to isolate the two dominant modes of variability over the Pacific is interrelated naturally with other characteristics of the general circulation. The purpose of this section is to briefly characterize these flow variations.

Fig. 4.8. shows the pattern of sea level pressure obtained by regression onto the decadal CT index. This pattern exibits close qualitative agreement with the familiar correlation structure characteristic of variations of the Hadley and Walker circulations associated with the Southern Oscillation (Trenberth and Shea, 1987). The pressure seesaw between the Maritime Continent and the central to eastern Pacific is clearly evident. The North Pacific exhibits anomalously low pressure while there is a weaker response over the North Atlantic with a weakened difference between the Azores high and the Icelandic low. The agreement between the observational result and the regression pattern for the decadal CT mode suggests that the response of the circulation is as expected for tropical SST anomalies associated with the ENSO phenomenon. It is therefore crucial to note that Roeckner et al. (1996a) established the realistic response of the general circulation in the coupled model to ENSO related SST anomalies. Model Southern Oscillation Index (SOI) was strongly anticorrelated with the NINO3 averaged SST anomaly, as in the familiar observational relationship.

The regression pattern for the NP mode related variations in SLP are shown in fig. 4.9. It is at once obvious that this mode is associated with circulation anomalies distinct from those associated with the Southern Oscillation. Instead of a south-eastward displacement of the Aleutian low during ENSO (Bjerknes, 1969) there is a pressure anomaly which extends all across the North Pacific. This anomalous centre is strongly dominant and only weak variations of opposite polarity occur across the entire polar region. These extend southward beyond 60° N over western Siberia and over Greenland. Such a pressure distribution was obtained for observations by taking the difference of the decades 1977-86 minus 1967-1976 by Kawamura et al. (1995). A similar result was obtained by Trenberth (1990) using the periods 1977-88 and 1924-76. Only the sign of the anomalies differed between the two observational studies and the result shown in fig. 4.9. However, this can be explained by the relation to the dominant SST anomaly which for the observations was given by Namias (1979) and Nitta and Yamada (1989). The sign for the observations was opposite to the sign exhibited by the pattern of fig. 4.5.b and consequently matched the sign of the pattern of fig. 4.5.a in the North Pacific. Thus in both the coupled model and the observations SLP is related to SST in a similar manner. This suggests that the NP mode in the coupled model is an anologue to the NP index used by Trenberth and Hurrel (1994). Their index timeseries exhibited large decadal amplitude in association with the 1976 'climate shift'. As noted, controversy persists as to whether this secular climate anomaly was the result of tropical SST forcing. The results from the coupled model simulation indicate that variations similar to those associated with the 'climate shift' are possible without a linear association to the tropical SST forcing characterized by the CT index. A tropical SST influence is not altogether excluded, since the NP mode related SST pattern in fig. 4.5 exhibits a weak west and central Pacific contribution in the tropics. The main point is that both the SLP pattern of fig. 4.8 and the SST pattern of fig. 4.5.b, as well as the results for net surface heat flux (section 5.1) and surface wind stress (section 5.2) resemble the observational findings sufficiently to suggest that the NP mode is the relevant model mode regarding the 'climate shift'.

From the patterns of sea level pressure, fig. 4.8 and fig. 4.9, it can be expected that the circulation changes associated with both the CT and NP modes are substantially different. Fig. 4.10 shows the CT regression patterns for zonal wind in two meridional sections at 160° E, and at 160° W, respectively. For the same sections, fig. 4.11 shows the CT related regression pattern for temperature. As expected thermal wind balance applies. For the zonal wind, common to both sections is an out of phase variation of zonal wind at 850 hPa and 200 hPa in the equatorial trough but with larger amplitude of the upper tropospheric variation to the east of the date line. The vertical structure is indicative of changes in the zonally oriented Walker circulation as familiar from El Niño warm events. I.e. the upper tropospheric westerlies are attenuated mainly east of the date line while the equatorial easterlies associated with the Southern Hemisphere trades in boreal summer and autumn are also diminished, in accordance with the anomalous sea level pressure field. The extratropical portion as expected exhibits a marked asymmetry about the date line. Substantial amplitudes are only found in the eastern half of the Pacific. In particular, the Northern Hemisphere portion is characterized by an equivalent barotropic structure affecting the Pacific jet near its exit region, as described similarly by May (1995). The anomaly is characterized by out of phase variation of winds near 35° N and 55° N. These latitudes are used by Ting et al. (1996) in their study of zonal-mean-stationary-eddy interactions important in establishing or maintaining seasonal anomalies of the circulation. They use an index given by the difference of zonal mean geostrophic wind for these latitudes, based on 500 hPa height. The linear relationships of various circulation characteristics, as well as sea surface temperature, to this zonal index and to an index of tropical sea surface temperatures similar to our CT index,

are intercompared. Interestingly, results are also discussed regarding interannual to decadal variability. As relevant for our case, they find a relationship between the tropical SST index and 200 hPa zonal wind which is similar to the standard El Niño response (e.g. Arkin, 1982) and to the CT response of 200 hPa zonal wind in the coupled model (not shown).

A similar correspondence with the study by Ting et al. (1996) is obtained for the NP mode in the coupled model, though with restrictions. Fig. 4.12 shows the regression pattern for zonal wind in the same two sections. Again, the temperature pattern (fig. 4.13) is consistent with thermal wind balance. Several key differences to the CT related circulation pattern can be noted. First, the structure of the variations is more symmetric about the date line than in the case of the CT mode. In particular, the modifications in the Northern Hemisphere subtropical jet no longer occur only in the exit region but instead the effect is still felt close to its core. Consistent with the smallness of SST variations in the tropics (cf. fig. 4.5.b) little signal is found in the two sections for the equatorial trough. The latitudes which exhibit maximum variance are again close to the reference latitudes in the study by Ting et al. (1996) (and other studies referenced by those authors). It is of interest that Ting et al. also show the pattern of surface temperature linearly related to their zonal index. Similar to our NP related pattern (fig. 4.5.b) the result exhibits little variance in the tropical Pacific but instead has a more zonally oriented North Pacific contribution. The timeseries for the zonal index, however, exhibits only partial similarity to fig. 4.4.a. This may be related to differences between the 200 hPa pattern obtained by regression onto the NP index (not shown) and the pattern related to the zonal index discussed by Ting et al. For the coupled model, the effect over the North Atlantic is much weaker than over the North Pacific, while the pattern in Ting et al. exhibits stronger wind anomalies over the Atlantic than their North Pacific analogue. Ultimately, this can be ascribed to the use of a zonal mean variable as different from the present analysis in which the index was based on Pacific only data. It is nevertheless of interest that an index independent of tropical Pacific SST with substantial decadal scale contributions was found in both approaches which led to at least partially consistent results. The equivalent barotropic structure, the surface expression of which is found in surface wind stress, is also characteristic of two modes of decadal variability obtained by Storch (1994) in a multi-century coupled simulation.

List of figures

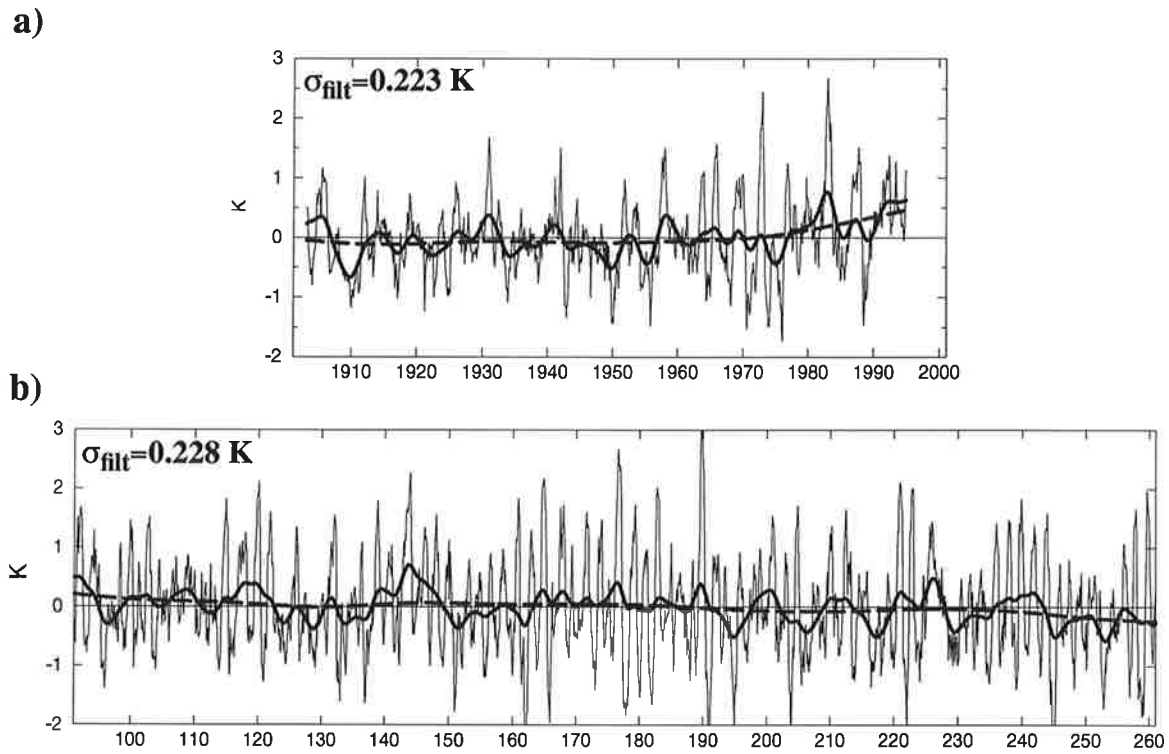

Fig. 4.1 Timeseries of anomalous SST averaged over the NINO3 region (90° W - 150° W, 5° N - 5° S). Thin line: raw data; thick full line: low pass filtered with half power at 7 yr; thick dashed line: low pass filtered with half power at 60 yr. The difference between the 7 yr and 60 yr filtered time-series is divided by its standard deviation (indicated in top left corner) and used as an index timeseries for subsequent regression analyses. a) GISST dataset, b) coupled model. Units: K

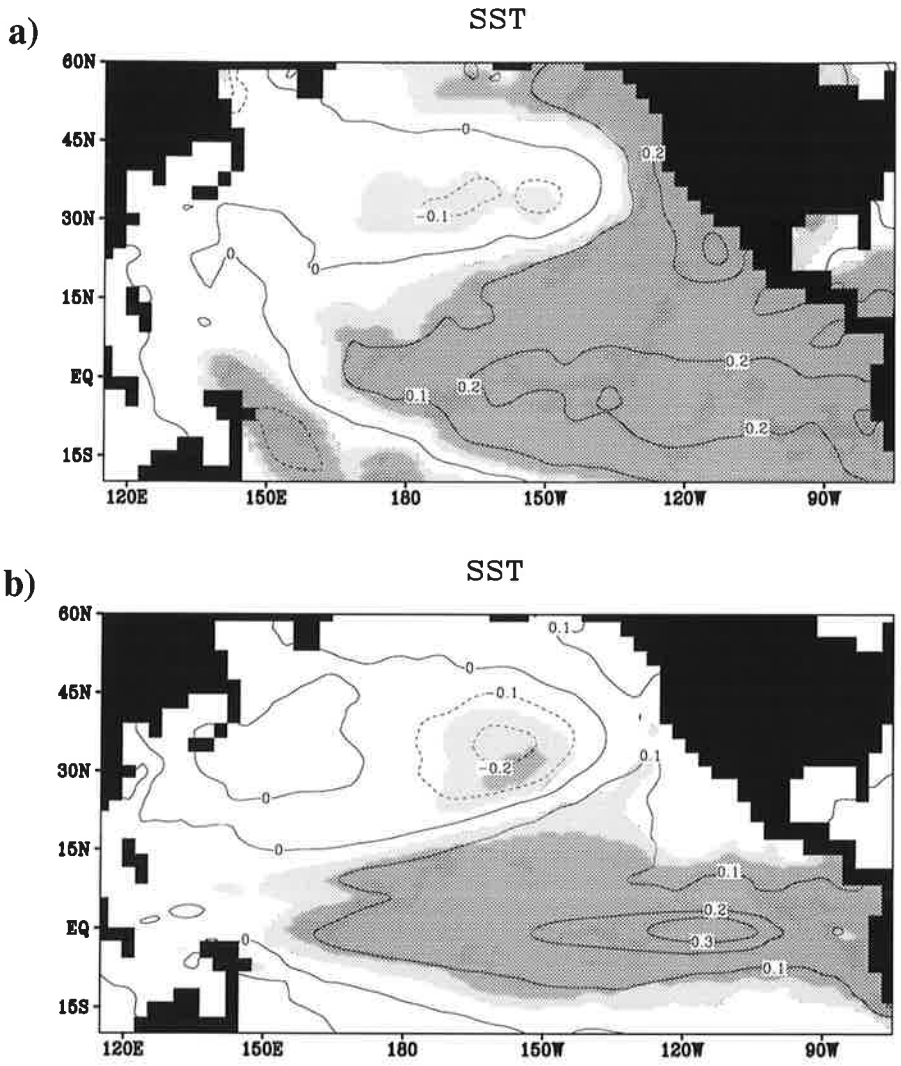

Fig. 4.2 Regression of filtered SST anomalies on filtered NINO3 region average of SST anomaly ('CT index'). a) ECHAM4 with GISST SST; b) coupled model. Units: K. Areas significant at the 5 % (1 %) significance level are represented by light (dark) shading. The significance estimate is based on an appropriate F-test for an effective number of degrees of freedom which is estimated according to Oort and Yienger (1996) at each gridpoint separately, although the reference F-value has been taken as spatially independent, being 4.1 (7.3) for 5 % (1 %) significance level.

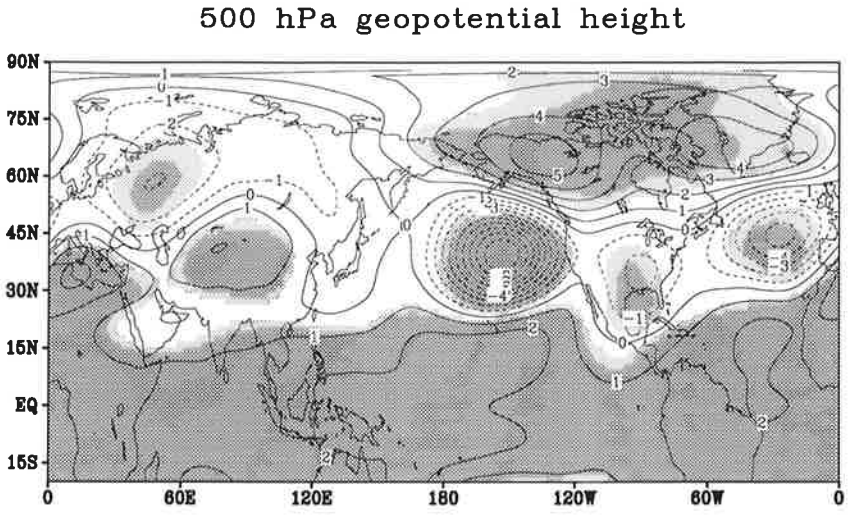

Fig. 4.3 Filtered coupled model 500 hPa height regressed on CT index. Units: gpm. Areas significant at the 5 % (1 %) significance level are represented by light (dark) shading.

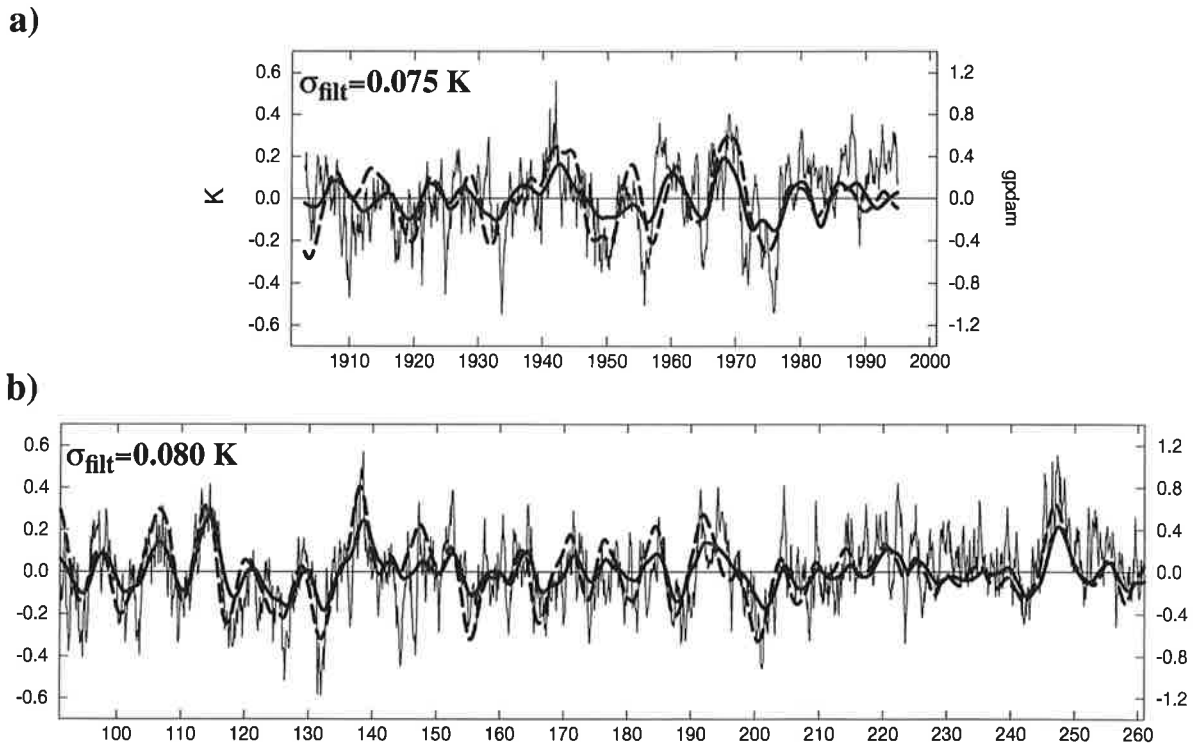

Fig. 4.4 Timeseries of expansion coefficient of leading SVD mode of SST and 500 hPa geopotential height based on residual quantities. Thick solid line: SST coefficient timeseries, used as NP index after division by its standard deviation (see top left corner). Units: K. Thick dashed line: 500 hPa height coefficient timeseries. Units: gpdam. Thin solid line: timeseries obtained by projecting unfiltered SST anomaly (without first removing CT related variability) on SST pattern associated with the leading SVD mode. a) GISST dataset, b) coupled model

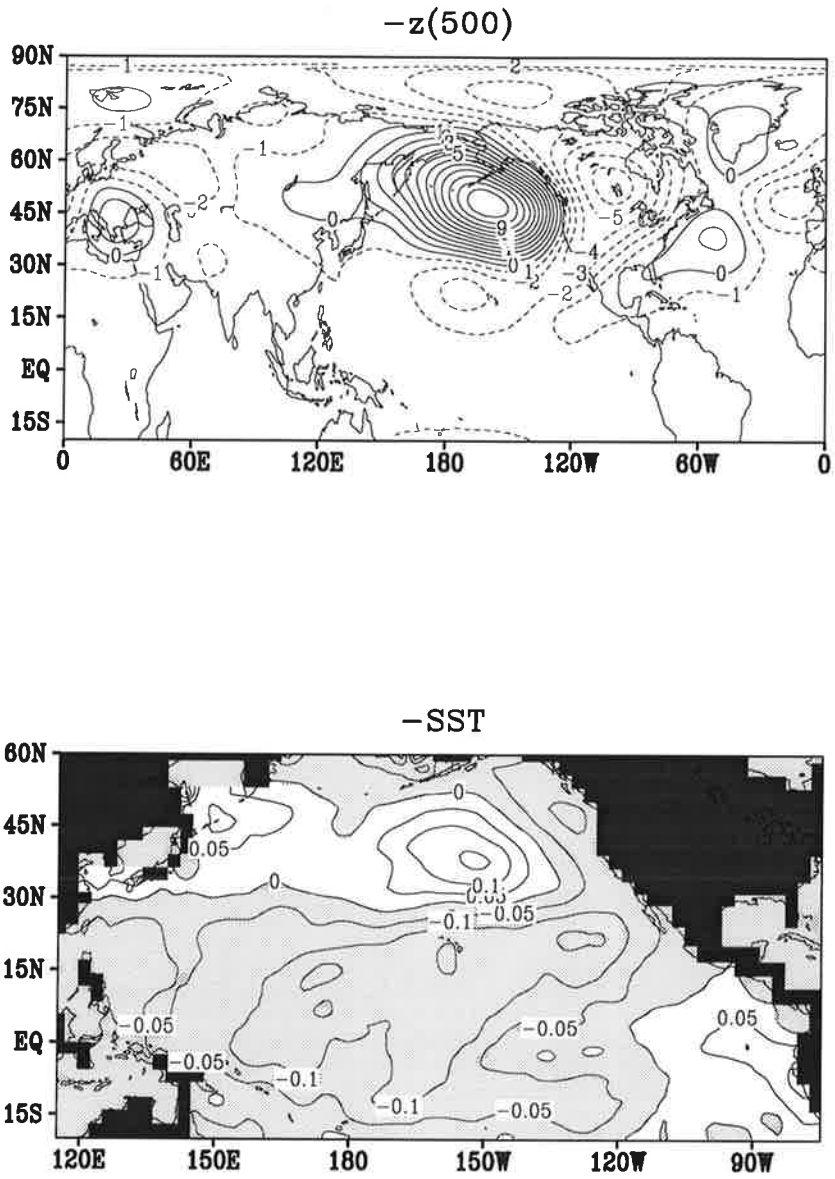

Fig. 4.5.a) Leading pattern pair from SVD of the filtered residuals of 500 hPa height and SST for the ECHAM4 run forced by GISST SST. The patterns relate to SVD timeseries which are normalized to unit variance. Units: gpm for z_{500} and K for SST.

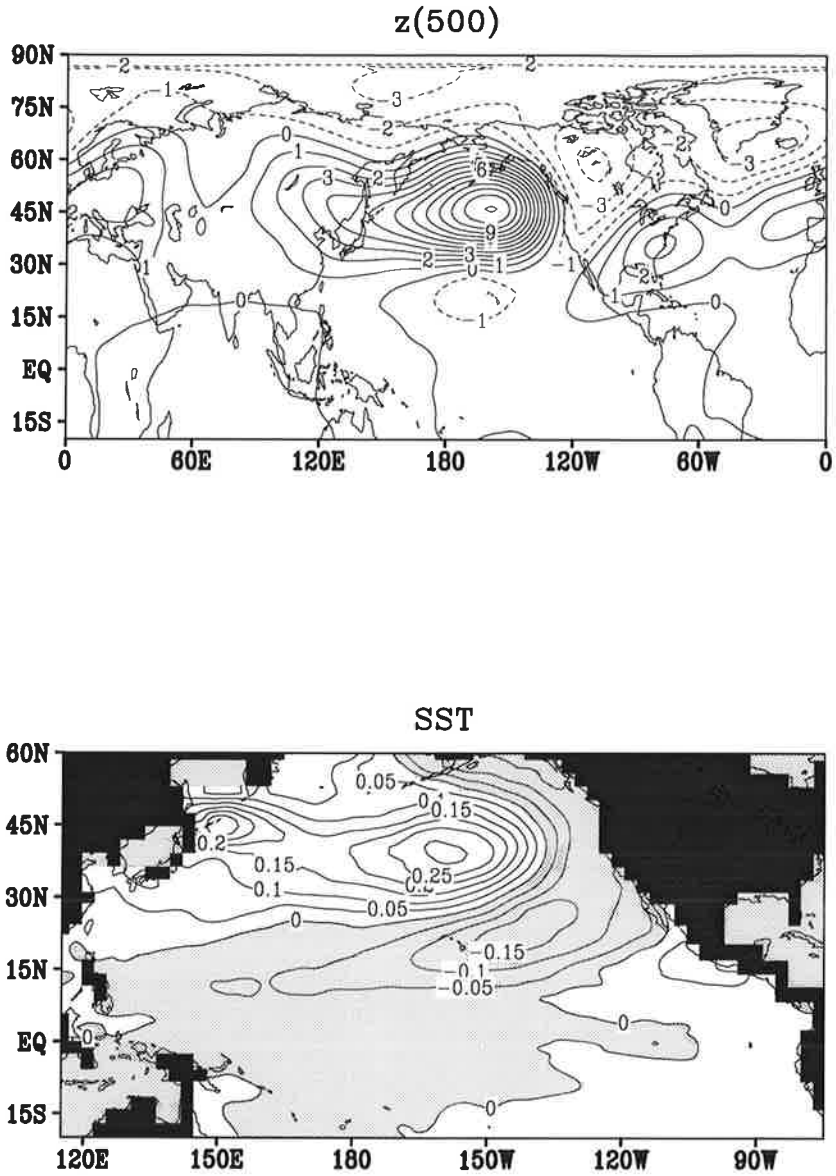

Fig. 4.5.b) Leading pattern pair from SVD of the filtered residuals of 500 hPa height and SST for the coupled model. The patterns relate to SVD time-series which are normalized to unit variance. Units: gpm for z_{500} and K for SST.

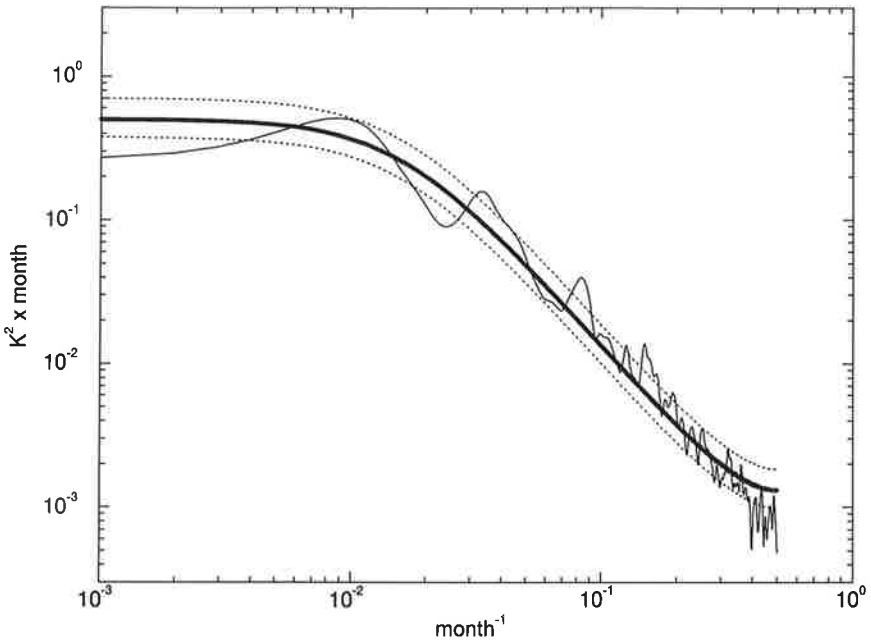

Fig. 4.6 Power spectral density for the unfiltered timeseries in fig. 4.4.b. The bold line represents an equal variance AR(1) process. The dashed lines are obtained by multiplying the AR(1) spectrum by the factors for 2.5/97.5 % χ^2 confidence limits with approx. 80 degrees of freedom, used for the smoothed spectrum shown as the thin full line

a)

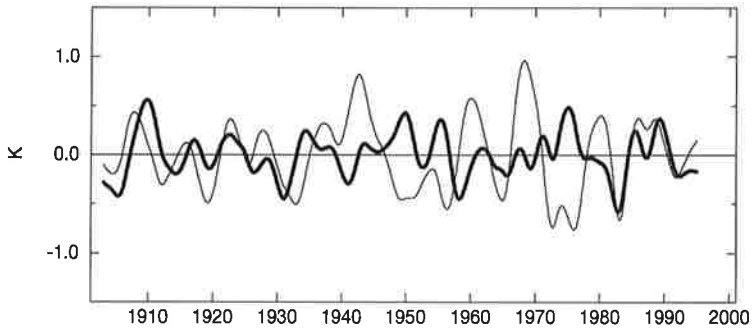

b)

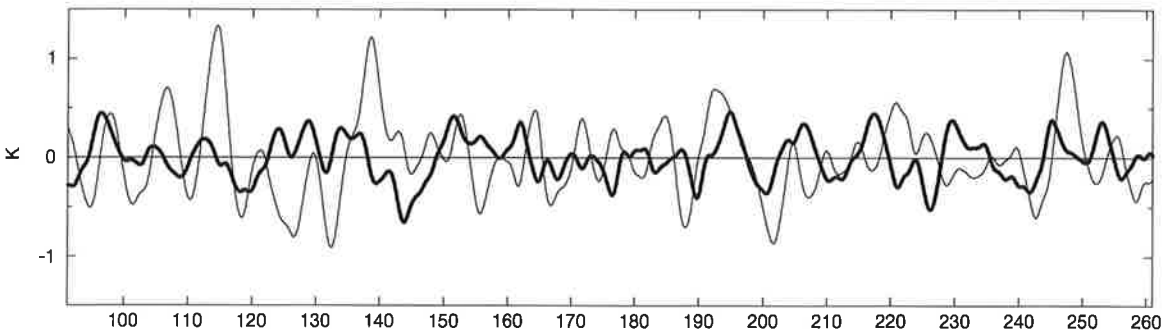

Fig. 4.7 CT index (thick line) and NP index (thin line) for a) ECHAM4 forced by GISST SST, b) coupled model. The CT index has been inverted, and the NP index has been multiplied by 5. Units: K

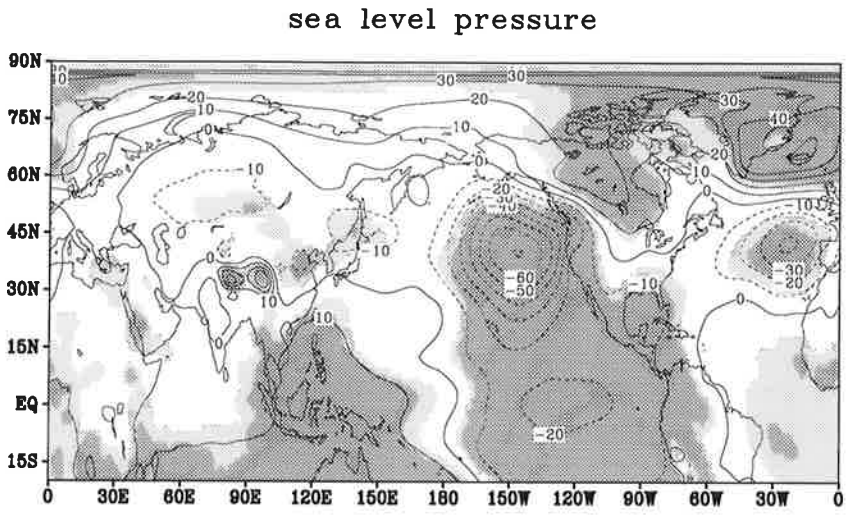

Fig. 4.8 Regression of sea level pressure on CT index. Unit: Pa. Areas significant at the 5 % (1 %) significance level are represented by light (dark) shading.

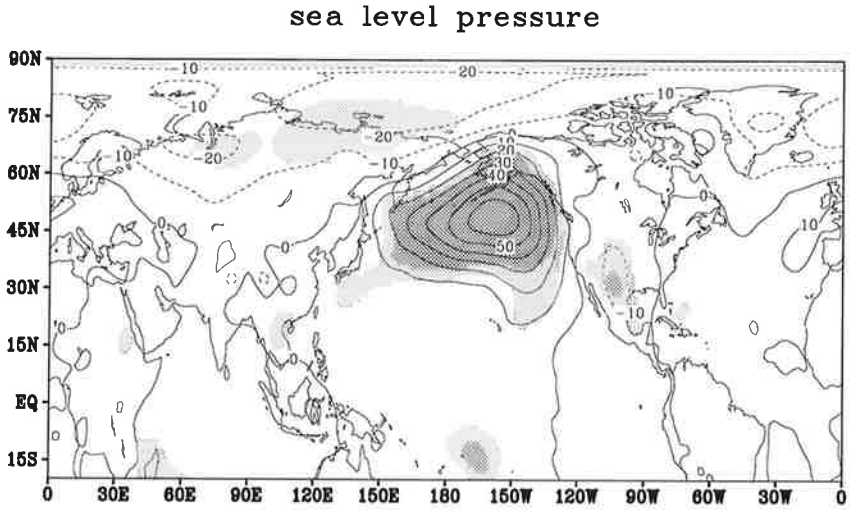

Fig. 4.9 Regression of sea level pressure on CT index. Unit: Pa. Areas significant at the 5 % (1 %) significance level are represented by light (dark) shading.

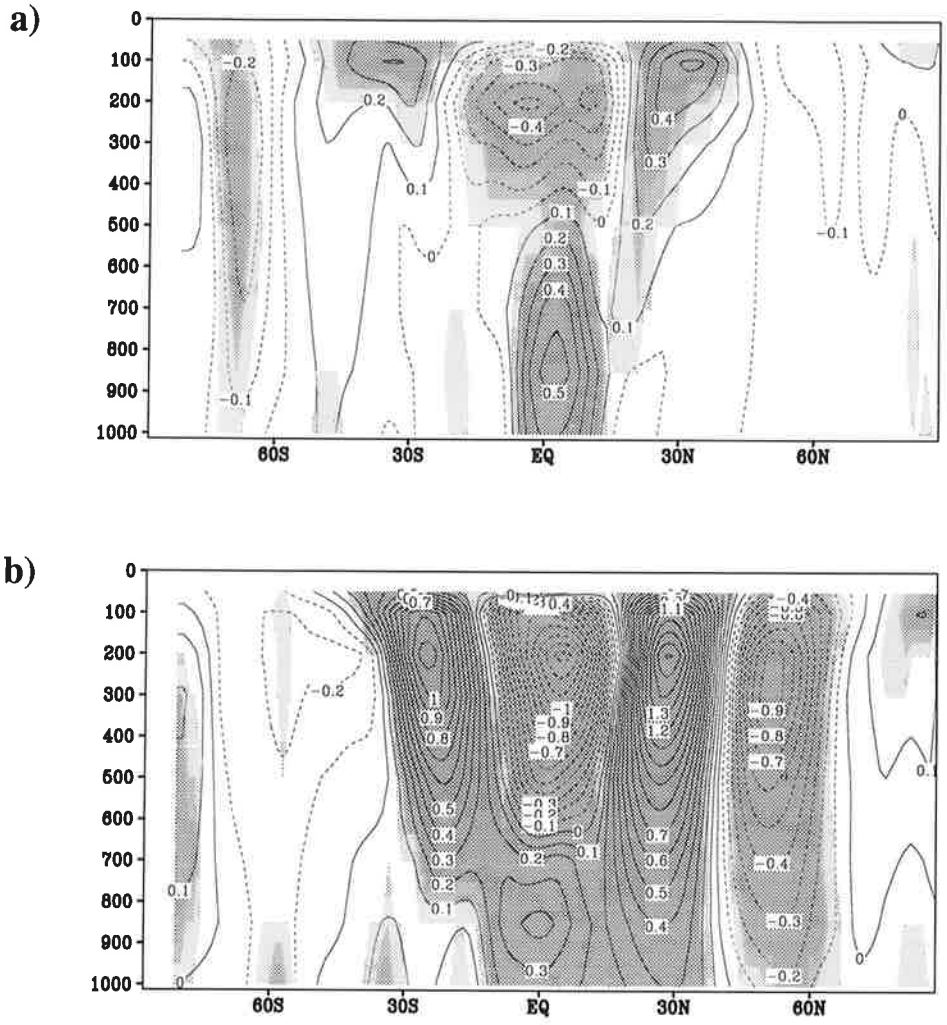

Fig. 4.10 Latitude-pressure distribution of regression of zonal wind on CT index a) at 160° E, b) at 160° W. Unit: ms^{-1}. Areas significant at the 5 % (1 %) significance level are represented by light (dark) shading.

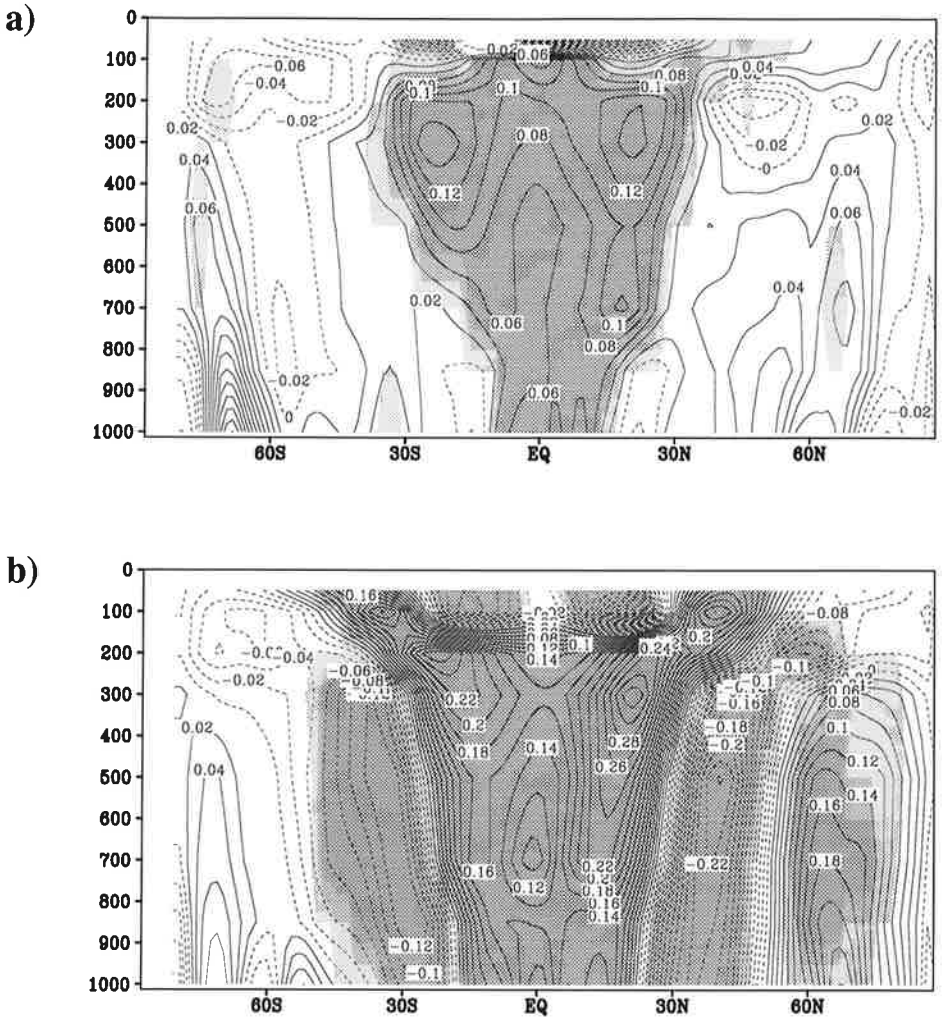

Fig. 4.11 Latitude-pressure distribution of regression of temperature on CT index a) at 160° E, b) at 160° W. Unit: K. Areas significant at the 5 % (1 %) significance level are represented by light (dark) shading.

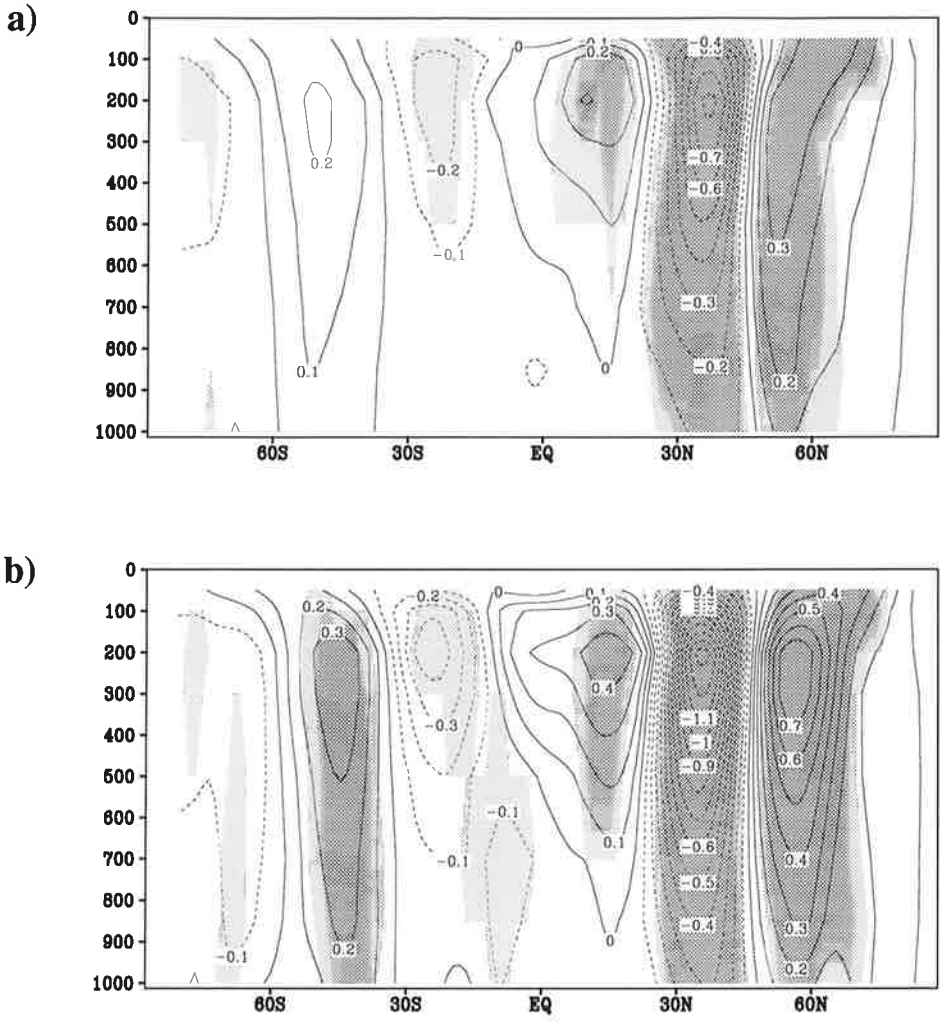

Fig. 4.12 Latitude-pressure distribution of regression of zonal wind on NP index a) at 160° E, b) at 160° W. Unit: ms^{-1}. Areas significant at the 5 % (1 %) significance level are represented by light (dark) shading.

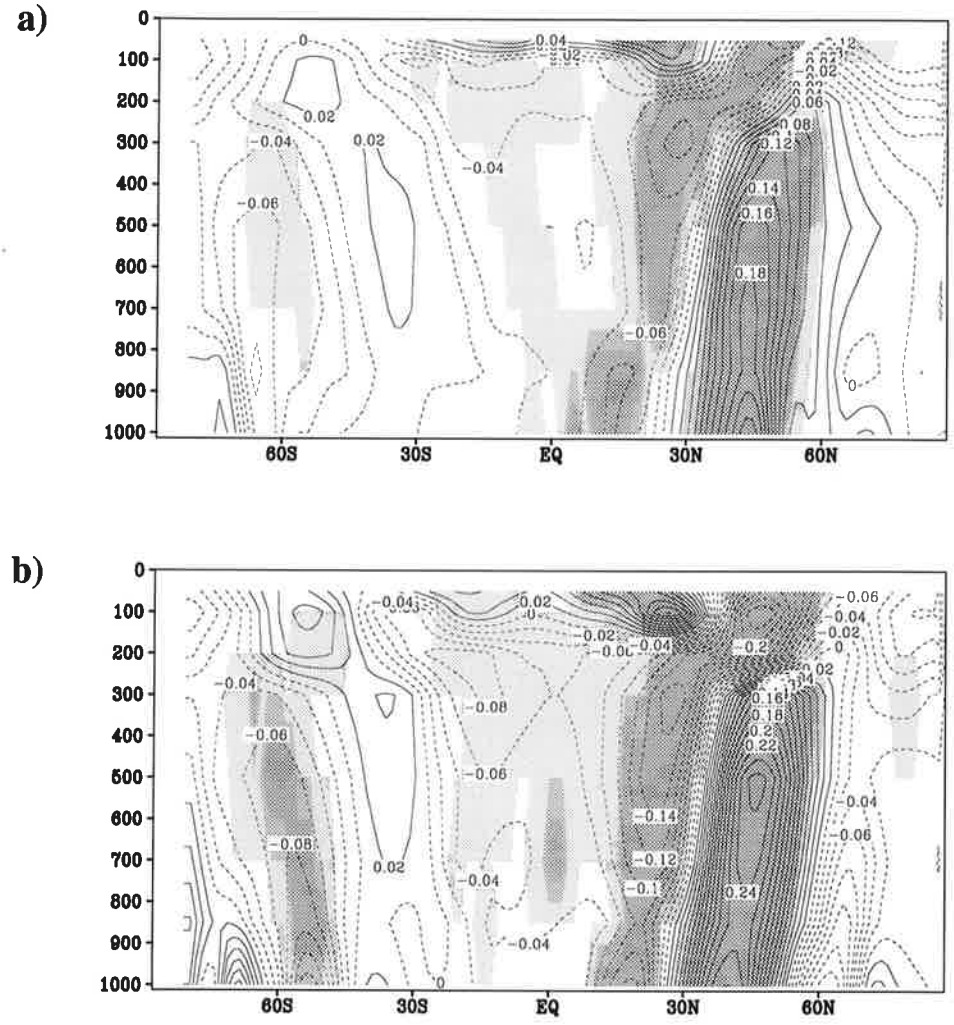

Fig. 4.13 Latitude-pressure distribution of regression of temperature on NP index a) at 160° E, b) at 160° W. Unit: K. Areas significant at the 5 % (1 %) significance level are represented by light (dark) shading.

Chapter 5

Tendency terms for the decadal SST variations

The previous chapter analysed aspects of the large scale circulation response to the decadal CT mode SST anomaly and discussed parallels to the established ENSO response. For the NP mode similar analyses indicated a detectable distinct atmospheric response. This response will involve changes in the low level winds and temperature of advected air mass and hence, in turbulent heat fluxes. A feedback on the SST anomalies can result from these effects on the forcing for the oceanic mixed layer. Heat flux driving seasonally persistent SST anomalies is discussed by, e.g., Luksch and von Storch (1992), Cayan (1992), Bladé (1997) and Ronca and Battisti (1997). Wind changes may also affect the entrainment at the mixed layer base and the wind driven ocean currents, leading to anomalies of Ekman and Sverdrup transports. Miller et al. (1994) using an OGCM forced by observed heat flux and wind stress anomalies find that the 1976 'climate shift' was accompanied by strong anomalies of both heat flux and advective SST tendency due to anomalous wind stress. Circulation changes affecting midlatitude SSTs may depend on forcing by tropical SST anomalies, a mechanism that was found to contribute to generating seasonally persistent SST anomalies by Luksch and von Storch (1992) and Alexander (1992). The model study by Lau and Nath (1994) examines the atmospheric response to tropical and extratropical SST anomalies and additionally analyzes the associated heat flux patterns, pointing to feedbacks which are generally negative in the tropics.

This chapter analyses the heat flux patterns for the decadal CT and NP modes. Feedbacks in the tropics and extratropics may differ in pattern structure and strength from their interannual analogue. In particular, differences from the interannual scale are found for cloud-radiative feedbacks for the CT mode as discussed below, taking into account the effect of large scale transport of water vapour. Regarding the observed changes during the 'climate shift' reference is made to the observational study by Yasuda and Hanawa (1996). Patterns of wind-induced vertical and lateral heat exchange terms in the mixed layer for both the CT and the NP modes are discussed in a further section.

5.1. Surface heat flux contributions

In the present work, similar to, e.g., Nakamura et al. (1987) or Lau and Nath (1994), each surface heat flux component is first subject to the filtering described in section 4.1 and then regressed onto the filtered and normalized (CT or NP) index timeseries.

For the CT mode, fig. 5.1.a shows the variation of net heat flux at the ocean surface linearly related to the CT index. Fig. 5.1.b shows the same for the sensible heat flux, fig. 5.1.c, fig. 5.1.d and fig. 5.1.e apply to the latent heat flux, shortwave and longwave fluxes, respectively. All heat flux terms follow the standard sign convention, i.e. the sign of the heat flux anomaly is positive when there is a greater than normal heat flux into the ocean. Consistent with expectation, the equatorial Pacific, particularly the area within the cold tongue, exhibits a negative correlation with the SST variations, and this relationship is also significant. Comparing the position of the 0.2 K isotherm in fig. 4.2 and the contours for -2 and -3 Wm^{-2} of related heat flux variation, we find a feedback of about -10 to -15 $Wm^{-2} K^{-1}$. Comparison with fig. 5.1.b through 5.1.e shows that the latent heat flux apart from absorbed shortwave radiation provides the dominant contribution of all components.

The feedback strength in the coupled simulation is thus consistent with the estimate obtained by Lau and Nath (1994) for the case of their uncoupled GCM of coarser resolution forced by SSTs with anomalies confined to the tropical Pacific, being one of a set of runs with varying SSTs prescribed globally or in more specific domains. In this TOGA case (TOGA=Tropical Ocean/Global Atmosphere) they proceeded very similarly to the analysis done above, performing an SVD of tropical Pacific SST and 500 hPa geopotential height. Their analysis however, in contrast to the above procedure, omitted the step of removing cold tongue-related variability (since the TOGA setup is specialized to examine it) and thus directly recovered a timeseries equivalent to our cold tongue or NINO3 index. Also, they did not pre-filter the data which, consisting of winter season values, can consequently contain interannual as well as lower frequency variability. This timeseries was then used to estimate feedback strengths using regression, and the results were given separately for the turbulent boundary layer fluxes and the radiative fluxes. For the turbulent fluxes they found a negative feedback of -10 Wm^{-2} K^{-1} which is consistent with the above analysis.

In view of the smallness of the sensible heat flux variations, to explain the net heat flux outside the cold tongue area apart form latent heat flux requires the radiative flux components. Over the eastern part of the Maritime Continent the net warming is due to shortwave radiative flux. The attribution to deep convective cloud is confirmed by the variations of vertically integrated cloud liquid water content (fig. 5.3.b). These are linked to variations in vertically integrated water vapour transport which in this area exhibits anomalous divergence (fig. 5.4). Since the only opposing tendency for mixed layer temperature in this area, the entrainment term, does not yield a balance, positive heat input occurs in this region during warm CT mode SST anomalies.

Balancing of net surface heat flux variation to near zero occurs in the are extending from Papua New Guinea south-eastward to the region south west of Tahiti. Small negative SST anomalies occur in this area and are linked to anomalous PBL divergence which induces positive shortwave flux variations due to reduced convection. Stronger winds (cf. fig. 5.9) are responsible for enhanced evaporation which compensates the shortwave flux term.

Roughly within 5° of the equator, from 160° E to the date line, weak positive CT mode SST anomalies occur. Here, net heat flux variations are dominated by shortwave radiation, and opposed by the longwave component. The southern half of the area experiences a reduction in evaporative cooling which thus cannot provide a stabilizing feedback which instead is provided by the shortwave flux. This is consistent with the 'thermostat hypothesis' (Ramanathan and Collins, 1991) which points to the negative feedback to warm pool SST by shortwave reflection at cirrus cloud tops. This feedback acts to stabilize SST against the super greenhouse effect, i.e. the superlinear increase of the trapping of longwave radiation by water vapour as a function of SST. The variations in water vapour, cloud liquid water, water vapour flux and its divergence are consistent with the radiative fluxes.

Per 1 K of SST variation the sum of both radiative flux component variations provides about 20 Wm^{-2} in the central equatorial Pacific region and about 10 Wm^{-2} in the area centred about 15° N. Thus, regarding radiative fluxes we obtain similar results for the decadal scale as discussed for interannual variability by Lau and Nath (1994). Tropical Pacific cold tongue SST variations generally induce negative feedback both from the turbulent and the radiative components which in turn are dominated by the latent heat flux and the shortwave radiative flux. Different from the interannual scale (Lau and Nath, 1994), near 15° N there are decadal radiative flux variations of more than half the magnitude as on the equator. Inspection of the vertically integrated cloud liquid water content

(fig. 5.3.b), along with the divergence of vertically integrated water vapour transport (fig. 5.4.b), points to a cloud radiative effect different from that in the region of anomalous deep convection on the equator where the response is similar to that found for 'canonical ENSO' conditions (as, e.g., in the analysis of Outgoing Longwave Radiation by Heddinghaus and Krueger, 1981; see also Bony et al., 1997). While, similarly to the equatorial region, anomalous convergence of water vapour flux leads to an increase in cloud liquid water, it is likely associated with midlevel convection since this region still experiences the influence of the trade inversion. The convergence is mostly given by boundary layer convergence, as evident from comparing the vector plot of vertically integrated water vapour flux, fig. 5.4.a, with the CT related wind stress vector, fig. 5.9.b. Anomalous deep convection will likely be confined to the equatorial region. No analysis of cloud top pressure is presented here, however, and further research is needed (see also Weare, 1997; Ringer and Shine, 1997).

In the North Pacific where SST varies out of phase with the tropics another similarity between the single year SST anomalies, some portion of which can be explained by ENSO forcing (Luksch and von Storch, 1992), and the decadal scale anomalies considered here is found. The heat flux varies in phase with SST, fig. 4.2.b, and is dominated by turbulent heat flux and longwave radiative flux contributions. The cooling over areas with decreasing SSTs can thus be attributed to advection of anomalously cold air, similar to the mechanism discussed by Luksch and von Storch (1992). The effect of the midlatitude heat flux variations is much smaller than in the tropics. This points out that mechanisms other than the variations in the heat flux induced by near surface wind may be important to maintain the multi-year SST anomalies. A detailed study of all heat budget terms for the mixed layer will be necessary and will be performed in section 5.2.

For the NP mode the patterns of net heat flux and the sensible, latent, shortwave and longwave contributions for this mode are displayed in fig. 5.2.a through e. For this mode, net heat fluxes are smaller and statistically significant areas are smaller. Throughout the tropics heat flux variations are small and correlate negatively with the SST variations of fig. 4.5.b. The area which most clearly exhibits positive correlation is situated south-east of Japan. The remainder of the subtropics and midlatitudes are characterized by negative correlation between heat flux and SST.

The characteristic features in the heat flux variations are largely explained by the latent heat flux and shortwave contributions. A negative correlation is found between latent heat flux and SST in the central North Pacific. The sensible heat flux variations are only important in the area extending east of Japan, where they contribute equally strongly to the net heat flux as the latent heat flux term. The positive correlation here can be explained by advection of continental air over the anomalously warm or cold sea surface. From fig. 4.5.b we have anomalous anticyclonic flow associated with a weakening and northward contraction of the Aleutian low which correlates with anomalously warm water stretching across the North Pacific. In conjunction with that there will be reduced advection of cold air which implies a higher equilibrium temperature of the sea surface and thus a weaker heat flux out of the ocean. This mechanism has been discussed in several studies concerned with midlatitude SST anomalies (e.g., Luksch and von Storch, 1992). This local feedback mechanism, however, for the decadal scale does not account for maintaining the basin-scale midlatitude decadal SST anomaly pattern, since heat flux correlates positively with it only in the western North Pacific. The full heat balance of the mixed layer including advective contributions must be examined.

Although markedly distinct from the CT mode related patterns, the patterns for the shortwave and longwave radiative flux components for the NP mode, fig. 5.2.d and 5.2.e, indicate similar cloud

radiative effects in the tropical central/western Pacific, in particular. Attributing the radiative flux anomalies to clouds is suggested by the well matched patterns for the shortwave and the longwave components. Also, as with the CT patterns, the divergence of vertically integrated water vapour flux, fig. 5.6, exhibits similar structure between the date line and 150° W as the radiative fluxes. The anomalously cold SST in fig. 4.5.b thus induce anomalous divergence similar to negative CT mode anomalies. Differences are found in the West Pacific where a characteristic response is seen in the CT mode related pattern but not for the NP mode.

For shortwave radiation the decadal anomalies in the North Pacific exhibit strong positive correlation with the NP mode decadal SST anomalies (fig. 4.5.b), and the longwave radiation pattern matches that for the shortwave flux but exhibits opposite sign. This at first appears surprisingly inconsistent with the patterns of moist variables (fig. 5.5). In water vapour, a significant positive anomaly across the North Pacific is found that matches the anomalous warm midlatitude SST pattern in fig. 4.5.b. Similarly, for liquid water content, positive but weak anomalies are found in the same area. Thus the correlation of shortwave flux and SST could be expected to be negative. A plausible explanation is related to the fact that the analysis involved decadal filtering of monthly data, and the anomalies therefore represent approximate annual average anomalies. However, if, in contrast to the mean seasonal cycle (Norris, 1998), the anomalies in moisture in the boundary layer in the midlatitude North Pacific are strongest in winter and thus dominate the pattern in fig. 5.5.a, it may have little effect on radiation during the summer maximum. Indeed, moisture anomalies weaker than in winter but of the reverse sign might assist in positive shortwave flux anomalies being produced over warm SST anomalies during summer. This would be consistent with several recent studies, e.g. Norris and Leovy (1994). However, for a definitive assessment a separate analysis of the winter and summer seasons is needed, thus requiring research beyond the present thesis.

For the NP mode there is a much stronger correlation between the eastern North Pacific and the tropical variations in radiative fluxes than for the CT mode. It is not clear from the regression analysis whether the anomalous convergence or divergence in the tropics significantly influences the extratropics. Analyses by Nitta and Yamada (1989) and Graham (1994) indicate that a shift in the background of tropical SST variation most likely induced the 'climate shift' in 1976. More specifically, the difference of winter mean SST for the period 1977-82 minus 1971-76 shown by Graham (1994) exhibits a similar structure compared to the pattern from the coupled integration shown in fig. 4.5.b, in that the values in the east Pacific are substantially smaller than in the western part, although out of phase variation compared to the western part is only found in a small region close to the eastern boundary in Graham (1994). In chapter 4 results were presented supporting the identification of the NP mode as variability that explained the 'climate shift'. Our analysis for the radiative fluxes, fig. 5.2.d and 5.2.e, leads to similar patterns as those for Outgoing Longwave Radiation (OLR, not shown). The OLR pattern corresponding to the SST difference obtained by Graham (1994) is oriented similarly as for the NP mode in the coupled simulation but has somewhat larger extent. Thus, for the coupled model, the NP mode patterns are related to the 'climate shift' but as part of the NP related variability, modulation of tropical convection is also found to be statistically significant. For the CT mode, the North Pacific contribution to the heat flux pattern was rather weak but a strong signal associated with displaced areas of deep convection. The NP mode signal lacks the pattern associated with midlevel convection in the off-equatorial tropics that was found for the CT mode.

Extending the comparison with observations related to the 'climate shift', a remarkable match is also

found when comparing the pattern of net heat flux for the NP mode (fig. 5.2) and the result obtained by Yasuda and Hanawa (1996) using the Comprehensive Ocean Atmosphere Dataset (COADS, Woodruff et al., 1987). Up to sign, the net heat flux, fig. 5.2.a, corresponds to their result for the difference between the decades after and before the 'climate shift', i.e. 1976 to 1985 minus 1966 to 1975. Furthermore, for the surface wind stress (see next section) the coupled model also reproduces the result by Yasuda and Hanawa (1996). Taken together with our results for the 500 hPa height residual and the sea level pressure, which we found correspond to Trenberth and Hurrel's (1994) results, this indicates that the model, in a statistically robust fashion, captures the characteristics of the mid-seventies 'climate shift'.

A summary of the main results for the heat flux contributions is given in table 5.1. Italic type is used for positive correlations.

Table 5.1: Feedback by surface heat flux components for CT and NP modes

	main geographical domain **CT**	main geographical domain **NP**
net heat flux	equatorial region, mainly cold tongue; *pos. correlation subtropical eastern North Pacific*	Northwest Pacific, *pos. correlation east of southern Japan*
sensible heat flux	small values; *pos.correlation midlatitude North Pacific*	similar to net heat flux; *pos.correlation east of southern Japan*
latent heat flux	cold tongue and zonal stretch in east Pacific, 15° N, *pos. correlation near date line on equator*	subtropical central Pacific; *pos.correlation east of southern Japan*
shortwave radiation	central/western Pacific, warm pool region, southern flank of subtropical anticyclone, *pos. correlation subtropical/tropical North eastern Pacific and midlat. North Pacific*	central South Pacific near equator, east Pacific 15° N, *pos.correlation near 150° W collocated with the centre of the North Pacific SST anomaly*
longwave radiation	as shortwave radiation, but signs reversed	as shortwave but with reversal of signs

5.2. Heat budget terms in the oceanic mixed layer and large scale wind driven ocean dynamics

Generation and maintenance of the decadal SST anomaly patterns can be attributed to a particular term or combination of terms in the SST equation,

$$\rho h c_p \cdot \left(\frac{\partial}{\partial t} T + \hat{v} \cdot \nabla T \right) = \delta Q + \nabla \bullet A_s \nabla (\rho h c_p T) + c_p \cdot (w \rho T)_{entrain} \qquad (5.1)$$

In this equation the local change in mixed layer temperature is related to the advective contribution (second term on left hand side), the net surface heat flux minus the amount of shortwave radiation penetrating the mixed layer, the eddy diffusion and entrainment related heat fluxes (first, second and third terms on the right, respectively) (cf. Oberhuber, 1993a,b).

The surface heat flux analysis showed that except near the western boundary region of separation of the Kuroshio and in regions of seasonal stratus cloud cover, the net heat flux generally correlates negatively with SST. Positive feedbacks if present must be provided by other terms. The OGCM used here includes a scheme for the prognostic calculation of mixed layer depth and entrainment/ detrainment rate which is a variant of the traditional Kraus and Turner (1967) parameterization and is discussed in detail by Oberhuber (1993a,b). This provides the opportunity to examine the mixed layer integrated SST tendency terms as well as changes in the depth of the mixed layer. An indication for the increasing importance of ocean-dynamical contributions in the mixed layer heat budget on longer than seasonal timescales is given by Ronca and Battisti (1997). Their analysis of data from ocean weather ship N (140° W, 30° N) underscores the predominance of heat flux contributions to the SST tendency for the seasonal scale. However, for longer timescales their one-dimensional mixed layer model analysis yields a residual term corresponding to lateral exchange which becomes substantial for winter in longer term averages.

The first term on the right in eqn. (5.1) is the net heat flux at the surface minus the amount of short-wave radiation that penetrates below the mixed layer. This term has been shown to be of importance particularly for the seasonal cycle (e.g., Ohlmann et al., 1996). For the CT and NP decadal modes regressions were computed for this vertical heat flux differential. Since the resulting patterns closely resemble the ones associated with the net surface heat flux itself both in magnitude and shape, this term is not discussed further. For the regressions of the lateral diffusion heat budget term for both modes small values result so that this term is not shown either.

Two further vertical exchange processes in principle influence SST tendency which are related either to the turbulence through the depth of the mixed layer and its interaction with the waters in contact with it, or convective exchange when the density stratification is close to neutral. In a coarse resolution model these processes are parameterized, the former by the parameterization of entrainment and detrainment at mixed layer base, the latter by a convective adjustment scheme. Details of these parameterizations are found in Oberhuber (1993a,b). Since the conditions for convective adjustment are rarely met in most of the tropical and extratropical North Pacific, the CT and NP regression patterns are of little importance and not displayed.

Fig. 5.7.a and fig. 5.11.a display the variations in the heat flux due to entrainment for the two modes. Differences between entrainment and detrainment rates at the base of the mixed layer are linked to changes in its depth, e.g., in the seasonal variation of mixed layer depths in the extratropical North Pacific (cf. fig. 3.24 and 3.26). Assuming a steady state, in a given mixed layer column an entrainment surplus continuously replaces water flowing off laterally in the presence of a nonzero divergence of horizontal wind driven transport. The compensating transport at the mixed layer base is associated with the vertical Ekman velocity

$$w_E\big|_{-h} = curl\left(\frac{\vec{\tau}}{\rho_0 f}\right) \qquad (5.2)$$

h is mixed layer depth, $\vec{\tau}$ wind stress, ρ_0 a typical density, f the Coriolis parameter.

Positive (negative) $w_E\big|_{-h}$ describes upwelling (downwelling). Isolation of the dynamical contribution to the mixed layer entrainment heat budget term for the CT(NP) modes is possible by considering the mixed layer depth, fig. 5.8 (5.12), the surface wind stress and its curl, fig. 5.9 (5.13), and the

flux of turbulent kinetic energy (TKE, represented by the cube of the friction velocity, u_*^3), fig. 5.10 (5.14) which the seminal paper by Kraus and Turner (1967) identifies as the relevant term governing the entrainment rate. The role of buoyancy flux in the entrainment rate is disregarded in this thesis.

For the CT mode a positive decadal SST anomaly causes deep convection associated with the SPCZ to occur further eastward. From Papua New Guinea to the area south-west of Tahiti stronger wind stirring occurs, evident from the regression pattern for u_*^3 (fig. 5.10). Mixed layer depths increase (fig. 5.8) and thus the cooling of mixed layer temperature is enhanced, consistent with the cooling in this region evident in fig. 5.7. Cooling by entrainment also occurs near 15° N west of the date line. However, no increase in mixed layer depths is found in this region. Anomalous positive wind stress curl is found at that latitude (fig. 5.9), as well as positive TKE flux (fig. 5.10) slightly north of the anomalous curl. The entrainment anomalies here are linked to anomalous Ekman divergence.

East of the date line, between the equator and 20° N relatively strong anomalous heating by anomalous reduction of entrainment occurs. It is this contribution which, compared to the remaining terms, dominates the triangularly shaped decadal SST warm anomaly off the equator in fig. 4.2.b. Direct forcing by surface wind stress and curl contributes little, moreover there is no substantial mixed layer depth change. More important than modifications in entrainment rate are variations in temperature such that warmer subsurface water leads to weaker surface cooling when entrained into the mixed layer. A candidate mechanism for explaining the subsurface anomalies discussed in the recent literature is anomalous subduction (Deser et al., 1996). Water subducted with anomalous properties in the North Pacific subduction zone may advectively influence the subsurface region. However, tracer trajectories found, e.g., in the forced OGCM study by Gu and Philander (1997), performed at higher resolution, would suggest a greater westward displacement of particles at this latitude. Barnett et al. (1998) in a coupled model simulation find that, although subducted water mass at anomalous temperature can be diagnosed, the influence on the tropics regarding the ENSO signal is minor.

Since the atmospheric patterns related to the CT mode, e.g., SLP, fig. 4.8, resemble the familiar ENSO response, an oceanic decadal ENSO related mechanism for subsurface anomalies should be considered. Reduced cooling by entrainment may be due to lowering of the thermocline in consequence of downwelling westward propagating Rossby waves. As Rossby wave fronts radiate from the eastern boundary, the zonal propagation speed decreases with latitude such that as the wave front progresses its northern portion becomes lagged compared to the low latitude part and a triangular thermocline anomaly may result.

Excitation of Rossby waves at the eastern boundary can be due to poleward propagating coastal Kelvin waves (White and Saur, 1983, Jacobs et al., 1994, Meyers et al., 1996). These in turn originate from equatorial Kelvin wave energy incident on the coast in the course of ENSO. The latitude dependence of the Rossby wave speed and lags induced by poleward propagation along the coast may lead to long term remote thermocline effects due to ENSO in the North Pacific (Jacobs et al., 1994). It also seems natural that effects of successive ENSO phases overlay each other. The net effect on the thermocline conveniently explains the entrainment modulation responsible for the CT mode decadal SST anomaly in the area in question. Such thermocline effects have a weak mirror image in sea level which is discussed later.

Decadal ENSO induced thermocline variations are consistent with the pattern of advective heat budget contribution for the CT mode, fig. 5.7.b. In a 'canonical ENSO' (Rasmussen and Carpenter,

1982), Kelvin wave energy is radiated eastward along the equator from excitation by anomalous westerly wind near the date line which results from anomalous deep convection in place of the south-eastern trades during the second half of an ENSO year. The thermocline in the east is lowered by this stream of Kelvin waves while compensating lateral convergence occurs which leads to advective heating within the cold tongue. If effects of more than one ENSO overlay each other, the thermocline excursions, which are a succession of warm/downwelling and cold/upwelling phases, can form a residual which appears as a slowly drifting background on which the faster ENSO anomalies evolve.

The CT mode wind stress variations, fig. 5.9, are consistent with decadal ENSO background variation. For the 'mature phase' of the 'canonical ENSO', around the turn of the year, anomalous easterlies are found over the Maritime Continent and anomalous westerlies on the equator near the date line (Rasmussen and Carpenter, 1982). If in a succession of more than one event the west Pacific easterly anomalies weaken along with strengthening midbasin anomalous westerlies, taking the average over more than one event results in a westerly residual from Indonesia to the central Pacific. A drifting background thus is capable of inducing a pattern such as found in fig. 5.9. However, recently arguments have been put forward for the mechanism to operate in the reverse direction. Barnett et al. (1998) reason that the pattern, possibly excited by decadal variations in the North Pacific, would modulate the equatorial thermocline and thus induce the background signal, rather than being a response to ENSO background drift. The midlatitude source for the decadal wind stress modulation is identified in a wind stress pattern similar to fig. 5.9.a obtained by a canonical correlation analysis (CCA) of wind stress and SST in the 10-40 year band. Neither their analysis nor the regression in the present thesis definitively reveal the cause for the pattern of fig. 5.9.a which, based on the observations of da Silva et al. (1994), is also reproduced by Latif (1997). The surface wind stress field associated with a decadal warm CT anomaly will exhibit weakened contribution of the south-eastern trades on the equator and therefore less Ekman divergence and the resulting downwelling in the east Pacific is further accompanied by a deepening mixed layer (cf. fig. 5.8).

The decadal ENSO signature can be seen in the subtropical eastern North Pacific. In the region of cooling found east of the date line in fig. 4.2.b anomalous advection is the dominant contribution to the heat budget. The principal cause is Ekman induced southward shifting of the eastern extremity of the Kuroshio extension, as evident from the wind stress anomalies of fig. 5.9. From the pattern of wind stress curl, weak anomalous downward motion (Ekman pumping) occurs about 25° N near the date line, while stronger upward motion (Ekman suction) is implied near 40° N in the east Pacific. The vertical Ekman velocity given by eqn. (5.2) induces vortex stretching or compression in the main thermocline below the mixed layer, leading to horizontal subsurface transports consistent with the conservation of potential vorticity (Luyten et al., 1983). Compared to the Ekman transports, the subsurface geostrophic transport is the dominant contribution to the Sverdrup transport obtained from integration between the sea surface and the thermocline, according to the Sverdrup relation

$$\beta \int_{-H}^{0} v\,dz = curl\left(\frac{\vec{\tau}}{\rho_0}\right) \qquad (5.3)$$

(β being the meridional derivative of the Coriolis parameter, ρ_0 average density, H depth of the thermocline below which zero motion can be assumed, compared to the wind driven flow).

Anomalous wind stress curl therefore implies a change in the baroclinic structure of the upper ocean

and this is detectable by its effect on sea level, which is discussed below.

The location of the North Pacific anomalies in advective heating agrees with the position of the cold anomaly in fig. 4.2.b. In view of the known response to ENSO in the extratropical North Pacific (e.g., Alexander, 1992, Luksch and von Storch, 1992) the model anomaly can be interpreted as a response to the decadal background which is similar in extent. These results are also consistent with the pattern for the first EOF of Pacific SST in Deser and Blackmon (1995).

The independent role of the NP mode is reflected in the heat budget terms for the mixed layer. The entrainment pattern, fig. 5.11.a, exhibits negative values nearly everywhere but is spatially organized in a manner similar to the SST pattern in fig. 4.5.b. Near 45° N, entrainment correlates negatively with SST, and thus acts to damp SST anomalies. A similar result was quoted by Frankignoul (1985) for single year anomalies. The strongest variations occur in the tropical-subtropical wedge-shaped area where cooling by anomalous entrainment is associated with the cold-phase SST anomalies. In this area, compared to the remaining heat budget terms the entrainment variations are the strongest influence on the mixed layer temperature and their spatial extent matches that of anomalous SST. As with the CT mode, local wind stirring (cf. fig. 5.13) is not a consistent explanation. Upwelling or downwelling thermocline signals again form the most natural explanation. Although no significant advective contribution is obtained on the equator, thermocline variations in the off-equatorial tropics could be a consequence of equatorial and coastal Kelvin waves in view of the time lag in the subtropical signal with respect to generation of a disturbance in the equatorial waveguide. If a signal with nonzero lag with respect to the origin dominates in the real-valued pattern, the source can appear substantially attenuated in the pattern.

The dominant mixed layer heat budget contribution in the midlatitude North Pacific is by advection, similarly as in the CT mode. Northward directed anomalous Ekman transport of warmer water can be inferred from the wind stress pattern in fig. 5.13. The pattern of wind stress curl, fig. 5.13.b, is a north-south dipole which extends all across the Pacific. The northern lobe exhibits negative sign and is thus consistent with anomalous southward Sverdrup transport. The reverse is true for the southern lobe. The resulting meridional convergence is consistent with a positive sea level anomaly which is confirmed below (fig. 5.16). Consistency of anomalous currents with Sverdrup balance was also found in the forced OGCM integration used to hindcast the 1976 'climate shift' by Miller et al. (1997). Moreover, the pattern shown in fig. 5.13 closely resembles the result obtained in the observational study of Yasuda and Hanawa (1996) who used COADS data (Woodruff et al., 1987) to form a decadal difference between the averages over the decades before and after the 1976 'climate shift'. The only difference, the reverse orientation of the wind stress vector in the coupled model result compared to Yasuda and Hanawa (1996) is consistent with the sign of the associated SST anomaly which is positive in the coupled model but a negative decadal difference was obtained in the observational study (see also fig. 4.5.a). Since the net heat flux pattern quoted from the same publication was also reproduced by the coupled model up to sign, we conclude that the climate shift around 1976 is identifiable in the coupled model in both dynamics and thermodynamics.

Wavelike propagating thermocline displacements are generally well approximated by considering only the lowest baroclinic modes. Simple models of ENSO (Cane et al., 1986, Schopf and Suarez, 1988) contain one or two baroclinic modes in the ocean component. The observational study of White and Saur (1983) found that along the San Francisco - Honolulu transect westward propagating interannual signals could be explained well by the gravest baroclinic Rossby mode. Propagating

thermocline anomalies due to low baroclinic modes lead to displacements in sea level which mirror the thermocline displacements. Based on coupled model simulations it has been proposed (Storch, 1994, Latif and Barnett, 1994) that long term variations in sea level in the extratropical North Pacific may include a strong quasi-cyclic basinscale mode. In a response experiment Latif and Barnett (1994) reproduce a pattern of 500 hPa height which resembles fig. 4.5.b of the present thesis, and the SST anomaly producing this response is largely similar to the SST pattern given in fig. 4.5.b. Further examining a coupled AOGCM simulation they find a cyclic evolution of upper ocean heat content represented by their leading complex empirical orthogonal function (CEOF) mode. The upper ocean heat content anomaly is a measure of thermocline disturbances essentially anticorrelated to sea level. Using lagged regression, Yukimoto et al. (1996) also find large scale coherent thermocline variation but with a somewhat different spatial structure and little sign of propagation.

Given a sufficiently long spatially extended sea level record, recurrent propagating signals can be analyzed statistically. The phase lag between any two locations can be captured by a complex-valued notation. At each grid point the recorded real-valued timeseries, formally written as

$$x(t) = \int_0^\infty [a(\omega)\cos\omega t + b(\omega)\sin\omega t]d\omega \qquad (5.4)$$

is associated with a complex-valued representation, the 'analytic signal', of the form

$$\xi(t) = \int_0^\infty \left[a(\omega)e^{-i\omega t} + b(\omega)e^{-i\left(\omega t - \frac{\pi}{2}\right)} \right] d\omega \qquad (5.5)$$

Equivalently, i times the Hilbert transform can be added to $x(t)$. If, similarly, one obtains a complex-valued representation of a given index timeseries then a regression analysis in the complex domain is possible. As in Principal Oscillation Pattern (POP) analysis (Hasselmann, 1988), the regression pattern has an imaginary part which leads the real part by a phase of 90°. For truly cyclic evolution, this corresponds to a quarter period, but this is a special case. Propagation with preferred orientation will nonetheless be captured by real and imaginary parts. This is used here to determine propagating features in sea level for the CT and NP modes.

Fig. 5.15 shows the complex regressions of sea level for the CT mode, respectively. A slowly propagating sea level anomaly is found about midbasin in the North Pacific. In contrast to this propagating feature, the tropics are characterized by a growing west-east contrast formed by the two strengthening off-equatorial lobes straddling the equator near the western boundary and a more or less triangular region of positive sea level anomalies with the outline running south-westward from the Californian coast, reversing on the equator at about 165° E to head south-eastward towards the coast of Chile. The region equatorward of 20° latitude, in particular the two west Pacific lobes, suggests an eastward spreading of anomalies but in the far west and in the eastern half the disturbances greatly amplify, and the amplification occurs in place.

The west Pacific pattern is reminiscent of well-known patterns of thermocline anomalies during canonical ENSO events (e.g., Barnett et al., 1993, Bacher et al., 1998). The excitation of equatorial Kelvin waves during the second half of a canonical ENSO year occurs by anomalous wind stress on

the equator close to the date line. In the off-equatorial regions containing the pair of lobes in fig. 5.15 there are contemporaneous westward moving disturbances generally identified as Rossby waves. Applying the paradigm of decadal ENSO signals associated with successive warm phases of greater amplitude the strength of downwelling Kelvin and upwelling Rossby signals should be enhanced along with the growing decadal signal. In each event in such a sequence, the Kelvin waves generated over the second half of the year radiate eastward at speeds given primarily by the first two baroclinic modes, implying that two to almost four months would be taken to fully traverse the Pacific basin. The continuous excitation from near the date line generates a stream of waves that via interaction with the eastern boundary cause poleward Kelvin wave propagation along the eastern boundary where Rossby waves separate and form a westward travelling front. The speed of westward propagation decreases with latitude and the increasing lag at subtropical latitudes with respect to the tropics leads to the triangular outline. The decadal scales considered now imply that more than one El Niño/ La Niña are effectively averaged and the residual thermocline and sea level anomalies on the equator are given by successive excitation of the eastern half of the equatorial waveguide. A similar effect is expected for the off-equatorial lobe regions where westward propagation characterizes the interannual signals. Wavelike propagation in the waveguide is therefore associated with timescales of months and the decadal residual does not reflect the detailed evolution. This explains why amplification of west-east contrast is predominantly found.

The triangular sea level anomaly in the east, evident in the real part of fig. 5.15, is in phase with the triangularly shaped warm anomaly in the SST pattern of fig. 4.2.b. This association, together with the anomalous heating by entrainment, fig. 5.7.a in part of this region, therefore strongly support the attribution of the decadal east/central Pacific warming to a residual ENSO effect with tropical/subtropical Rossby wave propagation contributing importantly, as in the simple ocean-dynamical calculation of Meyers et al. (1996). The complete Pacific basin sea level structure is consistent with the decadal ENSO paradigm which also explains the North Pacific response. It clearly differs from the Latif and Barnett (1994) pattern. More closely it resembles the result obtained by Yukimoto et al. (1996) for the decadal scale.

For the NP mode, the pattern (fig. 5.16) much more closely resembles the results of Storch (1994) or Latif and Barnett (1994). The cyclic propagation of upper ocean heat content that is captured in the leading CEOF mode for the coupled model of Latif and Barnett (1994) is analyzed by means of periodically forced integrations by Latif et al. (1996) and by coupling their OGCM to a statistical atmosphere model to obtain a hybrid coupling in Xu et al. (1998). The latter produce a self-sustained oscillation with a period of about 20 yr (control case, including wind stress feedback) which results primarily from the delayed baroclinic response of wind-driven currents to changes in the wind which by construction reacts to SST according to a linear relationship. Heat advection anomalies due to wavelike velocity perturbations then lead to modification of SST, and the basin geometry and the delayed response of the gyre circulation to wind changes involving baroclinic waves (Anderson and Gill, 1975) produce the oscillation. It should be noted that in this hybrid coupled model study the construction of the feedback relationship is based on 7 year low-pass filtered output from the run described in Latif and Barnett (1994). Propagating multiyear SST anomalies are found for that OGCM, similar to observed SST anomalies north of 40° N between 1953 and 1959 (Favorite and McLain, 1973). For the present simulation the dominant modes exhibit standing character in SST, and repeating the entire analysis from section 4.1, using a complex representation throughout, no propagating features emerged. For sea level fig. 5.16 suggests clockwise propagation around the

North Pacific. However, since the oscillatory character in the timeseries in fig. 4.4.b is aperiodic, no specific timescale for propagation is evident. In the simulation by Yukimoto et al. (1996) no strongly dominant timescale was present. While Storch (1994) found that this variability exhibited a red spectrum, Robertson (1996) using Multichannel Singular Spectrum Analysis (MSSA) found an oscillation with period of about 17 yr in a 700 year AOGCM run and two timescales, 6 yr, and 30 yr, in a 122 year version of the GISST dataset.

The possibility of using sea level data in the region of separation of the Kuroshio for predicting SST near the date line in the North Pacific at several years lead was indicated by Latif (1997) for a forced OGCM simulation using observed data for the period 1953 to 1988. It is demonstrated that anomalies in sea level originating in the boundary current region propagate eastward to modify SST near the date line. In our longer coupled simulation the imaginary and real parts indeed provide an indication of propagation but the real part is stronger than the imaginary part. This indicates that a positive feedback amplifies the phase in which SST anomalies are fully developed.

The above findings should be of importance in simple and analytic model approaches to explaining decadal variability in the North Pacific (Jin, 1997, Münnich et al., 1998). First, the decadal ENSO background evident in the coupled model CT mode is usually disregarded in these simple models. Yet, its influence on the North Pacific by atmospheric teleconnection is at least as strong as North Pacific variability in the NP mode (compare fig. 5.15 with 5.16). Second, for the NP mode in particular the spatial alignment of the wind anomalies and anomalous SST and the advective heat budget term are consistent with Sverdrup balance in line with several studies based on observations (Miller et al. 1997, Deser and Blackmon 1995, Yasuda and Hanawa, 1996). In Jin's (1997) analytical study, wind is assumed to coincide with regions of meridional SST gradient. The even simpler approach in Münnich et al. (1998) is to relate wind stress to thermocline anomaly in a particular region. Oscillatory behaviour only results if this region has less than basinwide extent but this assumption is not supported by our results. In particular, the in-phase contribution in fig. 5.16 is clearly basinwide. A final point is that the spectrum in fig. 4.6 exhibited no peaks above the red noise background whereas the simple models quoted above lead to spectra with peaks at decadal timescales. Thus, the findings of this thesis indicate that more complexity should be included in the simple and analytic models.

List of figures

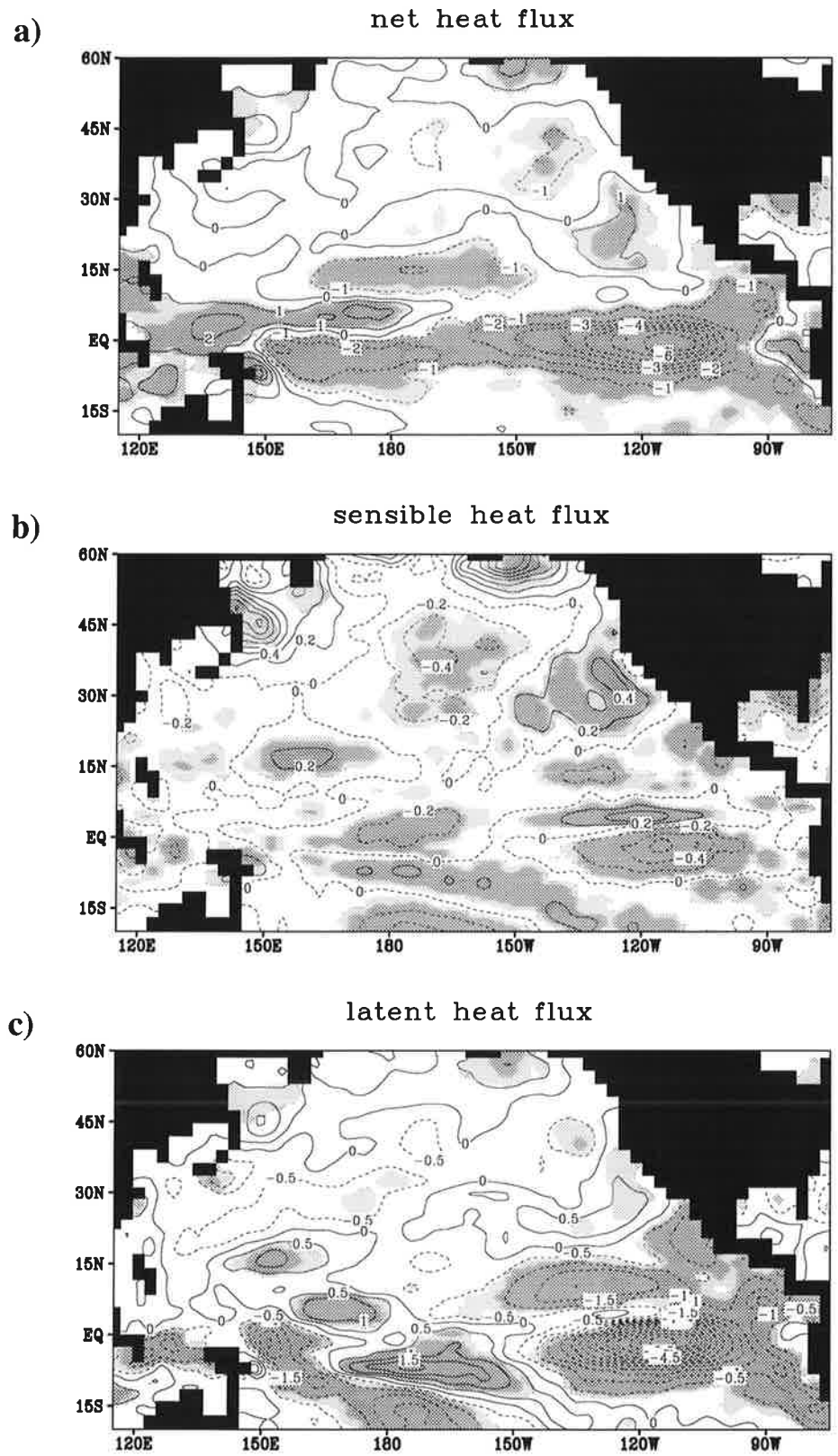

Fig. 5.1 Surface net heat flux and heat flux components regression on CT index. a) net heat flux, b) sensible heat flux, c) latent heat flux. Units: Wm^{-2}. Areas significant at the 5 % (1 %) significance level are represented by light (dark) shading.

d)

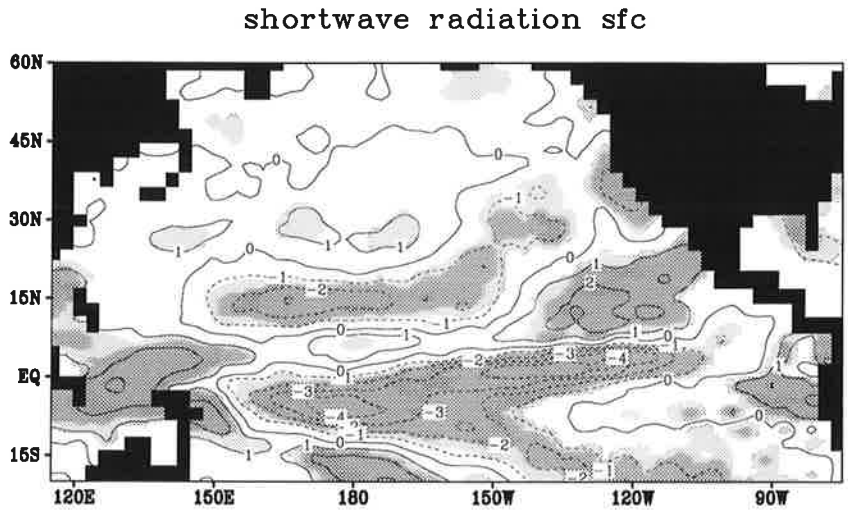

e)

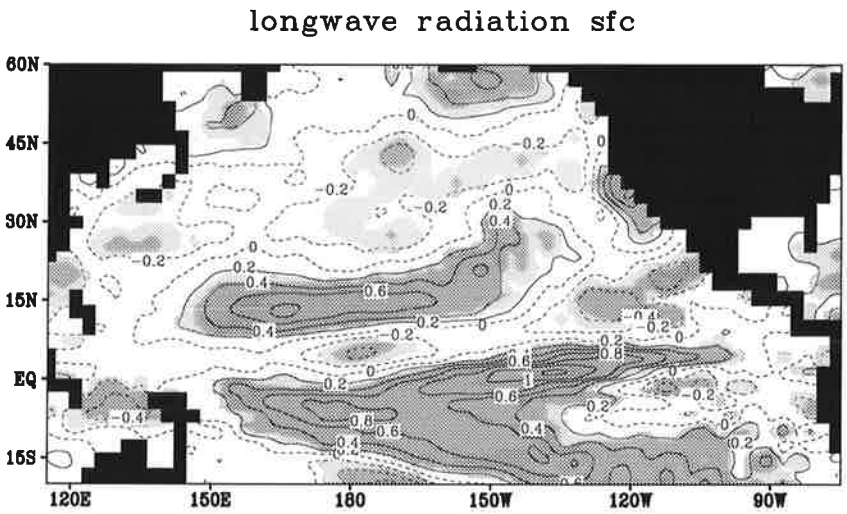

Fig. 5.1 (contd.) d) surface shortwave radiation, e) surface longwave radiation.

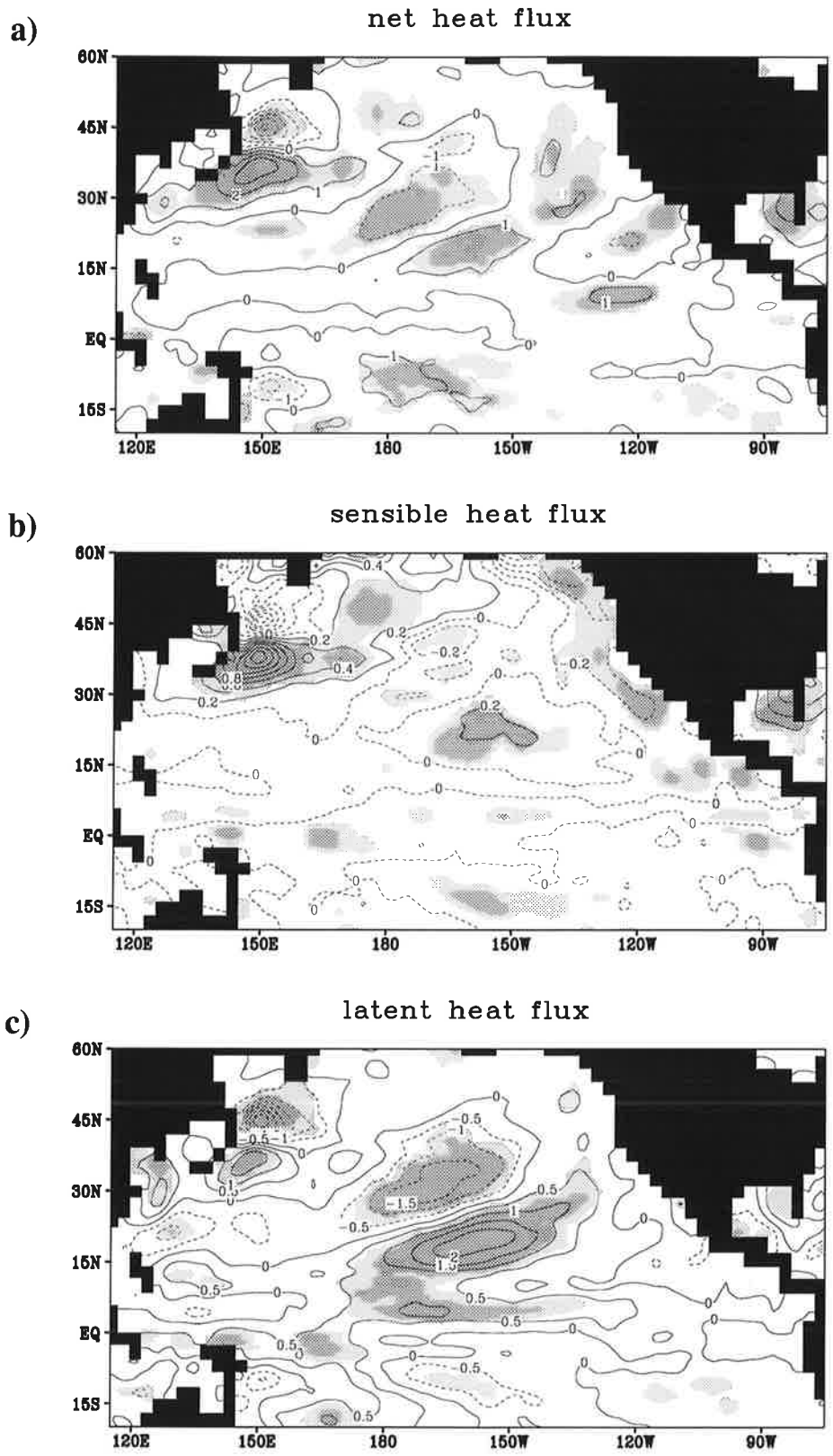

Fig. 5.2 Surface net heat flux and heat flux components regression on NP index. a) net heat flux, b) sensible heat flux, c) latent heat flux. Units: Wm^{-2}. Areas significant at the 5 % (1 %) significance level are represented by light (dark) shading.

d)

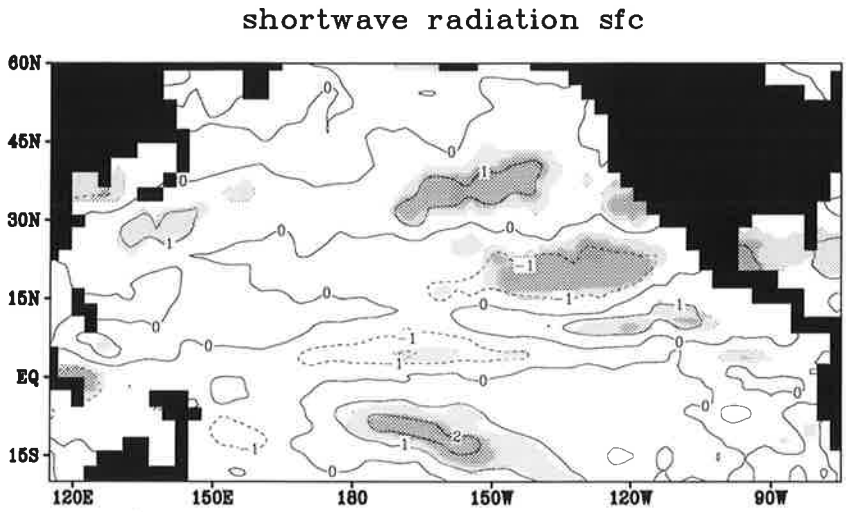

e)

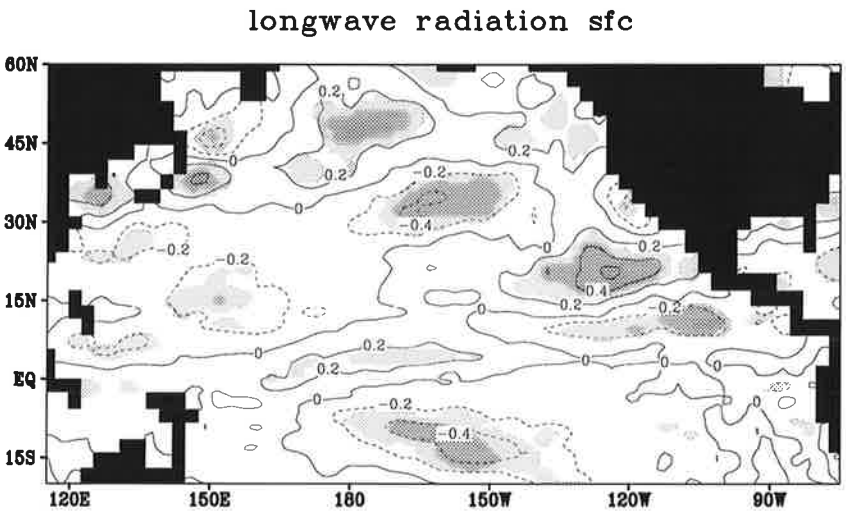

Fig. 5.2 (contd.) d) surface shortwave radiation, e) surface longwave radiation.

a)

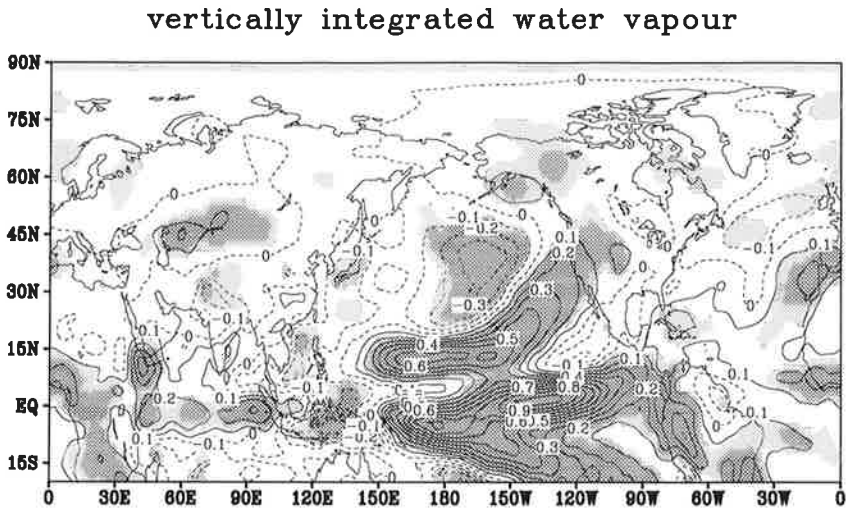

b)

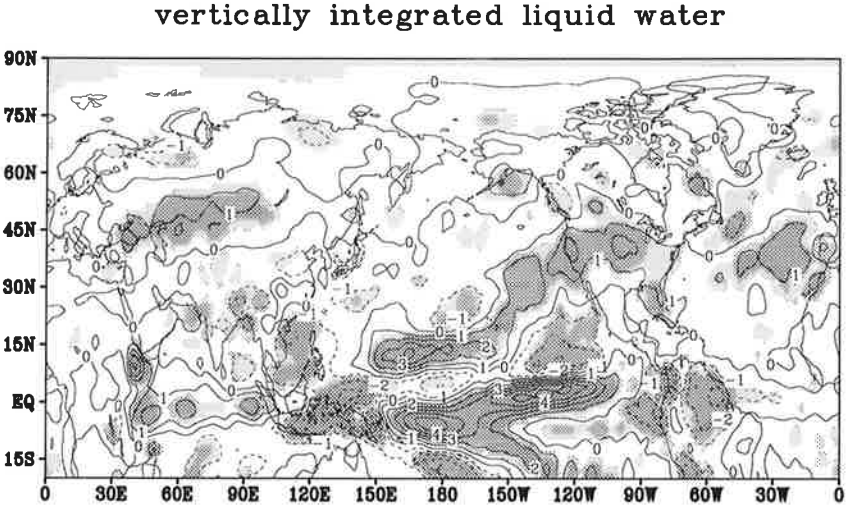

Fig. 5.3 Regression of moist variables on CT index. a) vertically integrated water vapour; unit: kgm^{-2} b) vertically integrated cloud liquid water; unit: gm^{-2}. Areas significant at the 5 % (1 %) significance level are represented by light (dark) shading.

a)

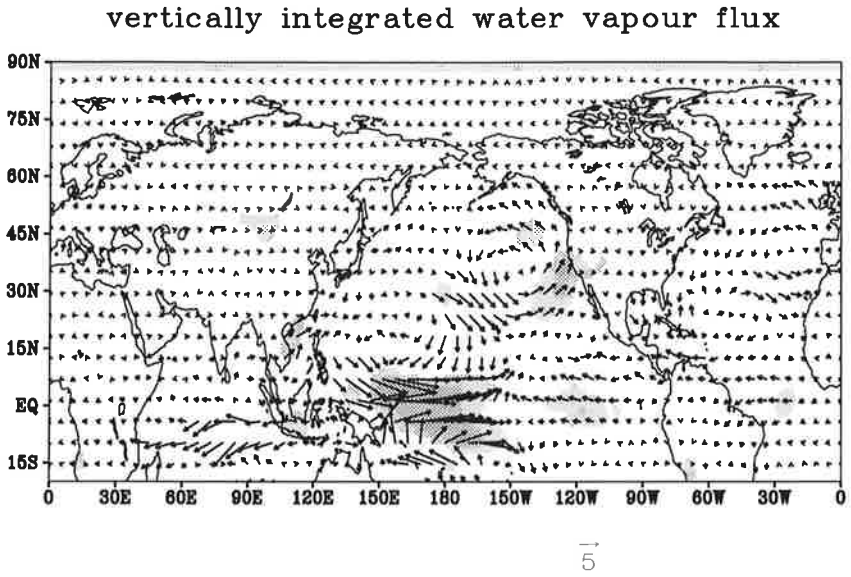

b)

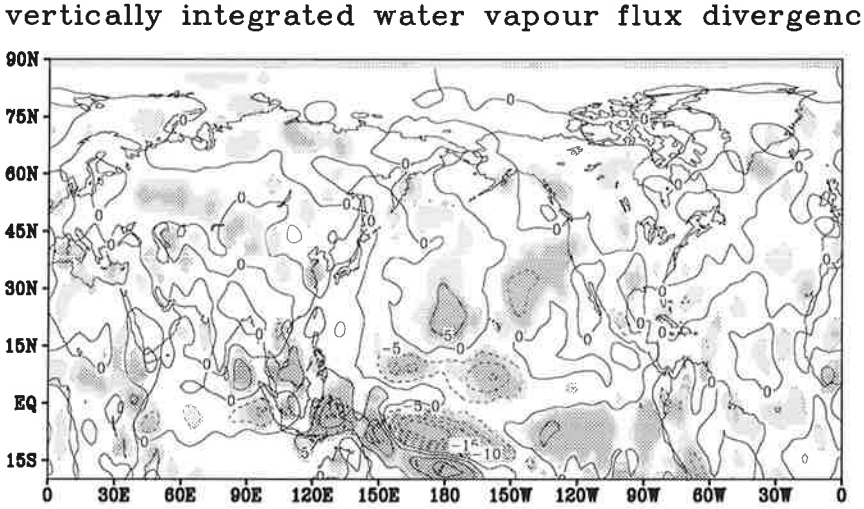

Fig. 5.4 Regression of moist variables on CT index. a) vertically integrated water vapour flux; unit: $kgm^{-1}s^{-1}$, b) vertically integrated water vapour flux divergence; unit: mmd^{-1}. Areas significant at the 5 % (1 %) significance level are represented by light (dark) shading.

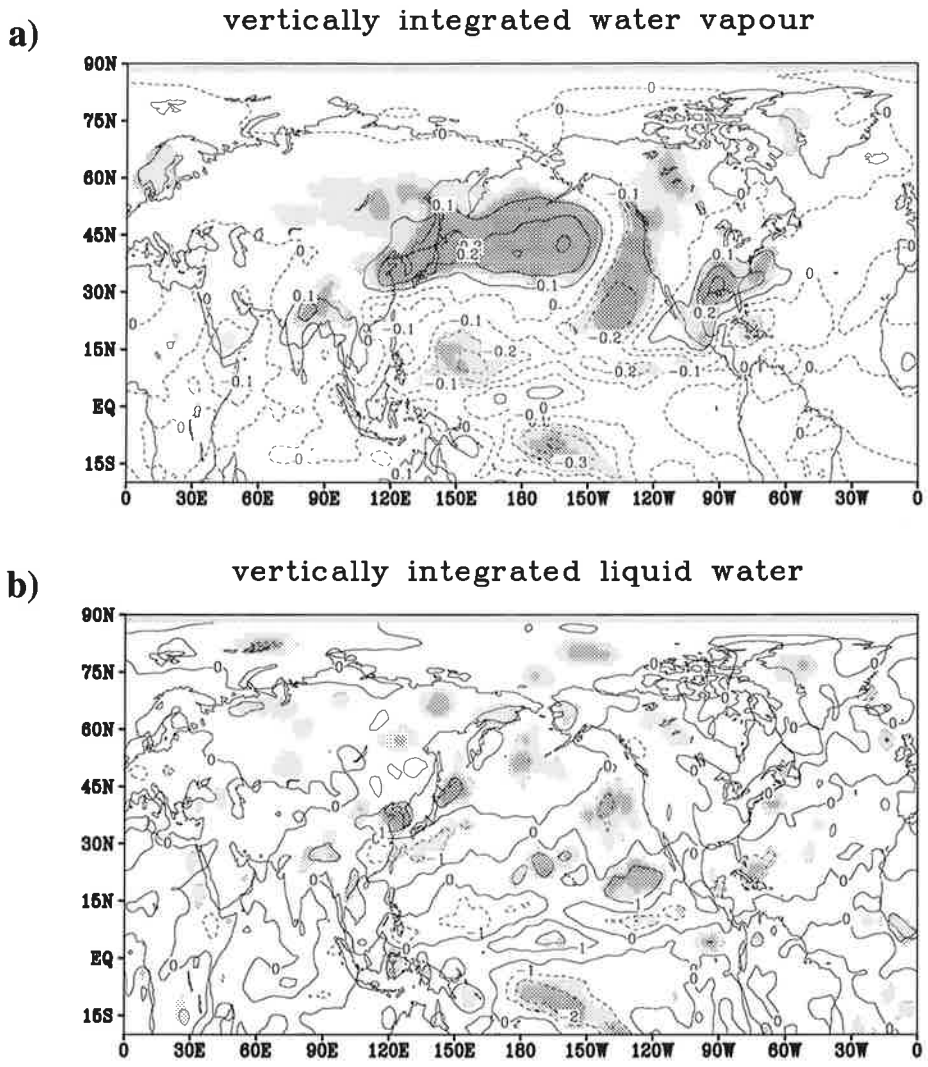

Fig. 5.5 Regression of moist variables on NP index. a) vertically integrated water vapour; unit: kgm^{-2} b) vertically integrated cloud liquid water; unit: gm^{-2}. Areas significant at the 5 % (1 %) significance level are represented by light (dark) shading.

a)

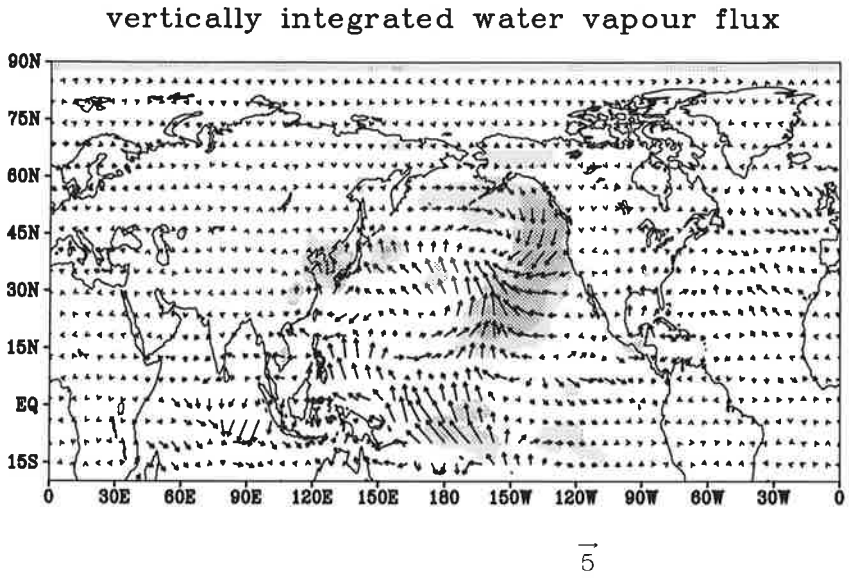

b)

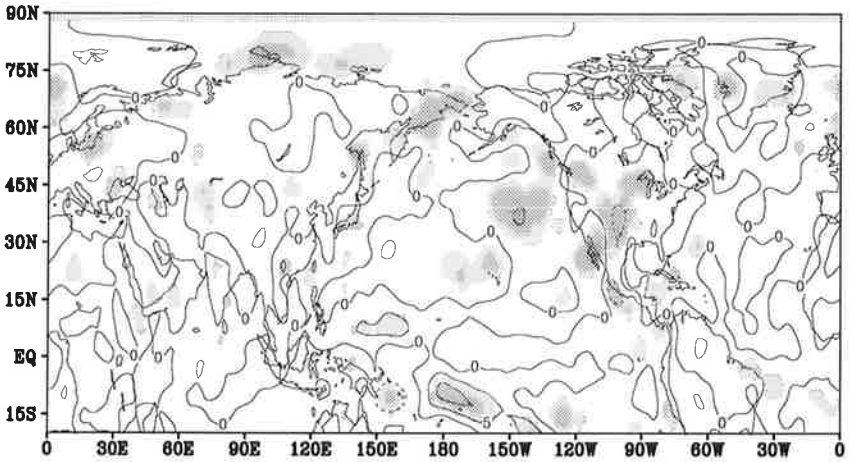

Fig. 5.6 Regression of moist variables on NP index. a) vertically integrated water vapour flux; unit: $kgm^{-1}s^{-1}$, b) vertically integrated water vapour flux divergence; unit: mmd^{-1}. Areas significant at the 5 % (1 %) significance level are represented by light (dark) shading.

a)

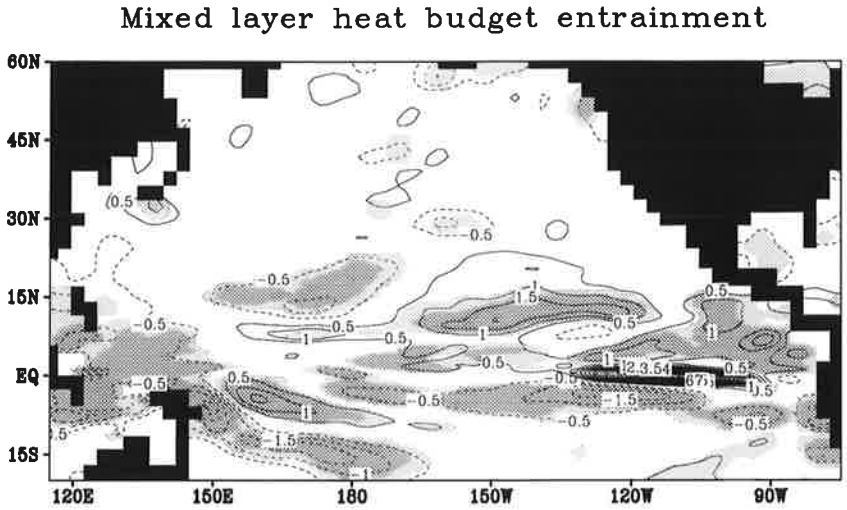

b)

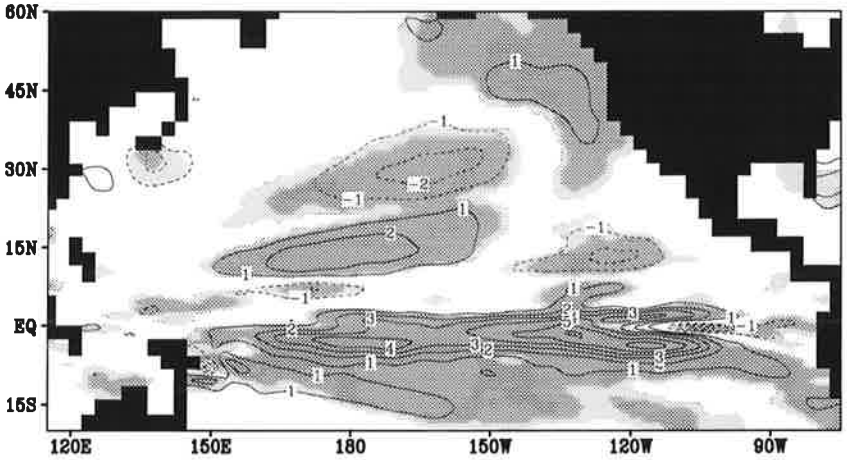

Fig. 5.7 Regression of mixed layer heat budget contributions on CT index. a) entrainment, b) advection. Unit: Wm^{-2}.

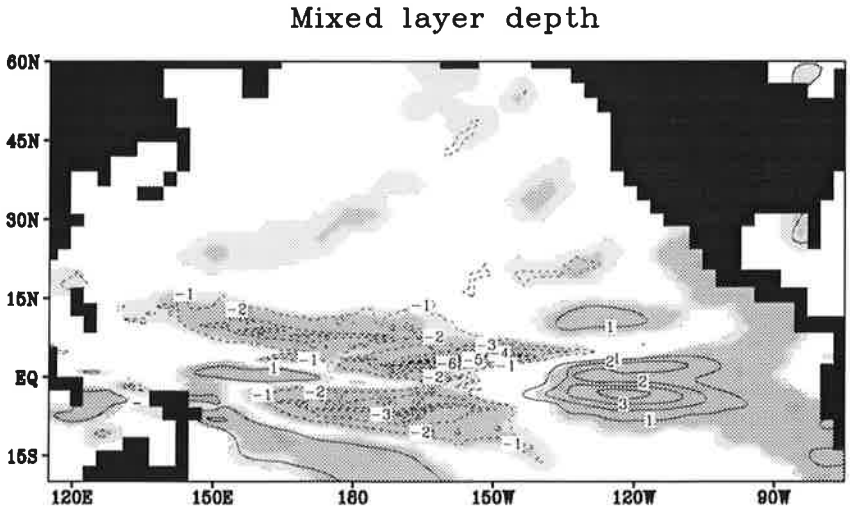

Fig. 5.8 Regression of mixed layer depth on CT index. Unit: m

a)

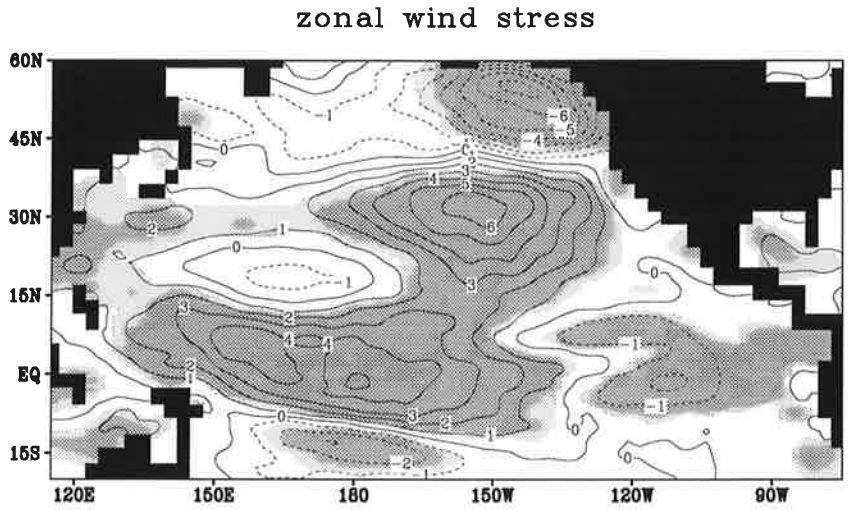

b)

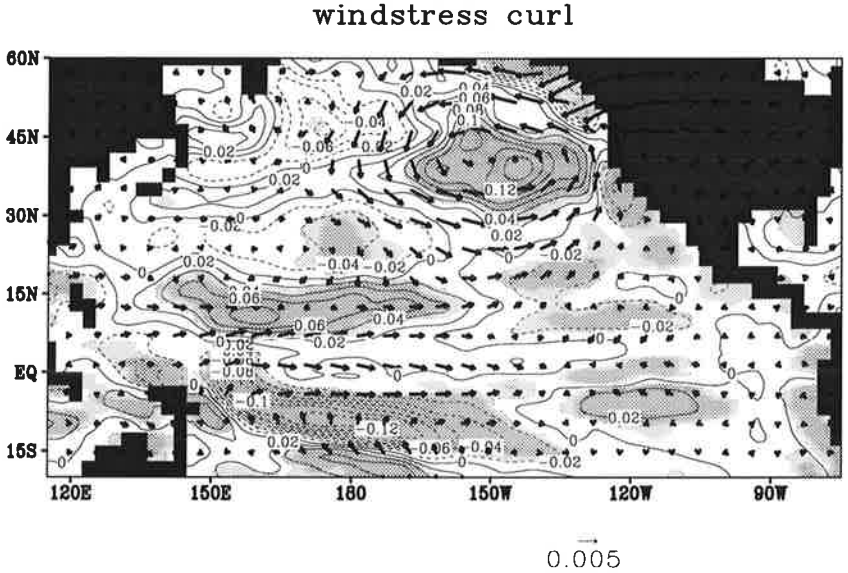

Fig. 5.9 Regression of zonal surface wind stress component, a), and both wind stress vector and curl, b), on CT index. Unit: Nm^{-2} (zonal wind stress has been multiplied by 10^3, curl by earth's mean radius, 6378 km)

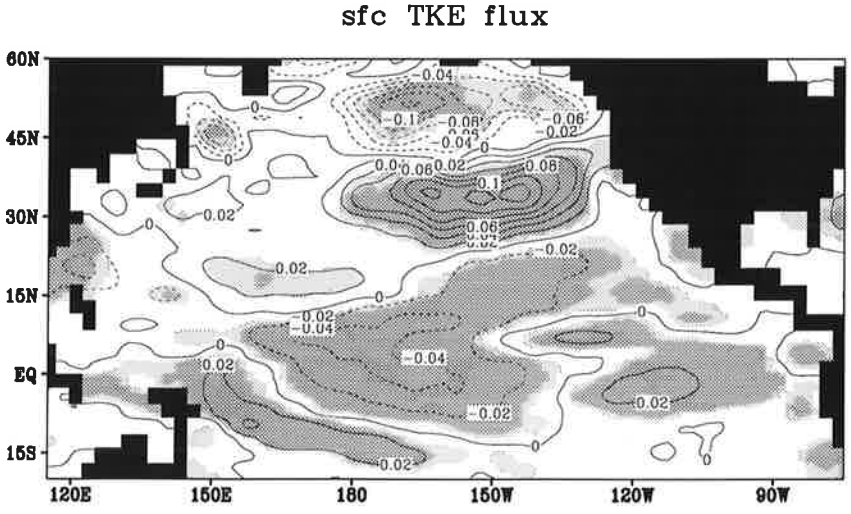

Fig. 5.10 Regression of cube of friction velocity on CT index. Unit: $cm^3 s^{-3}$

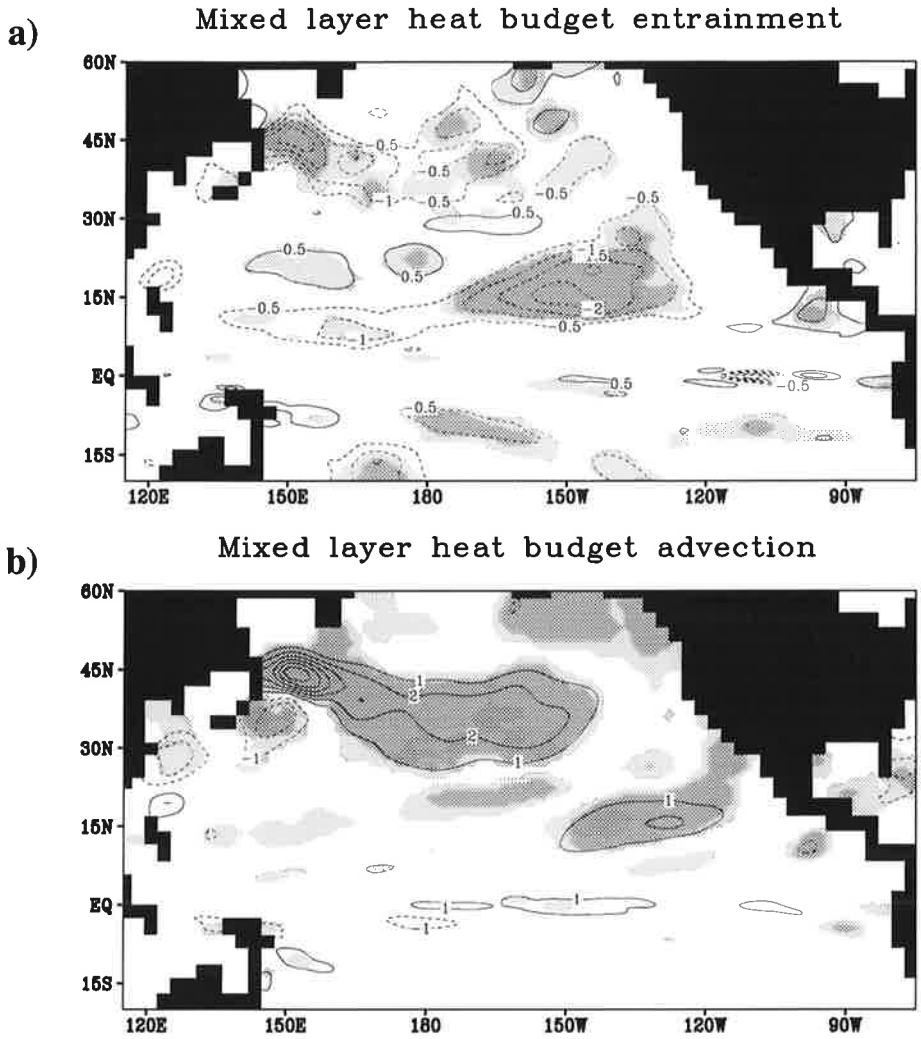

Fig. 5.11 Regression of mixed layer heat budget contributions on NP index. a) entrainment, b) advection. Unit: Wm^{-2}.

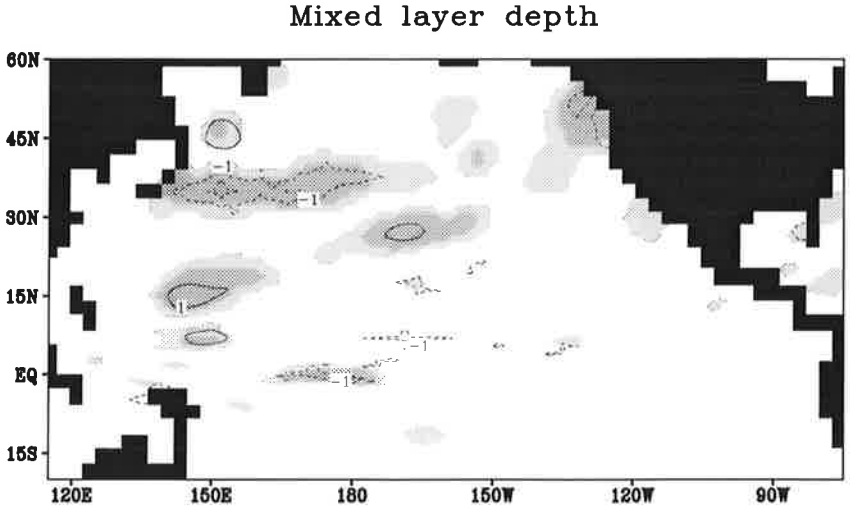

Fig. 5.12 Regression of mixed layer depth on NP index. Unit: m

a)

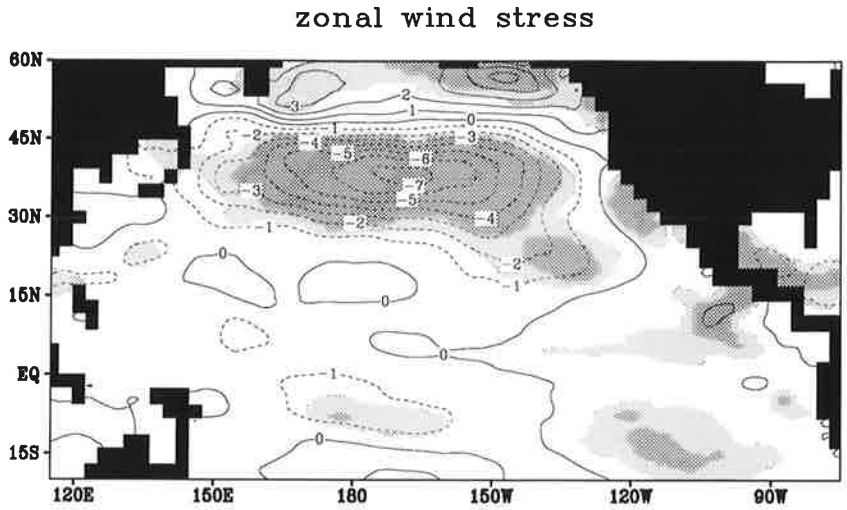

b)

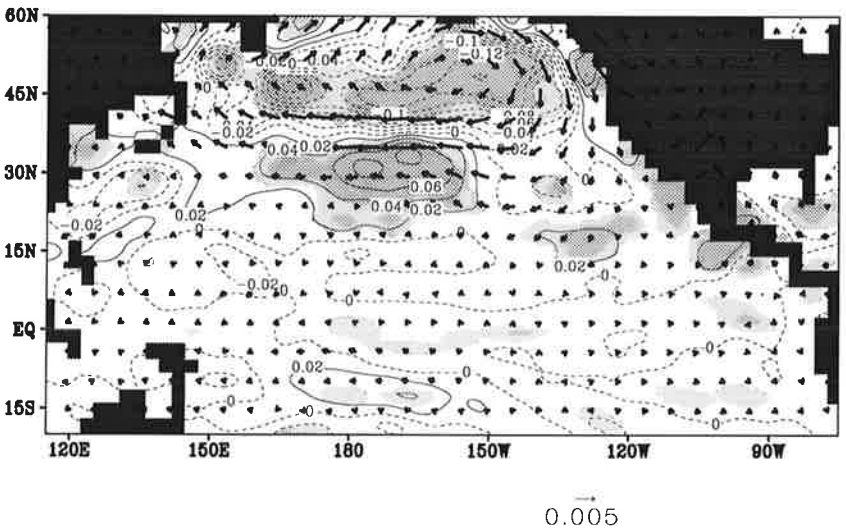

Fig. 5.13 Regression of zonal surface wind stress component, a), and both wind stress vector and curl, b), on NP index. Unit: Nm^{-2} (zonal wind stress has been multiplied by 10^3, curl by earth's mean radius, 6378 km)

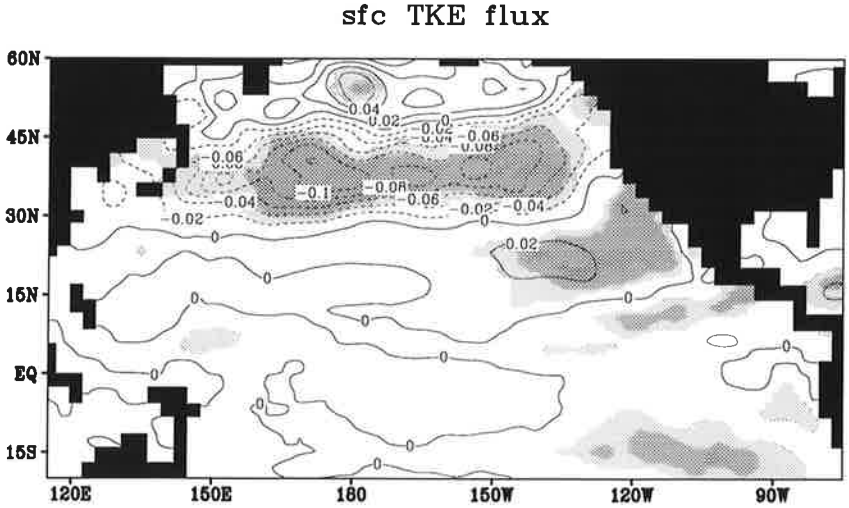

Fig. 5.14 Regression of cube of friction velocity on NP index. Unit: $cm^3 s^{-3}$

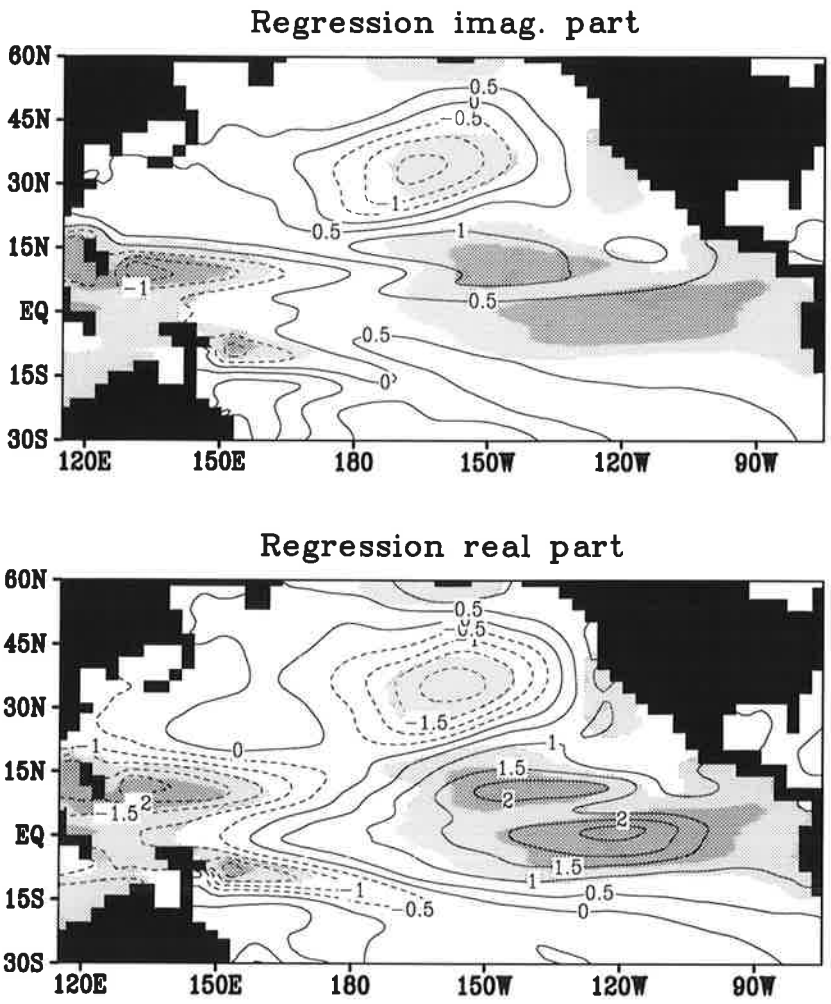

Fig. 5.15 Complex regression of sea level on the analytic signal associated with the CT index . The imaginary part leads the real part by 90° but this phase relationship cannot be specified in the form of a well-defined time interval. This is strictly possible only for periodic signals. Unit: cm

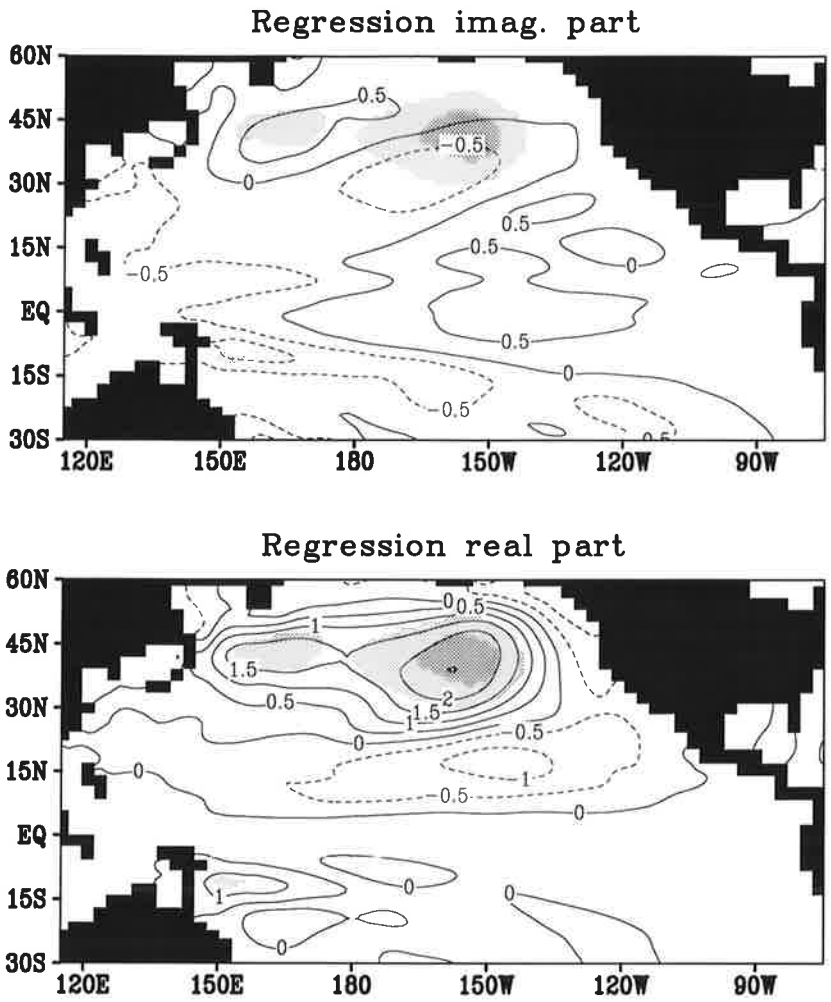

Fig. 5.16 Complex regression of sea level on the analytic signal associated with the NP index . The imaginary part leads the real part by 90° but this phase relationship cannot be specified in the form of a well-defined time interval. This is strictly possible only for periodic signals. Unit: cm

Chapter 6

Summary and concluding remarks

The work presented in this thesis consisted of both practical development work and analytical investigation of a run with the coupled climate model ECHAM4/OPYC3. The practical aspect was a contribution to the coupled model and involved the development of a coupling interface by the author. The technical portion which is innovative in coupled climate modelling is the core portion of this interface. It consists of a regridding scheme for transferring the surface fluxes computed over ocean areas by the atmosphere model from the computational grid used in the ECHAM4 model to the higher resolution grid used in the ocean model OPYC, and for the reverse mapping for the sea surface temperature simulated by the ocean model. While the meshwidth refinement strategy employed in the present interface is a common element in numerous computational problems, particularly in the field of Computer Aided Geometric Design (CAGD), for the present purpose original code was developed for the computational environment present at the Deutsches Klimarechenzentrum (DKRZ). An essential feature of this code is the handling of an irregular computational domain given by only the ocean gridpoints in the atmospheric and oceanic models, as well as the implementation of a free boundary condition at the latitudinal extremities of this domain. The structure of the code was laid out to provide computational efficiency on vector pipeline machines, such as the Cray C90 employed for the computations on which the scientific results of this thesis are based.

The climate simulated by the coupled model closely resembles the uncoupled simulation discussed in Roeckner et al. (1996b). Zonal mean temperature and zonal wind were virtually identical between the coupled and uncoupled runs. For 500 hPa height there was a very slight reduction (2 gpdam) in the positive bias over high latitudes. Precipitation in the coupled model was slightly closer to the climatology of Legates and Wilmott (1990). The proper alignment of areas of deep convection and the seasonal cycle of precipitation over the warm pool could be understood by the success in simulating the extent of the area with SST exceeding the value of 27.5° C which Graham and Barnett (1987) quote as a threshold for deep convection. While the seasonal evolution is simulated with success apart from a phase error of one to two months for the warm pool seasonal cycle, annual mean conditions are constrained by the heat- and freshwater flux adjustment. The surface heat fluxes are generally well within the observational uncertainty with respect to the Oberhuber (1988) climatology. Wind stress, compared to the data from ECMWF reanalysis, quantitatively agrees well over the North Pacific, while the trades, particularly the south eastern trades in boreal summer, are overestimated with a substantial error magnitude on the equator. Mixed layer thicknesses predicted by the ocean model for March and September exhibit reasonable quantitative agreement with the estimates given by Levitus (1982); similar success is found for simulated sea ice cover except for the underestimation of the maximum Antarctic sea ice extent. Despite a successful alignment of the tropical thermocline and currents and capturing of some observed seasonal surface current variation, equatorial currents are artificially broadened and reduced in mean speed. The vertical structure of the main thermocline is evident in satisfactory temperature and salinity distributions.

The analysis of climate variability associated with large scale anomalous sea surface temperatures (SST) of the Pacific Ocean on decadal scales largely produced results comparable with other coupled

modelling studies (Storch, 1994, Latif and Barnett, 1994, Yukimoto et al., 1996). Two decadal modes of variability are dominant in the low pass filtered anomalous SST which exhibits irregular temporal variability but are associated with patterns of SST anomalies which are similar to the leading patterns extracted from an integration of the atmospheric model with SST prescribed from the GISST 2.2 dataset (Parker et al., 1995). One of these patterns is linearly associated with the decadal variability of the oceanic cold tongue ('CT') in the eastern equatorial Pacific, represented by the mean SST anomaly in the NINO3 region. Compared to the familiar structure for the El Niño/Southern Oscillation (ENSO) phenomenon it is less dominated by the variability in the cold tongue itself. Instead there is a stronger contribution from the off-equatorial tropical and subtropical Pacific such that a more or less triangularly shaped area is associated with the decadal ENSO. The other pattern is temporally uncorrelated, the variability exhibits an intrinsically decadal scale, although the power spectrum exhibits no peaks above the red noise background. This pattern is characterized by a zonally oriented anomaly across the Pacific underneath the stormtrack and two enhanced centres in the central eastern and in the western North Pacific towards Japan. The subtropical and tropical Pacific for this pattern exhibited oppositely signed anomalies, but in the cold tongue this mode is not responsible for substantial variability. Some similarity to the horseshoe type anomaly discussed, e.g., by Latif et al. (1997) was found. The patterns extracted from the coupled and similarly from the uncoupled simulation resemble those found in independent studies (e.g. Deser and Blackmon, 1995).

Each mode of SST variability is linearly associated with an anomalous circulation pattern, with significant PNA contribution in both. The mode given by the residual (obtained after removal of ENSO-related variability) exhibits a strong North Pacific centre of the PNA, implying that its time dependence is well captured by a North Pacific (NP) index similar to the one defined by Trenberth and Hurrel (1994). In the cold tongue (CT) mode related pattern of 500 hPa height a Southern Oscillation contribution was evident. These two indices both contribute to decadal SST variability over the North Pacific. Whether or not SST anomalies contribute significantly to the anomalous circulation is an open question for midlatitude SST anomalies.

The correlations between surface heat fluxes and SST are generally negative, a result that was anticipated after the GCM experiments by Lau and Nath (1994) who considered tropical as well as midlatitude cases of SST variation. Their results for El Niño type SST anomalies are largely reproduced. That is, the feedback deduced from regressing surface heat fluxes is largely negative and a pronounced response mainly occurs in the tropics. A key difference is that in the off-equatorial tropics there is a negative feedback dominated by shortwave radiative flux which occurs in the area of the main route for water vapour flux from the subtropical anticyclone towards the area of deep convection. The off-equatorial flank of the triangularly shaped SST anomaly modifies convergence in the PBL such that one expects an increased amount of midlevel convection which leads to this negative shortwave radiative flux feedback. In the tropics the negative feedback by shortwave radiation is associated with deep convection. The longwave radiative flux, apart from being about a factor of four smaller in magnitude, forms a mirror image of the shortwave flux. In the cold tongue region the negative heat flux feedback is dominated by latent heat flux. Only a small region in the eastern subtropical North Pacific exhibits a positive feedback by shortwave radiation. In this region which exhibits similar behaviour for the NP mode, the reason is a reaction of stratus to modulation of the cold water area generated by offshore Ekman drift of coastally upwelled water. Diminished stratus implies increased insolation of the sea surface and an enhancement of the Ekman induced warming. This occurs similarly in the case of the NP mode. For this mode, however, positive feedback through sur-

face heat fluxes essentially only occurs in the area of separation of the Kuroshio western boundary current where sensible and latent heat fluxes provide the dominant contribution. This spatial confinement is in contrast to results for SST anomalies persisting for one season by, e.g., Luksch and von Storch (1992) who describe the positive feedback by turbulent fluxes due to cold air advection by a strengthened Aleutian low caused by anomalously cold SST. For generating the large-scale SST anomaly associated with the NP mode, other terms in the heat budget of the surface mixed layer must be considered.

Analysis of the terms in the mixed layer heat budget indicated the role of dynamical and vertical exchange contributions. Warm CT mode SST anomalies are associated with advective heating on the equator which could be explained by anomalous lateral convergence. This is consistent with equatorial downwelling associated with a lowering of the equatorial thermocline particularly in the east which normally occurs during the ENSO warm phase. On the decadal scale, however, the net effect of more than one El Niño/La Niña cycle appears as a residual downward displacement of the thermocline. This is consistent with the net positive SST anomaly on the decadal scale. The lowering of the equatorial thermocline by Kelvin waves during one El Niño warm phase generally leads to the generation of a coastal Kelvin wave signal which propagates poleward but in turn causes separation of a westward propagating Rossby wave front. The latter, due to the latitudinal dependence of the Rossby wave speed, propagates fastest at low latitudes such that the lowering of the thermocline affects a more or less triangular region. Successive El Niño cycles may lead to a net effect in the form of a triangular thermocline depth anomaly that dominates the SST anomaly by a reduction in the cooling caused by entrainment at the base of the mixed layer. This is a consequence of the warmer subsurface water in connection with the lowered thermocline. It is plausible that the phase lags induced by the propagation speeds in the equatorial waveguide and for poleward and westward propagation may lead to complicated time dependence of the SST with decadal components. Results consistent with these ideas were obtained in the forced simulation by Jacobs et al. (1994) and from the simplified ocean dynamical calculation by Meyers et al. (1996). The spatial structure found for the entrainment/detrainment heat budget contribution in our model was partly consistent with the thermocline mechanism. In the North Pacific a response was obtained which closely resembles the familiar ENSO response. Thus there is a cold anomaly near 150° W at about 35° N which is explained by anomalous advection due to rerouting of flow in the eastern part of the Kuroshio extension by Ekman drift. The thermocline integrated heat transport by Sverdrup balance could be inferred to cause heat content changes of the same sign as the SST changes. This was confirmed by the anomalous wind stress curl linearly explained by the decadal CT index.

For the NP index little signal was obtained in the equatorial region. Similar to the CT variability, the dominant contribution to the anomalous heat budget in the off-equatorial tropics is the entrainment term. The tropical/subtropical SST pattern as well as the associated entrainment pattern occur in a triangular domain. The effect of the entrainment at midlatitudes, however, is not to enhance but to damp the anomalous SST. Again the enhancement of SST anomalies is due to the advective heat budget contribution which for the NP mode was consistent with northward dsplacement of the Kuroshio extension across the entire North Pacific due to anomalous Ekman drift. The relationship between Ekman and Sverdrup transport anomalies and SST changes was found to be analogous to that in the CT mode, as evident from the pattern of wind stress curl.

The role of surface wind driving anomalous currents associated with the CT and NP modes is con-

sistent with these simple conceptual dynamics. The CT mode related anomalous wind stress pattern, particularly for the zonal component, resembles independent observational findings (da Silva et al., 1994) and was consistent with the concept of a residual from averaging over several swings of the Southern Oscillation. If in a succession of more than one event the canonical ENSO wind pattern (Rasmusson and Carpenter, 1982) occurs with successively weakening easterlies over the Maritime Continent and strengthening westerlies on the equator near the date line, the averaging will result in a residual which exhibits westerlies from Indonesia into the Central Pacific. The North Pacific wind anomalies likewise are explained by the familiar ENSO response. Most naturally such evolution can be ascribed to a decadal background of cold tongue SST variability on which the faster El Niño peaks (and La Niña valleys) are superimposed. For the NP mode the wind stress pattern is dominated entirely by a zonally oriented easterly anomaly across the Pacific overlying the warm North Pacific SST anomaly. A tropical contribution was not evident for this mode.

The decadal thermocline variations that are expected to be linked to the CT related SST variability are evident in the equatorial portion of the advective mixed layer heat budget contribution. Since baroclinic modes apart from the thermocline also displace the sea surface a complex regression of sea level onto the CT index confirmed that residual variability was present after averaging over more than one ENSO. The North Pacific response exhibited an anomaly of opposite sign and similar extent as the SST anomaly but with slow eastward propagation. It does not resemble the structure found by Latif and Barnett (1994), but has similar shape as the anomalies in the model of Yukimoto et al. (1996). By contrast the complex valued sea level pattern associated with the NP mode is similar to the result of Latif and Barnett (1994) as well as the result obtained by Storch (1994) for a longer coupled integration. A periodicity which could have aided long term prediction is not associated with the NP index. Evidence for eastward propagation is present and therefore in principle support was obtained for attempts to predict anomalous North Pacific SST near the date line from sea level evolution near the western boundary (Latif, 1997). However, the in-phase contribution to the sea level pattern given by the real part is much stronger than the imaginary part associated with a lead of several years; if signals amplify during propagation this may be difficult to predict. Details of these decadal fluctuations should be discussed theoretically, and a comprehensive investigation - by means of both forced and coupled simulations and a simple dynamical model - could be made. Several recent studies attack the problem of midlatitude decadal variability in the Pacific with simple dynamical models (Jin, 1997, Münnich et al., 1998). In these models, however, the presence of a forced response to tropical variability which appears in our coupled simulation as CT related variability is not taken into account.

The vertical structure of circulation changes associated with the CT and NP modes was examined for two meridional sections at 160° E and 160° W. In the section representing the eastern half of the Pacific both modes exhibits similar modifications near the exit region of the East Asian jet. Out of phase anomalies are evident close to 35° N and 55° N. An equivalent barotropic structure is found with maximum amplitude near 200 hPa. A difference is evident in the equatorial trough where for the NP mode there is hardly any substantial contribution found. By contrast, for the CT mode an out of phase variation of winds at 850 hPa and 200 hPa is found which is indicative of changes in the Walker circulation associated with tropical SST variability. This tropical signal is also evident in the western Pacific. The west Pacific section exhibits the second major difference between the CT and NP modes which concerns the extratropical Northern Hemisphere circulation. While in the CT mode the signal is only found in the section at 160° W, in the NP mode there is less than a factor of two

between the east and west Pacific anomalies. Wind anomalies for both modes are consistent with the changes in surface wind while their vertical structure is consistent with thermal wind balance, as expected.

The CT mode anomalies are evidently consistent with forcing by the ENSO background whereas for the NP mode the confinement of circulation anomalies to the extratropics and the zonality in patterns of wind and SST and tendency terms points to a different mechanism for generating this variability. It was noted in the study by Ting et al. (1996) that decadal variability apart from the portion related to an index equivalent to the cold tongue index also exhibited a significant contribution related to a zonal index given by the difference of 200 hPa zonal wind anomalies at 35° N and 55° N. While possibly the midlatitude SST anomaly is essential in generating the NP mode, the SST might also simply respond to intrinsic variability of the atmosphere. Results in support of a purely passive ocean in recent work include Battisti et al. (1995) while the alternative view found support in the response obtained by Latif and Barnett (1994) for an SST anomaly similar to our NP related one. If intrinsic atmospheric variability is the source then the SST can be expected to adjust to this forcing and therefore reduce the damping of circulation anomalies. On seasonal scales this is established by reducing the surface heat flux anomaly, and it leads to an increase in persistence of flow patterns predetermined by the atmosphere (Bladé, 1997). On the decadal scale it was found here that, similar to recent modelling and observational work (Miller et al., 1997, Yasuda and Hanawa, 1996) the response of wind-driven currents to imposed wind stress is crucial in magnifying the SST anomaly. The increase in persistence on seasonal scales therefore also applies to the decadal scale but the dominant mechanism is different. Whether a remote response of central North Pacific SST due to thermocline displacements which propagate with decadal basin-crossing times was significant and could modify the atmospheric circulation, is not determined fully by the above sea level analysis. This would be the case for the propagation of a thermocline anomaly as in Latif and Barnett (1994) or in simple models, e.g. Münnich et al. (1998). The possibility to predict decadal circulation changes on the basis of measurements or model calculations for vertically integrated temperature or sea level has thus not been examined in detail in the present thesis.

In several respects the coupled simulation proves a useful analog of the real world. The NP mode related patterns closely resemble observational findings regarding the mid-seventies climate shift, such as in Namias (1979) for SST (compare also the results for ECHAM4 forced with GISST SSTs in this thesis), Trenberth and Hurrel (1994) for sea level pressure, Yasuda and Hanawa (1996) for net surface heat flux and surface wind stress. Moreover the coupled model simulates these patterns at the same variance level as in the GISST observations. This probably is attributable to the relatively high resolution, T42, in the climate model which allows a realistic simulation of the transient eddies which are expected to influence the generation of circulation anomalies as discussed by, e.g., Trenberth and Hurrel (1994), an aspect not considered in the present thesis. The ocean simulation, despite using the coarse resolution common in climate simulations, reproduces the SST variability on the interannual and decadal scale that excites an atmospheric response similar in strength to integrations with the uncoupled model forced by prescribed SST. The realistic strength of the atmospheric response to tropical SST anomalies which is an important achievement of the present model (Roeckner et al., 1996a) is important for assessing the role of tropical forcing in the generation of decadal extratropical decadal variability. Our results indicate that, while the response to the decadal ENSO background in the extratropics (e.g. Nitta and Yamada, 1989, Graham, 1994) is substantial, extratropically generated variability, whether due to an active role of ocean dynamics according to Latif

and Barnett (1994) or intrinsically generated by the atmosphere but with persistence prolonged by the ocean (Bladé, 1997), is more likely to account for climate anomalies such as the mid-seventies climate shift. Work by Storch (1994), Latif and Barnett (1994), Robertson (1996), Yukimoto et al. (1996), and others already indicate the usefulness of coupled models in studying the variability related to the climate shift. The present model which was also used to perform transient experiments could provide additional insight into the dynamics and predictability of such climate anomalies.

Acknowledgements

Gratitude is expressed to Prof. L. Bengtsson for making work on this doctoral thesis possible at the Max Planck Institute for Meteorology. He provided significant input to the present research, through his responsibility for the established circulation model at the institute, and, more directly, by critical comments and helpful suggestions. The opportunity for attendance at an ocean dynamics conference in Cambridge and a visit to the Scripps Institution of Oceanography is gratefully acknowledged.

To Dr. E. Roeckner I am grateful for the opportunity to work on the present topic. The atmospheric circulation model used in this thesis draws strongly on his parameterization work. Comments on cloud radiative interactions and their thermodynamic role over the tropical Pacific ocean have motivated and aided this thesis. Collaboration in the context of the coupled model was essential for a successful completion.

Dr. J.M. Oberhuber is thanked for supplying the oceanic general circulation model used in the present thesis and for active user support. Close co-work on the oceanic aspects of the coupled model, as well as numerous comments and fruitful discussions on the dynamics of equatorial oceans and thermocline problems are gratefully acknowledged. He is thanked for carefully reading the manuscript.

My colleagues in the climate modelling group are thanked for numerous scientific conversations. More individuals than could be listed completely have been helpful and a source of motivation. Dr. I. Kirchner tended the coupled spinup run for determining flux adjustments. Mr. U. Schlese and Mrs. M. Esch were the essential backup regarding work with the ECHAM code. Dres. H.F. Graf, M. Latif, M. Münnich, T.P. Barnett, N. Schneider, A.J. Miller, X. Zhang, Z. Hu, U. Luksch, R. Voss, M. Giorgetta made stimulating comments at various stages.

To my parents and my family I am grateful for all support that benefited this work through the entire course.

This research was supported by the Bundesminister für Bildung und Forschung (BMBF), grant No. 07VKV01/1, integrated within project 'Klimavariabilität und Signalanalyse'.

Appendix A

Numerics of thermal diffusion in the two layer sea-ice/snow cover system for the coupled ECHAM model

The numerical treatment of thermodynamics and snow accumulation for sea ice was pioneered by Maykut and Untersteiner (1969). Semtner (1976) developed a simplified approach using three layers, one representing snow cover, the other two comprising the ice slab. Semtner used a system of coupled prediction equations for the assumed piecewise linear temperature profile with boundary condition given by the temperature of water in contact with the ice at its bottom and the atmospheric heat flux at the top of the snow. In the OPYC model, a two layer sea ice/snow cover system for thermal diffusion is used (Oberhuber 1993b). As opposed to Semtner (1976), the OPYC scheme includes no brine pocket parameterization. A further difference consists in the vertical arrangement of the point values of predicted temperatures of snow and ice. While Semtner's (1976) three layer model uses midlayer temperatures, implying the need for an additional top temperature for the specification of the upper boundary condition, the OPYC scheme predicts two temperatures, at the interface of snow and ice and at the top of the snow. In the OPYC scheme, a piecewise linear temperature profile applies between the snow-ice interface and the snow top. The identical temperature gradient at both the top and bottom of the snow layer induces a problem of interpretation since the product of conductivity and vertical temperature gradient defines thermal diffusive (or 'conductive') flux and therefore the flux difference between the top and the bottom of the snow layer, if derived from the profile, is zero.

To circumvent this problem, the approach developed by the present author allows for a variable vertical temperature gradient through the snow layer, and similarly the sea ice layer. No brine pockets are considered, and the simplest form of vertical temperature dependence consistent with the variable gradient is assumed which implies a piecewise quadratic temperature profile.

In addition to the notation used in chapter 2, we denote the vertical coordinate as z . The bottom and top of the ice layer are denoted as z_w , z_i , respectively. The top of the snow layer is at z_s . Thermal conductivities for snow, c_s and ice, c_i , are given as

$$c_s = 0.3 \text{ Wm}^{-1}\text{K}^{-1} , \; c_i = 2.0 \text{ Wm}^{-1}\text{K}^{-1}$$

The densities of snow, ρ_s , and ice, ρ_i are

$$\rho_s = 300 \text{ kgm}^{-3} , \; \rho_i = 900 \text{ kgm}^{-3}$$

The heat capacity of sea ice is

$$c_{pi} = 2090 \text{ Jkg}^{-1}\text{K}^{-1}$$

Within snow or ice no penetration of solar radiation is assumed. For the upper boundary condition the heat flux depends on the albedo over sea ice with possible snow cover, as described in chapter 2,

and the Taylor expansion about T_{eff} is used for longwave radiation and sensible and latent heat fluxes. Thus, defining $Q_{SW,i} = (1 - \alpha_i)\, Q^{\downarrow}_{SW}$, we have

$$Q_s = Q_{SW,i} + Q_{LW}(T_{eff}) + Q_{LH}(T_{eff}) + Q_{SH}(T_{eff}) + \left.\frac{\partial Q}{\partial T}\right|_{T_{eff}} (T_s - T_{eff}) \qquad (A.1)$$

If snow is present, the upper boundary condition is

$$c_s \left.\frac{\partial T}{\partial z}\right|_{z_s} = Q_s \qquad (A.2)$$

whereas in the absence of snow

$$c_i \left.\frac{\partial T}{\partial z}\right|_{z_i} = Q_s \qquad (A.3)$$

The lower boundary condition is

$$T(z_w) = T_w \qquad (A.4)$$

The temperatures at the top and bottom of the snow layer are defined as

$$T_s = T(z_s)\ ,\ T_i = T(z_i)$$

The requirement for the continuity of energy flux at the snow/ice interface is

$$\lim_{\varepsilon_s \to 0} c_s \left.\frac{\partial T}{\partial z}\right|_{z_i + \varepsilon_s} = \lim_{\varepsilon_i \to 0} c_i \left.\frac{\partial T}{\partial z}\right|_{z_i - \varepsilon_i} \qquad (A.5)$$

The thermal diffusion equation, integrated over each layer, is

$$\begin{aligned} &\int_{z_i}^{z_s} \left(\rho_s c_{pi} \frac{\partial T}{\partial t} - c_s \frac{\partial^2 T}{\partial z^2} \right) dz = 0 \qquad , \text{ snow layer} \\ &\int_{z_w}^{z_i} \left(\rho_i c_{pi} \frac{\partial T}{\partial t} - c_i \frac{\partial^2 T}{\partial z^2} \right) dz = 0 \qquad , \text{ ice layer} \end{aligned} \qquad (A.6)$$

Taking into account the continuity of energy flux at z_i, the vertical temperature dependence is specified in the approximate form

$$T(z) = \begin{cases} T_i + a(z - z_i) + \left(\frac{T_w - T_i}{d_i} + a\right)\frac{(z - z_i)^2}{d_i} & , \; z_w \le z < z_i \\ T_i + \frac{c_i}{c_s}a(z - z_i) + \left(\frac{T_s - T_i}{d_s} - \frac{c_i}{c_s}a\right)\frac{(z - z_i)^2}{d_i} f_s(z) & , \; z_i \le z < z_s \end{cases} \qquad (A.7)$$

with $\lim_{z \to z_s} f_s(z) = 1$, $\lim_{z \to z_i} f_s(z) < \infty$.

The purpose of the factor $f_s(z)$ is to ensure numerical stability under special circumstances. Assuming $f_s(z) = 1$ for the moment, substitution of $T(z)$ and performing the integrals yields

$$\begin{aligned} 2\left(c_s\frac{T_s - T_i}{d_s} - c_i a\right) &= \rho_s c_{pi} d_s\left(\frac{1}{3}\frac{\partial T_s}{\partial t} + \frac{2}{3}\frac{\partial T_i}{\partial t} + \frac{c_i d_s}{c_s}\frac{6}{\partial t}\frac{\partial a}{\partial t}\right) \\ 2\left(c_i a - c_i\frac{T_i - T_w}{d_i}\right) &= \rho_i c_{pi} d_i\left(\frac{2}{3}\frac{\partial T_i}{\partial t} - \frac{d_i}{6}\frac{\partial a}{\partial t}\right) \end{aligned} \qquad (A.8)$$

since $\frac{\partial T_w}{\partial t} = 0$.

The upper boundary condition can be expressed in terms of parameter a as

$$Q_s = \begin{cases} c_s\left(2\frac{T_s - T_i}{d_s} - \frac{c_i}{c_s}a\right) & , \text{ if } \; d_s > 0 \\ 2c_i a & , \text{ otherwise} \end{cases} \qquad (A.9)$$

allowing subtitution for a in (A.8).

For the timestepping a semi-implicit method is used. T_i and T_s on the left hand side of eqn. (A.8) are taken at the new time level; this also applies in the case of $\frac{\partial Q}{\partial T}\Big|_{T_s}$ T_s in eqn. (A.1)

For the case $d_s = 0$ only the second ordinary differential equation in (A.8) remains, and T_s is replaced by T_i as appropriate.

If the predicted T_s exceeds $T^* = 273.15$ K it is reset to T^* and $\frac{\partial T}{\partial z}\Big|_{z_s}$ is predicted instead. In this case the jump in energy flux at the top is

$$Q_s - c_s\frac{\partial T}{\partial z}\Big|_{z_s} = Q_{s,melt} \qquad (A.10)$$

The timestepping for (A.8) can under special circumstances fail numerically. To circumvent this in the coupled model, $f_s(z)$ is allowed to deviate from unity, in particular when d_s is of the same order as d_i . Introducing a parameter, $\zeta \in \mathrm{R}_0^+$, we take

$$f_s(z) = \frac{1}{\zeta+1}\left(1+\zeta\left(\frac{z-z_i}{d_s}\right)^{\zeta}\right) \qquad (A.11)$$

This changes the first eqn. in (A.8) to

$$\frac{\zeta^2+2\zeta+2}{\zeta+1}\left(c_s\frac{T_s-T_i}{d_s}-c_i a\right) \qquad (A.12)$$
$$= \frac{\rho_s c_{pi} d_s}{\zeta+1}\left[\left(\frac{1}{3}+\frac{\zeta}{\zeta+3}\right)\frac{\partial T_s}{\partial t}+\left(\zeta+1-\frac{1}{3}-\frac{\zeta}{\zeta+3}\right)\frac{\partial T_s}{\partial t}+\frac{c_i}{c_s}d_s\left(\frac{\zeta+1}{2}-\frac{1}{3}-\frac{\zeta}{\zeta+3}\right)\frac{\partial a}{\partial t}\right]$$

The upper boundary condition now reads

$$Q_s = \frac{\zeta^2+2\zeta+2}{\zeta+1}c_s\frac{T_s-T_i}{d_s}-\frac{\zeta^2+\zeta+1}{\zeta+1}c_i a \qquad (A.13)$$

For making the system (A.8) as modified by (A.12) well-behaved it is reasonable to require that, adding the snow and the ice eqn. to eliminate a , one is left with coefficients on the right hand side which have the same sign for all combinations of d_i and d_s which is critical only for the coefficient of $\frac{\partial a}{\partial t}$. The latter is proportional to the function

$$g(\gamma) = \frac{\zeta^2+2\zeta+2}{2}-3\gamma\left(\zeta+1-2\left(\frac{1}{3}+\frac{\zeta}{\zeta+3}\right)\right) \quad , \text{ with } \gamma = \frac{\rho_s d_s^2 c_i}{\rho_i d_i^2 c_s} \qquad (A.14)$$

The choice made is

$$g(\gamma) = e^{-\gamma} \qquad (A.15)$$

so that for small γ the case $\zeta = 0$ is approached asymptotically and a well-behaved time integration results in all cases, with an appropriate value of ζ determined from the snow and ice thicknesses and this choice of $g(\gamma)$ at each timestep.

Appendix B

Regridding of surface fluxes and SST

For computing the flux adjustments and for coupling between the models in general the discrepancy between the two model grids in the tropics and the subtropics necessitates regridding of SST and surface fluxes. For this reason a numerically efficient regridding scheme was developed by this author. The method is purely discrete but produces gradually varying high resolution gridded fields at intermediate stages. Positivity of a surface flux field, e.g., for u_*^3 or river discharge, is not violated by the regridded result. To the knowledge of the author, among the schemes used in coupling model components with disparate grids, the present development represents a new approach.

The essential problem in regridding a surface flux field delivered by the ECHAM4 model on the T42-Gaussian grid to obtain a boundary condition on the gridpoints of the OPYC ocean model equatorially refined grid consists in preserving the area integrated flux. For definiteness net surface heat flux, denoted by Q in what follows, is considered. Suppose that a domain assumed to be entirely ocean covered is bounded zonally by longitudes λ_W and λ_E and meridionally by latitudes φ_S and φ_N , and that these coordinates coincide with grid box boundaries in either grid. I. e. λ_W exactly denotes the western bounding longitude for a set of boxes in immediate meridional succession in the ECHAM4 grid, and a similar set in the OPYC grid, while λ_E similarly bounds two sets of boxes from the east. φ_S and φ_N similarly act as southern and northern bounding latitudes, respectively. The discretization of this domain in the Gaussian grid is given by

$$\begin{aligned} \lambda_W &= \lambda_0^a, \lambda_1^a, \ldots, \lambda_{M_a}^a = \lambda_E \\ \varphi_S &= \varphi_0^a, \varphi_1^a, \ldots, \varphi_{N_a}^a = \varphi_N \end{aligned} \qquad \text{(A.16)}$$

For the grid used in the OPYC model in the present integration, longitudes coincide with those used in the Gaussian grid

$$\begin{aligned} \lambda_i^o &= \lambda_i^a, i = 0, 1, \ldots, M_o = M_a \\ \varphi_S &= \varphi_0^o, \varphi_1^o, \ldots, \varphi_{N_o}^o = \varphi_N \end{aligned} \qquad \text{(A.17)}$$

If we denote the net downward surface heat flux values as computed over the Gaussian grid boxes, defined as the sets

$$[\lambda_{i-1}^a, \lambda_i^a) \times [\varphi_{j-1}^a, \varphi_j^a), i = 1, 2, \ldots, M_a; j = 1, 2, \ldots, N_a \qquad \text{(A.18)}$$

by $Q_{i,j}^a$, and the values after regridding to the OPYC grid

$$[\lambda_{k-1}^o, \lambda_k^o) \times [\varphi_{l-1}^o, \varphi_l^o), k = 1, 2, \ldots, M_o; l = 1, 2, \ldots, N_o \qquad \text{(A.19)}$$

by $Q_{k,l}^o$, then the requirement of flux conservation reads

$$\sum_{\substack{i = 1, \ldots, M_a \\ j = 1, \ldots, N_a}} w^a_{i,j} Q^a_{i,j} = \sum_{\substack{k = 1, \ldots, M_o \\ l = 1, \ldots, N_o}} w^o_{k,l} Q^o_{k,l} \qquad (A.20)$$

The weights $w^a_{i,j}$, $w^o_{k,l}$ account for spherical geometry and are given by

$$\begin{aligned} w^a_{i,j} &= \sin\varphi^a_j - \sin\varphi^a_{j-1} \\ w^o_{k,l} &= \sin\varphi^o_l - \sin\varphi^o_{l-1} \end{aligned} \qquad (A.21)$$

Generally, the $Q^o_{k,l}$ will be functions of all $Q^a_{i,j}$; i.e.

$$Q^o_{k,l} = \Psi(Q^a_{1,1}, Q^a_{2,1}, \ldots, Q^a_{M_a,1}, Q^a_{1,2}, \ldots, Q^a_{M_a,N_a}) \qquad (A.22)$$

The simplest choice for the function Ψ is such that an OPYC grid box that is fully covered by a Gaussian grid box is assigned the identical Q value, and that where two Gaussian grid boxes each cover part of an OPYC grid box a simple weighted average is used.[1] Because of the matching longitudes, we consider, for any k , a specific l for which a Gaussian latitude index j is to be found such that $\varphi^a_{j-1} \le \varphi^o_{l-1} < \varphi^a_j$. The appropriate definition for $Q^o_{k,l}$ then is

$$Q^o_{k,l} = \begin{cases} Q^a_{k,j}, \text{ if } \varphi^a_j \ge \varphi^o_l \\ (1-\zeta) Q^a_{k,j} + \zeta Q^a_{k,j+1}, \text{ otherwise} \end{cases} \qquad (A.23)$$

where

$$\zeta = \frac{\sin\varphi^o_l - \sin\varphi^a_j}{\sin\varphi^o_l - \sin\varphi^o_{l-1}}$$

However, the OPYC grid used presently, compared to the Gaussian grid exhibits significantly higher meridional resolution at low latitudes. In this case the above simple choice for Ψ induced by (A.23) can lead to non-smooth appearance of the field after regridding to the higher resolution grid. In a meridional succession of adjacent grid boxes several would be covered by the same Gaussian grid box and thus attain the same value of Q , then there would be a single interspersed OPYC grid box dependent on two Gaussian grid boxes, and subsequent OPYC grid boxes would again attain a repeated value. Thus a staircase function shape of Q in the OPYC grid would be obtained. This is the result of the constancy of Q over an entire Gaussian grid box. The common approach to permit a more gradual variation of the regridded field with latitude is to first introduce a smooth function Φ which preserves the values of integrals of Q over the Gaussian grid boxes, such that normalization by the grid box area yields $Q^a_{i,j}$. Then using analytic expressions for the integrals over OPYC grid boxes followed by normalization yields $Q^o_{k,l}$. There are major drawbacks in common strategies, particularly when continuity of the function Φ and some of its derivatives is to be guaranteed. For

1. Other cases are excluded since no OPYC grid box is larger than any Gaussian grid box in its vicinity

example, for the vast amount of spline algorithms, the numerics usually involve the inversion of a large matrix, and despite the special matrix structure and the existence of advanced optimized computational strategies, for the present regridding problem excessive computational cost results (e.g., Freeden, 1984). A further problem is induced by the presence of a land-sea distribution with irregular continental boundaries. If function Φ is required to be continuous, land-sea contrasts present, e.g., in turbulent fluxes may cause overshooting and spurious decaying oscillations in a direction away from the coast. Further complication generally results from requiring positivity or boundedness for Φ which among the fields to be regridded applies to the cube of the friction velocity or river discharge, for example.

A suitable approach can be set up in analogy to interpolatory subdivision which is frequently applied in two or three-dimensional problems in the field of Computer Aided Geometric Design (CAGD). An elementary approach is discussed in the paper by Le Méhauté and Utreras (1994). Interpolatory subdivision considers function values given at discrete points of a one-dimensional coordinate sequence or a two or three-dimensional lattice, which is iteratively subdivided, e.g., by iteratively doubling the density of nodes in each dimension when stepping through a recursion. Instead of iteratively increasing the density of point sampling of a field, the present regridding problem requires iteratively increasing the number of grid boxes with grid box averaged values of the field for a given domain. The requirement to preserve integrals over the original grid boxes applies in each recursion step. After a few recursion steps, a procedure similar to that given by (A.23), involving only weighted linear combinations, can be used to transform from values on the refined grid to values on the OPYC grid boxes. Since the refinement recursion produces smaller jumps between grid boxes, the resulting quantity on the OPYC grid is expected to exhibit much less of a staircase function character.

Let n be the number of steps used in the recursion. The choice in the coupled model is $n = 3$. Then define the index of a step in the recursion as $r \in \{0,1,2,3\}$. $r = 0$ denotes the state before the first recursion step, such that

$$z_{i,j}^{(0)} \equiv Q_{i,j}^{a} \qquad \text{(A.24)}$$

To define the recursion, we start by considering the case where positivity of the function is not required which is appropriate for net surface heat flux.

The definition of the refined grid is given in an obvious way by halving the grid spacing in both directions in each recursion step. Revising the above nomenclature such that the entire domain where regridding is performed is identified with the set $[\lambda_W^a, \lambda_E^a) \times [\varphi_S^a, \varphi_N^a)$, for $r = 0$ we define

$$\begin{aligned} \lambda_i^{(0)} &= \lambda_i^a,\ i = 0, 1, \ldots, M_a \\ \varphi_j^{(0)} &= \varphi_j^a,\ j = 0, 1, \ldots, N_a \end{aligned} \qquad \text{(A.25)}$$

and, for $r > 0$ in the recursion,

$$\lambda^{(r+1)}_{2i-2+(s_\lambda+1)/2} = \lambda^{(r)}_{i-1} + \frac{1}{4}(s_\lambda+1)(\lambda^{(r)}_i - \lambda^{(r)}_{i-1}) \ , \ i = 1, 2, \ldots, 2^r M_a$$

$$\text{similarly for } \varphi^{(r+1)}_{2j-2+(s_\varphi+1)/2} \qquad \text{(A.26)}$$

where $s_\lambda, s_\varphi \in \{-1, 1\}$

The recursion for the function undergoing refinement is defined by

$$z^{(r+1)}_{2i-1+(s_\lambda+1)/2,\, 2j-1+(s_\varphi+1)/2} = z^{(r)}_{i,j} + \frac{1}{4}\frac{\Delta^{(r)}_j}{2\Delta^{(r+1)}_{2j-1+(s_\varphi+1)/2}}(s_\lambda d^{(r)}_{\lambda,i,j} + s_\varphi d^{(r)}_{\varphi,i,j}) \qquad \text{(A.27)}$$

$$i = 1, 2, \ldots, 2^r M_a, j = 1, 2, \ldots, 2^r N_a$$

where

$$\Delta^{(r)}_j = \sin\varphi^{(r)}_j - \sin\varphi^{(r)}_{j-1}$$

It is not difficult to see that, for any choice of $d^{(r)}_{\lambda,i,j}, d^{(r)}_{\varphi,i,j}$

$$z^{(r)}_{i,j} = w^{(r+1)}_{2i-1,2j-1} z^{(r+1)}_{2i-1,2j-1} + w^{(r+1)}_{2i,2j-1} z^{(r+1)}_{2i,2j-1} + w^{(r+1)}_{2i-1,2j} z^{(r+1)}_{2i-1,2j} + w^{(r+1)}_{2i,2j} z^{(r+1)}_{2i,2j} \qquad \text{(A.28)}$$

where

$$w^{(r+1)}_{2i-1+(s_\lambda+1)/2,\, 2j-1+(s_\varphi+1)/2} = \frac{\Delta^{(r+1)}_{2j-1+(s_\varphi+1)/2}}{2\Delta^{(r)}_j}$$

In other words, each step in the recursion satisfies the requirement of integral conservation.

Since positivity or other constraints were not imposed, $d^{(r)}_{\lambda,i,j}$ is not subject to constraints either and can be chosen as the simple centered difference

$$d^{(r)}_{\lambda,i,j} = \frac{1}{2}(z^{(r)}_{i+1,j} - z^{(r)}_{i-1,j})$$

$$\text{similarly for } d^{(r)}_{\varphi,i,j} \qquad \text{(A.29)}$$

At the continental boundaries and the meridional extremities of the domain which undergoes regridding, special treatment is required; these cases are described below.

A positivity constraint must be satisfied, e.g., for the cube of the friction velocity or for river discharge, either of which satisfies

$$z_{i,j}^{(0)} \geq 0 \quad \text{for all } i,j$$

so that at each step of the recursion no negative new values are permitted.

Considering the function

$$g : \mathrm{R_0}^+ \times \mathrm{R} \rightarrow \mathrm{R}$$

$$(x,y) \rightarrow g(x,y) = 2x\,\mathrm{sgn}(y)\left(1 - \left(\frac{2}{\frac{|y|}{\rho x} + 2}\right)^{\rho}\right) \quad ; \quad \rho \geq 1 \qquad \text{(A.30)}$$

which for small $|y|$ asymptotes to

$$g_0 : \mathrm{R_0}^+ \times \mathrm{R} \rightarrow \mathrm{R}$$

$$(x,y) \rightarrow y$$

we may replace definition (A.29) with

$$d_{\lambda,i,j}^{(r)} = g\left(z_{i,j}^{(r)}, \frac{1}{2}\left(z_{i+1,j}^{(r)} - z_{i-1,j}^{(r)}\right)\right) \qquad \text{(A.31)}$$

similarly for $d_{\varphi,i,j}^{(r)}$

Then, if, for all i, j, $z_{i,j}^{(0)} > 0$, the definition of the recursion in (A.27) leads to strictly positive results. The parameter ρ approximately determines over what range the asymptotic behaviour given by g_0 can be assumed; this range is larger for greater ρ . In the coupled model, $\rho = 5$ is used.

In the coupled simulation regridding is necessary over all three oceans within the tropics and part of the subtropics. Regridding may pose problems near continental boundaries for quantities like net surface heat flux for which sharp gradients near coasts may be induced by the land-sea contrast in turbulent boundary layer fluxes. If the regridding procedure permitted the contribution of continental values to the $d_{\lambda,i,j}^{(r)}, d_{\varphi,i,j}^{(r)}$, severe distortions could result at sea grid points adjacent to land points. Hence, the strategy is to avoid centred differencing near coasts and define $d_{\lambda,i,j}^{(r)}, d_{\varphi,i,j}^{(r)}$ on the basis of sea points only. This will be explained for the case of $d_{\lambda,i,j}^{(r)}$; similar definitions apply for $d_{\varphi,i,j}^{(r)}$.

Let the land-sea distribution on the Gaussian grid within the regridding domain be given by

$$K^a : \{1, \ldots, M_a\} \times \{1, \ldots, N_a\} \rightarrow \{0, 1\}$$

$$(i,j) \rightarrow K_{i,j}^a = \begin{cases} 1 & \text{for sea points} \\ 0 & \text{for land points} \end{cases} \qquad \text{(A.32)}$$

Without loss of generality, consider an ocean covered Gaussian grid box for which

$3 \le i < M_a - 2$, $3 \le j < N_a - 2$ [1]. Two integer values, $m^{(0)}_{\lambda,i,j}, m^{(0)}_{\varphi,i,j}$, are defined. $m^{(0)}_{\lambda,i,j}$ carries information about the presence of land points on the two pairs of grid longitudes adjacent both to the west and the east of index pair (i,j), and is defined as in table A.1

Table A.1: Definition of $m^{(0)}_{\lambda,i,j}$

$m^{(0)}_{\lambda,i,j}$	$K^a_{i-2,j}$	$K^a_{i-1,j}$	$K^a_{i,j}$	$K^a_{i+1,j}$	$K^a_{i+2,j}$
-3	*arbitrary*	*arbitrary*	0	*arbitrary*	*arbitrary*
3	*arbitrary*	0	1	0	*arbitrary*
-2	0	1	1	0	*arbitrary*
2	*arbitrary*	0	1	1	0
-1	1	1	1	0	*arbitrary*
1	*arbitrary*	0	1	1	1
0	*arbitrary*	1	1	1	*arbitrary*

A recursion is now defined in parallel with the recursion for the refinement of $z^{(r)}_{i,j}$ to update $m^{(r)}_{\lambda,i,j}, m^{(r)}_{\varphi,i,j}$ which in the case of $m^{(r)}_{\lambda,i,j}$ is given by table A.2

Table A.2: Recursion for $m^{(r)}_{\lambda,i,j}$

$m^{(r)}_{\lambda,i,j}$	-3	-2	-1	0	1	2	3
$m^{(r+1)}_{\lambda,2i-1,2j}$	-3	0	0	0	1	1	2
$m^{(r+1)}_{\lambda,2i,2j}$	-3	-1	-1	0	0	0	-2

with

$$m^{(r+1)}_{\lambda,2i-1,2j-1} = m^{(r+1)}_{\lambda,2i-1,2j}$$
$$m^{(r+1)}_{\lambda,2i,2j-1} = m^{(r+1)}_{\lambda,2i,2j}$$

The recursion for $m^{(r)}_{\varphi,i,j}$ is defined similarly.

In the absence of a positivity constraint the definition of $d^{(r)}_{\lambda,i,j}$ now reads

$$d^{(r)}_{\lambda,i,j} = \frac{1}{6}(\tau^{(r)}_{\lambda,i-2,j} z^{(r)}_{i-2,j} + \tau^{(r)}_{\lambda,i-1,j} z^{(r)}_{i-1,j} + \tau^{(r)}_{\lambda,i,j} z^{(r)}_{i,j} + \tau^{(r)}_{\lambda,i+1,j} z^{(r)}_{i+1,j} + \tau^{(r)}_{\lambda,i+2,j} z^{(r)}_{i+2,j}) \quad (A.33)$$

Table A.3 summarizes the definition of $\tau^{(r)}_{\lambda,i,j}$.

A similar definition is employed for $d^{(r)}_{\varphi,i,j}$, $\tau^{(r)}_{\varphi,i,j}$. The result of the above definitions, as evident for the case $m^{(r)}_{\lambda,i,j} = \pm 2$, is essentially to replace the centered difference of (A.29) by an appropriate

1. in the coupled model, cyclic boundary conditions are employed

Table A.3: Definition of $\tau^{(r)}_{\lambda,i,j}$

$m^{(r)}_{\lambda,i,j}$	$\tau^{(r)}_{\lambda,i-2,j}$	$\tau^{(r)}_{\lambda,i-1,j}$	$\tau^{(r)}_{\lambda,i,j}$	$\tau^{(r)}_{\lambda,i+1,j}$	$\tau^{(r)}_{\lambda,i+2,j}$
-3	0	0	1	0	0
3	0	0	1	0	0
-2	0	0	-6	6	0
2	0	-6	6	0	0
-1	1	-8	7	0	0
1	0	0	-7	8	-1
0	0	-3	0	3	0

'upstream' difference, if an adjacent land point is assumed to lie 'downstream'. The case $m^{(r)}_{\lambda,i,j} = \pm 1$ differs little from the case $m^{(r)}_{\lambda,i,j} = \pm 2$ and is not applied when regridding is performed for river discharge.

If a positivity constraint is to be satisfied, $d^{(r)}_{\lambda,i,j}, d^{(r)}_{\varphi,i,j}$ as defined in (A.33), and subsequently, are used as the second argument on the right hand side in (A.31).

Boundary conditions at the northern and southern boundaries of the domain subject to regridding are needed because $d^{(r)}_{\varphi,i,j}$ on the extreme rows cannot be taken as a centered difference. Open boundary conditions are straightforward to implement. Beyond the outermost Gaussian grid box which requires refinement, for definiteness taken at φ_N, such that $j = N_a$ prior to the recursion, a pad consisting of several boxes with $j > N_a$ is defined in the meridional direction. Then the recursion is performed within the augmented domain. In those boxes generated by sudivision of the outermost box which is not part of the pad, values $z^{(r)}_{\bullet,\bullet}$ for all recursion steps contain no contribution from the area with $j \geq N_a + 2$ prior to the recursion, as shown below. Hence it is sufficient if the pad consists of two additional Gaussian rows. The row with $j = N_a + 2$ is assumed to have land adjacent to the north of it, and thus it is assumed that $m^{(0)}_{\varphi,i,N_a+2} \in \{\pm 3, -1, -2\}$, depending on the land-sea distribution in the northernmost three Gaussian rows. The choice of $m^{(0)}_{\varphi,i,N_a+2}$ ensures that $d^{(0)}_{\varphi,i,N_a+2}$ are properly defined. The padding south of φ_S is done in a similar way. It should be noted that in cases where, for fixed i, the land sea distribution has a land value on the row north of the pad, or on the two pad rows, the specification of a boundary condition is redundant.

To show that the recursion in the area south of the northern pad is not affected by the boundary condition that determines $m^{(0)}_{\varphi,i,N_a+2}$, without loss of generality assume that the latitudes $\varphi^{(0)}_j, j = -2, -1, 0, 1, \ldots, N_a, N_a+1, N_a+2$ are evenly spaced, with $\varphi^{(0)}_j - \varphi^{(0)}_{j-1} = 1$ and $\varphi^{(0)}_{N_a+2} = 0$. For $r = 1,2,3,\ldots$, a sequence of latitudes $\varphi^{(r)}_b$, is considered which represents, for each step, the southernmost latitude $\varphi^{(r)}_j$ generated by the recursion at which $z^{(r)}_{i,j}$ can possibly depend on $m^{(0)}_{\varphi,i,N_a+2}$. Clearly,

$$\varphi^{(1)}_b = -\frac{3}{4}$$

because $z^{(1)}_{i,2N_a+3}$ depends on $m^{(0)}_{\varphi,i,N_a+2}$ via $d^{(0)}_{\varphi,i,N_a+2}$.

Subsequently, stepping forth in the recursion induces dependence of some on $m^{(0)}_{\varphi,i,N_a+2}$ via the contribution to $d^{(r)}_{\varphi,\bullet,\bullet}$ by a $z^{(r)}_{\bullet,\bullet}$ value at $\varphi^{(r)}_b$. The step $r = 2$ induces an influence of $\varphi^{(1)}_b$ via $d^{(1)}_{\varphi,i,2N_a+2}$. Out of the two latitudes constructed from this according to (A.26) for $r = 2$, the one further south is

$$\varphi^{(2)}_b = -\frac{3}{4} - \frac{5}{8}$$

Repeating this procedure, one obtains

$$\varphi^{(3)}_b = -\frac{3}{4} - \frac{5}{8} - \frac{5}{16}$$

Generally,

$$\varphi^{(r)}_b = -\frac{3}{4} - 5\sum_{\nu=3}^{r+1} 2^{-\nu} \qquad \text{for} \quad r \geq 2 \qquad (A.34)$$

Hence,

$$\lim_{r\to\infty} \varphi^{(r)}_b = -\frac{3}{4} - 5\sum_{\nu=3}^{\infty} 2^{-\nu} = -2 \qquad (A.35)$$

By construction this value characterizes the border between the pad and the unpadded area. Therefore no dependence on $m^{(0)}_{\varphi,i,N_a+2}$ is possible in the unpadded area.

Although it is beyond the scope of the present description to discuss in detail the technical properties of the refinement scheme, it is worth noting that computational efficiency was achieved on the Cray C90 supercomputer used to perform the coupled model simulations at the Deutsches Klimarechenzentrum (DKRZ), Hamburg, Germany. In particular, vector pipelines at each recursion step can treat complete sets of 128 elements which is the number of Gaussian logitudes at T42 resolution, and purely scalar loops are avoided. A disadvantage is the considerable complexity needed in coding the recursion so as to meet this criterion and to allow the number of recursions, n, to be prescribed arbitrarily.

The last stage of the refinement scheme forms the basis for a transform to the OPYC grid based on simple linear combinations of cells in defining a value for an OPYC grid cell similar to the algorithm in (A.23). It is then straightforward to see that the requirement of flux conservation, eqn. (A.20), is satisfied over suitable domains.

In an exactly analogous way regridding was applied to the land-sea distribution given in (A.32), such that as a raw result fractional land portion values on the OPYC grid boxes were obtained which were rounded to the nearest integer, 0 or 1, to obtain the OPYC grid land-sea distribution. This distribution was already used in the ocean only spinup integration such that no disruption or 'shock' due to disparate grids between coupled and uncoupled runs could be induced.

The match between the land sea masks in the two models cannot be perfect, however. Thus, along continental boundaries land covered grid boxes in the OPYC grid may partially overlap Gaussian grid boxes, and vice versa. The target grid box (for regridding a flux to OPYC, or the SST to the Gaussian grid) always receives a weighted average which is based solely on sea points. This in general implies that the integral over the entire domain in the target grid slightly deviates from the result in the original grid. Since one of the requirements in the coupled model must be that the integral over the globe is equal before and after the regridding, a correction is made in the case of the surface heat flux and preciptation minus evaporation. The present approach is designed not to cause regions with a close balancing of the surface flux to receive a significantly nonzero flux by the correction term. If the correction is additive, this might not be satisfied. Therefore, a multiplicative correction is applied, but only to regions where the flux is of a pre-selected sign. The integral over regions with positive flux is compared to that over areas with negative flux. Whichever is of greater abolute value, is multiplied by an appropriate correction factor, such that the total integral over the regridded field is made equal to the integral computed before regridding.

Regridding of ocean variables from the OPYC grid to the T42 Gaussian grid is much simpler than the reverse which was discussed above. Sea ice concentration, thickness, and snow coverage throughout the integration only occur outside the domain subject to regridding. Where they occur the Gaussian grid and OPYC grid are congruent such that values for these quantities can simply be copied from the OPYC grid boxes to the ECHAM4 grid. For SST, conservation of area integrals is granted by simple averaging of OPYC grid boxes incident on a Gaussian grid box, taking into account spherical geometry.

Care must be taken of a particular effect of the averaging of SST from the OPYC to the ECHAM grid which yields the lower boundary condition for the computation of surface heatflux in the ECHAM4 model. The turbulent surface heat fluxes which depend on the averaged SST values may in special situations fail to account properly for strongly confined regions of extreme SST values. In such a situation, the lack of resolution normally induces a lack of control of the development of such extreme SST values by surface heat flux. The feedback, expressed by the partial derivative of net surface heat flux, Q , with respect to sea surface temperature, $\frac{\partial Q}{\partial T_w}$, is usually negative (e.g., Oberhuber, 1988), thus if SST evolves on the ocean grid but heat flux can only be obtained as the average over the coarser T42 grid box, the extreme SST features will experience less damping than appropriate. This motivates an approach which in a similar fashion has been used in various coupled simulations (e.g., Lunkeit et al. 1996). On the Gaussian grid cell, $\frac{\partial Q}{\partial T_w}$ as computed by ECHAM4 has contributions from longwave radiation and the turbulent heat flux components. The product of this derivative and the difference between the SST on the OPYC grid T_w^o and SST on the Gaussian grid $T_w^{a,(0)}$ yields an additional feedback term. Obviously, adding such a feedback term does not violate integral conservation.[1]

To form the appropriate SST difference, the refined grid for the last recursion step, $r = n$, is used. First, within a Gaussian grid cell all sub-cells generated by the refinement are given the identical value of SST,

---

1. Over a single Gaussian grid box, $\frac{\partial Q}{\partial T_w}$ is constant, and $T_w^{a,(0)} - T_w^o$ integrates to zero.

$$T^{a,(n)}_{w,\,2^n i-\mu,2^n j-\nu} = T^{a,(0)}_{w,i,j} \quad , \ \mu,\nu \in \{0,1,\ldots,2^n-1\} \tag{A.36}$$

which is obtained as the result of averaging appropriate OPYC grid boxes to the Gaussian grid box. Similarly, an identical value

$$\left(\frac{\partial Q_{tot}}{\partial T_w}\right)^{(n)}_{2^n i-\mu,2^n j-\nu} = \left(\frac{\partial Q_{tot}}{\partial T_w}\right)^{(0)}_{i,j} \tag{A.37}$$

is assigned to these sub-cells. Then, by averaging the SST from the OPYC grid to the same subcells directly, values $T^{o,(n)}_{w,\,2^n i-\mu,2^n j-\nu}$ are defined which capture the fine structure of the SST on the OPYC grid. As with the final step in the standard Gaussian to OPYC regridding the transform from the refined grid to the OPYC grid is applied, to the term

$$\delta Q^{a,(n)}_{2^n i-\mu,2^n j-\nu} = \left(\frac{\partial Q}{\partial T_w}\right)^{(n)}_{2^n i-\mu,2^n j-\nu} (T^{o,(n)}_{w,\,2^n i-\mu,2^n j-\nu} - T^{a,(n)}_{w,\,2^n i-\mu,2^n j-\nu}) \tag{A.38}$$

and, since the first factor on the right is generally negative, adding the transformed result to the transformed net surface heat flux adds a negative feedback term.

The algorithm for constructing a refined mesh with appropriate function values from the original quantity on the Gaussian grid is now demonstrated by application to two quantities computed by the ECHAM4 model. The stages of the refinement given by $r = 1,2,3$ are shown for the month of January yr 91, the first month of the coupled integration using fixed flux adjustment. Fig. A.1 shows these stages for net surface heat flux. Although the original Gaussian grid representation is not given, the result after the first refinement step, $r = 1$ (fig. A.1.a) still exhibits characteristics of a staircase function shape, particularly in areas of small gradients, e.g., in the central North Pacific. This is substantially reduced for the stage $r = 2$ (fig. A.1.b). Remaining staircase function behaviour is most apparent about the central equatorial Pacific. A further refinement step, fig. A.1.c, renders this area as well as the entire remaining refined field strongly oversampled, i.e. any substantial gradients are spread out over many of the fine meshwidths. This leads to a very smooth appearance in the graphical representation, and one expects that the ultimate regridded OPYC grid version faithfully represents the original quantity as delivered by ECHAM4 on the Gaussian grid.

A similar sequence is shown for a positive definite quantity to demonstrate the capability of the algorithm defined in (A.31). The quantity subject to the regridding is the surface flux of turbulent kinetic energy, represented by the cube of the friction velocity, u_*^3. This is shown in fig. A.2 for the same month and year as in fig. A.1. This field is characterized by a spatial variation spanning several orders of magnitude. In some locations, e.g., in the vicinity of 10° N, east of 120° W sharp horizontal gradients occur that are associated with relative changes of almost an order of magnitude within a few hundred kilometers. In such areas a common problem exhibited by regridding schemes that fail to take into account the positivity constraint is a regridded result that exhibits negative overshooting in the vicinity of sharp maxima. Obviously it is important that the positivity constraint be satisfied to provide a proper input to the mixed layer entrainment/detrainment rate. The shape-preserving characteristics of the procedure are also evident particularly near Japan.

List of figures

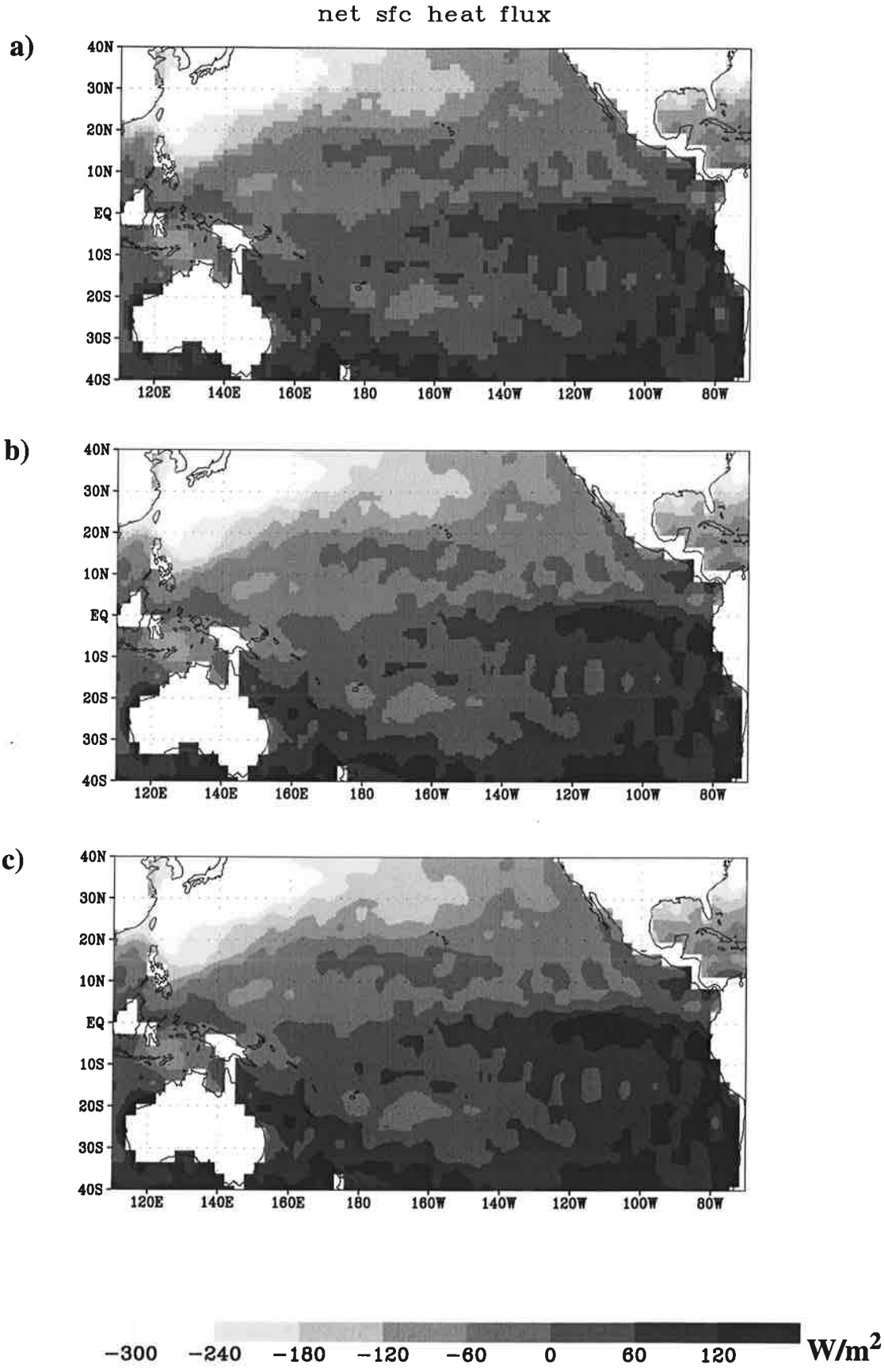

Fig. A.1 Recursive meshwidth halving grid refinement before transforming to OPYC grid for net surface heat flux, Jan, yr 91. a) recursion step r=1, b) r=2, c) r=3

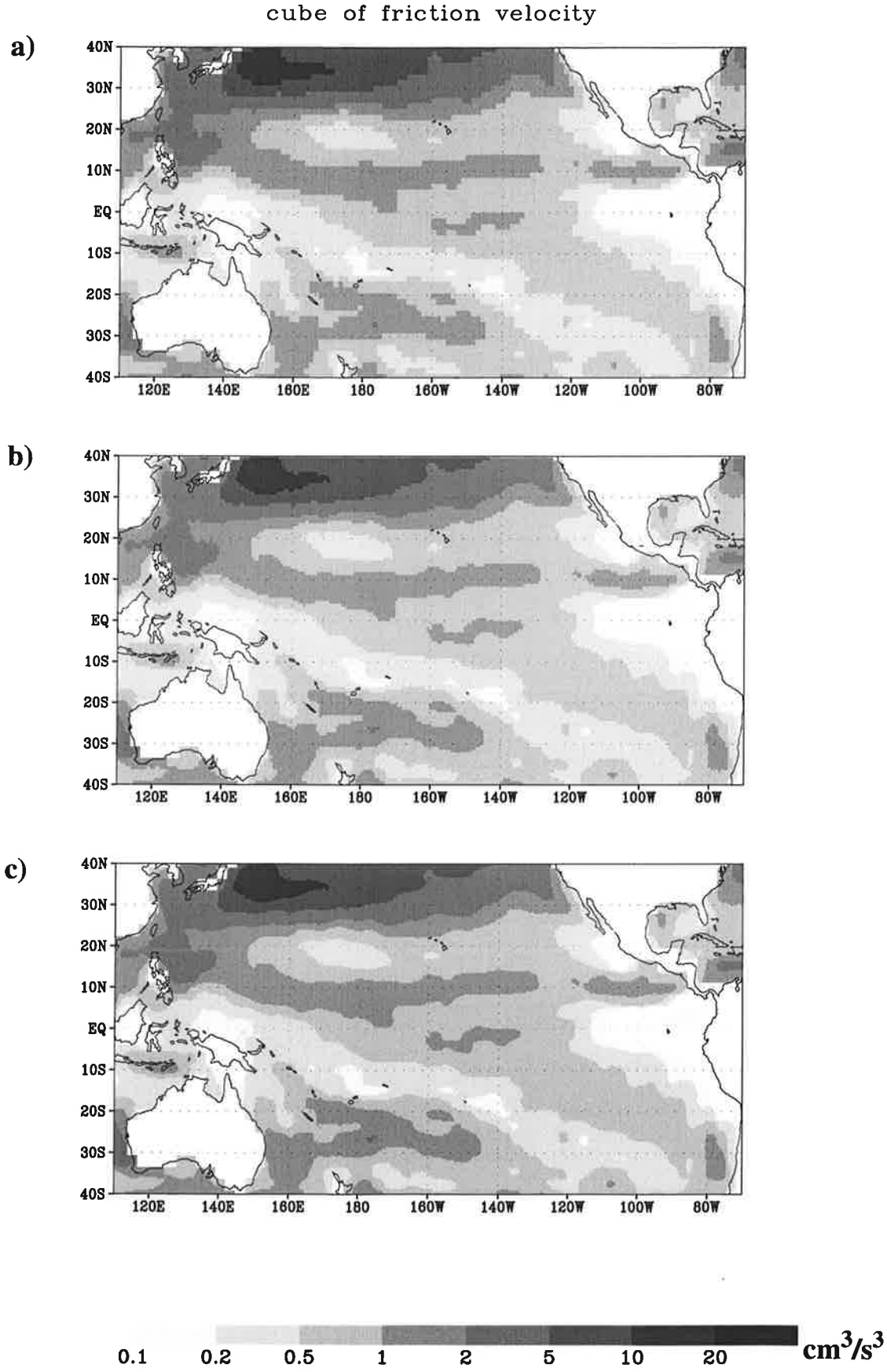

Fig. A.2 as fig. A.1 but for the cube of friction velocity

References

Alexander M. A. (1992) Midlatitude Atmosphere-Ocean Interaction during El Niño. Part I: The North Pacific Ocean. *J. Climate*, **5**: 944-958

Anderson D.L.T., A.E. Gill (1975) Spin-up of a stratified ocean, with applications to upwelling. Deep-Sea Res., **22**, 583-596

Anderson D.L.T., J. Willebrand (ed.) (1996) Decadal Climate Variability: Dynamics and Predictability. *NATO ASI Series, Series I: Global Environmental Change*, Vol. **44**, Springer. 496 pp.

Arkin P.A. (1982) The Relationship Between Interannual Variability in the 200 mb Tropical Wind Field and the Southern Oscillation. *Mon. Wea. Rev.*, **110**, 1393-1404

Arkin P.A., P. Xie (1994) The Global Precipitation Climatology Project: First Algorithm Intercomparison Project. *Bull. American Meteor. Soc.*, **75**, 401-419

Bacher A., J.M. Oberhuber, E. Roeckner (1998) ENSO dynamics and seasonal cycle in the tropical Pacific as simulated by the ECHAM4/OPYC3 coupled general circulation model. *Climate Dyn.* **14**: 431-450

Barnett T. P. (1981) Statistical Prediction of North American Air Temperatures from Pacific Predictors. *Mon. Wea. Rev.*, **109**, 1021-1041

Barnett T.P., M. Latif, N.E. Graham, M. Flügel, S. Pazan, W. White (1993) ENSO and ENSO-related predictability. Part I: Prediction of equatorial Pacific sea surface temperature with a hybrid coupled ocean-atmosphere model. *J. Climate*, **6**, 1545-1566

Barnett T.P., Pierce D., Latif M. (1998) Interdecadal interactions between the tropics and midlatitudes in the Pacific basin. *J. Climate*, subm.

Battisti D.S., U. Bhatt, M.A. Alexander (1995) A modeling study of the interannual variability in the wintertime North Atlantic Ocean. *J. Climate*, **8**, 3067-3083

Bengtsson (1996) The climate response to the changing greenhouse gas concentration in the atmosphere. in: Anderson and Willebrand (1996), 293-332.

Bengtsson L., K. Arpe, E. Roeckner, U. Schulzweida (1996) Climate predictability experiments with a general circulation model. *Climate Dyn.*, **12**: 261-278

Berlage H.P. (1966) The Southern Oscillation and world weather. *K. Ned. Meteor. Inst., Meded. Verh.*, **88**, 1-152

Bjerknes J. (1966) A Possible Response of the Atmospheric Hadley Circulation to Equatorial Anomalies of Ocean Temperature. *Tellus*, **18**, 820-829.

Bjerknes J. (1969) Atmospheric teleconnections from the equatorial Pacific. *Mon. Wea. Rev.* **97**: 163-172

Bladé I. (1997) The Influence of Midlatitude Ocean-Atmosphere Coupling on the Low-Frequency Variability of a GCM. Part I: No Tropical SST Forcing. *J. Climate*, **10**, 2087-2106

Bony S., K.M. Lau, Y.C. Sud (1997) Sea Surface Temperature and Large-Scale Circulation Influences on Tropical Greenhouse Effect and Cloud Radiative Forcing. *J. Climate*, **10**, 2055-2077

Brinkop S., E. Roeckner (1995) Sensitivity of a general circulation model to parameterizations of cloud-turbulence interactions in the atmospheric boundary layer. *Tellus*, **47A**, 197-220

Cane M.A., Zebiak S., Dolan S.C. (1986) Experimental forecasts of El Niño. *Nature*, **321**, 827-32

Cayan D. (1992) Latent and sensible heat flux anomalies over the northern oceans: Driving the sea surface temperature. *J. Phys. Oceanogr.*, **22**, 859-881

Chen C.-T., Roeckner E. (1996) Warm pool heat budget as simulated by different versions of the ECHAM model. *NATO ASI series*, Vol. I 34: 95-105

Claussen M., U. Lohmann, E. Roeckner, U. Schulzweida (1994) A global dataset of land-surface parameters. *Max-Planck-Institut für Meteorologie*, Report No. **135**, Hamburg, 34 pp.

Cleaveland M.K., E.R. Cook, D.W. Stahle (1992) Secular variability of the Southern Oscillation detected in tree-ring data from Mexico and the southern United States. in: Diaz and Mark-

graf (1992), pp. 271-291

Colin C., C. Henin, P. Hisard, C. Oudot (1971) Le Courant de Cromwell dans le Pacific central en fevrier. Cah. ORSTOM, *Ser Oceanogr.* **9**, 167-186

Cubasch U., K. Hasselmann, H. Höck, E. Maier-Reimer, U. Mikolajewicz, B.D. Santer, R. Sausen (1992) Time-dependent greenhouse warming computations with a coupled ocean-atmosphere model. *Climate Dyn.*, **8**, 55-69

da Silva, A.M., C.C. Young, and S. Levitus (1994) Atlas of surface marine data 1994, volumes 1 and 3. NOAA Atlas NESDIS 6 and 8. Available from NODC, NOAA/NESDIS E/OC21, Washington, D.C. 20235, USA

Deser C., M.L. Blackmon (1995) On the Relationship between Tropical and North Pacific Sea Surface Temperature Variations. *J. Climate*, **8**, 1677-1680

Deser C., M.A. Alexander, M.S. Timlin (1996) Upper-Ocean Thermal Variations in the North Pacific during 1970-1991. *J. Climate*, **9**, 1840-1855

Diaz H.F., V. Markgraf (ed.) (1992) El Niño. Historical and Paleoclimatic Aspects of the Southern Oscillation. *Cambridge University Press*, 480 pp.

Favorite F., D.R. McLain (1973) Coherence in Transpacific Movements of Positive and Negative Anomalies of Sea Surface Temperature, 1953-60. *Nature*, **244**, 139-143

Fouquart Y., B. Bonnel (1980) Computations of solar heating of the Earth's atmosphere: A new parameterization. *Beitr. Phys. Atmos.*, **53**, 35-62

Frankignoul C. (1985) Sea Surface Temperature Anomalies, Planetary Waves, and Air-Sea Feedback in the Middle Latitudes. *Rev. Geophys.*, **23**, 357-390

Frankignoul C., E. Zorita, P. Müller (1997) A simple model of the decadal response of the ocean to stochastic wind forcing. *J. Phys. Oceanogr.*, **27**, 1533-1546

Freeden W. (1984) Spherical spline interpolation - basic theory and computational aspects. *J. Comput. Appl. Math*, **11**, 367-375

Frey H., M. Latif, T. Stockdale (1997) The coupled GCM ECHO2. Part I: The tropical Pacific. *Mon. Wea. Rev.*; special issue on "Coupled Ocean-Atmosphere Models", **125**, 703-720

Fu L.L., E.J. Christensen, C.A. Yamarone, M. Lefebvre, Y. Menard, M. Dorrer, P. Escudier (1994) TOPEX/POSEIDON mission overview. *J. Geophys. Res.*, **99**, 24369-24381

Gates W.L. (1992) AMIP: The atmospheric model intercomparison project. *Bull. Am. Meteor. Soc.*, **73**, 35-62

Gibson J.K., P. Källberg, S. Uppala (1997) The ECMWF Re-Analysis (ERA) project. *ECMWF Reanalysis Newsletter*, **73**, 7-17.

Giorgetta M., M. Wild (1995) The water vapour continuum and its representation in ECHAM4. *Max-Planck-Institut für Meteorologie*, Report No. **162**, Hamburg, 38 pp.

Gleckler P.J., B. C. Weare (1997) Uncertainties in Global Ocean Surface Heat Flux Climatologies Derived from Ship Observations. *J. Climate*, **10**: 2764-2781

Graham N.E. (1994) Decadal-scale variability in the tropical and North Pacific during the 1970s and 1980s: observations and model results. *Climate Dyn.*, **10**:135-162

Graham N.E., T.P. Barnett (1987) Sea surface temperature, surface wind divergence, and convection over tropical oceans. *Science*, **238**, 657-659

Gu D., S.G.H. Philander (1997) Interdecadal Climate Fluctuations That Depend on Exchanges Between the Tropics and Extratropics. *Science*, **275**, 805-807

Haney R.L. (1971) Surface thermal boundary condition for ocean circulation models. *J. Phys. Oceanogr.*, **1**, 241-248

Hasselmann K. (1976) Stochastic climate models. Part I. Theory. *Tellus*, **28**, 473-485

Hasselmann K. (1988) PIPs and POPs. The reduction of complex dynamical systems using Principal Interaction and Oscillation Patterns. *J. Geophys. Res.*, **93**, 11015-11021

Hasselmann K. (1997) Are we seeing global warming? *Science*, **276**, 1997, 914-915

Heddinghaus T.R., A.F. Krueger (1981) Annual and interannual variations in Outgoing Longwave Radiation over the Tropics. *Mon. Wea. Rev.*, **109**, 1208-1218

Hibler W.D. III (1979) A dynamic thermodynamic sea-ice model. *J. Phys. Oceanogr.*, **9**, 815-846

Holland D.M., L.M. Mysak, D.K. Manak, J.M. Oberhuber (1993) Sensitivity Study of a Dynamic Thermodynamic Sea Ice Model. *J. Geophys. Res.*, **98**, 2561-2586

Ichie T., J. Petersen (1963) The anomalous rainfall of the 1957-58 winter in the equatorial central Pacific arid area. *J. Meteor. Soc. Japan.*, **41**, 172-182

Jacobs G.A., H.E. Hurlburt, J.C. Kindle, E.J. Metzger, J.L. Mitchell, W.J. Teague, A.J. Wallcraft (1994) Decade-scale trans-Pacific propagation and warming effects of an El Niño anomaly. *Nature*, **370**, 360-363

Janowiak J.E., P.A. Arkin, P. Xie, M.L. Morrissey, D.L. Legates (1995) An Examination of the East Pacific ITCZ Rainfall Distribution. *J. Climate*, **8**, 2810-2823

Ji M., A. Leetmaa, V.E. Kousky (1996) Coupled model predictions of ENSO during the 1980s and 1990s at the National Centers for Environmental Prediction. *J. Climate*, **9**, 3105-3120

Jin F.-F. (1997) A Theory of Interdecadal Climate Variability of the North Pacific Ocean-Atmosphere System. *J. Climate*, **10**, 1821-1835

Johns T.C., R.E. Carnell, J.F. Crossley, J.M. Gregory, J.F.B. Mitchell, C.A. Senior, S.F.B. Tett, R.A. Wood (1997) The second Hadley Centre coupled ocean-atmosphere GCM: model description, spinup and validation. *Climate Dyn.*, **13**, 103-134

Kawamura R. (1994) A rotated EOF analysis of global sea surface temperature variability with interannual and interdecadal timescales. *J. Phys. Oceanogr.*, **24**, 707-715

Kawamura R., M. Sugi, N. Sato (1995) Interdecadal and Interannual Variability in the Northern Extratropical Circulation Simulated with the JMA Global Model. Part I: Wintertime Leading Mode. *J. Climate* **8**: 3006-3019

Kraus E.B., J.S. Turner (1967) A one-dimensional model of the seasonal thermocline. *Tellus*, **1**, 88-97

Latif M., T. Stockdale, J.-O. Wolff, G. Burgers, E. Maier-Reimer, M.M. Junge, K. Arpe, L. Bengtsson (1994) Climatology and Variability in the ECHO coupled GCM. *Tellus*, **46A**, 351-366

Latif M., T.P. Barnett (1994) Causes of decadal climate variability over the North Pacific and North America. *Science*, **266**, 634-637

Latif M., T.P. Barnett (1996) Decadal variability over the North Pacific and North America: Dynamics and predictability. *J. Climate*, **9**, 2407-2423

Latif M., A. Grötzner, M. Münnich, E. Maier-Reimer, S. Venzke, T.P. Barnett (1996) A mechanism for decadal climate variability. in: Anderson and Willebrand (1996), 263-292.

Latif M., R. Kleeman, C. Eckert (1997) Greenhouse Warming, Decadal Variability, or El Niño? An Attempt to understand the Anomalous 1990s. *J. Climate* **10**: 2221-2239

Latif M. (1997) Dynamics of Interdecadal Variability in Coupled Ocean-Atmosphere Models. *J.Climate*, in press

Lau N.-C., M. J. Nath (1994) A Modeling Study of the Relative Roles of Tropical and Extratropical SST Anomalies in the Variability of the Global Atmosphere-Ocean System. *J. Climate* **7**: 1184-1207

Legates D.R., C.J. Wilmott (1990) Mean seasonal and spatial variability in gauge corrected global precipitation. *J. Climatol.* **10**, 111-127

Le Méhauté A., F. I. Utreras (1994) Convexity-preserving interpolatory subdivision. *Computer Aided Geometric Design*, **11**, 17-37

Levitus S. (1982) Climatological Atlas of the World Ocean. *NOAA Professional Paper* **13**

Lindzen R.S., Nigam S. (1987) On the role of sea surface temperature gradients in forcing low-level winds and convergence. *J. Atmos. Sci.*, **45**, 2416-2427

Lukas R., E.J. Lindstrom (1991) The mixed layer of the western equatorial Pacific ocean. *J. Geophys. Res.*, **96**, 3343-3357

Luksch U., H.v. Storch (1992) Modeling the Low-Frequency Sea Surface Temperature Variability in the North Pacific. *J. Climate*, **5**, 893-906

Lunkeit F., R. Sausen, J.M. Oberhuber (1996) Climate simulations with the global coupled atmosphere-ocean model ECHAM2/OPYC. Part I: present-day climate and ENSO events. *Cli-*

mate Dyn., **12**, 195-212

Luyten J.R., J. Pedlosky, H. Stommel (1983) The Ventilated Thermocline. *J. Phys. Oceanogr.* **13**, 292-309

Manabe S., R.J. Stouffer, M.J. Spelman, K. Bryan (1991) Transient responses of a coupled ocean-atmosphere model to gradual changes of atmospheric CO_2. Part I: annual mean response. *J. Climate*, **4**, 785-818

Mantua N.J., S.R. Hare, Y. Zhang, J.M. Wallace, R.C. Francis (1997) A Pacific interdecadal oscillation with impacts on salmon production. *Bull. Amer. Meteor. Soc.*, **78**, 1069-1079

May W. (1995) Der Einfluß des El Niño/Southern Oscillation Phänomens auf die atmosphärische Zirkulation in den mittleren Breiten der Nordhalbkugel: Beobachtungen und Modellsimulationen. PhD dissertation. ISSN 0938-5177. Available from the *Max Planck Institut für Meteorologie*, Bundesstr. 55, 20146 Hamburg, Germany

Maykut G.A., N. Untersteiner (1969) Numerical prediction of the thermodynamic response of Arctic sea ice to environmental changes. *The Rand Corporation, Santa Monica, Calif.*, RM-6093-PR

McFarlane N.A. (1987) The effect of orographically excited gravity wave drag on the general circulation of the lower stratosphere and troposphere. *J. Atmos. Sci.*, **44**, 1775-1800

Meyers S.D., M.A. Johnson, M. Liu, J.J. O'Brien, J.L. Spiesberger (1996) Interdecadal Variability in a Numerical Model of the Northeast Pacific Ocean: 1970-89. *J. Phys. Oceanogr.*, **26**, 2635-2652

Miller A.J., D.R. Cayan, W.B. White (1997) A Decadal Change in the North Pacific Thermocline and Gyre-Scale Circulation. *J. Climate, submitted*

Miller A.J., D.R. Cayan, T.P Barnett, N.E. Graham, J.M. Oberhuber (1994) Interdecadal Variability of the Pacific Ocean: model response to observed heat flux and wind stress anomalies. *Climate Dyn.*, **9**, 287-302

Miller M.J., T.N. Palmer, R. Swinbank (1989) Parameterizations and influence of sub-grid scale orography in general circulation and numerical weather prediction models. *Met. Atm. Phys.*, **40**, 84-109

Minobe S. (1997) Climate variability with periodicity of 50-70 years over the North Pacific and North America. *Geophys. Res. Lett.*, **24**, 683-686

Mitchell T.P., J.M. Wallace (1996) ENSO Seasonality: 1950-78 versus 1979-92. *J. Climate*, **9**, 3149-3161)

Morcrette J.J. (1991) Radiation and cloud-radiative properties in the European Centre for Medium Range Weather Forecasts forecasting system. *J. Geophys. Res.*, **96**, 9121-9132

Münnich M., M. Latif, S. Venzke, E. Maier-Reimer (1998) Decadal oscillations in a simple coupled model. *J. Climate*, accepted

Murphy J.M. (1995) Transient response of the Hadley Centre coupled ocean-atmosphere model to increasing carbon dioxide. Part I: control climate and flux adjustment. *J. Climate*, **8**, 36-80

Mysak L.A. (1986) El Niño, interannual variability and fisheries in the northeast Pacific Ocean. *Can. J. Fish Aquat. Sci.*, **43**, 464-497

Nakamura H., M. Tanaka, J.M. Wallace (1987) Horizontal structure and energetics of Northern Hemisphere wintertime teleconnection patterns. *J. Atmos. Sci.*, **44**, 3377-3391

Namias J. (1959) Recent seasonal interactions between North Pacific waters and the overlying atmospheric circulation. *J. Geophys. Res.*, **64**, 631-646

Namias J. (1979) Northern Hemisphere seasonal 700 mb height and anomaly charts, 1947-1978, and associated North Pacific sea surface temperature anomalies, CALCOFI Atlas No. **27**, *Scripps Institution of Oceanography*, 275 pp. (Library of Congress Catalog Card Number 67-4238)

Nitta T., S. Yamada (1989) Recent Warming of Tropical Sea Surface Temperature and Its Relationship to the Northern Hemisphere Circulation. *J. Met. Soc. Japan*, **67**, 375-383

Nordeng T.E. (1996) Extended versions of the convective parameterization scheme at ECMWF and their impact on the mean and transient activity of the model in the tropics. *Q. J. Roy. Met.*

Soc. (subm.)

Norris J.R. (1998) Low Cloud Type over the Ocean from Surface Observations. Part II: Geographical and Seasonal Variations. *J. Climate*, **11**, 383-403

Norris J.R., Leovy C.B. (1994) Interannual Variability in Stratiform Cloudiness and Sea Surface Temperature. *J. Climate*, **7**, 369-382

Oberhuber J. M. (1988) The budgets of heat, buoyancy and turbulent kinetic energy at the surface of the Global Ocean. *Max-Planck-Institut für Meteorologie* Report No. **15**

Oberhuber J.M. (1993a) Simulation of the Atlantic circulation with a coupled sea-ice mixed layer-isopycnal general circulation model. Part I: model description. *J. Phys. Oceanogr.*, **13**: 808-829

Oberhuber J.M. (1993b) The OPYC Ocean General Circulation Model. Deutsches Klimarechenzentrum (DKRZ), Technical Report No. **7**, 130 pp.; available from the *Deutsches Klimarechenzentrum*, Bundesstr. 55, 20146 Hamburg

Oberhuber J. M., E. Roeckner, M. Christoph, M. Esch, M. Latif (1998) Predicting the '97 El Niño event with a global climate model. *Geophys. Res. Lett.*, **25(13)**, 2273-2276

Ohlmann J.C., D. A. Siegel, C. Gautier (1996) Ocean Mixed Layer Radiant Heating and Solar Penetration: A Global Analysis. *J. Climate* **9**: 2265-2280

Oort A.H., J.Y. Yienger (1996) Observed Interannual Variability in the Hadley Circulation and Its Connection to ENSO. *J. Climate*, **9**, 2751-2767

Palmer T.N., G.J. Shutts, R. Swinbank (1986) Alleviation of a systematic westerly bias in general circulation and numerical weather prediction models through an orographic gravity wave drag parameterization. *Quart. J. Roy. Meteor. Soc.*, **112**, 1001-1031

Palmer T.N., D.A. Mansfield (1986a) A study of wintertime circulation anomalies during past El Niño events using a high resolution general circulation model. I: Influence of model climatology. *Quart. J. Roy. Meteor. Soc.*, **112**, 613-638

Palmer T.N., D.A. Mansfield (1986b) A study of wintertime circulation anomalies during past El Niño events using a high resolution general circulation model. II: Variability of the seasonal mean response. *Quart. J. Roy. Meteor. Soc.*, **112**, 639-660

Parker D.E., P.D. Jones, C.K. Folland, A. Bevan (1994) Interdecadal changes of surface temperature since the late nineteenth century. *J. Geophys. Res.* **99**, 14373-14399

Parker D.E., C.K. Folland, M. Jackson (1995) Marine surface temperature: observed variations and data requirements. *Clim. Change*, **31**, 559-600

Pedlosky J. (1987) An inertial theory of the equatorial undercurrent. *J. Phys. Oceanogr.*, **17**, 1978-1985

Peng S., W.A. Robinson, M.P. Hoerling (1997) The Modeled Atmospheric Response to Midlatitude SST Anomalies and Its Dependence on Background Circulation States. *J. Climate*, **10**, 971-987

Perlwitz J. (1997) Zeitscheibenexperimente mit dem atmosphärischen Zirkulationsmodell T42-ECHAM3 für eine verdoppelte und verdreifachte CO_2-Konzentration unter besonderer Beachtung der Änderungen der nordhemisphärischen troposphärischen Dynamik. PhD dissertation. ISSN 0938-5177. Available from the *Max Planck Institut für Meteorologie*, Bundesstr. 55, 20146 Hamburg, Germany

Picaut J., Tournier R. (1991) Monitoring the 1979-1985 equatorial Pacific current transports with expendable bathythermograph data. *J. Geophys. Res.*, **96**, suppl: 3263-3277

Pitcher E. J., M. L. Blackmon, G. T. Bates, S. Muñoz (1988) The Effect of North Pacific Sea Surface Temperature Anomalies on the January Climate of a General Circulation Model. *J. Atmos. Sci.*, **45**: 173-188

Power S.B.(1995) Climate Drift in a global ocean general circulation model. *J. Phys. Oceanogr.*, **25**, 1025-1036

Ramanathan V., W. Collins (1991) Thermodynamic regulation of ocean warming by cirrus clouds deduced from observations of the 1987 El Niño. *Nature*, **351**, 27-32

Rasmussen E.M., T.H. Carpenter (1982) Variations in tropical sea surface temperature and surface

wind fields associated with the Southern Oscillation/El Niño. *Mon. Wea. Rev.*, **110**, 354-384

Reinsch C.H. (1967) Smoothing by spline functions. *Numerische Mathematik*, **10**, 177-183

Ringer M.A., K.P. Shine (1997) Sensitivity of the Earth's radiation budget to interannual variations in cloud amount. *Climate Dyn.*, **13**, 213-222

Robertson A. W. (1996) Interdecadal variability over the North Pacific in a multi-century climate simulation. *Climate Dyn.*, **12**: 227-241

Rockel B., E. Raschke, B. Weyres (1991) A parameterization of broadband radiative transfer properties of water, ice and mixed clouds. *Beitr. Phys. Atmos.*, **64**, 1-12

Roeckner E., K. Arpe, L. Bengtsson, S. Brinkop, L. Dümenil, M. Esch, E. Kirk, F. Lunkeit, M. Ponater, B. Rockel, R. Sausen, U. Schlese, S. Schubert, M. Windelband (1992) Simulation of the present-day climate with the ECHAM model: impact of model physics and resolution. *Max-Planck-Institut für Meteorologie*, Report No. **93**, Hamburg, 171 pp.

Roeckner E. (1995) Parameterization of cloud-radiative properties in the ECHAM4 model. In: Proceedings of the WCRP Workshop on "Cloud Microphysics Parameterizations in Global Atmospheric Circulation Models", May 23-25, 1995, Kananaskis, Alberta, Canada, *WCRP-report* No. **90**, 105-116, WMO/TD-No.732

Roeckner E., Oberhuber J.M., A. Bacher, M. Christoph and I. Kirchner (1996a) ENSO variability and atmospheric response in a global coupled atmosphere-ocean GCM. *Climate Dyn.* **12**: 737-754

Roeckner E., Arpe K., Bengtsson L., Christoph M., Claussen M., Dümenil L., Esch M., Giorgetta M., Schlese U., Schulzweida U. (1996b) The atmospheric general circulation model ECHAM-4: model description and simulation of present-day climate. *Max-Planck-Institut für Meteorologie* Report No. **218**, 90 pp., Max-Planck-Institut für Meteorologie, Hamburg, Germany

Rogers J.C., R.V. Rohli (1991) Florida citrus freezes and polar anticyclones in the Great Plains. *J. Climate*, **4**, 1103-1113

Rogers J.C., M.N. Raphael (1992) Meridional eddy sensible heat fluxes in the extremes of the Pacific/North American teleconnection pattern. *J. Climate*, **5**, 127-139

Ronca R.E., D.S. Battisti (1997) Anomalous Sea Surface Temperatures and Local Air-Sea Energy Exchange on Intraannual Timescales in the Northeastern Subtropical Pacific. *J. Climate*, **10**, 102-117

Ropelewski C.F., M.S. Halpert (1987) Global and regional scale precipitation associated with El Niño/Southern Oscillation. *Mon. Wea. Rev.*, **115**, 1606-1626

Rowntree P.R. (1972) The influence of tropical east Pacific Ocean temperature on the atmosphere. *Quart. J. Roy. Meteor. Soc.*, **98**, 290-321

Sausen R., K. Bartel, K. Hasselmann (1988) Coupled ocean-atmosphere models with flux correction. *Climate Dyn.*, **2**, 145-163

Sausen R., F. Lunkeit (1990) Some remarks on the Cause of the Climate Drift of Coupled Ocean-Atmosphere Models. *Beitr. Phys. Atmos.*, **63**, 141-146

Sausen R., S. Schubert, L. Dümenil (1994) A model of river run-off for use in coupled atmosphere-ocean models. *J. Hydrol.*, **155**, 337-352

Schopf P.S., M.J. Suarez (1988) Vacillations in a coupled ocean-atmosphere model. *J. Atmos. Sci.*, 45, 549-566

Semtner A.J. (1976) A Model for the Thermodynamic Growth of Sea Ice in Numerical Investigations of Climate. *J. Phys. Oceanogr.*, **6**, 379-389

Shukla J., J.M. Wallace (1983) Numerical Simulation of the Atmospheric Response to Equatorial Pacific Sea Surface Temperature Anomalies. *J. Atmos. Sci.*, **40**, 1613-1630

Stockdale T.N., D.L.T. Anderson, J.O.S. Alves, M.A. Balmaseda (1998) Global seasonal rainfall forecasts using a coupled ocean-atmosphere model. *Nature*, **392**, 370-373

Storch J.S. (1994) Interdecadal variability in a global coupled model. *Tellus*, **46A**, 419-432

Stricherz J.N., J.J. O'Brien, D.M. Legler (1992) Atlas of Florida State University tropical Pacific winds for TOGA 1966-1985. *The Florida State University*, Mesoscale Air-Sea Interaction

Group, Tallahassee, Florida
Stricherz J.N., J.J. O'Brien, D.M. Legler (1993) Atlas of Florida State University Indian Ocean winds for TOGA 1970-1985. *The Florida State University*, Mesoscale Air-Sea Interaction Group, Tallahassee, Florida
Suarez M.J., P.S. Schopf (1988) A delayed oscillator for ENSO. *J. Atmos.Sci.*, 45, 3283-3287
Tiedtke M. (1989) A comprehensive mass flux scheme for cumulus parameterization in large-scale models. *Mon. Wea. Rev.*, **117**, 1779-1800
Ting M., M. P. Hoerling, Taiyi Xu, A. Kumar (1996) Northern Hemisphere Teleconnection Patterns during Extreme Phases of the Zonal-Mean Circulation. *J. Climate*, **9**: 2614-2633
Trenberth K.E. (1990) Recent observed interdecadal climate changes in the Northern Hemisphere. *Bull. Am. Meteor. Soc.*, **71**, 988-993
Trenberth K. E., J. W. Hurrell (1994) Decadal atmosphere-ocean variations in the Pacific. *Climate Dyn.*, **9**: 303-319
Trenberth K. E., D. J. Shea (1987) On the evolution of the Southern Oscillation. *Mon. Wea. Rev.*, **115**, 3078-3096
Walker G.T: (1924) Correlations in seasonal variations of weather. VII. A preliminary study of world weather. *Mem. Indian Meteor. Dep.* **24**(4), 75-131
Walker G.T: (1925) Correlations in seasonal variations of weather. IX. A further study of world weather. *Mem. Indian Meteor. Dep.* **24**(9), 275-332
Walker G.T. (1928) World Weather. III. *Mem. R. Meteor. Soc.*, **2**, 97-106
Walker G.T., E.W. Bliss (1930) World Weather. IV. *Mem. R. Meteor. Soc.*, **3**, 81-95
Walker G.T., E.W. Bliss (1932) World Weather. V. *Mem. R. Meteor. Soc.*, **4**, 53-84
Walker G.T., E.W. Bliss (1937) World Weather. VI. *Mem. R. Meteor. Soc.*, **4**, 119-139
Wallace J.M., D.S. Gutzler (1981) Teleconnections in the geopotential height field during the Northern Hemisphere winter. *Mon. Wea. Rev.*, **109**, 784-812
Wallace J.M., C. Smith, Q. Jiang (1990) Spatial Patterns of Atmosphere-Ocean Interaction in the Northern Winter. *J. Climate*, **3**, 990-998
Wallace J.M., C. Smith, C.S. Bretherton (1992) Singular value decomposition of wintertime sea surface temperature and 500-mb height anomalies. *J. Climate*, **5**, 561-576
Wallace J.M., Y. Zhang, K.-H. Lau (1993) Structure and Seasonality of Interannual and Interdecadal Variability of the Geopotential Height and Temperature Fields in the Northern Hemisphere Troposphere. *J. Climate*, **6**: 2063-2082
Weare B.C., A.R. Navato, R.E. Newell (1976) Empirical orthogonal analysis of Pacific sea surface temperatures. *J. Phys. Oceanogr.*, **6**, 671-678
Weare B.C. (1997) Climatic variability of cloud radiative forcing. *Quart. J. R. Meteor. Soc.*, **123**, 1055-1073
White W.B. (1995) Design of a global observing system for gyre-scale upper ocean temperature variability. *Progr. Oceanogr.*, **36**(3), 169-217
White W.B., T.P. Barnett (1972) A Servomechanism in the Ocean/Atmosphere System of the Mid-Ltitude North Pacific. *J. Phys. Oceanogr.*, **2**, 372-381
White W.B., J.F.T. Saur (1983) Sources of Interannual Baroclinic Waves in the Eastern Subtropical North Pacific. *J. Phys. Oceanogr.*, **13**, 531-544
Williamson, D.L., P.J. Rasch (1994) Water vapor transport in the NCAR CCM2. *Tellus*, **46A**, 34-51
Woodruff S.D., R.J. Slutz, R.L. Jenne, P.M. Steurer (1987) A comprehensive ocean-atmosphere dataset. *Bull. Amer. Meteor. Soc.*, **68**, 1239-1250
Wyrtki K. (1975) El Niño - The dynamic response of the equatorial Pacific Ocean to atmospheric forcing. *J. Phys. Oceanogr.*, **5**, 572-584
Wyrtki K., Kilonsky B. (1984) Mean water and current structure during the Hawaii-to-Tahiti shuttle experiment, *J. Phys. Oceanogr.*, **14**, 242-254
Xu W., T.P. Barnett, M. Latif (1998) Decadal Variability in the North Pacific as Simulated by a Hybrid Coupled Model. *J. Climate*, **11**, 297-312
Yasuda T., K. Hanawa (1996) Decadal Changes in the Mode Waters in the Midlatitude North

Pacific. *J. Phys. Oceanogr.*, **27**, 858-870

Yukimoto S., M. Endoh, Y. Kitamura, A. Kitoh, T. Motoi, A. Noda, T. Tokioka (1996) Interannual and interdecadal variabilities in the Pacific in an MRI coupled GCM. *Climate Dyn.*, **12**, 667-683

Zhang R.-H., S. Levitus (1997) Structure and Cycle of Decadal Variability of Upper Ocean Temperature in the North Pacific. *J. Climate* **10**, 710-727

Zhang R.-H., L.M. Rothstein, A.J. Busalacchi (1998) Origin of upper-ocean warming and El Niño change on decadal scales in the tropical Pacific Ocean. *Nature*, **391**, 879-883

Zhang Y., J.M. Wallace, N. Iwasaka (1996) Is Climate Variability over the North Pacific a Linear Response to ENSO? *J. Climate*, **9**: No. 7, 1468-1478

Zhang Y., J. M. Wallace, D. S. Battisti (1997) ENSO-like Interdecadal Variability: 1900-93. *J. Climate*, **10**, 1004-1020